

**Two-Dimensional Spatial Control using
Multiple Circular Loudspeaker Arrays
and Elliptical Loudspeaker Array**

by

Yi Ren

A thesis submitted for the degree of
Doctor of Engineering

Department of Informatics,
Graduate School of Informatics and Engineering,
The University of Electro-Communications

March 2022

**Two-Dimensional Spatial Control using
Multiple Circular Loudspeaker Arrays
and Elliptical Loudspeaker Array**

Approved by the Supervisory Committee

Chairperson: Professor Yoichi HANEDA
Member: Professor Kouichi HIROTA
Member: Professor Hideyuki NOMURA
Member: Associate Professor Naoya KOIZUMI
Member: Associate Professor Hiroki TAKAHASHI

Copyright © 2022 Yi Ren

All rights reserved.

論文要旨

本研究は、スピーカアレイを用いた2次元音場制御に関する研究である。音場制御とは空間において音の波面全体を制御する技術であり、音場再現、指向性制御や空間騒音制御などに応用される。特に音場再現では、高臨場感音響再生技術の一環として、現実空間と距離の離れた別の空間のユーザが擬似的に重なり、その場にいるかのような聴覚体験を提示することが可能になる。これらの音場制御技術の発展に伴って、立体テレビ、立体コミュニケーションシステムやバーチャルライブなどの実現が期待できる。

これまで多くのスピーカアレイを用いた音場制御手法が提案されているが、特に理論的解析や形状のわかりやすさから直線や円といった基本的なアレイ形状が多く用いられてきた。一方、素子配置が決まっているシステムや素子配置の設計を含めたプロジェクトに適している最適化手法は、性能を最大限に引き出すことができるが、一般家庭での実装が困難で、汎用性に欠けている。そこで、シンプルではないスピーカ配置においても解析的な制御を可能とするスピーカアレイの形状に着目した研究を行う。

本研究では、音場制御システムの基本要素の1つであるスピーカアレイの音響的特性に着目し、新たなスピーカアレイの形状を提案することによって、制御の多様性を増やし、制御性能を向上させることを試みる。本来、考慮すべきアレイ形状は無限にあるが、本論文においてはまず2つのアレイ形状に注目する。従来の円形スピーカアレイを変形させることによって、複数の円形アレイを用いた再生モデルである複数剛円スピーカアレイおよび円形アレイを扁平させたような形状である楕円スピーカアレイを提案する。複数剛円スピーカアレイに対し、アレイ中心のずれや無限に往来する散乱作用を考慮した解析的制御手法を提案する。楕円スピーカアレイに対し、楕円座標系およびその波動関数解を用いた新たな解析的音場制御手法を提案する。計算機シミュレーションの結果により制御手法は有効であることがわかった。複数の場面において、提案アレイは従来のアレイ形状より良い結果を得られ、アレイ形状の提案による制御性能向上の可能性を示した。また、アレイ形状の特徴が音場制御の性能に与える影響について調べた。

ABSTRACT

This study discusses two-dimensional spatial control using loudspeaker arrays. Spatial control is a technique for the spatial processing of sound waves in a confined space. Sound field reproduction, directivity control, and spatial active noise control are applications of spatial control. In particular, sound field reproduction, which replicates the sound experience in space, is extremely important for 3D audio systems. Further development of this technique would allow 3D television, 3D communication systems, and virtual live concerts to be realised.

A variety of methods on spatial control, using loudspeakers, have been proposed. Basic array shapes, e.g., linear or circular loudspeaker arrays, have been the special focus of these studies. The optimised methods are applied to specific array geometries to maximise performance. However, it is difficult to apply these methods to general audio systems with the performances differing from place to place. In this study, analytical methods controlling complex array geometries are discussed.

The focus is on the acoustical properties of the loudspeaker array, which is the basic component of a spatial control system. This study suggests a novel approach on enhancing the spatial control technique: proposing new array geometries that have analytical solution to diversify the control. Although there are a multitude of array geometries that can be taken into consideration, this study focuses on two array models as the first attempt on the approach. The conventional circular array is modified to consider the two models: the multiple rigid circular arrays model which sets up multiple conventional arrays as one model and the elliptical array model which can be considered a flattened conventional array. Analytical control methods are proposed for both array models, either considered the centre-shifted arrays with multiple scattering effect, or introduced a novel spatial control theory based on elliptical coordinate system. The results reveal the validity of the proposed methods. The proposed arrays outperform conventional arrays in several situations, showing a possibility of the approach on proposing analytical controllable arrays. In addition, the influence of several array features on spatial control is investigated, giving a further prospect on designing a high performance array geometry.

Acknowledgements

I would like to express my heartfelt gratitude and respect to my supervisor *Prof. Yoichi Haneda*. THANK YOU for all of your support and advice during the years. You have not only taught me all the knowledge and techniques, supervised the whole thesis, but also been my life mentor.

I would like to give special acknowledgement to *the NEC C&C Foundation* and *Tonen International Scholarship Foundation* for contributing financial support during my PhD. I would not have managed to balance between research and living this well without your help.

I would also like to thank the people who directly and indirectly gave me advice on my work and career, beginning with the members of the Review Board, *Prof. Koichi Hirota*, *Prof. Hideyuki Nomura*, *Prof. Hiroki Takahashi*, and *Prof. Naoya Koizumi* for their advice on improving the thesis; *Prof. Emer. Kiyoshi Sugiyama* from *Tokyo Polytechnic University* for the advice and discussion on the multiple scattering effect; *Prof. Yutaka Kaneda* from *Tokyo Denki University* for the advice on impulse response measurement and also personal advice; *Dr. Takuma Okamoto* from *National Institute of Information and Communications Technology* and *Dr. Natsuki Ueno* from *Tokyo Metropolitan University* for the discussions and ideas for improving this study; *Dr. Yuma Koizumi* (from *Google Research*) as the representative of *ASJ Student & Young Researchers Forum* for his advice, as well as the whole forum for being an amazing community for young researchers in Japan; *Dr. Kimitaka Tsutsumi* from *NTT Human Informatics Laboratories* as one co-author of a related paper. Thank you all for your kindness help and being great examples in my academic career.

My thanks also go to all my colleagues at the laboratory, especially the former members *Mr. Koya Sato* (now in *Sony Corporation*) and *Mr. Kenta Imaizumi* (now in *NTT Human Informatics Laboratories*) who directly supported this work, and *Mr. Yu Ito* (now in *Honda Motor Co., Ltd*) for hanging out with me a long time inside and outside the laboratory. Every moment in the laboratory has been the most precious memory of mine.

A special thank to *Mr. Israel Mendoza Velázquez*, a great colleague and a great friend. The simplest word stands for all: Gracias! Also thanks to my best friend *Mr. Chen Chen*, who helped immensely during my life here in Japan.

Finally, I would like to thank my dearest parents for their continuous support and endless love throughout my life. 爸爸、妈妈，感谢你们的培养和一直以来的支持，我爱你们！

Contents

Nomenclature	1
1 Introduction	4
1.1 Background	4
1.2 Motivation	7
1.3 Outline of Thesis	8
2 Fundamentals of Spatial Control	10
2.1 Wave Equation and Kirchhoff-Helmholtz Integral Equation	10
2.2 Spatial Fourier Transform	12
2.2.1 In Cartesian Coordinate System	13
2.2.2 In Polar Coordinate System	14
2.3 Sound Field Representation in Polar Coordinate System	15
2.4 Approaches of Sound Field Reproduction	16
2.4.1 Traditional Wave Field Synthesis	16
2.4.2 Simple Source Approach	17
2.5 Sound Field Reproduction Methods	18
2.5.1 Inverse Filter Based Method (A Numerical Approach)	18
2.5.2 Wave Domain Method (An Analytical Approach)	19
2.6 Applications of Spatial Control	21
2.6.1 Interior Sound Field Reproduction	21
2.6.2 Exterior Sound Field Reproduction	24
2.6.3 Beamforming	29
2.7 Summary	35
3 Multiple rigid circular loudspeaker array	36
3.1 Multiple scattering effect	36
3.2 Transfer function of the multiple rigid circular loudspeaker array	38
3.3 Circular harmonics based sound field reproduction method	39
3.4 Mode strength	42
3.5 Interior sound field reproduction	45
3.6 Exterior sound field reproduction	47
3.6.1 Comparison with CLA	47
3.6.2 2CLA Properties on Exterior Sound Field Reproduction	56
3.7 Beamforming	63
3.7.1 Comparison with CLA	63
3.7.2 2CLA Properties on Beamforming	68
3.8 Summary	73

4	Elliptical loudspeaker array	74
4.1	Elliptical coordinate system	74
4.2	Wave representation in elliptical coordinates	74
4.2.1	Mathieu functions	75
4.2.2	Mathieu function expansion	76
4.2.3	Rigid elliptical scatter	77
4.3	Mathieu function based sound field reproduction method	78
4.4	Circle-ellipse transformation	80
4.5	Mode strength	82
4.6	Interior sound field reproduction	83
4.6.1	MFE-based method	83
4.6.2	Circle-ellipse transformation	85
4.7	Exterior sound field reproduction	87
4.7.1	Comparison with CLA, 2CLA, and LLA	87
4.7.2	ELA Properties on Exterior Sound Field Reproduction	91
4.8	Beamforming	97
4.8.1	Comparison with CLA, 2CLA, and LLA	97
4.8.2	ELA Properties on Beamforming	103
4.9	Summary	110
5	General sound field reproduction method based on MFE	111
5.1	The general method	111
5.2	Truncation order	112
5.3	Interior sound field reproduction	114
5.4	Exterior sound field reproduction	115
5.5	Summary	116
6	Conclusion	117
	APPENDIX	120
A	Spectral Division Method	120
B	Exterior Multi-zone Reproduction	122
B.1	Conventional studies	122
B.2	Proposed Method	123
B.3	Limitations	125
B.4	Results	126
C	Mathieu function based multi-zone reproduction	128
D	Experimental results in an anechoic chamber	130
D.1	Loudspeaker array prototypes	130
D.2	Results on exterior sound field reproduction	130
D.3	Results on beamforming	133
	References	137
	List of Publications	145

List of Figures

1.1	Sound field reproduction using a linear loudspeaker array.	5
1.2	Infinite reflections exist between rigid baffles.	7
1.3	Methods of sound field reproduction [26, 37, 38, 43–45]	9
2.1	A two-dimensional space Ω and its boundary $\partial\Omega$	11
2.2	A closed boundary divides a two-dimensional space into two.	13
2.3	Polar coordinate system.	14
2.4	Circular harmonic modes with respect to orders	15
2.5	The boundary $\partial\Omega$ divides the two-dimensional space.	17
2.6	A model of interior sound field reproduction.	22
2.7	An example of reproducing the interior sound field of a plane wave.	23
2.8	Reproduction error of the reproduced sound field.	23
2.9	A model of exterior sound field reproduction.	24
2.10	A model of focused source reproduction.	25
2.11	An example on reproducing a focused source.	26
2.12	An example on reproducing a focused source with regularisation.	27
2.13	Reproduction error of the reproduced sound field.	27
2.14	Reproduction error over a region.	28
2.15	An example beam.	31
2.16	Beam pattern at 1000 Hz of the example beam.	32
2.17	Directivity index of the example beam.	32
2.18	Beam width of the example beam.	33
2.19	Side lobe level of the example beam.	34
3.1	A configuration of three scatters.	37
3.2	Relative amplitude of each reflection of a 2CLA.	39
3.3	Mode strength of a rigid 2CLA.	42
3.4	Mode strength of a rigid CLA.	43
3.5	Mode strength of an open 2CLA.	44
3.6	Interior reproduction without multiple scattering.	45
3.7	Interior reproduction with mismatched multiple scattering.	46
3.8	Interior reproduction with multiple scattering.	46
3.9	Contours of five arrays.	47
3.10	Reproducing a focused source using a CLA.	49
3.11	Reproducing a focused source using 2CLA.	50
3.12	Reproducing a focused source using a rotated 2CLA.	50
3.13	Reproducing a focused source using 3CLA.	50
3.14	Reproducing a focused source using a rotated 3CLA.	51
3.15	Reproducing random focused sources using CLA.	51
3.16	Reproducing random focused sources using 2CLA.	52
3.17	Reproducing random focused sources using 3CLA.	52
3.18	Reproduction error over a region (Group A).	53
3.19	Reproducing a focused source using an off-centred 2CLA.	54

3.20	Reproducing a focused source using an off-centred 3CLA.	54
3.21	Reproduction error over a region (Group B).	55
3.22	Reproducing a focused source using CLA.	56
3.23	Reproducing a focused source using 3CLA.	56
3.24	Reproducing a focused source using 5CLA.	57
3.25	Reproduction error over a region (Group C).	58
3.26	Direction dependence of 2CLA on focused source reproduction. . .	59
3.27	Direction dependence of an off-centred 2CLA.	60
3.28	The influence of radii and inter-array distance of 2CLA, (i)	61
3.29	The influence of radii and inter-array distance of 2CLA, (ii)	61
3.30	Beam patterns of MCLAs in group A.	63
3.31	DI, BW, and SLL of MCLAs in group A	65
3.32	Beam patterns of MCLAs in group C.	66
3.33	DI, BW, and SLL of MCLAs in group C.	67
3.34	DI, BW, and SLL of 2CLA for look directions between 0° and 90° . .	69
3.35	Radius and distance dependence of DI, BW, and SLL, 0°	71
3.36	Radius and distance dependence of DI, BW, and SLL, 90°	72
4.1	Elliptical coordinate system.	75
4.2	Harmonic modes of Mathieu functions with different orders.	76
4.3	A sound field with a rigid elliptical scatter.	78
4.4	A flow chart of the proposed circle-ellipse transformation.	81
4.5	Mode strength of a rigid ELA.	82
4.6	A plane wave reproduced by an ELA, (i)	83
4.7	A plane wave reproduced by an ELA, (ii)	83
4.8	Reproduction error with different truncation orders.	84
4.9	A plane wave reproduced with circle-ellipse transformation, (i) . . .	85
4.10	A plane wave reproduced with circle-ellipse transformation, (ii) . . .	85
4.11	Reproduction error with different number of microphones.	86
4.12	Focused source reproduced by an “on x” rigid ELA	87
4.13	Focused source reproduced by an “on y” rigid ELA	87
4.14	Reproduction error over a region: ELA, CLA, and 2CLA.	89
4.15	Reproduction error over a region: ELA, CLA, 2CLA, and LLA.	90
4.16	Direction dependency of an ELA on focused source reproduction. . .	91
4.17	Influence on the axis length, (i), focused source reproduction	93
4.18	Influence on the axis length, (ii), focused source reproduction	94
4.19	Influence on the flattening, (i), focused source reproduction	95
4.20	Influence on the flattening, (ii), focused source reproduction	96
4.21	Beam patterns of ELAs, CLA and 2CLAs.	97
4.22	DI, BW, and SLL of ELAs, CLA, and 2CLAs.	99
4.23	Beam patterns of ELA, CLAs, 2CLA, and LLAs.	100
4.24	DI, BW, and SLL of ELA, CLAs, 2CLA, and LLAs, 0°	101
4.25	DI, BW, and SLL of ELA, CLAs, 2CLA, and LLAs, 90°	102
4.26	DI, BW, and SLL of ELA in look directions between 0° and 90° . .	104
4.27	Influence on the axis length, (i), beamforming.	106
4.28	Influence on the axis length, (ii), beamforming.	107
4.29	Influence on the flattening, (i), beamforming.	108
4.30	Influence on the flattening, (ii), beamforming.	109
5.1	Truncation error of plane waves.	112
5.2	Single plane wave reproduced by a rectangular array.	114
5.3	Random plane waves reproduced by a rectangular array	115

5.4	Focused source reproduced by a rectangular array.	116
B.1	Model of exterior sound field reproduction.	124
B.2	Results of multi-zone reproduction.	127
C.1	Reproduced sound field of an ELA.	129
D.1	Photograph of the CLA prototype.	131
D.2	The model of the sound field measurement device.	132
D.3	Photograph of sound field measurement setup.	132
D.4	Theoretical two-dimensional primary sound field.	133
D.5	Focused source reproduced by a CLA.	133
D.6	Focused source reproduced by a 2CLA	134
D.7	Focused source reproduced by a CLA, local reproduction.	134
D.8	A photograph of the directivity measurement.	135
D.9	Beam patterns of experimental data in the 0° look direction.	136
D.10	Beam patterns of experimental data in 90° look direction.	136

Nomenclature

Special functions

$\delta(\cdot)$ Dirac delta function

$\delta_{\nu\nu'}$ Kronecker delta

$\text{sgn}(\cdot)$ Signum function

$e^{j\nu\phi}$ ν -th order circular harmonics

$H_\nu^{(1)}(\cdot), \mathcal{B}_\nu^{(3)}(\cdot)$ ν -th order Hankel function of the first kind

$H_\nu^{(2)'}(\cdot)$ Derivative of ν -th order Hankel function of the second kind

$H_\nu^{(2)}(\cdot), \mathcal{B}_\nu^{(4)}(\cdot)$ ν -th order Hankel function of the second kind

$J'_\nu(\cdot)$ Derivative of ν -th order Bessel function

$J_\nu(\cdot), \mathcal{B}_\nu^{(1)}(\cdot)$ ν -th order Bessel function

$M_\nu^{(\zeta)' }(\cdot)$ Derivative of ν -th order Mathieu radial function of the ζ -th kind ($\zeta \in \{1, 2, 3, 4\}$)

$M_\nu^{(\zeta)}(\cdot)$ ν -th order Mathieu radial function of the ζ -th kind ($\zeta \in \{1, 2, 3, 4\}$)

$me_\nu(\cdot)$ ν -th order Mathieu angular function

$Y_\nu(\cdot), \mathcal{B}_\nu^{(2)}(\cdot)$ ν -th order Neumann function

Number sets, vectors and matrices

(ξ, η) Elliptical coordinates of \mathbf{x}

(r, ϕ) Polar coordinates of \mathbf{x}

(x, y) Cartesian coordinates of \mathbf{x}

$\mathbf{0}_{l \times k}$ Zero matrix of size $l \times k$ ($\mathbf{0}_{ij} = 0$)

\mathbf{n} Normal vector

\mathbf{x} Position vector

\mathbb{C} Complex numbers

\mathbb{R} Real numbers

\mathbb{Z} Integer numbers

\mathbf{I}_l Identity matrix of size $l \times l$ ($\mathbf{I}_{ij} = \delta_{ij}$)

Ω	Space area
Ω_{\triangleleft}	Region of Ω inside $\partial\Omega$
Ω_{\triangleright}	Region of Ω outside $\partial\Omega$
$\partial\Omega$	Closed boundary of Ω

Operators

$(\cdot)^*$	Complex conjugate ($(a + bj)^* = a - bj$)
$(\cdot)^{-1}$	Inverse matrix ($\mathbf{A}^{-1}\mathbf{A} = \mathbf{A}\mathbf{A}^{-1} = \mathbf{I}$)
$(\cdot)^\dagger$	Pseudo inverse matrix
$(\cdot)^H$	Conjugate transpose ($[\mathbf{A}^H]_{ij} = \mathbf{A}_{ji}^*$)
$(\cdot)^T$	Transpose ($[\mathbf{A}^T]_{ij} = \mathbf{A}_{ji}$)
$\#\mathbb{A}$	Number of elements in set \mathbb{A}
$\frac{\partial}{\partial \mathbf{n}}$	Derivative of the normal direction
∇^2	Laplace operator
$\sigma_{\max}(\cdot)$	Maximum eigenvalue
$\ \cdot\ _2^2$	Squared L2 norm ($\ \mathbf{a}\ _2^2 = \sum_i a_i^2$)
$\text{diag}(\cdot)$	Diagonal matrix of a vector

Physics and mathematical constants

π	Archimedes' constant (≈ 3.1415926)
c	Speed of sound in air (≈ 340 m/s)
e	Euler's number (≈ 2.7182818)
j	Imaginary unit ($= \sqrt{-1}$)

Other symbols

\check{f}	Expansion coefficient of function f with respect to a basis including cylindrical functions and circular harmonics
\tilde{f}	Mathieu function expansion coefficient of function f with respect to a basis of Mathieu angular functions
\hat{f}	Expansion coefficient of function f with respect to a basis including Mathieu angular and radial functions
\hat{p}	Sound pressure reproduced by secondary sources
λ	Regularisation parameter
L	Number of loudspeakers
\mathring{f}	Circular harmonic expansion coefficient of function f with respect to a basis of circular harmonics

M	Number of microphones (as observation points)
ω	Angular frequency
\tilde{f}	Spatial Fourier transform of function f with respect to a basis $e^{jk_x x}$
ε	Error
d_l	Driving function of the l -th loudspeaker
k	Wave number
p	Sound pressure
t	Time

Chapter 1

Introduction

1.1 Background

Acoustic spatial control, which is also referred to as sound field control, is a technique that processes the sound field and is widely applied in the audio industry. With the recent development of new-generation network communication and electronic devices, applications of the spatial control technique, such as sound field reproduction, beamforming, and spatial noise control, have witnessed rapid growth.

Sound field reproduction, the best-known application of spatial control, aims to present the listener with the experience of a space of sound from somewhere else in the world, or even a fully virtual space. The basic idea of sound field reproduction was proposed based on Huygens' principle back in 1968 [1]. Subsequently, methods including wave field synthesis [2, 3] and Ambisonics [4, 5] were proposed. Over the decades, an enormous number of studies on sound field reproduction have been carried out, significantly improving both the versatility and practicability of the technique. Sound field reproduction is an important technique in immersive audio or 3D audio, with great potential for next-generation audio systems. It is expected to present people with a 'realistic' virtual world using 3D video techniques.

Beamforming is another important technique in array signal processing studies [6–10]. It is widely applied to antenna arrays, sensor arrays, and microphone arrays. In acoustics studies, the applications of beamforming include speech enhancement, source tracking, and acoustic imaging (even including medical use), among others. As for the reproduction part, the technique is also applied to loudspeaker arrays for controlling radiation patterns or directivity. Thus, it is also referred to as directivity control [11–15]. Applications including broadcasting, private audio zone, binaural reproduction have been discussed in this field of study. A recent study even reported that the acoustic force of a beam can be used to lift objects [16].

Another important application of spatial control is spatial noise control. Unlike the traditional noise control technique that cancels noise at specific positions, spatial noise control suppresses noise over a space region to generate a quiet area. The development of modern vehicles has rapidly increased the need for this application. However, cancelling noise over a large area remains challenging using existing techniques.

In this study, aiming for a perceptual reproduction, sound field reproduction is discussed as the main topic. As radiation patterns affect the sound field, the discussion also includes beamforming. Note that noise control over space can be considered as sound field reproduction, reproducing a phase-inverted noise field.

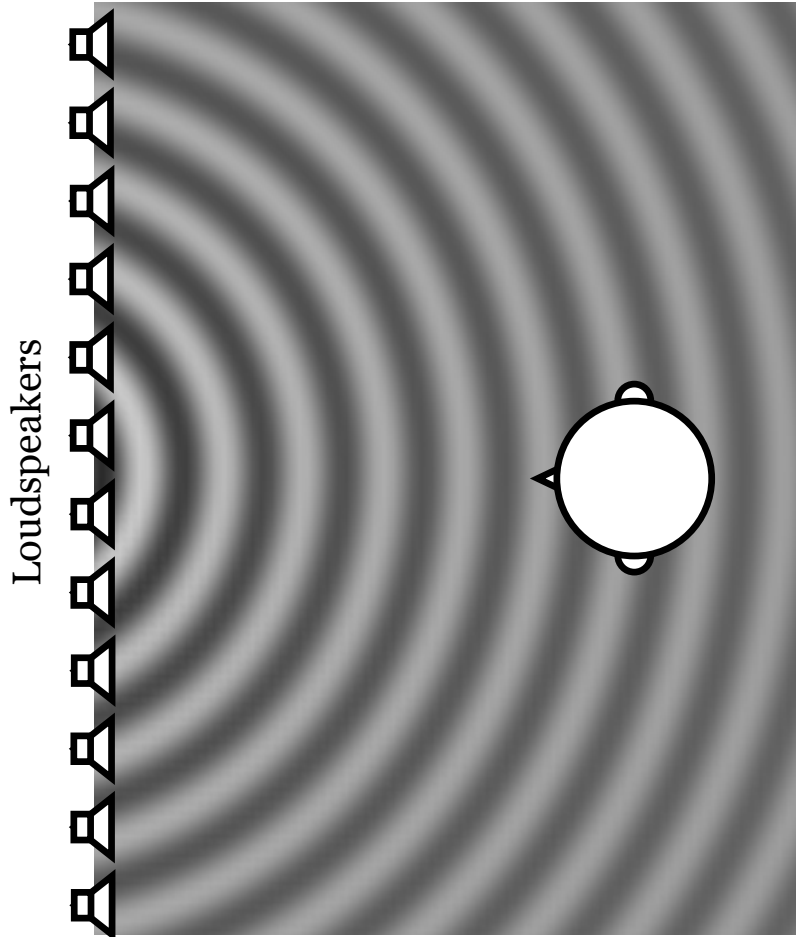


Figure 1.1: Sound field reproduction using a linear loudspeaker array.

It is possible to infer the performance of noise control over space through the results of sound field reproduction implicitly.

Methods for perceptual reproduction can be categorised as perception-based methods and physics-based methods. Stereophonic, periphonic, and binaural reproduction are examples of perception-based methods, and the sound field reproduction is an example of a physics-based method.

The conventional perception-based reproduction methods including stereophonic [17] and periphonic [18, 19] provide ideal perception in a limited sweet-spot. Another reproduction method called binaural audio, which is generally implemented by headphones, is not influenced by the listening position. In general, the perceptual sound does not react to the movement of a listener himself/herself, which results in an additional problem of lateralisation [20, 21]. Perception-based methods feature a better perceptual experience, while retaining sensitivity changes of the system. However, perception-based methods sometimes require specific settings or operations by professional engineers.

Various sound field reproduction methods have been proposed to implement a realistic perceptual environment using a set of loudspeakers, i.e., the loudspeaker array [3, 22]. Figure 1.1 shows an example of sound field reproduction using a linear loudspeaker array. The methods literally reproduce a sound field, i.e., reproduce/control the sound wave over a space region. Using this technique, it is possible to obtain ideal perception over the space region, meaning that the listening position is not limited to a sweet-spot. Furthermore, the problem

of binaural audio is solved; the sound field is physically reproduced; and the listener acquires the proper perception corresponding to the listener's position. This sound reproduction provides the listener with a realistic and immersive perceptual experience. In addition, in contrast to perception-based methods, physics-based methods are rather robust to system changes.

In this study, physics-based methods are employed for a wider listening area and a robust performance over systems. The methods are also highly compatible with beamforming.

The signal-processing part of physics-based methods can be divided into numerical approaches [23–25] and analytical approaches [26–29]. The numerical approaches can be applied to variable types of arrays and rooms. They can also provide optimised performance in specific reproduction scenarios. However, the performance over space is not predicable and further analysis of the results does not provide any additional clarification. In contrast, the analytical approaches are usually designed for a specific type of array, even without considering room reverberation. The results of analytical approaches are promising and can be explained by theories. Carrying out an analysis of its results is easy and further development of the methods is to be expected.

In addition to signal-processing methods, array geometry is also extremely important, especially for the analytical approach. Conventional studies on spatial control most often use the linear loudspeaker array (LLA), circular loudspeaker array (CLA), or spherical loudspeaker array [27,28]. As only the two-dimensional sound field is discussed in this study, further discussions on spherical arrays are excluded. In addition, irregular-shape arrays such as room-shape rectangular arrays are introduced for practical applications.

LLA [30–32] is the simplest array model with loudspeakers most often uniformly placed in a straight line. The original LLA concept is an infinite-length array because an infinite line can divide a two-dimensional space into two to satisfy the Kirchhoff-Helmholtz integral equation. However, in practical applications, common LLAs are usually finite-length arrays. This mismatch in the precondition further introduces errors in reproduction systems, which have a great influence on the performance at low frequencies. Moreover, LLAs exhibit direction dependent performance. Generally, sound field reproduction studies are applied in the direction perpendicular to the LLA, referred to as the board-side direction. Beamforming studies are more likely to be applied in the direction of the LLA, i.e., the direction of the line along which the loudspeakers are located, referred to as the end-fire direction). Note that the LLA has mirror symmetry such that the reproduced fields on both sides of the array are always the same.

CLA [33–36] is also one of the most common arrays used in two-dimensional spatial control. The CLA, benefits from rotation symmetry, having a robust performance over directions. In addition, an excellent property of CLA is that the circle is a basic shape in polar coordinates - one of the orthogonal coordinate systems. With the method introduced later in Chapter 2, the signal of CLA can be expanded in a series of harmonic modes. Furthermore, signal processing can be done in the wave domain (also explained in Chapter 2) to get an analytical solution. Although CLA is an ideal array geometry, using CLAs, in most common rectangular rooms, is rather inefficient because there will be spare side spaces.

In practical applications, irregular arrays such as room-shape arrays are more frequently used. (For three-dimensional studies, a cuboid array [19] and barrel-shape array [37] were also introduced). Algorithms for selecting the optimal array geometry have also been proposed [38,39]. These irregular arrays, especially the optimal arrays, can provide ideal results for certain environments and

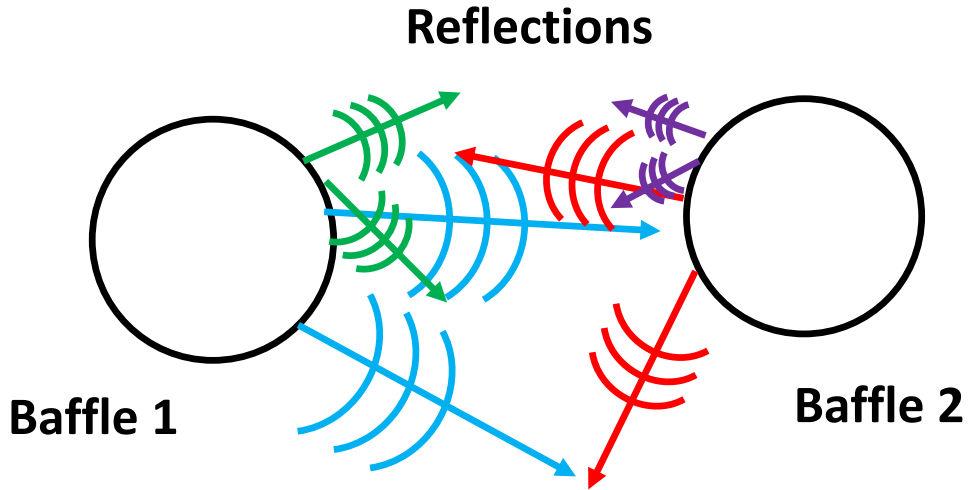


Figure 1.2: Infinite reflections exist between rigid baffles.

applications. However, the “optimal” array geometry needs to be designed for every environment. In addition, general analytical methods cannot support these irregular arrays, thus it can be difficult to perform further analyses.

The main issue with the current spatial control studies is a trade-off between the flexibility of loudspeaker arrangement and the method analyticity. Possibilities on array geometries for a flexible loudspeaker arrangement are given by numerical methods. In contrast, analytical methods provide predictable results, i.e., one can analyse how the performance of a system would be and how to make further improvements, and are also versatile for implementations, i.e., one can make implementations that have acceptable performance with theoretical data. The last few decades have been a witness to various discussions on the optimal balance of this trade-off in certain applications. However, addressing this trade-off remains an issue.

1.2 Motivation

The goal of this study is to introduce new analytically controllable array geometries to spatial control as an attempt for breaking through the trade-off. As the general goal of spatial control is to reproduce a complex sound field that contains multiple sources, directional sources, reflections etc., using a complex array geometry diversifies the sound field and may be more efficient than using basic and mathematically “perfect” array geometries, such as circular. However, as explained above, complex array geometries are lacking for analytical methods. To achieve predictable results and high implementation versatility, this study approaches new complex geometries that can be solved with analytical methods. As the first attempt on diversifying the sound field, two new array geometries are considered in this study: multiple CLAs (MCLA) and elliptical loudspeaker array (ELA).

In the first attempt to use MCLA, the array geometry is diversified by including multiple conventional CLAs. The model increases the flexibility on loudspeaker arrangement in space. Furthermore, all CLAs are considered to be acoustically rigid. It leads to infinite reflections between the CLAs (Fig. 1.2). This mutual interaction phenomenon is called the multiple scattering effect, which has been frequently discussed in underwater acoustics [40] and noise absorp-

	CLA	LLA	Irregular Array	MCLA	ELA
Sound Field Diversity	\triangle	\triangle	\odot	\odot	\circ
Reflections	–	–	\triangle	\circ	–
Asymmetric	\times	\triangle	\circ	\circ	\circ
Arrangement Flexibility	\times	\times	\odot	\circ	\circ
Method Analyticity	\circ	\circ	\times	\circ	\circ
Predicable Results	\circ	\circ	\times	\circ	\circ
Implementation Versatility	\circ	\circ	\times	\circ	\circ
Derivation Simplicity	\odot	\odot	–	\triangle	\circ
Number of Parameters	\odot	\odot	–	\triangle	\circ

Table 1.1: Features of array models mentioned in this study.

tion [41, 42]. In this study, the analytical control of MCLA is proposed, taking both the centre-shifting of the CLAs and multiple scattering effect into consideration.

In the second attempt, ELA is proposed. The general idea of the ELA model is to diversify the sound field by introducing asymmetry. More importantly, the elliptical coordinate system is one of the few two-dimensional orthogonal coordinate systems, meaning that there is another expansion for the signals of an ELA and an analytical method for ELA exists. Note that the elliptical arrays, including loudspeaker and microphone arrays, are rarely discussed in conventional studies. The analytical method proposed in this study is a novel method based on the spatial Fourier transform (later explained in Chapter 2) in an elliptical coordinate system. In addition, while the MCLA model has a high number of parameters and as such are difficult to determine, the ELA does not exhibit the multiple scattering effect and has fewer number of parameters. The features of the conventional and proposed array models are summarised in Table 1.1.

This study is distinct in proposing new array geometries and their analytical controlling methods simultaneously. The literature on spatial control (especially sound field reproduction) has two main types of studies: analytical studies that use simple array geometries and numerical studies that focus on optimal solutions. The analytical methods provide general solutions for a wide range of systems and are thus considered versatile, whereas the numerical methods considerably improve the total performance. This study, however, aims to find a generally well-conditioned solution (i.e., a system with improved physical characteristics) that can be controlled with analytical methods. In other words, the study is in between the two types of conventional studies and is focused on developing a new direction on approaching the general ideal method. This relationship is illustrated in Fig. 1.3.

1.3 Outline of Thesis

The thesis is structured as follows.

In Chapter 1, the background, motivation, and contribution of this study are introduced.

In Chapter 2, the fundamentals of spatial control, the conventional methods, are explained. Subsequently, the evaluation methods used in this study are introduced along with examples.

Chapters 3 and 4 discuss the two new array geometries, MCLA and ELA, respectively. In Chapter 3, the MCLA model is proposed. Initially, the multiple

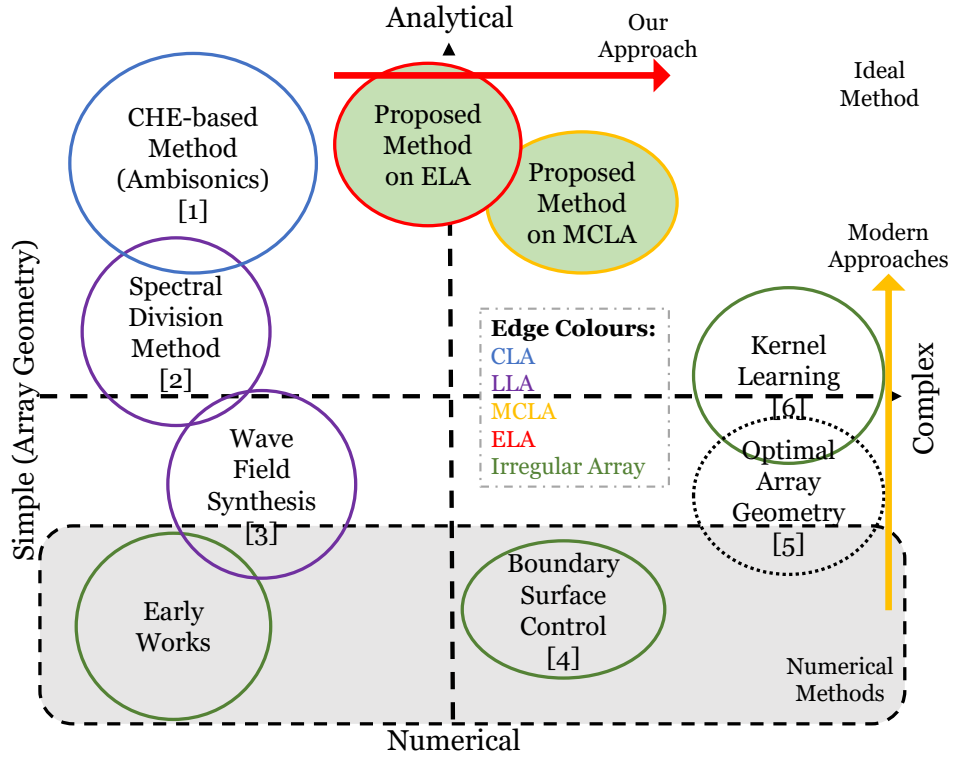


Figure 1.3: Methods of sound field reproduction [26, 37, 38, 43–45]

scattering effect and the accompanying calculations are introduced. Then a spatial control method that considers the multiple scattering effect is proposed. The performance of MCLA is discussed with respect to interior sound field reproduction, exterior sound field reproduction, and beamforming.

In Chapter 4, the ELA model is proposed. The elliptical coordinate system and the eigenfunctions of the Helmholtz equation, referred to as Mathieu functions, are introduced. A method based on the Mathieu function is then proposed for sound field reproduction using ELA. In line with the previous chapter, the performance of ELA is discussed with respect to interior sound field reproduction, exterior sound field reproduction, and beamforming. Finally, the results of ELA, CLA, MCLA, and LLA are compared.

In Chapter 5, the proposed method for ELA in the previous chapter is further extended and generalised. The general method can be implemented with arbitrary-shape arrays. The performance is verified with an irregular (rectangular) loudspeaker array for interior sound field reproduction and with CLA for exterior sound field reproduction.

Finally in Chapter 6, the results are summarised prior to concluding the study.

Chapter 2

Fundamentals of Spatial Control

In this chapter, the fundamentals of spatial control are introduced. The basic theories of sound field reproduction, which is one of the most important techniques of spatial control, are explained. Applications including both interior and exterior sound field reproduction and beamforming are covered through CLA examples.

2.1 Wave Equation and Kirchhoff-Helmholtz Integral Equation

The sound field reproduction technique was originally based on Huygen's principle which states that the wave of a primary source can be reconstructed by secondary sources located on the wavefront. The theory can be expressed in a mathematical model, the Kirchhoff-Helmholtz integral equation, which indicates that the sound field can be synthesised by secondary sources on the boundary.

Consider the wave equation in two-dimensional space [46,47] where the sound pressure $p(\mathbf{x}, t)$ as a function of position $\mathbf{x} = (x, y)$ and time t satisfies

$$\nabla^2 p(\mathbf{x}, t) - \frac{1}{c^2} \frac{\partial^2 p(\mathbf{x}, t)}{\partial t^2} = 0. \quad (2.1)$$

Here $c \approx 340$ m/s denotes the speed of sound in air. Laplace operator ∇^2 in the two-dimensional Cartesian coordinate system is

$$\nabla^2 = \frac{\partial^2}{\partial x^2} + \frac{\partial^2}{\partial y^2}. \quad (2.2)$$

We can obtain the wave equation in the frequency domain by applying a temporal Fourier transform to (2.1). This well-known equation is named the homogeneous Helmholtz equation [46,47].

$$\nabla^2 p(\mathbf{x}, \omega) + k^2 p(\mathbf{x}, \omega) = 0, \quad (2.3)$$

where ω denotes angular frequency, and $k \triangleq \omega/c$ denotes the wave number. The sound pressure in the frequency domain $p(\mathbf{x}, \omega)$ is the Fourier transform of the sound pressure in the time domain:

$$p(\mathbf{x}, \omega) = \int_{-\infty}^{\infty} p(\mathbf{x}, t) e^{-j\omega t} dt. \quad (2.4)$$

The imaginary unit $j = \sqrt{-1}$.

As shown in Fig. 2.1, within a two-dimensional space Ω and its boundary $\partial\Omega$, consider the partial derivative of a scalar function f as pointing outward from the boundary.

$$\frac{\partial f}{\partial \mathbf{n}} = \frac{\partial f}{\partial x} + \frac{\partial f}{\partial y} = \nabla f \cdot \mathbf{n}, \quad (2.5)$$

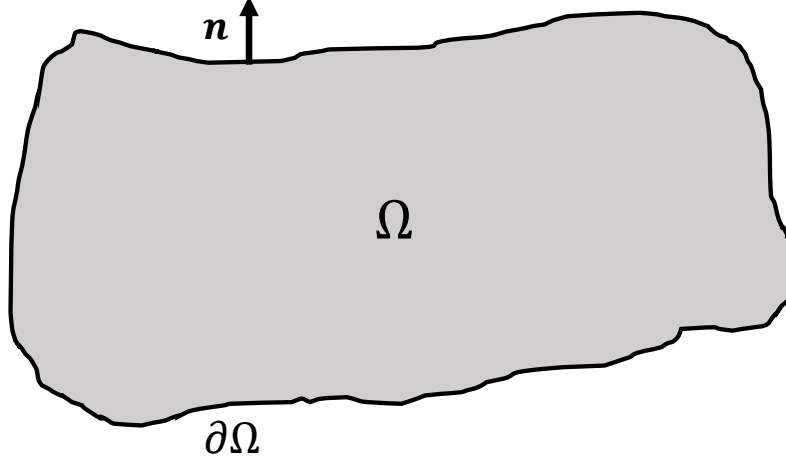


Figure 2.1: A two-dimensional space Ω and its boundary $\partial\Omega$.

where \mathbf{n} denotes the unit normal vector. Then, the Green's theorem can be expressed as [46],

$$\iint_{\Omega} (f\nabla^2 g - g\nabla^2 f) d\Omega = \int_{\partial\Omega} \left(f \frac{\partial g}{\partial \mathbf{n}} - g \frac{\partial f}{\partial \mathbf{n}} \right) d\mathbf{x}, \quad (2.6)$$

where f and g are continuous and finite functions.

Here, with a coordinate $\mathbf{x} = (x, y)$ located on the boundary $\partial\Omega$, it is assumed that the two functions $f(\mathbf{x}, \omega)$ and $g(\mathbf{x}, \omega)$ satisfy the homogeneous Helmholtz equation:

$$\nabla^2 f(\mathbf{x}, \omega) + k^2 f(\mathbf{x}, \omega) = 0 \quad (2.7)$$

$$\nabla^2 g(\mathbf{x}, \omega) + k^2 g(\mathbf{x}, \omega) = 0. \quad (2.8)$$

The following equation establishes:

$$\begin{aligned} & f(\mathbf{x}, \omega) \nabla^2 g(\mathbf{x}, \omega) - g(\mathbf{x}, \omega) \nabla^2 f(\mathbf{x}, \omega) \\ &= f(\mathbf{x}, \omega) (-k^2 g(\mathbf{x}, \omega)) - g(\mathbf{x}, \omega) (-k^2 f(\mathbf{x}, \omega)) \\ &= 0. \end{aligned} \quad (2.9)$$

Therefore, the left side of (2.6) becomes 0,

$$\int_{\partial\Omega} \left(f(\mathbf{x}, \omega) \frac{\partial g(\mathbf{x}, \omega)}{\partial \mathbf{n}} - g(\mathbf{x}, \omega) \frac{\partial f(\mathbf{x}, \omega)}{\partial \mathbf{n}} \right) d\mathbf{x} = 0. \quad (2.10)$$

Equation (2.10) represents a field where no sources exist.

The next representation is that of a field with a monopole source. Here, a monopole source can be considered as a singular point of $g(\mathbf{x}, \omega)$ in the space Ω . Denote the singular point \mathbf{x}' with the continuous $f(\mathbf{x}, \omega)$; the singularity yields $g(\mathbf{x}, \omega)$ as a solution of the inhomogeneous Helmholtz equation [46]:

$$\nabla^2 g(\mathbf{x}, \omega) + k^2 g(\mathbf{x}, \omega) = -\delta(\mathbf{x} - \mathbf{x}'), \quad (2.11)$$

$\delta(\mathbf{x})$ is the Dirac delta function. One solution of this equation is known as the two-dimensional free field Green function [46]:

$$G^{\text{open}}(\mathbf{x}|\mathbf{x}', \omega) = -\frac{j}{4} H_0^{(2)}(k|\mathbf{x} - \mathbf{x}'|), \quad (2.12)$$

where $H_\nu^{(2)}(z)$ is the ν -th order Hankel function of the second kind. In this study, (2.12) is referred to as the transfer function instead of the Green function.

Further consider the interior half space Ω^\natural , when $g(\mathbf{x}, \omega)$ in Green's theorem is substituted by $G^{\text{open}}(\mathbf{x}|\mathbf{x}', \omega)$, the functions on the closed boundary determine the wave field. Assume that sources exist outside the boundary $\partial\Omega$ only, the interior sound field is described by the interior Kirchhoff-Helmholtz integral equation [46]:

$$p(\mathbf{x}, \omega) = \int_{\partial\Omega} \left(G(\mathbf{x}|\mathbf{x}', \omega) \frac{\partial p(\mathbf{x}, \omega)}{\partial \mathbf{n}} - p(\mathbf{x}, \omega) \frac{\partial G(\mathbf{x}|\mathbf{x}', \omega)}{\partial \mathbf{n}} \right) d\mathbf{x}. \quad (2.13)$$

The full statement of the interior Kirchhoff-Helmholtz integral equation is:

$$\epsilon p(\mathbf{x}, \omega) = \int_{\partial\Omega} \left(G(\mathbf{x}|\mathbf{x}', \omega) \frac{\partial p(\mathbf{x}, \omega)}{\partial \mathbf{n}} - p(\mathbf{x}, \omega) \frac{\partial G(\mathbf{x}|\mathbf{x}', \omega)}{\partial \mathbf{n}} \right) d\mathbf{x}. \quad (2.14)$$

$$\epsilon = \begin{cases} 1 & \mathbf{x}' \text{ inside } \Omega \\ \frac{1}{2} & \mathbf{x}' \text{ on } \partial\Omega \\ 0 & \mathbf{x}' \text{ outside } \Omega \end{cases} \quad (2.15)$$

Similarly, consider the exterior half space, assuming that sources exist inside the boundary $\partial\Omega$ only, the exterior sound field is described by the exterior Kirchhoff-Helmholtz integral equation [46]:

$$\epsilon p(\mathbf{x}, \omega) = \int_{\partial\Omega} \left(G(\mathbf{x}|\mathbf{x}', \omega) \frac{\partial p(\mathbf{x}, \omega)}{\partial \mathbf{n}} - p(\mathbf{x}, \omega) \frac{\partial G(\mathbf{x}|\mathbf{x}', \omega)}{\partial \mathbf{n}} \right) d\mathbf{x}. \quad (2.16)$$

$$\epsilon = \begin{cases} 1 & \mathbf{x}' \text{ outside } \Omega \\ \frac{1}{2} & \mathbf{x}' \text{ on } \partial\Omega \\ 0 & \mathbf{x}' \text{ inside } \Omega \end{cases} \quad (2.17)$$

The Kirchhoff-Helmholtz integral equation, which describes a sound field by the integral on a closed boundary, implicitly explains that a sound field can be synthesised by components on the boundary. Hence, by dividing the two-dimensional sound field with closed boundaries such as an infinite line or a circle, as in Fig. 2.2, the sound field recording/reproduction can be achieved by using microphone arrays and loudspeaker arrays.

2.2 Spatial Fourier Transform

For certain array geometries, an analytical approach can be employed for spatial control by transforming sound fields into a wave domain. The concept of the transformation is introduced in this section.

As explained in (2.4), a temporal Fourier transform can transform a time domain function into a frequency domain function. A similar transform applied to a space domain function is referred to as the spatial Fourier transform [46, 48]. As the spatial Fourier transform has multiple representations, it has target domains such as the wavenumber domain (in Cartesian coordinates), circular harmonic domain (in polar coordinates), etc. For simplicity, they are all referred to as the wave domain in this paper.

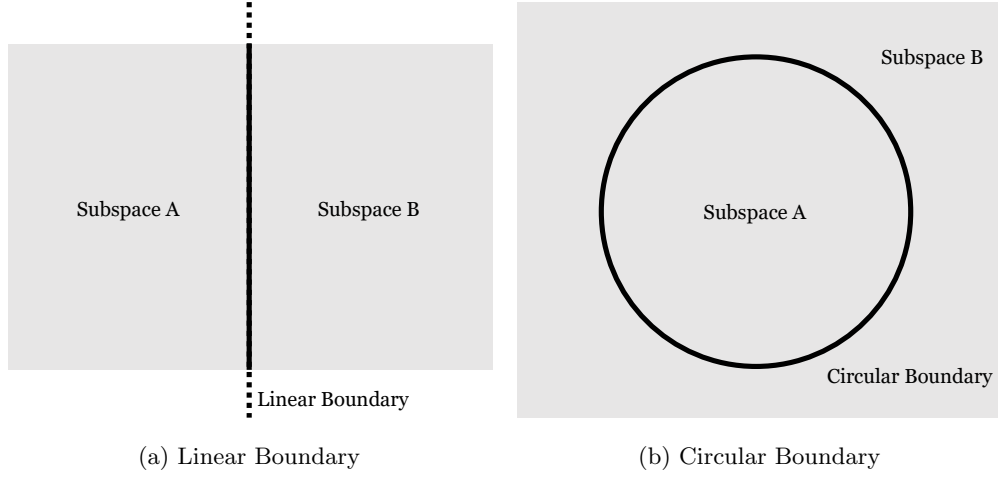


Figure 2.2: A closed boundary divides a two-dimensional space into two.

2.2.1 In Cartesian Coordinate System

Considering a function f of a one-dimensional space variable x , a spatial Fourier transform can be applied as:

$$\tilde{f}(k_x) = \int_{-\infty}^{\infty} f(x)e^{jk_x x} dx, \quad (2.18)$$

and its inverse transform is given as

$$f(x) = \frac{1}{2\pi} \int_{-\infty}^{\infty} \tilde{f}(k_x)e^{-jk_x x} dk_x. \quad (2.19)$$

k_x is the wavenumber of the x direction.

In a two-dimensional Cartesian coordinate system, a solution of the Helmholtz equation (2.3) is expressed as:

$$p(\mathbf{x}, \omega) = \tilde{p}(k_x)e^{-jk_x x}e^{-jk_y y}. \quad (2.20)$$

The solution represents a single-frequency plane wave progressing in a certain direction. Here, for each angular frequency ω , the following equation is established.

$$k^2 = k_x^2 + k_y^2. \quad (2.21)$$

Note that $k_y = \sqrt{k^2 - k_x^2}$ indicates that k_y is determined by k_x . Hence, $\tilde{p}(k_x)$ is a function of k_x only.

Then, a wave can be described as a sum of plane waves arriving from all directions:

$$p(\mathbf{x}, \omega) = \sum_{k_x} \tilde{p}(k_x)e^{-jk_x x}e^{-jk_y y}. \quad (2.22)$$

This equation is referred to as the plane wave decomposition of a sound field. Assuming k_x is continuous in \mathbb{R} , the sound pressure on the x -axis ($y = 0$) is then

$$p(x, 0, \omega) = \frac{1}{2\pi} \int_{-\infty}^{\infty} \tilde{p}(k_x)e^{-jk_x x} dk_x. \quad (2.23)$$

This equation is in the form of the spatial inverse Fourier transform.

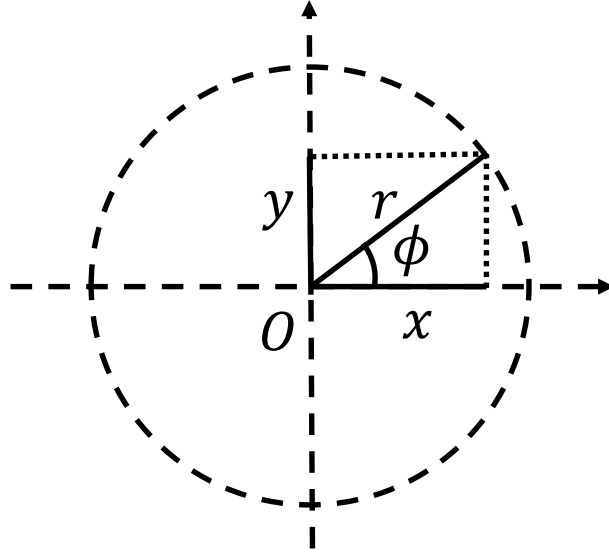


Figure 2.3: Polar coordinate system.

2.2.2 In Polar Coordinate System

In a two-dimensional polar coordinate system, there is another representation of the spatial Fourier transform. Defining a polar coordinate system as in Fig. 2.3, the coordinates $\mathbf{r} = (r, \phi)$ include distance r from the origin and rotation angle ϕ from the x -axis of the Cartesian coordinate system. Then, the polar coordinates (r, ϕ) can be transformed to the Cartesian coordinates (x, y) by

$$\begin{cases} x = r \cos \phi \\ y = r \sin \phi \end{cases}, \quad (2.24)$$

where

$$\begin{cases} r = \sqrt{x^2 + y^2} \\ \phi = \text{sgn } y \arccos \frac{x}{\sqrt{x^2 + y^2}} \end{cases}, \quad (2.25)$$

and

$$\text{sgn } y = \begin{cases} -1 & y < 0 \\ 0 & y = 0, \\ 1 & y > 0 \end{cases}, \quad (2.26)$$

is the signum function.

The Fourier series and its coefficients with respect to the space variable ϕ in the polar coordinate system are defined as follows.

$$f(r, \phi) = \sum_{\nu=-\infty}^{\infty} \mathring{f}_{\nu}(r) e^{j\nu\phi}, \quad (2.27)$$

$$\mathring{f}_{\nu}(r) = \frac{1}{2\pi} \int_0^{2\pi} f(r, \phi) e^{-j\nu\phi} d\phi. \quad (2.28)$$

They correspond to the inverse Fourier transform and the Fourier transform of the rotation direction, respectively. Here, ν denotes the order, which is also

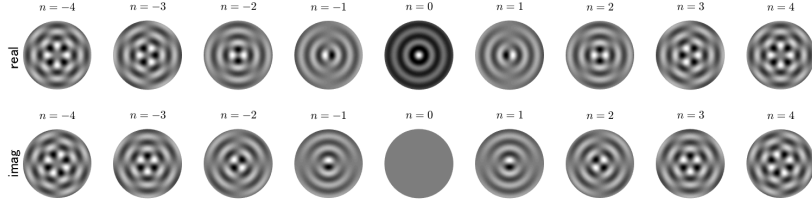


Figure 2.4: Circular harmonic modes with respect to orders, calculated by $J_\nu(kr)e^{j\nu\phi}$. All waves are at 1000 Hz.

referred to as ‘mode’ as it is related to the resonance modes on a circular plate. The basis $e^{j\nu\phi}$ has the following orthogonality

$$\int_0^{2\pi} e^{j\nu\phi} e^{-j\nu'\phi} d\phi = 2\pi\delta_{\nu\nu'}, \quad (2.29)$$

and completeness

$$\sum_{\nu=-\infty}^{\infty} e^{j\nu\phi} e^{-j\nu\phi'} = \delta(\phi - \phi'), \quad (2.30)$$

is extremely important in describing the radiation patterns of sound. δ_{ij} is the Kronecker delta. The basis is referred to as circular harmonics. The zeroth and the first order circular harmonics describe a monopole and dipoles, respectively. Figure 2.4 displays circular harmonics up to the fourth order. The series in (2.27), which is an expansion of circular harmonics, is referred to as the Circular Harmonic Expansion (CHE). The spatial Fourier transform can be applied within other coordinate systems, as well. A spatial Fourier transform in the elliptical coordinate system is introduced for the proposed method in Chapter 4.

2.3 Sound Field Representation in Polar Coordinate System

Similar to the time-domain frequency-domain transform described in the previous subsection, any sound pressure that is a function of space variables can be transferred to or from a wave domain by the spatial Fourier transform and its inverse [46, 48]. The set of sound pressures is referred to as a sound field.

Consider the Helmholtz equation in a polar coordinate system. The Laplace operator ∇^2 in the polar coordinate system is

$$\nabla^2 = \frac{\partial^2}{\partial r^2} + \frac{1}{r} \frac{\partial^2}{\partial r} + \frac{1}{r^2} \frac{\partial^2}{\partial \phi^2}. \quad (2.31)$$

Therefore, the Helmholtz equation can be rewritten as

$$\left(\frac{\partial^2}{\partial r^2} + \frac{1}{r} \frac{\partial^2}{\partial r} + \frac{1}{r^2} \frac{\partial^2}{\partial \phi^2} \right) p(r, \phi, \omega) + k^2 p(r, \phi, \omega) = 0. \quad (2.32)$$

One solution of the wave function can be derived as

$$p(r, \phi, \omega) = \sum_{\nu=-\infty}^{\infty} \hat{p}_\nu(r, k) e^{j\nu\phi}, \quad (2.33)$$

[46], which is the CHE of the sound field.

Any sound pressure $p(r, \phi, \omega)$ in a two-dimensional sound field can be described as a summation of an interior sound field $p^\triangleleft(r, \phi, \omega)$ (with sources radiating inward) and an exterior sound field $p^\triangleright(r, \phi, \omega)$ (with sources radiating outward):

$$p(r, \phi, \omega) = p^\triangleleft(r, \phi, \omega) + p^\triangleright(r, \phi, \omega). \quad (2.34)$$

The CHE can be applied to both interior and exterior sound fields. The general equations are given below [46]:

$$p^\triangleleft(r, \phi, \omega) = \sum_{\nu=-\infty}^{\infty} \check{p}_\nu^\triangleleft(k) J_\nu(kr) e^{j\nu\phi}, \quad (2.35)$$

$$p^\triangleright(r, \phi, \omega) = \sum_{\nu=-\infty}^{\infty} \check{p}_\nu^\triangleright(k) H_\nu^{(2)}(kr) e^{j\nu\phi}, \quad (2.36)$$

where $\check{p}_\nu^\triangleleft(k)$ and $\check{p}_\nu^\triangleright(k)$ are sound field coefficients of the interior and exterior fields, respectively; $J_\nu(z)$ denotes the ν -th order Bessel function. The expansion of the Bessel and Hankel functions separates the radius variable r from the sound field coefficient and the latter represents sound field features, independent of the observation position.

Then, consider a sound field observed in a circle of radius r . Let $\hat{p}_\nu(r, k)$ be the ν -th order CHE coefficient of the sound field. Assuming all sources are inside the circle, the sound field outside the circle degenerates to an exterior-only field as in (2.36). In the exterior field, the following equation applies [46].

$$\hat{p}_\nu(r^\triangleright, k) = \frac{H_\nu^{(2)}(kr^\triangleright)}{H_\nu^{(2)}(kr)} \hat{p}_\nu(r, k). \quad (2.37)$$

Here, $(r^\triangleright, \phi^\triangleright)$ is any point outside the circle thus $r^\triangleright > r$. The equation states that the CHE coefficient at radius r determines the CHE coefficient outside the circle. It indicates that the exterior sound field $p(r^\triangleright, \phi^\triangleright, \omega)$ can be expressed using the CHE coefficient $\hat{p}_\nu(r, k)$. Conversely, assuming all sources are outside the circle, an interior-only field (2.35) is given by,

$$\hat{p}_\nu(r^\triangleleft, k) = \frac{H_\nu^{(2)}(kr^\triangleleft)}{H_\nu^{(2)}(kr)} \hat{p}_\nu(r, k), \quad (2.38)$$

as demonstrated in [46]. $(r^\triangleleft, \phi^\triangleleft)$ is any point inside the circle and $r^\triangleleft < r$. Hence the interior field $p(r^\triangleleft, \phi^\triangleleft, \omega)$ can also be expressed using the CHE coefficient.

2.4 Approaches of Sound Field Reproduction

2.4.1 Traditional Wave Field Synthesis

With the Kirchhoff-Helmholtz integral equation (2.13) explained above, a sound/wave field can be synthesised by the components on the boundary. As $\frac{\partial G(\mathbf{x}|\mathbf{x}', \omega)}{\partial \mathbf{n}}$ in the right side of (2.13) is the transfer function of the dipole sources, both monopole and dipole sources are required to determine a sound field. Here, the gradient of sound pressure $\frac{\partial P(\mathbf{x}, \omega)}{\partial \mathbf{n}}$ should be expressed in special units such as adjacent microphone pairs or directional microphones. Overall, such a spatial control technique is difficult to realise.

One solution to the problem is to use a linear boundary. By defining a half space with an infinite linear boundary, the Rayleigh integral equation can replace

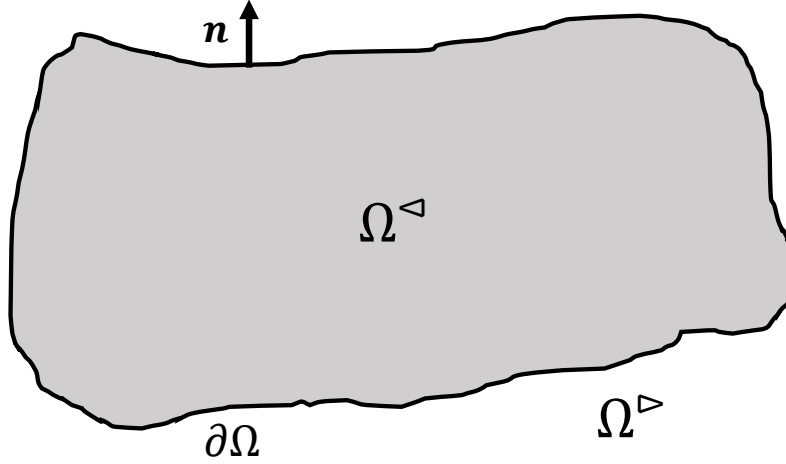


Figure 2.5: The boundary $\partial\Omega$ divides the two-dimensional space into interior Ω^{\triangleleft} and exterior Ω^{\triangleright} .

the Kirchhoff-Helmholtz integral equation. With a Neumann boundary condition, the Rayleigh I integral describes the sound field with the monopole terms only:

$$p(\mathbf{x}, \omega) = -2 \int_{\partial\Omega} G(\mathbf{x}|\mathbf{x}', \omega) \frac{\partial p(\mathbf{x}, \omega)}{\partial \mathbf{n}} d\mathbf{x}, \quad (2.39)$$

indicates that a sound field can be synthesised by reproducing doubled sound pressure gradient with continuous monopole sources on the boundary. In contrast, with a Dirichlet boundary condition, the Rayleigh II integral describes the sound field with dipole terms only:

$$p(\mathbf{x}, \omega) = 2 \int_{\partial\Omega} p(\mathbf{x}, \omega) \frac{\partial G(\mathbf{x}|\mathbf{x}', \omega)}{\partial \mathbf{n}} d\mathbf{x}, \quad (2.40)$$

indicates that a sound field can be synthesised by reproducing doubled sound pressure with continuous dipole sources on the boundary [22, 49]. Note that the $\partial \mathbf{n}$ in the Rayleigh integral equations is towards the target half space.

The spatial control method based on the Rayleigh integral equations is one of the best-known approaches, known as wave field synthesis [3, 44, 49–54]. Wave field synthesis uses linear (or planar for three-dimensional methods) loudspeaker arrays as monopole sources. Driving functions are obtained by further approximations. However, this method also requires that the gradients be recorded [30, 55, 56] unless the target primary field is known a priori.

2.4.2 Simple Source Approach

The spatial control method can be further simplified by driving monopole sources with the observed sound pressure [24, 57]. This method has a simple source formulation.

As shown in Fig. 2.5, the boundary $\partial\Omega$ divides a two-dimensional space into interior space Ω^{\triangleleft} and exterior space Ω^{\triangleright} . With $p^{\triangleright}(\mathbf{x}, \omega)$ denoting the exterior sound field and assuming that sources exist in the interior space only, a Kirchhoff-Helmholtz integral equation can be formulated. Similarly, with $p^{\triangleleft}(\mathbf{x})$ denoting the interior sound field and assuming that sources exist in exterior space only,

another Kirchhoff-Helmholtz integral equation can be formulated. Here, it is assumed that the exterior field $p^\triangleright(\mathbf{x}, \omega)$ satisfies the Sommerfeld radiation condition

$$\lim_{r \rightarrow \infty} r \left(\frac{\partial p(\mathbf{x}, \omega)}{\partial r} - jk p(\mathbf{x}, \omega) \right) = 0, \quad (2.41)$$

where $r = |\mathbf{x}|$ and ∂r point towards the direction of \mathbf{x} [46].

Next, assuming the sound pressure is continuous across both sides of the boundary, $p^\triangleright = p^\triangleleft$ on the boundary. Furthermore, assuming that $\frac{\partial p^\triangleright}{\partial \mathbf{n}} \neq \frac{\partial p^\triangleleft}{\partial \mathbf{n}}$ on $\partial\Omega$, the following equation is established.

$$\left. \begin{array}{l} p^\triangleright(\mathbf{x}, \omega) \quad (\mathbf{x} \in \Omega^\triangleright) \\ p^\triangleright = p^\triangleleft \quad (\mathbf{x} \in \partial\Omega) \\ p^\triangleleft(\mathbf{x}, \omega) \quad (\mathbf{x} \in \Omega^\triangleleft) \end{array} \right\} = \int_{\partial\Omega} \left(\frac{\partial p^\triangleright(\mathbf{x}, \omega)}{\partial \mathbf{n}} - \frac{\partial p^\triangleleft(\mathbf{x}, \omega)}{\partial \mathbf{n}} \right) G(\mathbf{x}|\mathbf{x}', \omega) d\mathbf{x}. \quad (2.42)$$

Here, define

$$u(\mathbf{x}', \omega) \triangleq \frac{\partial p^\triangleright(\mathbf{x}, \omega)}{\partial \mathbf{n}} - \frac{\partial p^\triangleleft(\mathbf{x}, \omega)}{\partial \mathbf{n}}, \quad (2.43)$$

the sound field $p(\mathbf{x}, \omega)$ can be described as:

$$p(\mathbf{x}, \omega) = \int_{\partial\Omega} u(\mathbf{x}', \omega) G(\mathbf{x}|\mathbf{x}', \omega) d\mathbf{x}. \quad (2.44)$$

Then, assuming that $u(\mathbf{x})$ is a secondary source distribution located on the boundary $\partial\Omega$, (2.44) states that the sound field can be described by the monopole sources located on the boundary. The theory above, known as the simple source approach [46], implies that spatial control can be achieved by controlling the sound pressure on the boundary of the sound field. Note that the theory can be implemented only if the sources and the controlling area are in the opposite side of the boundary, i.e., interior field control with exterior sources or exterior field control with interior sources.

2.5 Sound Field Reproduction Methods

2.5.1 Inverse Filter Based Method (A Numerical Approach)

The basic numerical approach introduced for sound field reproduction is based on the simple source approach and an inverse filter [24, 57].

Instead of using continuous secondary sources, the primary sound field $p(\mathbf{x}, \omega)$ is reproduced by a discrete loudspeaker array on the boundary of the sound field. With L loudspeakers, the secondary sound field $\hat{p}(\mathbf{x}, \omega)$ can be described as

$$\hat{p}(\mathbf{x}, \omega) = \sum_{l=1}^L G(\mathbf{x}|\mathbf{x}'_l, \omega) d_l(\omega), \quad (2.45)$$

where \mathbf{x}'_l and $d_l(\omega)$ denote the coordinates and the driving signal of the l -th loudspeaker, respectively.

The primary field, which is observed at M observation points (or microphones) $\{\mathbf{x}_1, \mathbf{x}_2, \dots, \mathbf{x}_M\}$, can be expressed as a vector:

$$\mathbf{p}_\omega = \left[p(\mathbf{x}_1, \omega), p(\mathbf{x}_2, \omega), \dots, p(\mathbf{x}_M, \omega) \right]^T. \quad (2.46)$$

The sound field can be reproduced when $\hat{p}(\mathbf{x}_m, \omega)$ matches $p(\mathbf{x}_m, \omega)$ at every $m \in [1, M]$. Therefore, the driving signal should minimise the following reproduction error:

$$\varepsilon(\omega) = \|\mathbf{G}_\omega \mathbf{d}_\omega - \mathbf{p}_\omega\|_2^2. \quad (2.47)$$

Here,

$$\mathbf{G}_\omega = \begin{bmatrix} G(\mathbf{x}_1|\mathbf{x}'_1, \omega) & G(\mathbf{x}_1|\mathbf{x}'_2, \omega) & \dots & G(\mathbf{x}_1|\mathbf{x}'_L, \omega) \\ G(\mathbf{x}_2|\mathbf{x}'_1, \omega) & G(\mathbf{x}_2|\mathbf{x}'_2, \omega) & \dots & G(\mathbf{x}_2|\mathbf{x}'_L, \omega) \\ \vdots & \vdots & \ddots & \vdots \\ G(\mathbf{x}_M|\mathbf{x}'_1, \omega) & G(\mathbf{x}_M|\mathbf{x}'_2, \omega) & \dots & G(\mathbf{x}_M|\mathbf{x}'_L, \omega) \end{bmatrix}, \quad (2.48)$$

$$\mathbf{d}_\omega = (d_1(\omega), d_2(\omega), \dots, d_L(\omega))^T. \quad (2.49)$$

are the matrix and vector of transfer functions and driving signals.

When $L = M$, the solution can be obtained using the inverse matrix of \mathbf{G}_ω . When $L \neq M$, the problem is solved by employing a least squares method with a pseudo inverse matrix $\mathbf{G}_\omega^\dagger$:

$$\mathbf{d}_\omega = \mathbf{G}_\omega^\dagger \mathbf{p}_\omega, \quad (2.50)$$

where

$$\mathbf{G}_\omega^\dagger = \mathbf{G}_\omega^H (\mathbf{G}_\omega^H \mathbf{G}_\omega)^{-1}, \quad (2.51)$$

$(\cdot)^H$ denotes the Hermitian matrix and $(\cdot)^{-1}$ denotes the inverse matrix. Furthermore, because the inverse matrix of $\mathbf{G}_\omega^H \mathbf{G}_\omega$ often diverges, in general, the least squares method is employed with a regularisation. The least squares method with a Tikhonov regularisation expresses the driving function as:

$$\mathbf{d}_\omega = (\mathbf{G}_\omega^H \mathbf{G}_\omega + \lambda \mathbf{I}_L)^{-1} \mathbf{G}_\omega^H \mathbf{p}_\omega, \quad (2.52)$$

where λ is the regularisation parameter.

If the primary field is an impulse, the driving function is an inverse filter of the transfer function. Thus, the method is the so-called inverse-filter-based method. Because the method derives the driving function by matching the sound pressure at observation points, it is also referred to as the pressure-matching method [15].

2.5.2 Wave Domain Method (An Analytical Approach)

An analytical approach is introduced whereby sound fields are transformed into the wave domain and the driving function is derived in the wave domain. This method is referred to as the wave domain method. Compared with the numerical approach, this approach can derive the driving function analytically without using an inverse matrix. Note that one of the most popular applications based on the wave domain method is Ambisonics, which includes the traditional first-order Ambisonics as well as higher-order Ambisonics [5, 29, 33, 58, 59].

In this study, the comparisons are carried out for circular arrays. A wave domain method based on CHE in (2.27) is introduced in this section. The CHE-based method defines a circular boundary and derives the driving function by matching the CHE coefficients of the primary and secondary fields in the wave domain. Following the Kirchhoff-Helmholtz integral equation, with a circular boundary, the field in either the interior or the exterior of the circle can be controlled. Here, for both interior and exterior fields, a general spatial control method based on CHE is introduced, as presented below.

Consider a secondary sound field with continuous sources located on a circle of radius r_0 . Let $G(r, \phi|r_0, \phi', \omega)$ be the transfer function between a source at (r_0, ϕ') and an observation point at (r, ϕ) , and let $d_{\phi'}(\omega)$ be the driving function of the source, then the sound field can be described as

$$\hat{p}(r, \phi, \omega) = \int_0^{2\pi} G(r, \phi|r_0, \phi', \omega) d_{\phi'}(\omega) r_0 d\phi'. \quad (2.53)$$

Applying CHE to the transfer function and the driving function,

$$G(r, \phi | r_0, \phi', \omega) = \sum_{\nu=-\infty}^{\infty} \mathring{G}_\nu(r | r_0, k) e^{j\nu(\phi-\phi')}, \quad (2.54)$$

$$d_{\phi'}(\omega) = \sum_{\nu=-\infty}^{\infty} \mathring{d}_\nu(k) e^{j\nu\phi'}. \quad (2.55)$$

$\mathring{G}_\nu(r | r_0, k)$ and $\mathring{d}_\nu(k)$ denote the CHE coefficient of the transfer function $G(r, \phi | r_0, \phi', \omega)$ and the driving function $d_{\phi'}(\omega)$, respectively. Substituting into the right side of (2.53),

$$\hat{p}(r, \phi, \omega) = 2\pi r_0 \sum_{\nu=-\infty}^{\infty} \mathring{G}_\nu(r | r_0, k) \mathring{d}_\nu(k) e^{j\nu\phi}, \quad (2.56)$$

is obtained by employing the orthogonality of circular harmonics.

By matching the CHE coefficients of the primary sound field (2.33) and the secondary sound field (2.56) for the circle of radius r ,

$$\hat{p}_\nu(r, k) = 2\pi r_0 \mathring{G}_\nu(r | r_0, k) \mathring{d}_\nu(k). \quad (2.57)$$

The CHE coefficient of the driving function is derived as

$$\mathring{d}_\nu(k) = \frac{\hat{p}_\nu(r, k)}{2\pi r_0 \mathring{G}_\nu(r | r_0, k)}, \quad (2.58)$$

with the transfer function expanded with the Bessel or Hankel functions as

$$G(r, \phi | r_0, \phi', \omega) = \begin{cases} \sum_{\nu=-\infty}^{\infty} \check{G}_\nu(k) H_\nu^{(2)}(kr_0) J_\nu(kr) e^{j\nu(\phi-\phi')} & r < r_0 \\ \sum_{\nu=-\infty}^{\infty} \check{G}_\nu(k) J_\nu(kr_0) H_\nu^{(2)}(kr) e^{j\nu(\phi-\phi')} & r > r_0 \end{cases}, \quad (2.59)$$

the driving function can be derived as

$$\mathring{d}_\nu(k) = \begin{cases} \frac{\hat{p}_\nu(k)}{2\pi r_0 \check{G}_\nu(k) J_\nu(kr_0)} & r < r_0 \\ \frac{\hat{p}_\nu(k)}{2\pi r_0 \check{G}_\nu(k) H_\nu^{(2)}(kr_0)} & r > r_0 \end{cases}. \quad (2.60)$$

Note that r is not included in the right side of the equation. Thus, $\mathring{d}_\nu(k)$ is radius independent once the interior or exterior field is selected. Finally, the driving function is obtained by substituting (2.58) into (2.55):

$$d_{\phi'}(\omega) = \sum_{\nu=-\infty}^{\infty} \frac{\hat{p}_\nu(r, k)}{2\pi r_0 \mathring{G}_\nu(r | r_0, k)} e^{j\nu\phi'}. \quad (2.61)$$

Now consider the discrete secondary sources that sample the circle, e.g. a circular loudspeaker array. Let L be the number of sources, then the sound field is described as

$$\hat{p}(r, \phi, \omega) = \sum_{l=1}^L G(r, \phi | r_0, \phi'_l, \omega) d_l(\omega). \quad (2.62)$$

Reapply discrete CHE [60] to $G(r, \phi | r_0, \phi'_l, \omega)$ and $d_l(\omega)$ to obtain

$$\hat{p}(r, \phi, \omega) = \sum_{l=1}^L \sum_{\nu=-N}^N \mathring{G}_\nu(r | r_0, k) e^{j\nu(\phi-\phi'_l)} \sum_{\nu'=-N}^N \mathring{d}_{\nu'}(k) e^{j\nu'\phi'_l}. \quad (2.63)$$

Here, N is the truncation order of the discrete CHE. The orthogonality of discrete $e^{j\nu\phi}$ is derived.

$$\hat{p}_\nu(r, k) = \mathsf{L}\hat{G}_\nu(r|r_0, k)\hat{d}_\nu(k), \quad (2.64)$$

[60]. By matching the CHE coefficients of the primary and secondary fields up to the N -th order, the CHE coefficient of the discrete driving function is derived as

$$\hat{d}_\nu(k) = \frac{\hat{p}_\nu(r, k)}{\mathsf{L}\hat{G}_\nu(r|r_0, k)}. \quad (2.65)$$

The discrete driving function is

$$d_l(\omega) = \sum_{\nu=-N}^N \frac{\hat{p}_\nu(r, k)}{\mathsf{L}\hat{G}_\nu(r|r_0, k)} e^{j\nu\phi_l}. \quad (2.66)$$

A Tikhonov regularisation can also be applied to this method to suppress the output level of loudspeakers.

In contrast to the pressure-matching method, i.e., the alternative name of inverse-filter-based method introduced in Sec. 2.4.2, the wave domain method matches the CHE coefficients of the primary and secondary sound fields for each mode (i.e. order) to derive the driving function. Therefore, the method is also referred to as mode-matching method [60].

There is also a wave domain method based on plane wave decomposition. The method, referred to as spectral division method (SDM), uses a planar or linear boundary. The method which is usually applied to linear loudspeaker arrays is explained in Appendix A.

It is also demonstrated that wave domain methods have common solutions with the wave field synthesis and inverse-filter-based method if certain constraints and approximations are applied [61, 62]. In this paper, the proposals and discussions mainly focus on the wave domain method.

2.6 Applications of Spatial Control

In this study, three important applications of spatial control are discussed: interior sound field reproduction, exterior sound field reproduction, and beamforming. The basic models and evaluation criteria are introduced in this section.

2.6.1 Interior Sound Field Reproduction

In the case of an array with a closed contour, such as CLA, the theories above indicate that either the interior sound field or the exterior sound field of the array can be reproduced. The majority of conventional studies, including the one involving the notable Ambisonics, focus on the interior sound field reproduction, where the target controlling region is literally surrounded by the loudspeaker array [5, 28, 29, 63–65]. As an example of this configuration, the listener can sit at the centre of a room while the loudspeakers are arranged in a few directions around the listener. As this is also the most common configuration of a surround sound system, the interior sound field reproduction can be implemented on conventional sound systems. In contrast, the listening area is limited by the scale of the loudspeaker array. In a normally furnished room, the loudspeaker configuration and reverberation can present additional issues. In this study, the interior sound field reproduction is discussed only for ideal environments, i.e., large scale loudspeaker arrays in free fields.

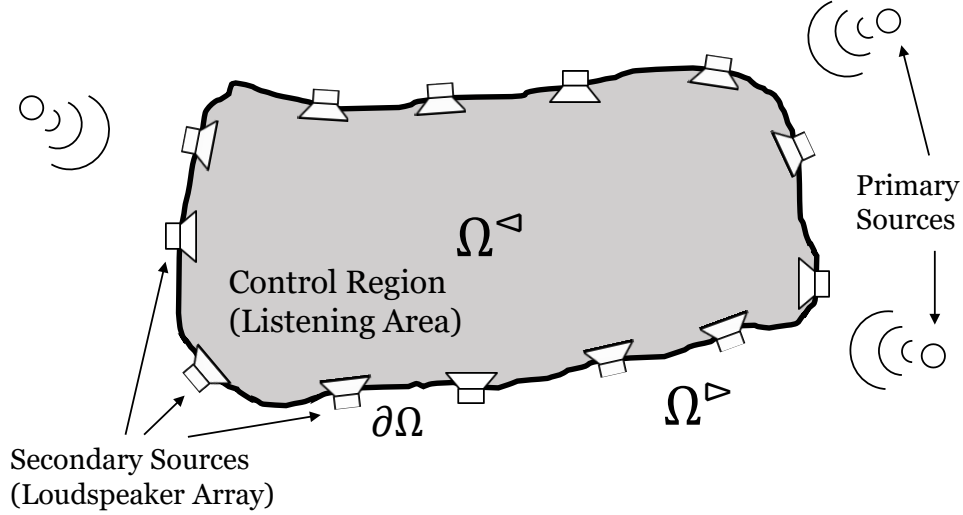


Figure 2.6: A model of interior sound field reproduction. Control region is the interior space Ω^\triangleleft .

In the interior sound field reproduction, the primary sources are located in Ω^\triangleright outside the closed boundary $\partial\Omega$, while the control region is the region Ω^\triangleleft inside $\partial\Omega$. A model of the interior sound field reproduction is illustrated in Fig. 2.6.

To evaluate the reproduction results, the most common index is used: the reproduction error.

Reproduction Error

Let $p(\mathbf{x}, \omega)$ and $\hat{p}(\mathbf{x}, \omega)$ be the complex sound pressure of a primary sound field and a reproduced secondary sound field at an angular frequency of ω , respectively. The reproduction error is calculated by

$$\varepsilon(\mathbf{x}) = 10 \log_{10} \frac{|\hat{p}(\mathbf{x}, \omega) - p(\mathbf{x}, \omega)|^2}{|p(\mathbf{x}, \omega)|^2}. \quad (2.67)$$

The reproduction error is a normalised error which indicates the reproduction accuracy at each position in space.

In this study, simple comparisons on interior sound field reproduction, e.g., the shape of the low-error region, are included. The evaluations are for a single frequency only.

Example simulation of a CLA

An example on interior sound field reproduction using CLA is presented. The primary sound field of an arriving plane wave is tested. The wave domain method of Sec. 2.5.2 was employed for the example. The primary source can be described as

$$\hat{p}_\nu = j^\nu \mathcal{A} e^{-j\nu\phi_{//}}, \quad (2.68)$$

where \mathcal{A} is the amplitude of the primary source. For a plane wave primary source, the direction of arrival is noted as $\phi_{//}$.

Figure 2.7 displays an example on reproducing a plane wave at 1000 Hz where $\phi_{//} = \frac{\pi}{2}$: (a) is the target primary sound field, (b) is the reproduced sound field.

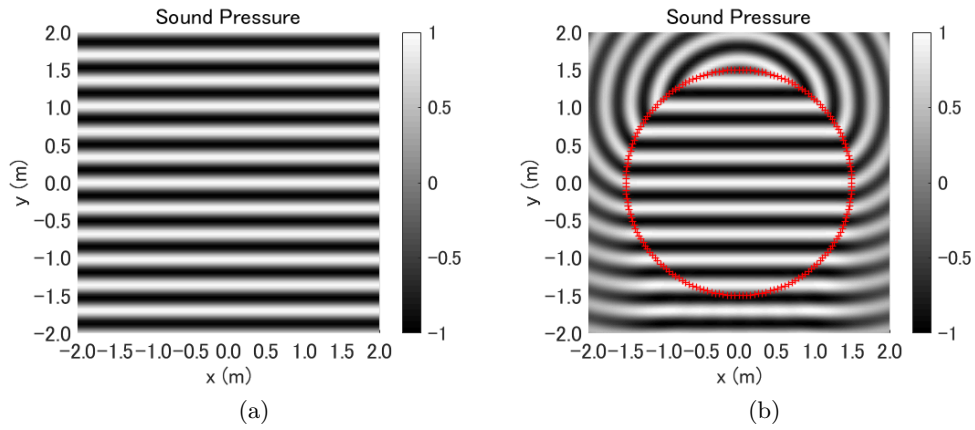


Figure 2.7: An example of reproducing the interior sound field of a plane wave. (a) Primary sound field of a plane wave. (b) Reproduced secondary sound field by CLA. Red crosses denote loudspeakers.

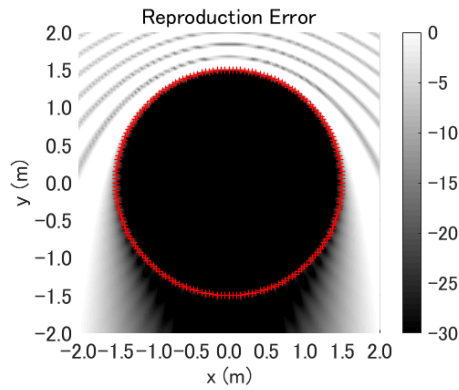


Figure 2.8: Reproduction error of the reproduced sound field.

In this study, only the real part of the sound field is displayed. The CLA was an open array that had 180 loudspeakers and a radius of 1.5 m. The sound field was calculated within a $4 \text{ m} \times 4 \text{ m}$ with a grid spacing of 0.04 m interval. The amplitude of the primary source was $\mathcal{A} = 1$. The wave domain method was employed for the example without a regularisation. The truncation order of CHE was 30. Comparing (a) to (b), it is observed that the wavefront of the primary source is reproduced in the secondary field.

Figure 2.8 displays the reproduction error (2.67) of the example above. The results clearly demonstrate that the sound field in the control region is reproduced with high accuracy (errors under -30 dB).

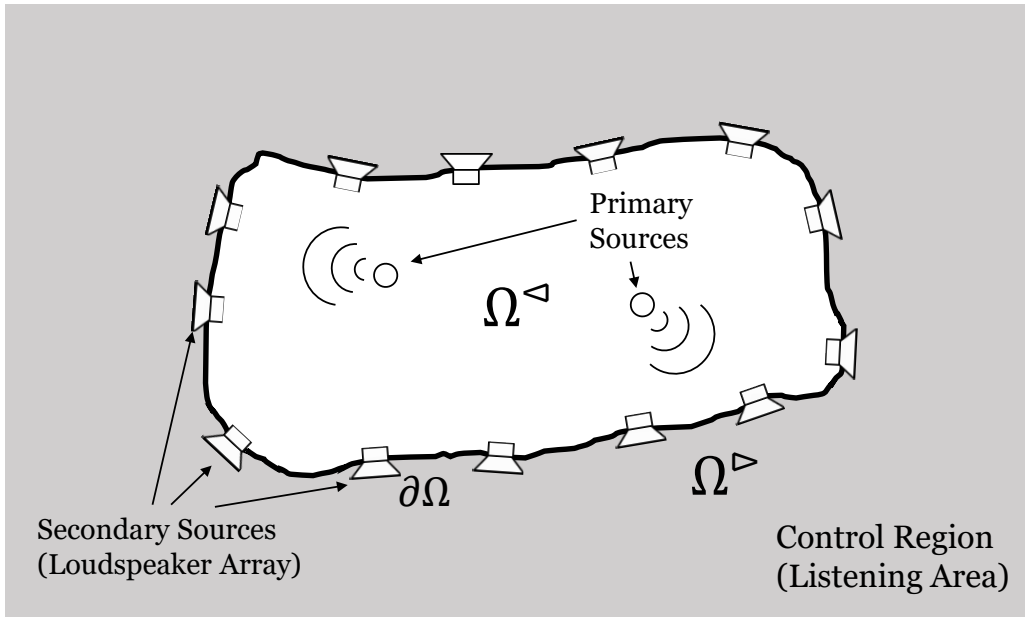


Figure 2.9: A model of exterior sound field reproduction. The control region is the exterior space Ω^\triangleright .

2.6.2 Exterior Sound Field Reproduction

The exterior sound field reproduction is the opposite of the interior reproduction in that the target controlling region is the field outside the enclosed area surrounded by the loudspeaker array. [66, 67]. Therefore, a wide listening area is guaranteed independent of the scale of the array. In addition, the exterior sound field reproduction can not ignore reverberation which can produce a natural sound. Consider reproducing the radiation sound field of a musical instrument that is recorded in an anechoic room: instead of a “clean” sound, exterior sound field reproduction will generate the sound of the instrument played in the listening room. However, regarding the configuration of loudspeakers in exterior sound field reproduction, the loudspeaker arrays are usually compact and consist of fewer loudspeakers than in interior sound field reproduction, resulting in lower reproduction accuracy.

Arrays, especially CLAs, used for exterior sound field reproduction are often considered to be rigid arrays. There are two reasons for this: One is the forbidden frequency issue [46] such that the open array used for exterior sound field reproduction tends to result in low radiation efficiency. The other is that generally compact arrays are used for exterior sound field reproduction, making it difficult to ignore the influence of the loudspeaker enclosure.

An important application of the exterior sound field reproduction is the focused source reproduction, which is also referred to as virtual source reproduction [54–56, 58]. Aiming to reproduce a virtual source outside the loudspeaker array, this application is capable of implementing acoustic holography. Additionally, the sensation of a source jumping out of the loudspeaker array is an impressive perceptual event, which is expected in the next generation of immersive audio systems.

In the exterior sound field reproduction, the primary sources are located in Ω^\triangleleft inside the closed boundary $\partial\Omega$ while the control region is the region Ω^\triangleright outside $\partial\Omega$. The model is illustrated in Fig. 2.9.

In focused source reproduction, the reproduction defines a boundary $\partial\Omega$ en-

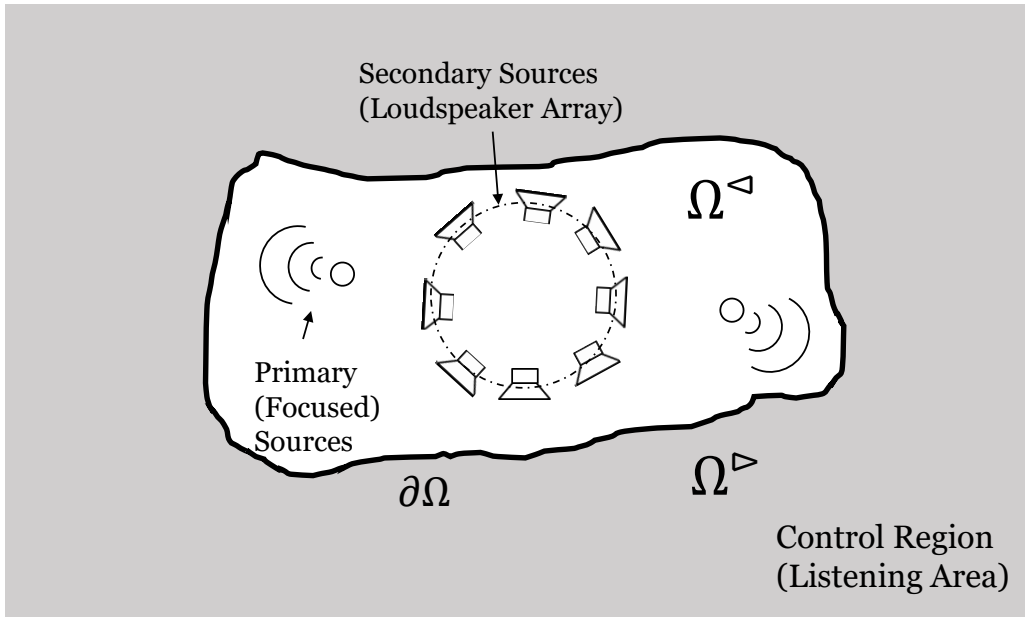


Figure 2.10: A model of focused source reproduction. The control region is the exterior space Ω^\triangleright while the primary sources are outside the loudspeaker array.

closing both the loudspeaker array and the target focused source. Instead of the whole field outside the loudspeaker array, the control region is reduced to the exterior area of the boundary, which means that there is no perceptual area between the array and the target source. A model of the focused source reproduction is shown in Fig. 2.10.

The performance of exterior sound field reproduction was evaluated with respect to three indices.

Reproduction Error

The reproduction error is the same as that of interior sound field reproduction, calculated by (2.67). The reproduction error is selected as the first index.

Reproduction Error over region

The performance of the exterior sound field was evaluated over the control region to make further comparisons easier. The reproduction error over a region Λ is calculated by

$$\varepsilon_\Lambda(\omega) = 10 \log_{10} \frac{\int_\Lambda |\hat{p}(\mathbf{x}, \omega) - p(\mathbf{x}, \omega)|^2 d\mathbf{x}}{\int_\Lambda |p(\mathbf{x}, \omega)|^2 d\mathbf{x}}. \quad (2.69)$$

As the control region is the infinite exterior field, the calculations are approximated by using a sample ring region. In this study, the sample ring region was selected as $\Lambda = \{\mathbf{x} | 0.4 \leq |\mathbf{x}| \leq 4\}$.

Maximum Controllable Frequency

The last index for evaluating the performance of exterior sound field reproduction is the maximum controllable frequency. For most configurations, the performance is better with lower frequencies than with higher frequencies, as exemplified by the results of CLA, presented later in this section. Setting a threshold of -15 dB in this study for reproduction, it is expected that for a specific frequency, the error

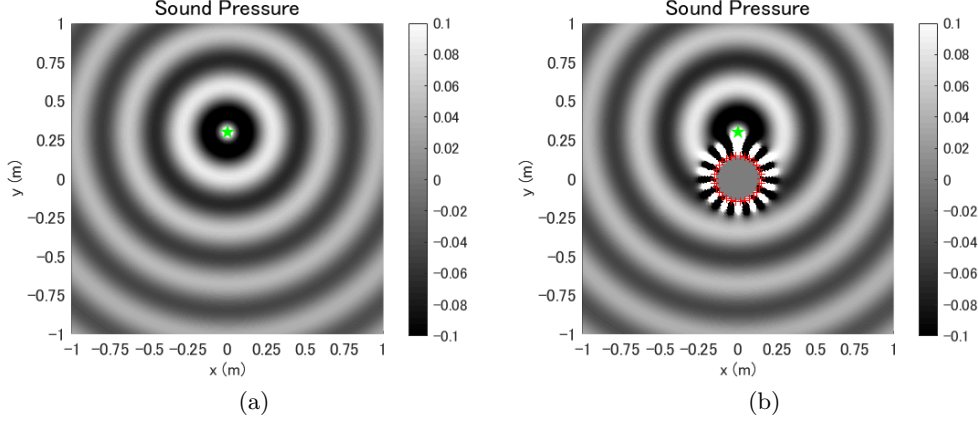


Figure 2.11: An example on reproducing a focused source. (a) Primary sound field of the target source. (b) Reproduced secondary sound field by a CLA. Red crosses denote loudspeakers. Green star denotes the target focused source.

will be higher than the threshold. This is referred to as the maximum controllable frequency in this paper. Note that the maximum controllable frequency is roughly related to the frequency at which spatial aliasing occurs.

Example simulation on a CLA

The example is that of an exterior sound field reproduction employing the wave domain method on a rigid CLA. The primary sound field of a primary source can be described as

$$\hat{p}_\nu = -\frac{j}{4}\mathcal{A}J_\nu(kr_\odot)e^{-j\nu\phi_\odot}, \quad (2.70)$$

where \mathcal{A} is the amplitude of the primary source. As the primary source should be inside $\partial\Omega$, it is not possible to have a plane wave source for the primary field. Thus, the cylindrical wave is the primary source with coordinates $\mathbf{x}_\odot = (r_\odot, \phi_\odot)$. The transfer function of a rigid CLA (where loudspeakers are mounted to the surface of a circle baffle) is [B6]:

$$G^{\text{rigid}}(r, \phi | r_0, \phi', \omega) = \sum_{\nu=-\infty}^{\infty} -\frac{e^{-j\nu\phi'}}{2\pi kr_0 H_\nu^{(2)\prime}(kr_0)} H_\nu^{(2)}(kr) e^{j\nu\phi}, \quad (2.71)$$

where r_0 is the radius of the CLA.

Figure 2.11 displays the example of 1000 Hz. In reproducing the focused source at $(r_\odot, \phi_\odot) = (0.3 \text{ m}, \frac{\pi}{2})$: (a) is the target primary sound field, (b) is the reproduced sound field. The CLA was a rigid array of radius 0.15 m consisting of 30 loudspeakers. The sound field was calculated within a $2 \text{ m} \times 2 \text{ m}$ space with a grid spacing of 0.02 m interval. The amplitude of the primary source was $\mathcal{A} = 1$. In the example, the wave domain method without regularisation was employed. Truncation order of CHE was set to $\lceil (L-1)/2 \rceil = 14$ (which is the maximum number of orthogonal bases that can be synthesised with L loudspeakers). Comparing (a) to (b), it is observed that the wavefront of the primary source is reproduced in the secondary field. However, Fig. 2.11(b) indicates that there was high level of sound pressure in the area close to the loudspeakers. This means loudspeakers have high level of input signals, i.e., high filter gain, resulting in distortions and a decline in performance in practical environments. Therefore, it is important to avoid such situations.

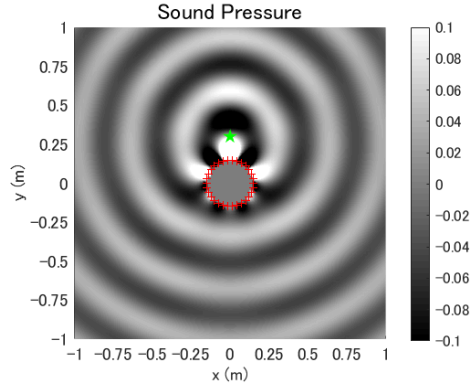


Figure 2.12: An example on reproducing a focused source with Tikhonov regularisation.

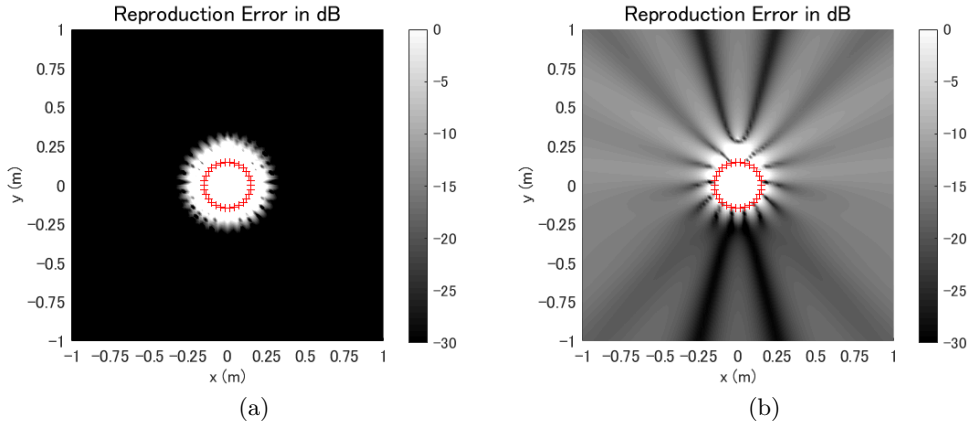


Figure 2.13: Reproduction error of the reproduced sound field. (a) Without regularisation. (b) With regularisation.

To avoid high output levels, Tikhonov regularisation was employed for exterior sound field reproduction. In this study, the regularisation was applied to all driving functions that had output level (calculated as $10 \log_{10} |d_l(\omega)/\mathcal{A}|^2$) higher than 0 dB to suppress the maximum level to 0 dB. An example of regularised driving function is illustrated in Fig. 2.12. Compared with the primary sound field of Fig. 2.11(a) the sound field is not perfectly reproduced whereas the silhouette of the wavefront is roughly maintained. The sound pressure around the loudspeakers (or the output level of loudspeakers) is significantly reduced from 53.6 dB to -0.2 dB.

The reproduction error of the two examples are shown in Fig. 2.13. In contrast to the high reproduction accuracy in (a), the regularised method produced higher yet acceptable error in the control region. In (b), the error is lower in the black striped areas.

The reproduction error over the control region of the regularised example is shown in Fig. 2.14. The dash-dot line denotes the threshold for reproduction as -15 dB, the maximum controllable frequency were 1000 Hz.

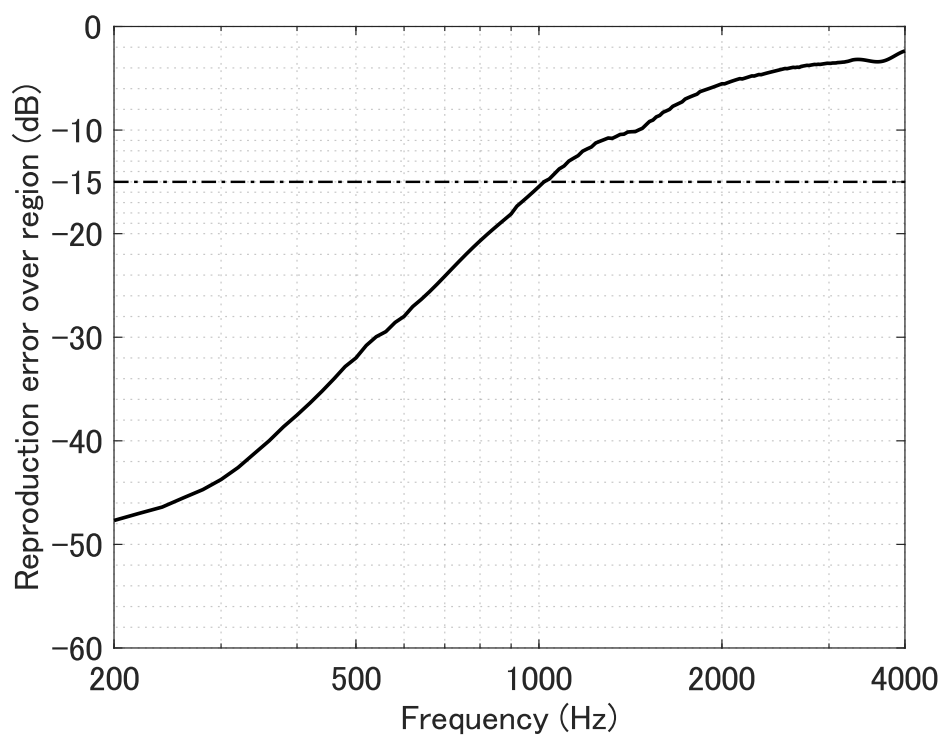


Figure 2.14: Reproduction error over a region.

2.6.3 Beamforming

Beamforming is one of the most important applications of spatial control [11–15, 68–71]. It is highly correlated with sound field reproduction. The exterior sound field reproduction, especially when the CHE-based method is applied, reproduces the complex sound pressure on a circle. This, in a wide sense, corresponds to complex directivity control. Thus, understanding the reproduction of the exterior sound field of a primary source can be interpreted as reproducing the directivity of the source, whether it is on or off the centre. Therefore, instead of reproducing the directivity of a source, controlling the directivity or forming a beam can also be considered as a kind of sound field reproduction.

Although beamforming and exterior sound field reproduction are similar techniques, they differ in their objectives and methods. Therefore, the discussions on beamforming are included as part of spatial control. Beamforming is a straightforward task when a simple target beam is set. In addition, the conclusions drawn from beamforming might have more general applicability than focused source reproduction.

In this study, the Minimum Variance Distortionless Response (MVDR) beamformer [9, 10, 72] is evaluated for performance on beamforming. The MVDR beamformer can produce a consistent distortionless output on constraint points i.e., the look direction, while minimising the radiation power in directions of suppression. The MVDR beamformer is ideal for loudspeakers because it can retain the frequency response of the input signal.

Let $M^{(\text{sup})}$ be the number of suppression points and $M^{(\text{con})}$ be the number of constraint points. With L loudspeakers, the method is based on constrained minimisation:

$$\begin{aligned} \min_{\mathbf{w}(\omega)} \quad & \mathbf{w}(\omega)^H \mathbf{R}(\omega) \mathbf{w}(\omega) \\ \text{subject to} \quad & \mathbf{C}(\omega) \mathbf{w}(\omega) = \mathbf{f}, \end{aligned} \quad (2.72)$$

where $\mathbf{R}(\omega) = \mathbf{S}(\omega)^H \mathbf{S}(\omega)$, $\mathbf{S}(\omega)$ is a $M^{(\text{sup})} \times L$ transfer function matrix between the loudspeakers and suppression points; $\mathbf{C}(\omega)$ is a $M^{(\text{con})} \times L$ transfer function matrix between the loudspeakers and constraint points; and \mathbf{w} is a $L \times 1$ filter vector. The $M^{(\text{con})} \times 1$ constraint vector \mathbf{f} are the target sound pressure on the constraint points. For a general MVDR beamformer, the \mathbf{f} is set to 1 for the look directions and 0 for null directions. The minimisation problem can be solved with a Lagrange multiplier vector $\boldsymbol{\lambda}$ and a Lagrangian function:

$$\mathcal{L}(\mathbf{w}, \boldsymbol{\lambda}) = \mathbf{w}(\omega)^H \mathbf{R}(\omega) \mathbf{w}(\omega) + \boldsymbol{\lambda}^H (\mathbf{C}(\omega) \mathbf{w}(\omega) - \mathbf{f}) + (\mathbf{w}(\omega)^H \mathbf{C}(\omega)^H - \mathbf{f}^H) \boldsymbol{\lambda}. \quad (2.73)$$

The partial differential on $\mathbf{w}(\omega)^*$ is

$$\frac{\partial \mathcal{L}(\mathbf{w}, \boldsymbol{\lambda})}{\partial \mathbf{w}(\omega)^*} = \mathbf{R}(\omega) \mathbf{w}(\omega) + \mathbf{C}(\omega)^H \boldsymbol{\lambda}. \quad (2.74)$$

The minimum corresponds to the point where this partial differential equals to 0 such that

$$\mathbf{w}(\omega) = -\mathbf{R}(\omega)^{-1} \mathbf{C}(\omega)^H \boldsymbol{\lambda}. \quad (2.75)$$

Substitute the equation into the constraint condition to get

$$-\mathbf{C}(\omega) \mathbf{R}(\omega)^{-1} \mathbf{C}(\omega)^H \boldsymbol{\lambda} = \mathbf{f}, \quad (2.76)$$

thus

$$\boldsymbol{\lambda} = -(\mathbf{C}(\omega)\mathbf{R}(\omega)^{-1}\mathbf{C}(\omega)^{\text{H}})^{-1}\mathbf{f}. \quad (2.77)$$

Finally the MVDR filter is derived by

$$\mathbf{w}(\omega) = (\mathbf{C}(\omega)\mathbf{R}(\omega)^{-1}\mathbf{C}(\omega)^{\text{H}})^{-1}\mathbf{R}(\omega)^{-1}\mathbf{C}(\omega)^{\text{H}}\mathbf{f}. \quad (2.78)$$

In addition, a Tikhonov regularisation can be employed to suppress the amplitude of the filters. The filter can be derived as

$$\mathbf{w}(\omega) = (\mathbf{C}(\omega)\mathbf{R}^{(\text{reg})}(\omega)^{-1}\mathbf{C}(\omega)^{\text{H}})^{-1}\mathbf{R}^{(\text{reg})}(\omega)^{-1}\mathbf{C}(\omega)^{\text{H}}\mathbf{f}, \quad (2.79)$$

where $\mathbf{R}^{(\text{reg})}(\omega) = \mathbf{S}(\omega)^{\text{H}}\mathbf{S}(\omega) + \lambda\mathbf{I}_{\text{L}}$ and λ is the regularisation parameter.

The performance of beamforming is evaluated on four indices. The first one is the beam pattern evaluated at a single frequency. The other three are the directivity index (DI), beam width (BW), and side-lobe level (SLL) evaluated over a range of frequencies.

Beam pattern

Beam pattern refers to the directivity of the beam. It is the most intuitive way to understand a beam including the beam width, side lobes, etc. The beam pattern is calculated as

$$\mathcal{D}(\phi, \omega) \text{ [dB]} = 10 \log_{10} \frac{\|p_{\phi}(\omega)\|^2}{\|p_{\varphi}(\omega)\|^2}, \quad (2.80)$$

where $\|p_{\phi}(\omega)\|^2$ is the power in direction ϕ , and φ is the look direction of the beam. Figure 2.15 displays an example beam pattern of a directional source. The x -axis in the figure is the relative angle $(\phi - \varphi)$. The y -axis represents the beam pattern.

Directivity Index

Directivity index is defined as the level of enhancement in the look direction of a directional source over all directions. It is generally used to evaluate the strength of a beam. A high DI indicates that the source has a strong directivity [12, 70, 73]. Herein, DI is calculated as,

$$\text{DI}(\omega) \text{ [dB]} = 10 \log_{10} \frac{2\pi\|p_{\varphi}(\omega)\|^2}{\int_0^{2\pi} \|p_{\phi}(\omega)\|^2 d\phi}. \quad (2.81)$$

Beam Width

Beam width is defined as the angle between the half-power (-3 dB) points of the main lobe and is used to evaluate the narrowness of the main beam. In transaural [74, 75] and personal audio [71] studies, a narrow main beam can be beneficial. The BW is displayed in Fig. 2.15 and calculated as,

$$\text{BW}(\omega) \text{ [degree]} = 2 \left| \arg \min_{\phi} \left(\frac{1}{2} \|p_{\varphi}(\omega)\|^2 - \|p_{\phi}(\omega)\|^2 \right) - \varphi \right| \times \frac{360^{\circ}}{2\pi}. \quad (2.82)$$

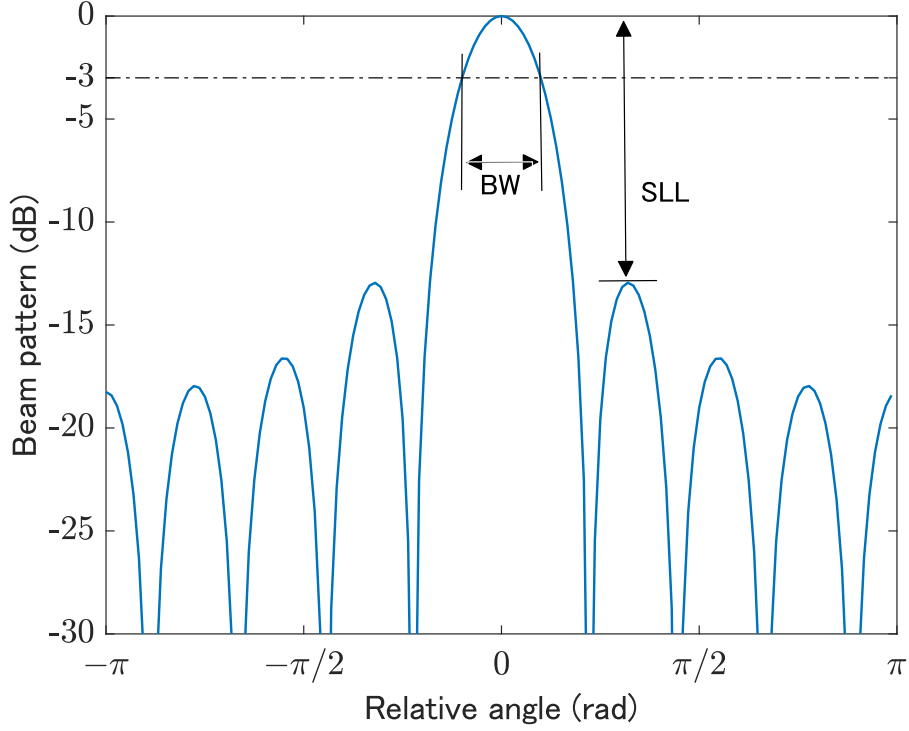


Figure 2.15: An example beam.

Side Lobe Level

The side lobe level describes the maximum level of the side lobe relative to the main lobe in decibels and is also evaluated at only observation points. The SLL is displayed in Fig. 2.15 and is calculated using the *findpeak* function in MATLAB.

$$\text{SLL}(\omega) \text{ [dB]} = 10 \log_{10} \frac{\|p_{\varphi}(\omega)\|^2}{\|p_{\bar{\varphi}}(\omega)\|^2}, \quad (2.83)$$

where $\bar{\varphi}$ is the second peak of the directivity p_{φ} .

In summary, higher DI, lower BW and lower SLL represent better performance. Moreover, BW and SLL might have trade-offs. Spatial aliasing, which is not expected in general, offers a high BW along with a high SLL.

Example simulation on a CLA

As an example, beamforming was applied to a rigid CLA. The CLA had $L = 30$ loudspeakers and a radius of $r_0 = 0.15$ m. The MVDR beamformer was employed. One-hundred-and-forty-four control points were set uniformly on a circle of radius 2 m: one constraint point in the look direction and 143 suppression points in other directions. The look direction was $\varphi = \frac{\pi}{2}$. The constraint vector was $\mathbf{f} = \frac{1}{8\pi}$ for all frequencies and included radius-based attenuation. The observation points were set on the same circle as those of the control points but with an angle interval of 0.5° , so there were 720 points in the set. As explained above, attention should be paid to the output level of the loudspeakers. For beamforming, Tikhonov regularisation was also applied as explained in the section on analytical methods to suppress filter gain to under 0 dB.

The beam pattern of the example beam is displayed in Fig. 2.16 for 1000 Hz. The results indicate that the beam has high energy in the look direction.

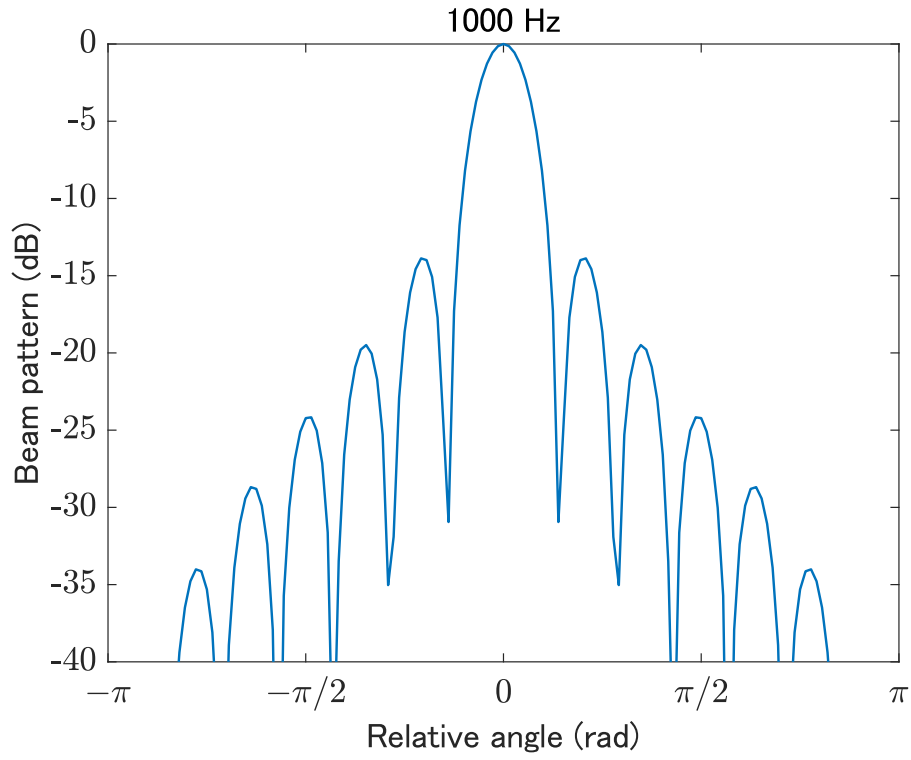


Figure 2.16: Beam pattern at 1000 Hz of the example beam.

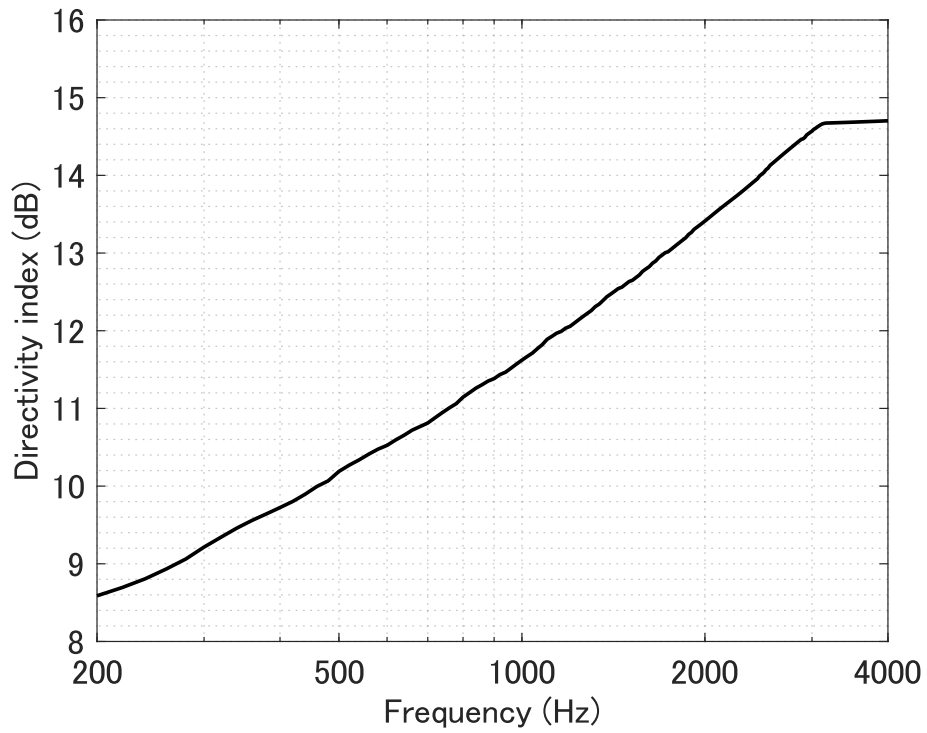


Figure 2.17: Directivity index of the example beam.

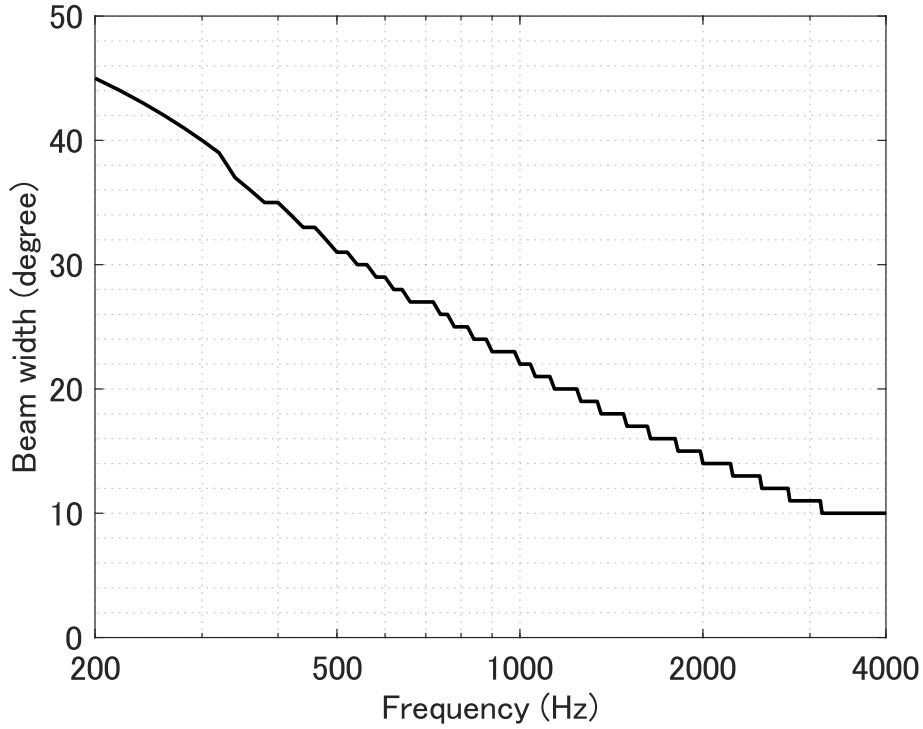


Figure 2.18: Beam width of the example beam.

The DI of the example beam is displayed in Fig. 2.17. The DI of the example increases with frequency, which means that the beam has higher energy focus in the look direction at high frequencies.

In this study, the BW was calculated only at observation points, meaning that its results are discontinuous at intervals of 0.5° . The BW of the example beam is displayed in Fig. 2.18. The BW decreases with increasing frequency, indicating that the main beam is narrower at high frequencies.

The SLL of the example beam is displayed in Fig. 2.19. The results demonstrate that SLL is not significantly affected by frequency. The maximum frequency in the figure, 4000 Hz, is under the aliasing frequency of the CLA (5411 Hz). The aliasing frequency of the CLA was approximated by $\frac{cL}{4\pi r_0}$.

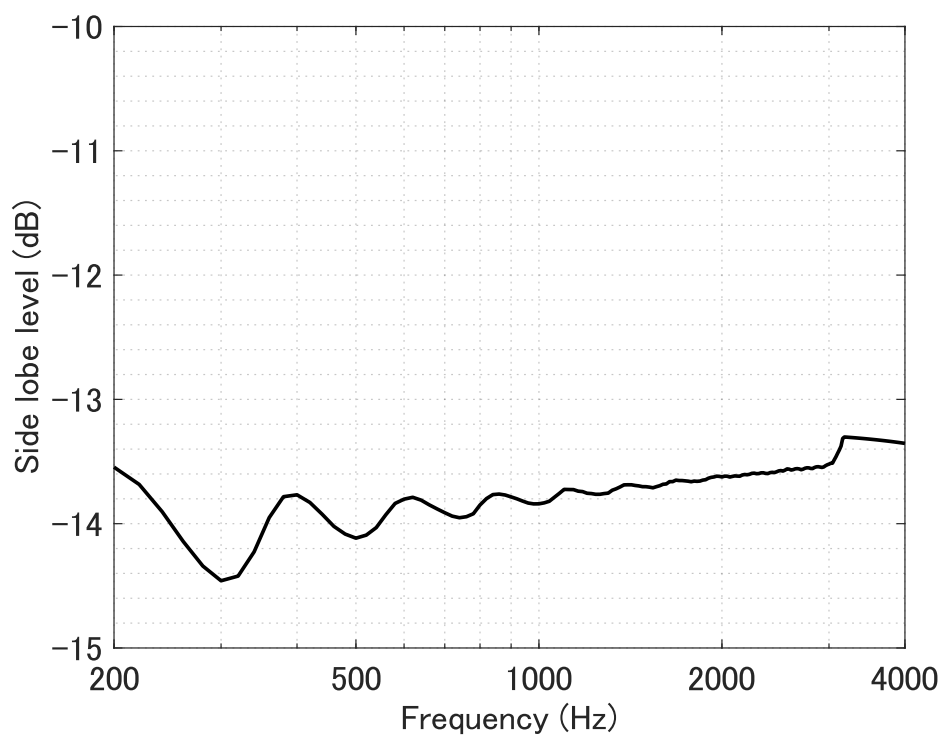


Figure 2.19: Side lobe level of the example beam.

2.7 Summary

In this chapter, the theory of spatial control was introduced. The fundamentals of sound field reproduction were explained from the mathematical and physics point of view. The spatial Fourier transforms in Cartesian and polar coordinate systems were also explained. In addition, two major methods were introduced for sound field reproduction, namely, the inverse-filter-based and the wave domain methods. Finally, the topics of interior sound field reproduction, exterior sound field reproduction, and beamforming were introduced, discussed, and evaluated.

Chapter 3

Multiple rigid circular loudspeaker array

In this chapter, a multiple circular loudspeaker array model [76, 77] is proposed in an attempt to diversify the spatial control. The array model consists of multiple compact CLAs. For reasons explained in Sec. 2.6.2, all CLAs are considered rigid. The transfer function of the array is introduced by considering the multiple scattering effect of the array. Then, a sound field reproduction method is proposed based on CHE. The performance of MCLA is discussed with respect to four topics: mode strength, which is a general property of MCLA; interior sound field reproduction; exterior sound field reproduction with implementation on focused source reproduction; and beamforming. Finally, a detailed analysis is carried out on the simplest model, 2CLA, selected for convenience. Note that MCLAs are named based on the number of CLAs such that in 2CLA, there are two circular loudspeaker arrays.

3.1 Multiple scattering effect

Unlike a simple scatter, multiple scatters reflect a wave between the scatters infinitely many times, complicating the derivation of the transfer function for the multiple rigid circular arrays. The calculation of multiple scattering is introduced in this section.

A multiple scattering model with parallel cylindrical rigid baffles has been discussed in previous studies [78]. The scattering properties of this model have been explored not only in acoustics, but also in studies of electromagnetic waves. Most studies consider the cylindrical coordinate system with the origin at the centre of each cylinder.

Letting O be the centre of a sound field, a reference coordinate system is established with O as the origin. Assuming that there are S scatters, i.e., rigid baffles, in the sound field, S coordinate systems are established for the scatters. The origins are set at the centre of each scatter, expressed as O_s ($s \in \{1, 2, \dots, S\}$ as an index). The location of centre O_s in the reference coordinate system is described as (R_s, Φ_s) . Thus, any point in the space can be represented by $S + 1$ sets of coordinates: $\mathbf{x} = (r, \phi)$ and $\mathbf{x}_s = (r_s, \phi_s)$. A configuration of $S = 3$ is illustrated in Fig. 3.1.

The wave in a sound field with multiple scatters can be described by the sum of the direct sound and its reflections. Consider a single reflection, in which a sound wave scattered by baffle s is an incident wave on scatter r ($r \in \{1, 2, \dots, S\}, r \neq s$). The Graf's addition theorem [79] can be used for this transform. Therefore, any wave incident on baffle r that had been scattered by (or radiated from) baffle s

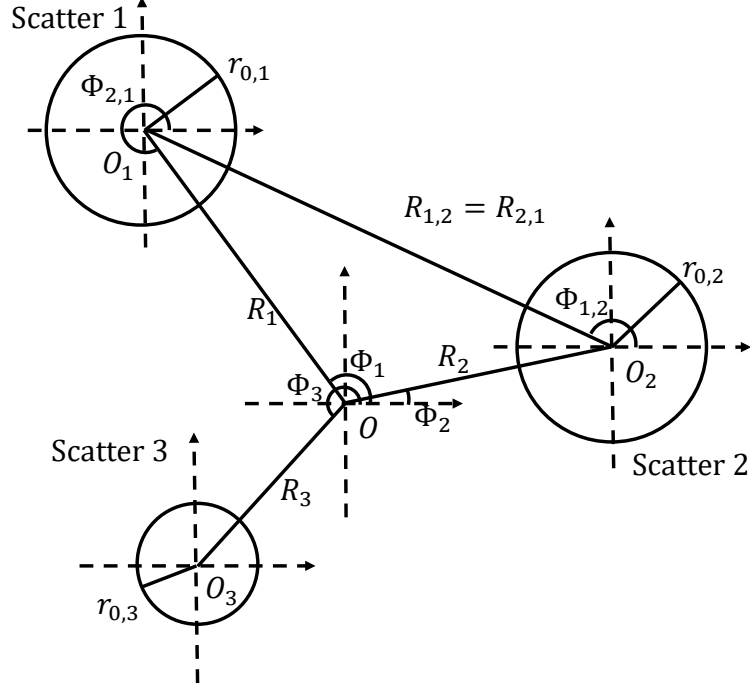


Figure 3.1: A configuration of three scatterers.

can be expressed as:

$$p_r^\triangleleft(r_r, \phi_r, \omega) = \sum_{\mu=-\infty}^{\infty} \sum_{\nu=-\infty}^{\infty} \check{p}_{\nu,s}^\triangleright(k) H_\nu(kr_s) e^{j\nu\phi_s} H_{\mu-\nu}(kR_{r,s}) e^{j(\mu-\nu)\Phi_{r,s}} J_\mu(kr_r) e^{j\mu\phi_r}. \quad (3.1)$$

The opposite situation in which a wave incident on baffle s had been scattered by (or radiated from) baffle r can be expressed as

$$p_s^\triangleleft(r_s, \phi_s, \omega) = \sum_{\mu=-\infty}^{\infty} \sum_{\nu=-\infty}^{\infty} \check{p}_{\nu,r}^\triangleright(k) H_\nu(kr_r) e^{j\nu\phi_r} H_{\mu-\nu}(kR_{s,r}) e^{j(\mu-\nu)\Phi_{s,r}} J_\mu(kr_s) e^{j\mu\phi_s}, \quad (3.2)$$

where $(R_{r,s}, \Phi_{r,s})$ are the coordinates of the centre of baffle r in coordinate system s and vice versa. Note that $r_{sr} = r_{rs}$ and $e^{j\phi_{sr}} = -e^{j\phi_{rs}}$. The field incident on baffle r is reflected from its surface. The scattered wave (i.e., reflection) can be derived with the Neumann boundary condition, which requires the particle velocity on the baffle to be 0 in the normal direction [46]. For circular scatters, the relation between an incident wave and its reflection is calculated by

$$\check{p}_{\nu,s}'(k) = \check{p}_{\nu,s}^{(\text{scattered})}(k) = -\frac{J_\nu'(kr_{0,s})}{H_\nu'(kr_{0,s})} \check{p}_{\nu,s}^\triangleleft(k) \quad (3.3)$$

where $r_{0,s}$ is the radius of the s -th circular scatterer. Thus, it is possible to calculate all the reflections among all rigid baffles.

3.2 Transfer function of the multiple rigid circular loudspeaker array

Let the zero-th reflection $\check{p}_{\nu,s}^{\check{>}}$ (the direct sound) be the radiation of a loudspeaker in MCLA. Clearly, the transfer function of the loudspeaker is the sum of all reflections.

The order of the circular harmonic expansion is truncated at N as the error is sufficiently small. The transfer function of the MCLA model can be expressed as a matrix product (details on the calculation can be found in [76, 78]), referred to as the T-matrix method [78]:

$$G^{(\text{MCLA})}(r, \phi | r', \phi', \omega) = \boldsymbol{\psi}^T \left(\sum_{i=0}^R \mathbf{T}^i \right) \boldsymbol{\gamma}, \quad (3.4)$$

where R denotes the number of reflections and $\mathbf{T}^0 := \mathbf{I}_{(2N+1)S}$. So,

$$\boldsymbol{\psi} = [\boldsymbol{\psi}_1^T, \boldsymbol{\psi}_2^T, \dots, \boldsymbol{\psi}_S^T]^T, \quad (3.5)$$

$$\boldsymbol{\gamma} = [\mathbf{0}_{(s-1) \times (2N+1)}, \boldsymbol{\gamma}_s^T, \mathbf{0}_{(S-s) \times (2N+1)}]^T. \quad (3.6)$$

$$\mathbf{T} = \begin{bmatrix} \mathbf{0}_{(2N+1) \times (2N+1)} & \mathbf{T}^{12} & \dots & \mathbf{T}^{1S} \\ \mathbf{T}^{21} & \mathbf{0}_{(2N+1) \times (2N+1)} & \dots & \mathbf{T}^{2S} \\ \vdots & \vdots & \ddots & \vdots \\ \mathbf{T}^{S1} & \mathbf{T}^{S2} & \dots & \mathbf{0}_{(2N+1) \times (2N+1)} \end{bmatrix}, \quad (3.7)$$

With the index $s \neq r \in S$, we have

$$\boldsymbol{\gamma}_s = [\gamma_{-N,s}(\mathbf{x}'_s, k), \gamma_{-N+1,s}(\mathbf{x}'_s, k), \dots, \gamma_{N,s}(\mathbf{x}'_s, k)]^T, \quad (3.8)$$

$$\boldsymbol{\psi}_s = [\psi_{-N,s}(\mathbf{x}_s, k), \psi_{-N+1,s}(\mathbf{x}_s, k), \dots, \psi_{N,s}(\mathbf{x}_s, k)]^T, \quad (3.9)$$

$$\mathbf{T}^{\text{sr}} = \begin{bmatrix} T_{-N,-N}^{\text{sr}}(k) & T_{-N,-N+1}^{\text{sr}}(k) & \dots & T_{-N,N}^{\text{sr}}(k) \\ T_{-N+1,-N}^{\text{sr}}(k) & T_{-N+1,-N+1}^{\text{sr}}(k) & \dots & T_{-N+1,N}^{\text{sr}}(k) \\ \vdots & \vdots & \ddots & \vdots \\ T_{N,-N}^{\text{sr}}(k) & T_{N,-N+1}^{\text{sr}}(k) & \dots & T_{N,N}^{\text{sr}}(k) \end{bmatrix}, \quad (3.10)$$

where

$$\gamma_{\nu,s}(\mathbf{x}'_s, k) = -\frac{e^{-j\nu\phi'_s}}{2\pi k r_{0,s} H'_\nu(k r_{0,s})}, \quad (3.11)$$

$$\psi_{\nu,s}(\mathbf{x}_s, k) = H_\nu(k r_s) e^{j\nu\phi_s}, \quad (3.12)$$

$$T_{\nu,\mu}^{\text{sr}}(k) = -\frac{J'_\mu(k r_{0,r})}{H'_\mu(k r_{0,r})} H_{\nu-\mu}(k R_{r,s}) e^{j(\nu-\mu)\Phi_{r,s}}. \quad (3.13)$$

Note that $r'_s = r_{0,s}$ if the source is on the s -th baffle. Here, $\boldsymbol{\psi}$ and $\boldsymbol{\gamma}$ contain position information on the control points and loudspeakers, respectively, and \mathbf{T} is a matrix that transforms a scattered sound into a reflected scattered sound. For computational convenience, the number of reflections is truncated to a finite number R .

An example is included to illustrate the necessity of considering the effects of multiple scattering. Figure 3.2 displays the relative amplitude for each reflection

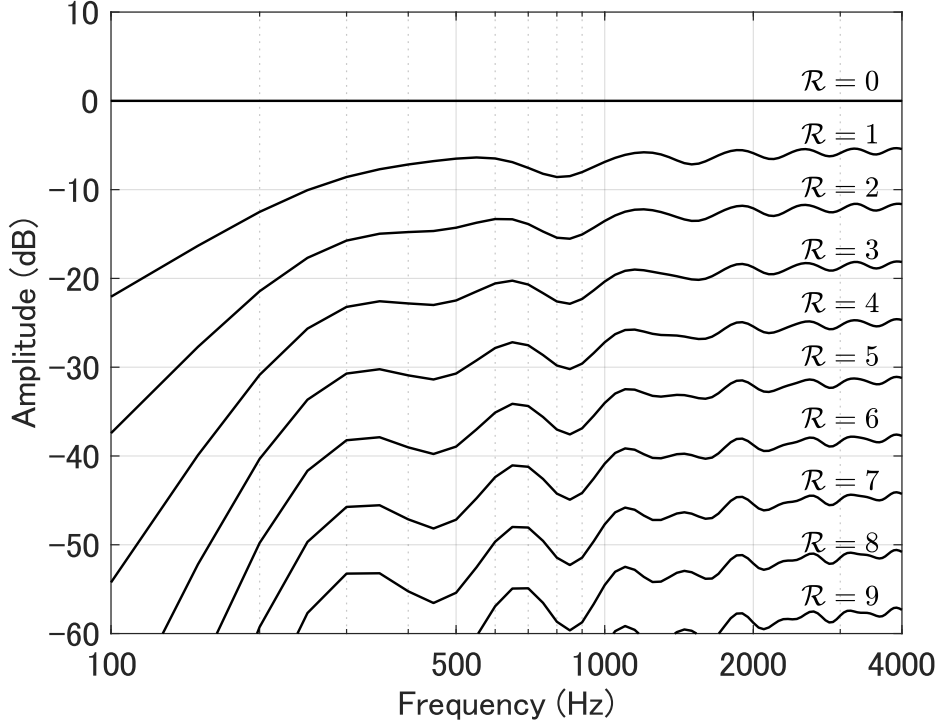


Figure 3.2: Relative amplitude of each reflection of a 2CLA. The relative amplitude is evaluated from the sound pressure measured by a microphone at (0 m, 2 m). The amplitude of the direct sound ($R = 0$) is set to 0 dB as a reference. The truncation order is $N = 30$.

for a 2CLA, with arrays centred at $(-0.25 \text{ m}, 0 \text{ m})$ and $(0.25 \text{ m}, 0 \text{ m})$. The radii of both arrays are 0.15 m. The system is driven by a loudspeaker at $(-0.1 \text{ m}, 0 \text{ m})$. In this type of setup, the reflections have a pronounced effect. The relative amplitudes of the first and second reflections are -6.9 dB and -13.5 dB , respectively. Note that, conventionally, the sound field should be reproduced within an error of -15 dB (about 4%). This indicates the necessity of taking into consideration multiple scattering, especially for higher frequencies.

3.3 Circular harmonics based sound field reproduction method

With the transfer function above, an inverse-filter-based method can be applied to the array model [76,80]. Furthermore, an analytical solution for MCLA can be obtained by applying a wave domain method to the array model [77]. However, simply applying the wave domain method is difficult as the transfer functions of loudspeakers on different baffles are expressed in different coordinate systems. In recent years, studies of multi-zone sound reproduction and higher-order sources [81,82] have identified methods for controlling the sound in non-concentric circular areas. There are two main goals in applying these methods:

- To expand the sound field using orthogonal bases, such as Bessel and Hankel functions.
- To describe the sound field in a reference coordinate system using Graf's addition theorem.

Inspired by such methods, a wave domain method for 2CLA is proposed. The method matches the sound-field coefficients by transforming the coordinate systems while taking into account the multiple scattering effect [77].

As in (2.53) and (2.55), the reproduced sound field of S discrete loudspeaker arrays (with L_s loudspeakers on the s -th array) can be expressed as:

$$\hat{p}(r, \phi, \omega) = \sum_{s=1}^S \left[\sum_{l=1}^{L_s} G^{(\text{MCLA})}(r_s, \phi_s | r_{l,s}, \phi_{l,s}, \omega) \sum_{\nu=-N_s}^{N_s} \hat{d}_{\nu,s}(k) e^{j\nu\phi_{l,s}} \right], \quad (3.14)$$

where $G^{(\text{MCLA})}(r_s, \phi_s | r_{l,s}, \phi_{l,s}, \omega)$ is the transfer function in Sec. 3.1. Here, $(r_{l,s}, \phi_{l,s})$ is the position of the l -th loudspeaker in the s -th array. The truncation order for the circular harmonic expansion is set as $N_s = \lfloor (L_s - 1)/2 \rfloor$. With the orthogonality of $e^{j\nu\phi}$, (3.14) can be transformed to:

$$\hat{p}(r, \phi, \omega) = \boldsymbol{\psi}^T \left(\sum_{i=0}^R \mathbf{T}^i \right) \mathring{\boldsymbol{\Gamma}} \mathring{\mathbf{d}} \quad (3.15)$$

where

$$\mathring{\boldsymbol{\Gamma}} = \begin{bmatrix} \mathring{\boldsymbol{\Gamma}}_1^T & \mathbf{0}_{(2N_2+1) \times (2N+1)} & \cdots & \mathbf{0}_{(2N_5+1) \times (2N+1)} \\ \mathbf{0}_{(2N_1+1) \times (2N+1)} & \mathring{\boldsymbol{\Gamma}}_2^T & \cdots & \mathbf{0}_{(2N_5+1) \times (2N+1)} \\ \vdots & \vdots & \ddots & \vdots \\ \mathbf{0}_{(2N_1+1) \times (2N+1)} & \mathbf{0}_{(2N_2+1) \times (2N+1)} & \cdots & \mathring{\boldsymbol{\Gamma}}_S^T \end{bmatrix}^T, \quad (3.16)$$

$$\mathring{\boldsymbol{\Gamma}}_s = L_s \begin{bmatrix} \mathbf{0}_{(N-N_s) \times (2N_s+1)} \\ \text{diag}(\hat{\gamma}_{-N_s,s}(k), \hat{\gamma}_{-N_s+1,s}(k), \dots, \hat{\gamma}_{N_s,s}(k)) \\ \mathbf{0}_{(N-N_s) \times (2N_s+1)} \end{bmatrix}, \quad (3.17)$$

$$\hat{\gamma}_{\nu,s}(k) = -\frac{1}{2\pi k r_{0,s} H'_\nu(k r_{0,s})}, \quad (3.18)$$

$$\mathring{\mathbf{d}} = [\mathring{\mathbf{d}}_1^T, \mathring{\mathbf{d}}_2^T, \dots, \mathring{\mathbf{d}}_S^T]^T, \quad (3.19)$$

$$\mathring{\mathbf{d}}_s = [d_{-N_s,s}^{\circ}(k), d_{-N_s+1,s}^{\circ}(k), \dots, d_{N_s,s}^{\circ}(k)]^T. \quad (3.20)$$

To derive a relation between the driving functions of each mode and the sound-field coefficients in the circular harmonic domain, it is necessary to perform a coordinate transformation. $\psi_{\nu,s}$, expressed in the coordinate system at the origin O_s can be transformed to the coordinate system at O [33]:

$$\psi_{\nu,s}(\mathbf{x}_s, k) = \sum_{\nu'=-\infty}^{\infty} (-1)^{\nu-\nu'} J_{\nu-\nu'}(k R_s) H_{\nu'}(kr) e^{j(\nu-\nu')\Phi_s} e^{j\nu'\phi}. \quad (3.21)$$

Here, Graf's addition theorem [79] has been applied; therefore, the conditions $\nu'_{\max} \gg \nu$ and $r > R_s$ must be satisfied. By truncating $\boldsymbol{\psi}$ in (3.15) for sufficiently large N , it can be transformed to:

$$\boldsymbol{\psi} = \check{\mathbf{K}} \check{\boldsymbol{\chi}}, \quad (3.22)$$

where

$$\boldsymbol{\chi} = [\chi_{-N}(\mathbf{x}, k), \chi_{-N+1}(\mathbf{x}, k), \dots, \chi_N(\mathbf{x}, k)]^T, \quad (3.23)$$

$$\chi_\nu(\mathbf{x}, k) = H_\nu(kr)e^{j\nu\phi}, \quad (3.24)$$

$$\check{\mathbf{K}} = \left[\check{\mathbf{K}}_1^T, \check{\mathbf{K}}_2^T, \dots, \check{\mathbf{K}}_S^T \right]^T, \quad (3.25)$$

$$\check{\mathbf{K}}_s = \begin{bmatrix} \check{\kappa}_{0,s}(k) & \check{\kappa}_{-1,s}(k) & \dots & \check{\kappa}_{-2N,s}(k) \\ \check{\kappa}_{1,s}(k) & \check{\kappa}_{0,s}(k) & \dots & \check{\kappa}_{-2N+1,s}(k) \\ \vdots & \vdots & \ddots & \vdots \\ \check{\kappa}_{2N,s}(k) & \check{\kappa}_{2N-1,s}(k) & \dots & \check{\kappa}_{0,s}(k) \end{bmatrix}, \quad (3.26)$$

$$\check{\kappa}_{\nu,s}(k) = (-1)^\nu J_\nu(kR_s)e^{j\nu\Phi_s}. \quad (3.27)$$

Then the reproduced sound field can be transformed to

$$\hat{p}(r, \phi, \omega) = \boldsymbol{\chi}^T \check{\mathbf{G}} \mathring{\mathbf{d}}, \quad (3.28)$$

where

$$\check{\mathbf{G}} = \check{\mathbf{K}}^T \left(\sum_{i=0}^R \mathbf{T}^i \right) \mathring{\boldsymbol{\Gamma}}. \quad (3.29)$$

The desired exterior sound field at the virtual observation points with a limited order N can be expressed as

$$p(r, \phi, \omega) = \sum_{\nu=-N}^N \check{p}_\nu H_\nu(kr)e^{j\nu\phi} \quad (3.30)$$

$$= \boldsymbol{\chi}^T \check{\mathbf{p}}, \quad (3.31)$$

where \check{p}_ν is the sound field coefficient [46]:

$$\check{\mathbf{p}} = [\check{p}_{-N}(k), \check{p}_{-N+1}(k), \dots, \check{p}_N(k)]^T. \quad (3.32)$$

A relation between each mode of the loudspeaker arrays and the sound-field coefficient can be obtained from (3.29). Thus, the driving function in the circular harmonic domain is calculated. However, as this relation is not orthogonal, the driving function cannot be obtained directly. Therefore, a least-squares method was applied with a Tikhonov regularisation [10] as follows:

$$\mathring{\mathbf{d}} = (\check{\mathbf{G}}^H \check{\mathbf{G}} + \lambda \mathbf{I}_{\sum_{s=1}^S (2N_s+1)})^{-1} \check{\mathbf{G}}^H \check{\mathbf{p}}, \quad (3.33)$$

where λ is a regularisation parameter.

As in (2.55), the driving function for the l -th loudspeaker on the s -th array can be obtained from

$$d_{l,s}(\omega) = \sum_{\nu=-N_s}^{N_s} \mathring{d}_{\nu,s}(k) e^{j\nu\phi_{l,s}}. \quad (3.34)$$

Intrinsically, this method is similar to methods with higher-order sources [65, 81, 83] and higher-order microphones [84–86]. This method is unique in that here the influence of the multiple scattering between the rigid baffles is taken into account.

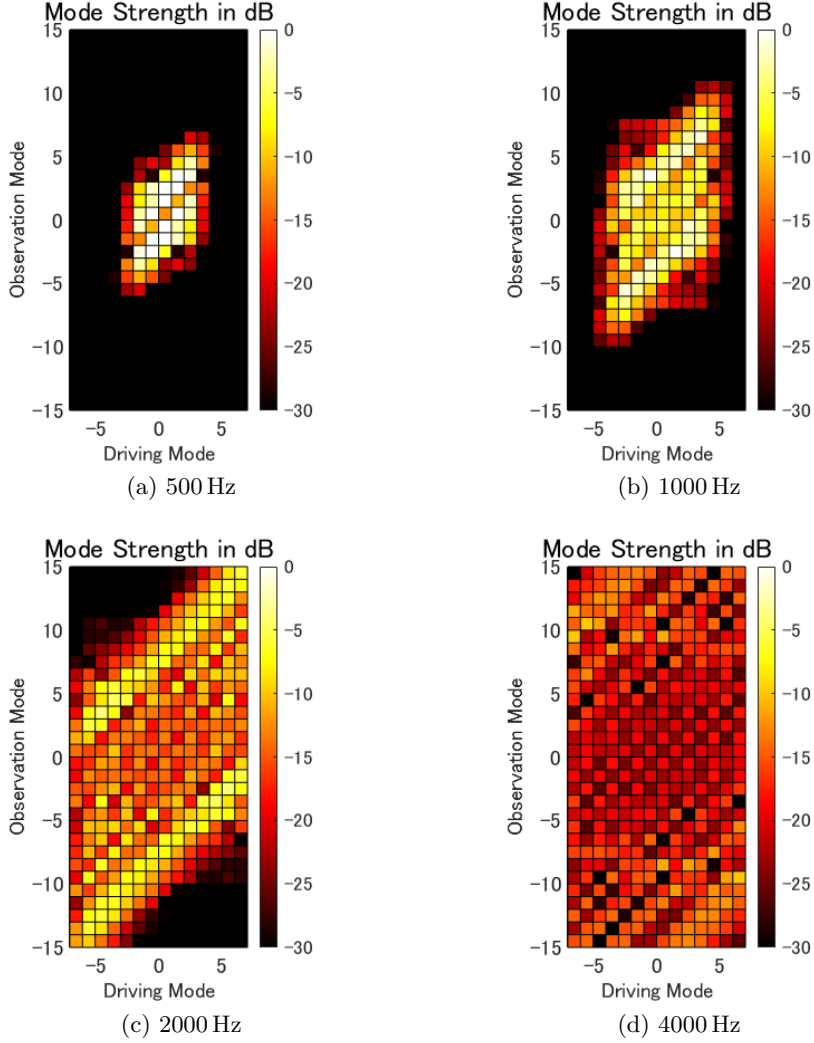


Figure 3.3: Mode strength of a rigid 2CLA. The two loudspeaker arrays have rigid surfaces with radii of 0.15 m and are located at $(-0.25 \text{ m}, 0 \text{ m})$ and $(0.25 \text{ m}, 0 \text{ m})$, respectively.

3.4 Mode strength

Here, a general property of MCLA: the mode strength is explored. In conventional studies, mode strength has been used to evaluate system efficiency. The mode strength of 2CLA is discussed as an example of MCLA.

In (3.33), the coefficient of the transfer function, $\check{\mathbf{G}}$, is the primary factor affecting reproduction efficiency. Here, the focus is on the power of $\check{\mathbf{G}}$, which represents the mode strength, to determine how array geometry affects sound field reproduction.

The power of $\check{\mathbf{G}}$ is shown in Fig. 3.3. The x -axis represents the driving modes of 2CLA, and the y -axis represents the observation modes for the secondary sound field. A driving mode is the mode used for driving loudspeakers, whereas observation mode is the mode of the circle centred at the origin O . The results demonstrate how an observation mode can be synthesised from the driving modes. A high mode strength indicates that the driving mode can easily be used to synthesise the observation mode.

Clearly, driving a single mode of the 2CLA generates multiple modes in the

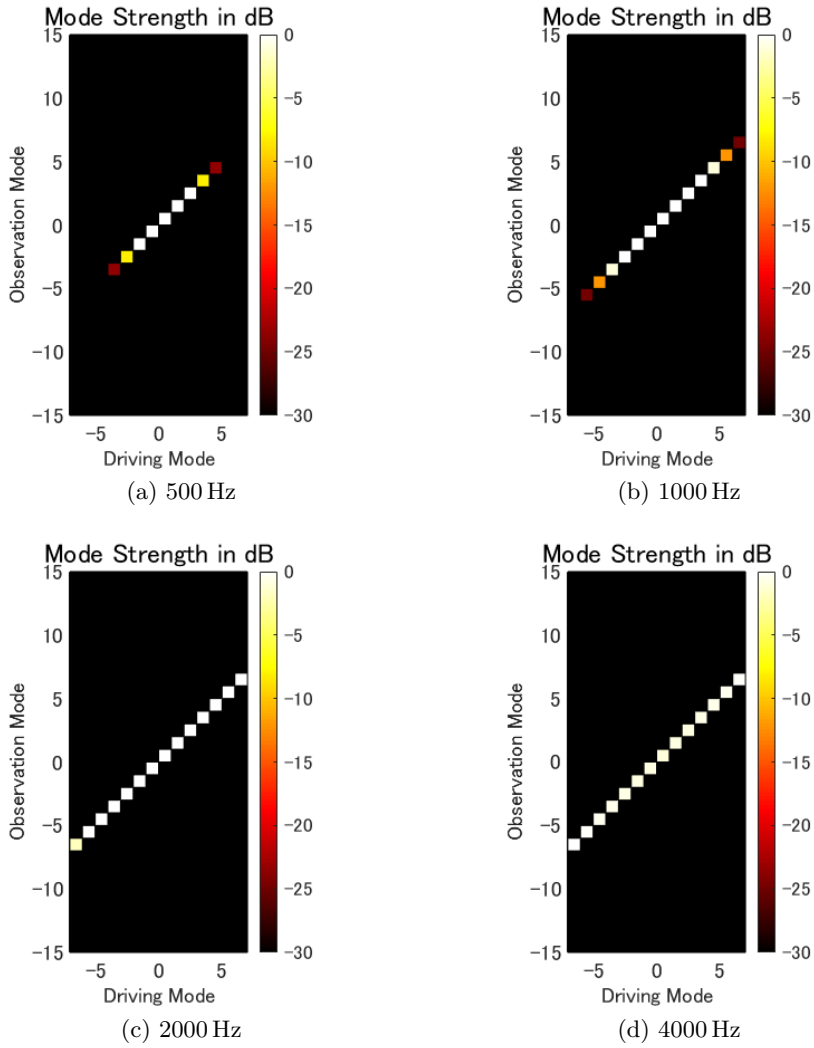


Figure 3.4: Mode strength of a rigid CLA. The loudspeaker array has rigid surfaces with a radius of 0.15 m and is located at (0 m, 0 m).

field. In contrast, each mode of CLA is usually related to only one observation mode, as shown in Fig. 3.4. Thus, two properties of MCLA are obtained:

1. The lower modes of a driving function can be used to synthesise the higher modes of the field. This indicates that 2CLA has good potential for reproducing complex fields.
2. Conversely, higher driving modes are needed to synthesise lower modes. If only lower modes are used, there will be errors and the amplitudes will depend on the frequency. Therefore, 2CLA is less useful in reproducing simple fields.

The mode strength of an open 2CLA is shown in Fig. 3.5. Comparing it with Fig. 3.3, it can be seen that the off-centred open array also provides a complex mode connection, whereas the mode strength is weaker than that of the rigid 2CLA.

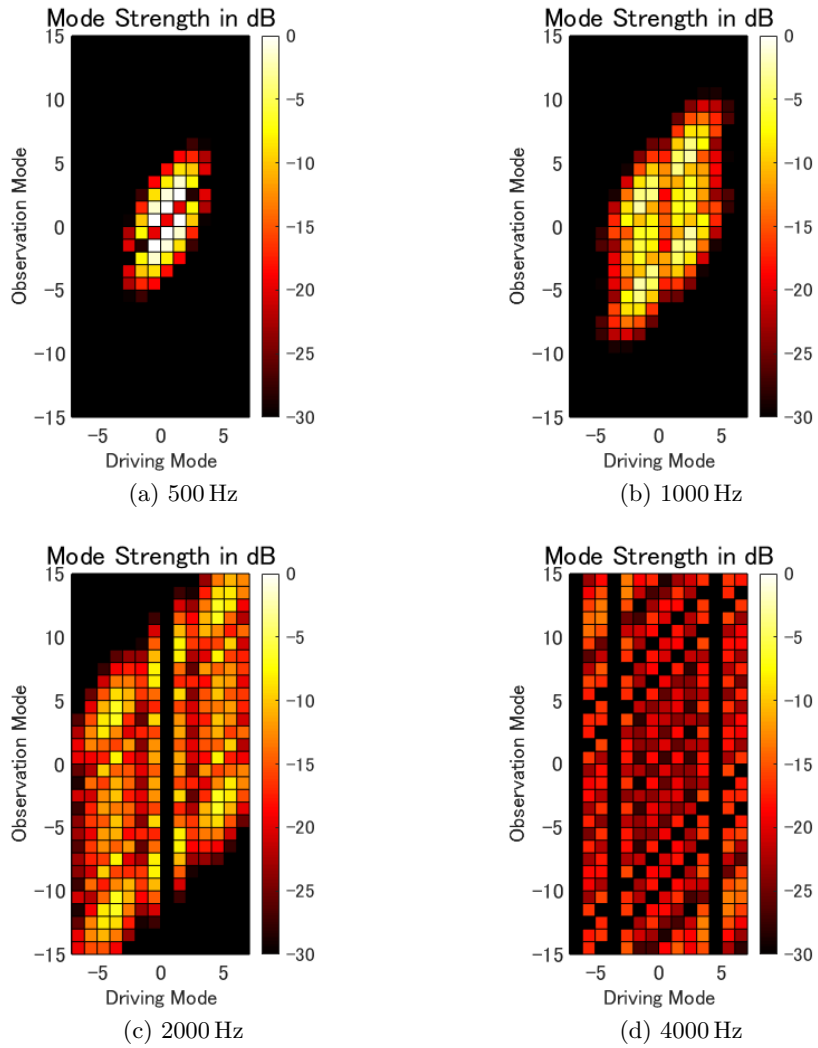


Figure 3.5: Mode strength of an open 2CLA. The two loudspeaker arrays are open arrays with radii of 0.15 m and are located at $(-0.25 \text{ m}, 0 \text{ m})$ and $(0.25 \text{ m}, 0 \text{ m})$, respectively.

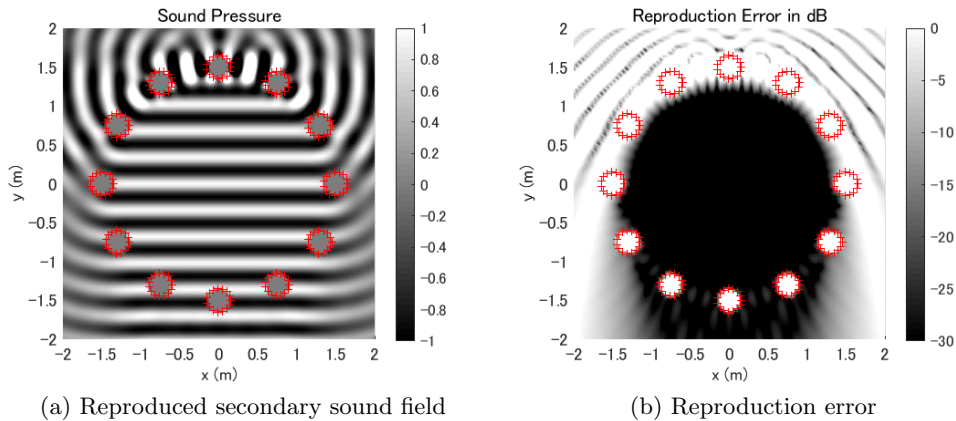


Figure 3.6: An example of the interior sound field reproduction using an MCLA. Only the first reflection was considered both in the derivation of the driving function and calculation of the sound field, i.e. identical to the method in [81].

3.5 Interior sound field reproduction

The idea of using MCLA for interior sound field reproduction was proposed previously [81, 83, 87, 88] where MCLA is referred to as a higher-order source. As the comparison on using an MCLA versus a single CLA has been discussed in previous studies, it is omitted in the thesis apart from referring to it by quoting the conclusion [81]:

‘Using the higher order sources allows a trade-off between the bandwidth of reproduction and the errors that occur above the spatial Nyquist frequency (i.e., the frequency at which spatial aliasing occurs), by limiting the maximum mode order that is controlled by the array.’

However, the previous studies have not considered the multiple scattering effect of MCLA. The transfer function of the higher-order source only considered the first reflection of the rigid baffle the source mounted on. Here, the method including multiple scattering is revised and the results are presented.

An example of the original method in [81] is shown in Fig. 3.6. A simulation was conducted to reproduce a plane wave at 1000 Hz, as was the case in Fig. 2.7(a). The simulation was carried out with 12 CLAs uniformly located on a circle of radius 1.5 m. Each CLA had 15 loudspeakers uniformly mounted on the rigid surface. The radii of the CLAs were equally set to 0.15 m. The reproduced secondary sound field is shown in (a). The maximum orders for deriving the driving functions were set to $N = 30$ and $N_s = \lceil (15 - 1)/2 \rceil = 7$. For the original method, only the first reflection was considered in the simulation: both in the derivation of the driving function and calculation of the sound field. This means that the transfer function is matched and that the performance displayed in (b) is ideal.

However, when the multiple scattering effect in the sound field (where it actual exists) is considered without changing the driving function, the mismatched transfer functions result in errors. As shown in Fig. 3.7, the wavefront has lost its shape and the errors are higher. Up to the twelfth reflection was considered. The maximum orders were truncated at $N = 60$ while calculating the sound field.

Then, with the proposed method, the multiple scattering effect is considered during the derivation of the driving function. The transfer functions matched again and provided the ideal reproduction of Fig. 3.8.

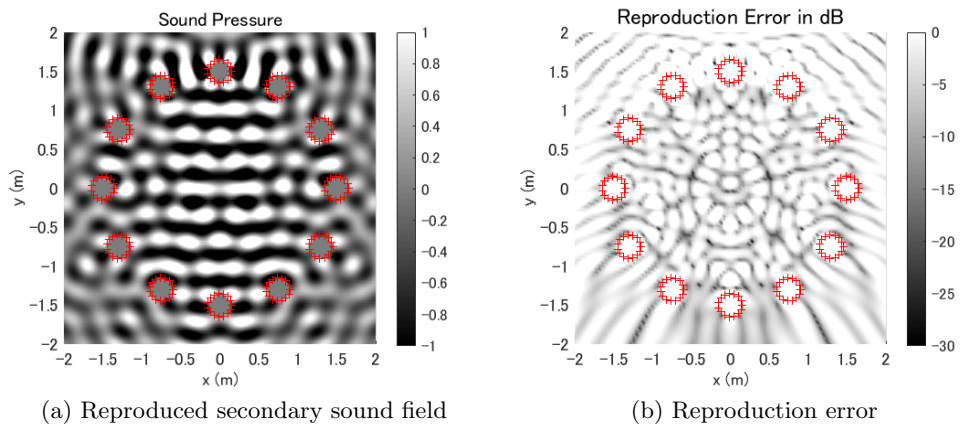


Figure 3.7: An example of the interior sound field reproduction using an MCLA. Only the first reflection was considered during the derivation of the driving function whereas multiple scattering was included in the calculation of the sound field.

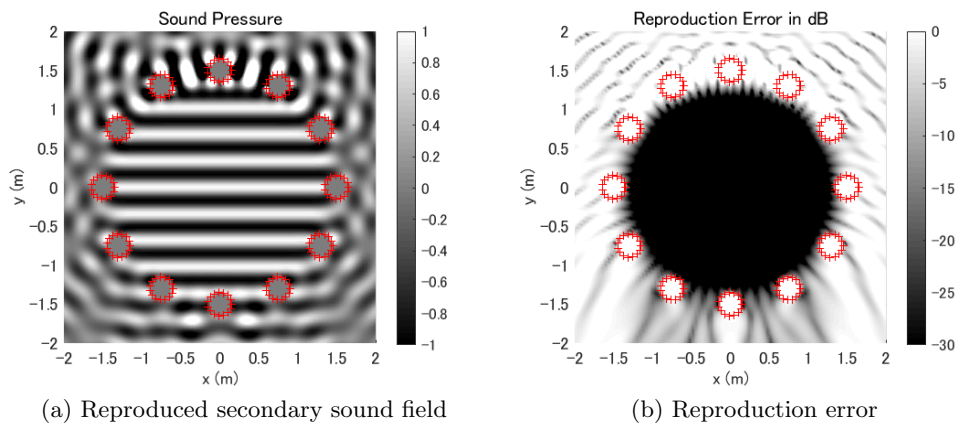


Figure 3.8: An example of the interior sound field reproduction using an MCLA. The multiple scattering was included both during derivation of the driving function and calculation of the sound field.

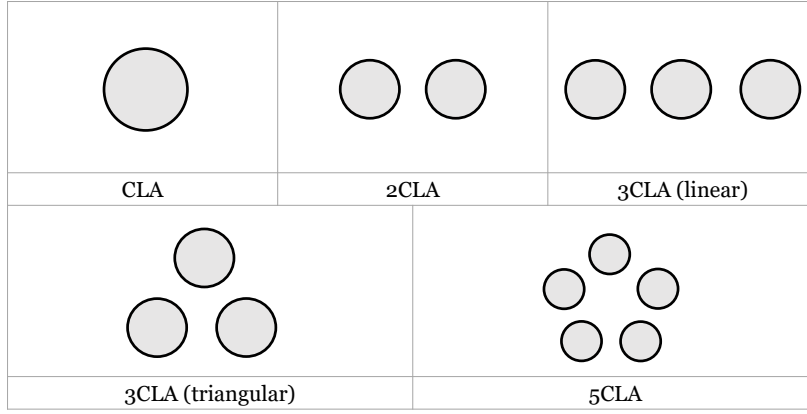


Figure 3.9: Contours of five arrays.

3.6 Exterior sound field reproduction

In this section, the effect of MCLA on exterior sound field reproduction is discussed. The performance is evaluated by implementing focused source reproduction. The discussion is on five different array configurations: (i) a CLA with 30 loudspeakers as a reference; (ii) a 2CLA with 15 loudspeakers in each array; (iii) a ‘linear’ 3CLA with 10 loudspeakers in each array; (iv) a ‘triangular’ 3CLA with 10 loudspeakers in each array; and (v) a 5CLA with 6 loudspeakers in each array. These array contours are shown in Fig. 3.9.

Each CLA was considered rigid, and within each CLA, loudspeakers were uniformly mounted onto the rigid surface. In all simulations, up to the twelfth reflection was considered, and the maximum order was truncated at $N = 60$ in the calculation of the transfer functions.

In the derivation of the driving function, N was truncated at 30 and N_s was truncated according to the number of loudspeakers in each CLA. As explained in Sec. 2.6.2, Tikhonov regularisation was applied to suppress the filter gain to under 0 dB in all of the simulations above.

3.6.1 Comparison with CLA

To explore the features of MCLA, three groups of arrays were selected for comparison:

Group A Group A consists of CLA, 2CLA, and 3CLA (linear). The radii of all CLAs were set to 0.15 m. The inter-array distances (between the centre of two arrays) for 2CLA and 3CLA were both 0.5 m. The centre of the single CLA was (0 m, 0 m); the centres of the 2CLA were (−0.25 m, 0 m) and (0.25 m, 0 m); the centres of the 3CLA were (−0.5 m, 0 m), (0 m, 0 m), and (0.5 m, 0 m). Two kinds of primary sound field were picked: (i) a focused source at (0 m, 0.5 m); (ii) twenty random focused sources inside a 0.5 m circle. For (i), because of the asymmetry of the arrays, the rotated (by exchanging the x and y coordinates of the centres) 2CLA and 3CLA were included in the comparison.

Group B Group B consists of CLA, off-centred 2CLA, and off-centred 3CLA (linear). The radii of all CLAs were set to 0.15 m. The inter-array distances (between the centre of two arrays) for 2CLA and 3CLA were both 0.5 m. The centre of the single CLA was (0 m, 0 m); the centres of

the 2CLA were $(0 \text{ m}, -0.5 \text{ m})$ and $(0 \text{ m}, 0 \text{ m})$; the centres of the 3CLA were $(0 \text{ m}, -1 \text{ m})$, $(0 \text{ m}, -0.5 \text{ m})$, and $(0 \text{ m}, 0 \text{ m})$. The target focused source was set at $(0 \text{ m}, 0.5 \text{ m})$.

Group C Group C consists of CLA, 3CLA (triangular), and 5CLA. The radius of the single CLA was set to 0.3 m; the radii of the 3CLA were set to 0.1 m; radii of the 5CLA were set to 0.06 m. The single CLA was located at the centre of the sound field; the CLAs of the 3CLA were uniformly located on a circle of radius 0.2 m; the CLAs of the 5CLA were uniformly located on a circle of radius 0.24 m. The target focused source was set at $(0 \text{ m}, 0.5 \text{ m})$.

The reason is explained as follows: Group A is selected to simply check the performance when additional CLAs are added. The 2CLA and 3CLA are expected to outperform the single CLA. Note that specific MCLAs in group A were located closer to the target source of (i), sound field reproduction would be easier in such a case. In Group B, on the other hand, the distances between the MCLAs and the target source are fixed. In Group C, a comparison similar to that of the interior sound field reproduction was adopted: a “complete” CLA was compared to distributed MCLAs. All arrays in group C are tangent to a circle with radius of 0.3 m. The array radii were selected to maintain the same loudspeaker interval for all arrays.

Group A

In Figs. 3.10–3.14, the results of reproducing a focused source at 1000 Hz are displayed. Figure 3.10(a) is the target primary sound field where a focused source is set at $(0 \text{ m}, 0.5 \text{ m})$. Comparing the wavefronts and errors in the figures, it is observed that the MCLAs, especially the rotated ones, outperform the conventional CLA.

To exclude direction dependence in the results, a simulation with 20 random target focused sources was conducted. All the virtual sources had amplitudes randomised between 0 and 1, phases randomised between 0 and 2π , positions randomised inside a circle of radius 0.5 m, and first-order directivities randomised whereby each directivity was synthesised by a combination of a monopole and a dipole in a random direction and with a random weight. The total amplitude was subsequently normalised. The array configuration and other conditions were the same as above, excluding rotations. The results of reproducing random multiple focused sources are displayed in Figs. 3.15–3.17. Without direction dependence, it is observed that MCLAs still outperform the conventional CLA.

Next, the arrays in the frequency band of 200–4000 Hz were compared. The primary field included a focused source at $(0 \text{ m}, 0.5 \text{ m})$. The error over the control region was evaluated by (2.69) in the sample ring region:

$$\Lambda = \{\mathbf{x} \mid \forall 1 \leq l \leq L, 0.1 + \max(r_{\odot}, r_l) \leq |\mathbf{x}| \leq 4\}, \quad (3.35)$$

r_l is the distance from the origin to the l -th loudspeaker of the MCLA. The results are shown in Fig. 3.18. The “on x” and “on y” legends denote the MCLA along the x -axis and along the y -axis, respectively.

With the threshold of reproduction set to -15 dB (the dash-dot line), all MCLAs displayed higher maximum controllable frequencies than the single CLA. The rest of the features are summarised as follows:

- 3CLA outperformed 2CLA (further outperformed CLA) for most conditions with spikes of errors at specific frequencies.

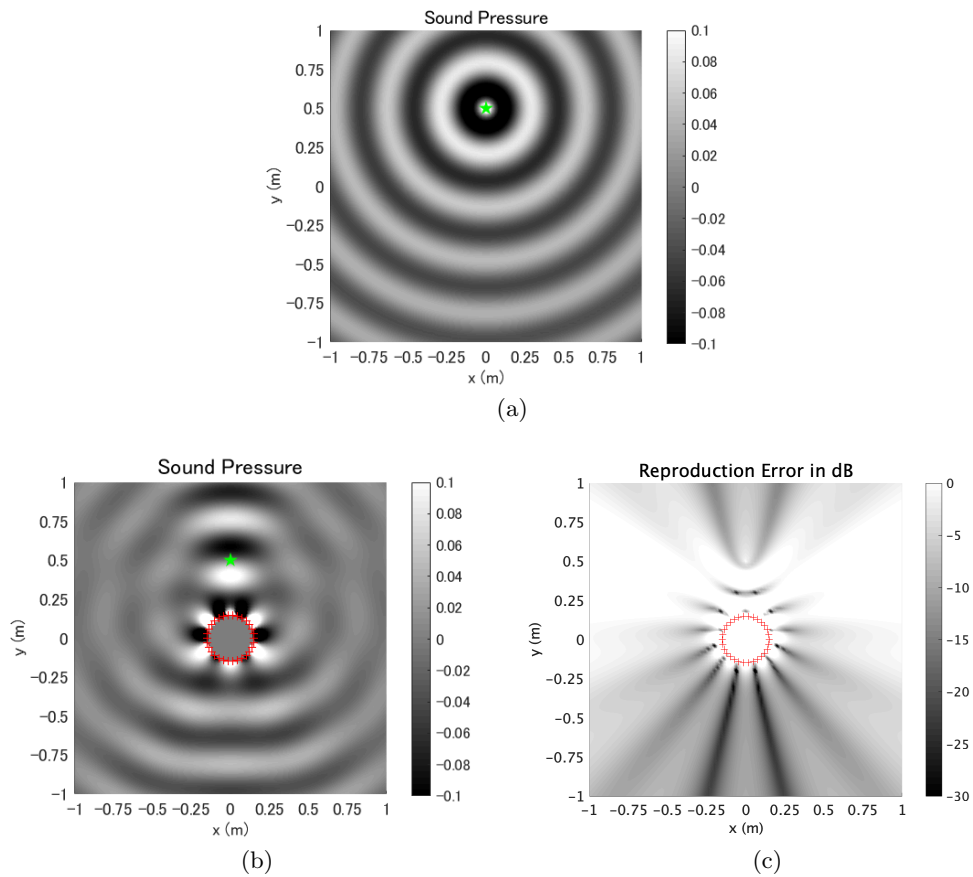


Figure 3.10: Reproducing a focused source using a CLA. (a) Primary sound field of the target source. (b) Reproduced secondary sound field by CLA. (c) Reproduction error.

- MCLAs performed better for the “on y” layout. This can be attributed to the array and focused source being closer to each other as a result of the layout.
- Apart from the threshold, MCLAs displayed higher error at high frequencies (above 2000 Hz).

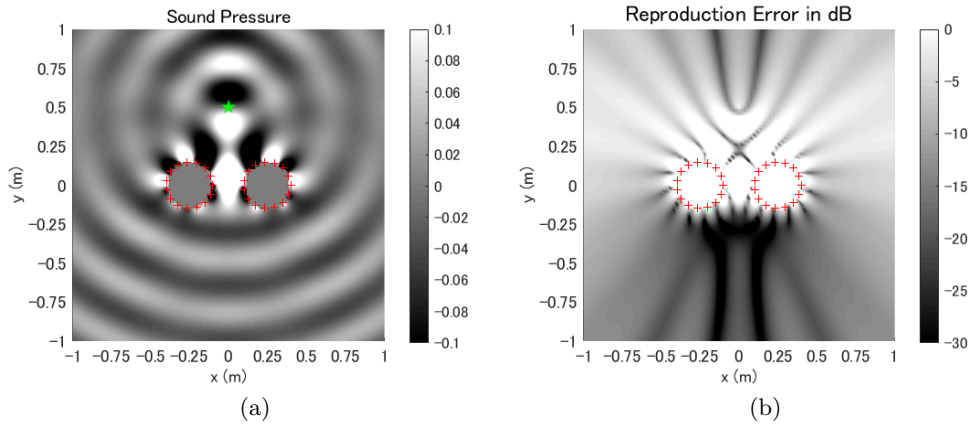


Figure 3.11: Reproducing a focused source using 2CLA. (a) Reproduced secondary sound field by 2CLA. (b) Reproduction error.

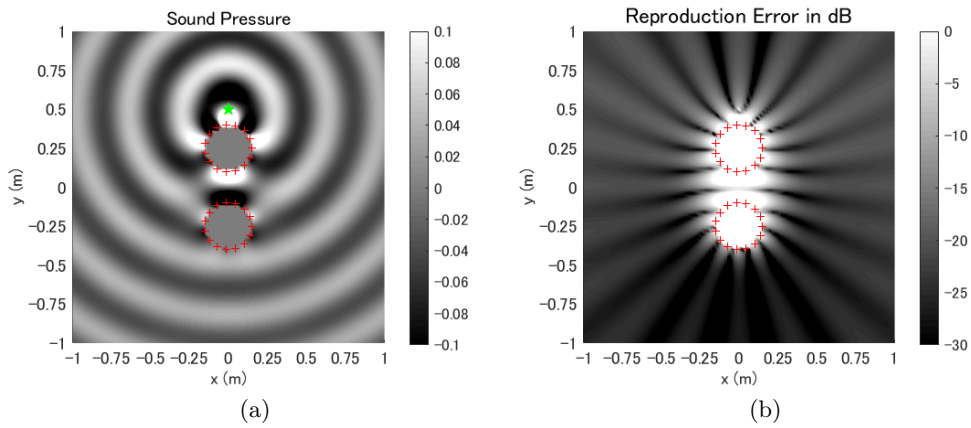


Figure 3.12: Reproducing a focused source using a rotated 2CLA. (a) Reproduced secondary sound field by 2CLA. (b) Reproduction error.

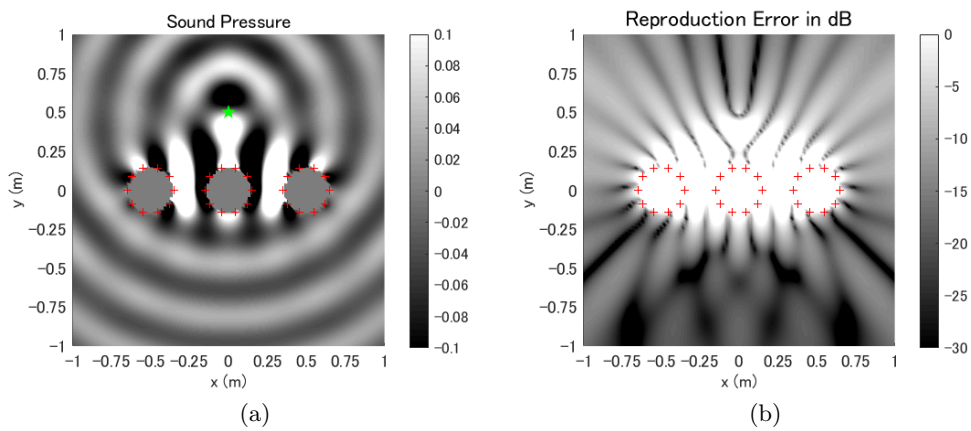


Figure 3.13: Reproducing a focused source using 3CLA. (a) Reproduced secondary sound field by 3CLA. (b) Reproduction error.

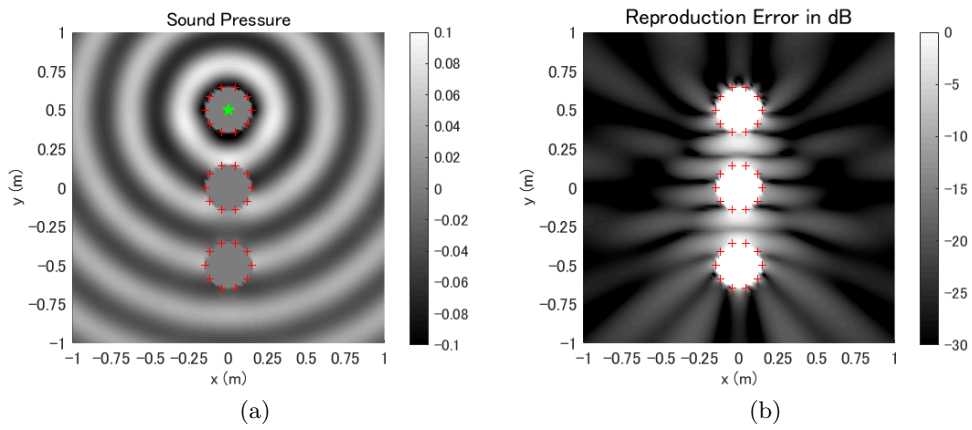


Figure 3.14: Reproducing a focused source using a rotated 3CLA. (a) Reproduced secondary sound field by 3CLA. (b) Reproduction error.

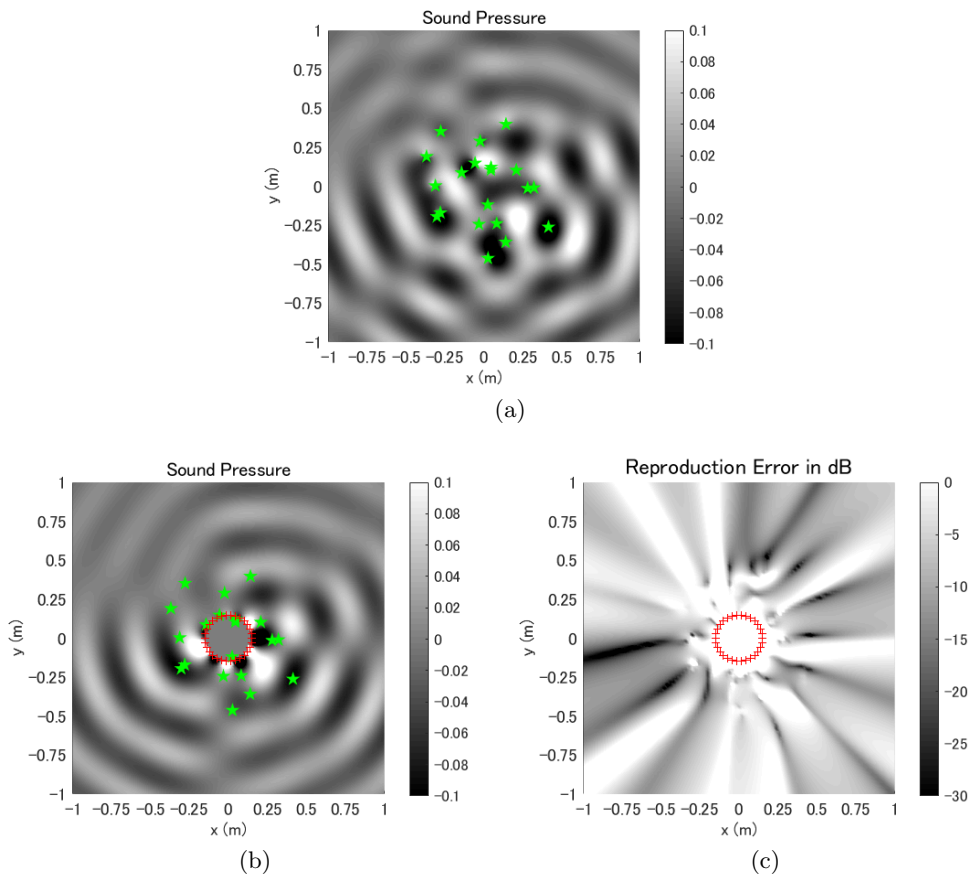


Figure 3.15: Reproducing random focused sources using CLA. (a) Primary sound field of the target source. (b) Reproduced secondary sound field by CLA. (c) Reproduction error.

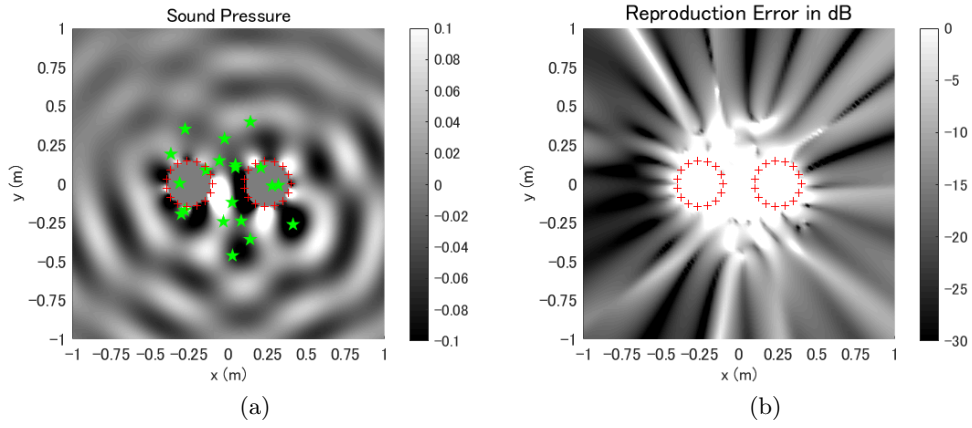


Figure 3.16: Reproducing random focused sources using 2CLA. (a) Reproduced secondary sound field by 2CLA. (b) Reproduction error.

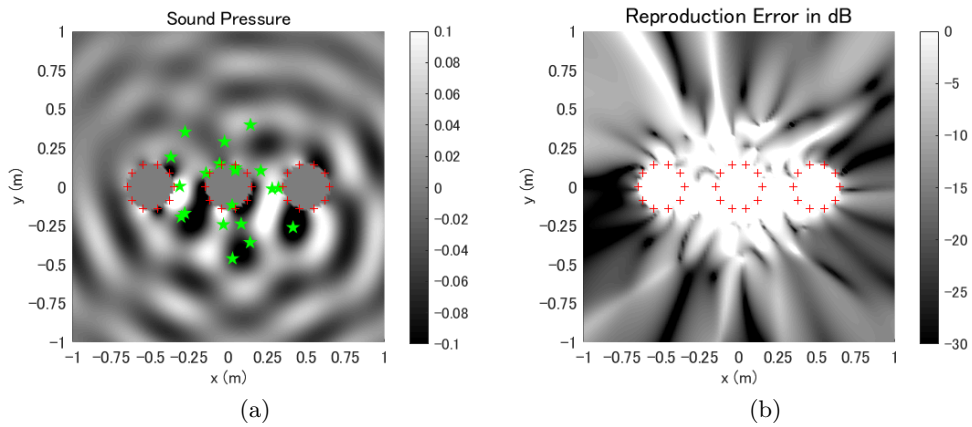
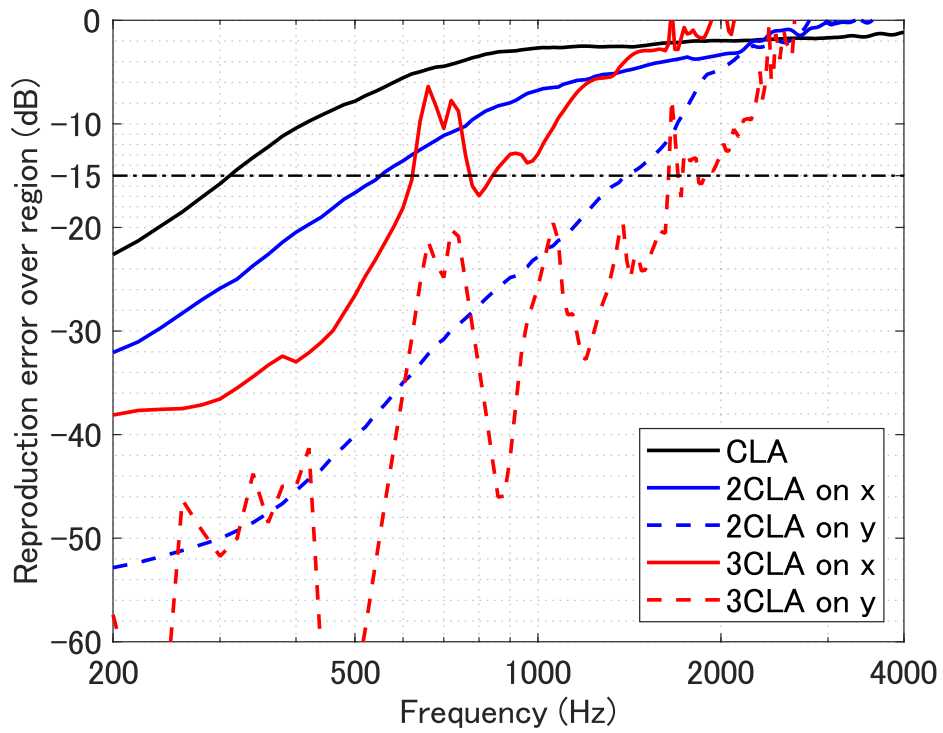
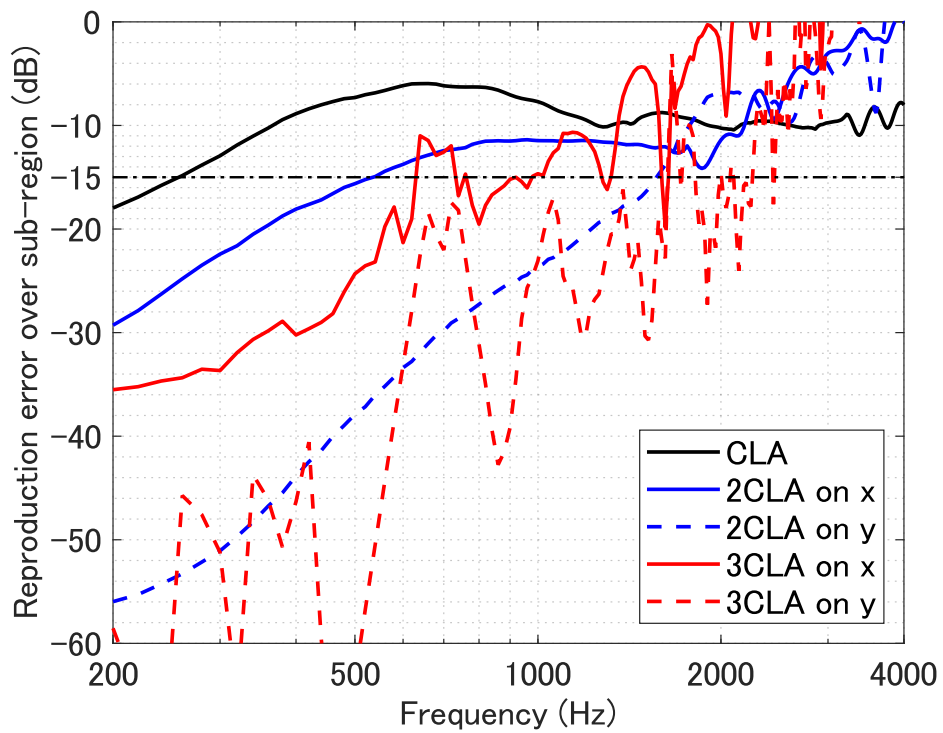


Figure 3.17: Reproducing random focused sources using 3CLA. (a) Reproduced secondary sound field by 3CLA. (b) Reproduction error.



(a)



(b)

Figure 3.18: Reproduction error over a region (Group A).

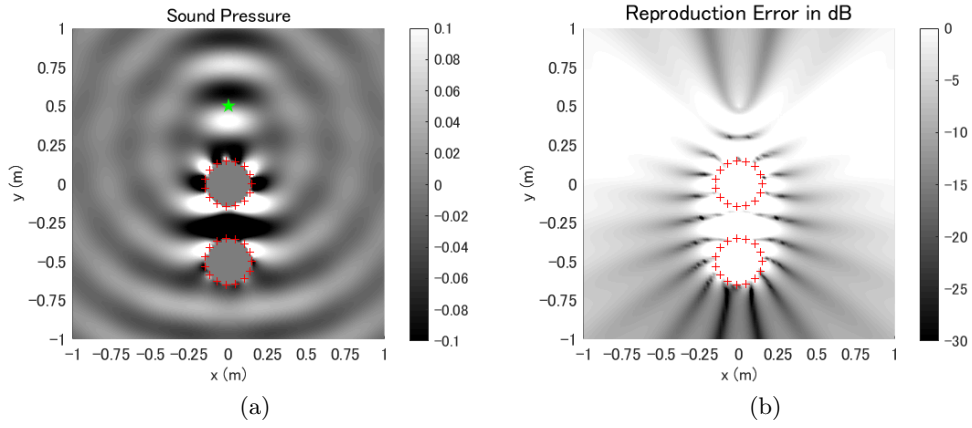


Figure 3.19: Reproducing a focused source using an off-centred 2CLA. (a) Reproduced secondary sound field by 2CLA. (b) Reproduction error.

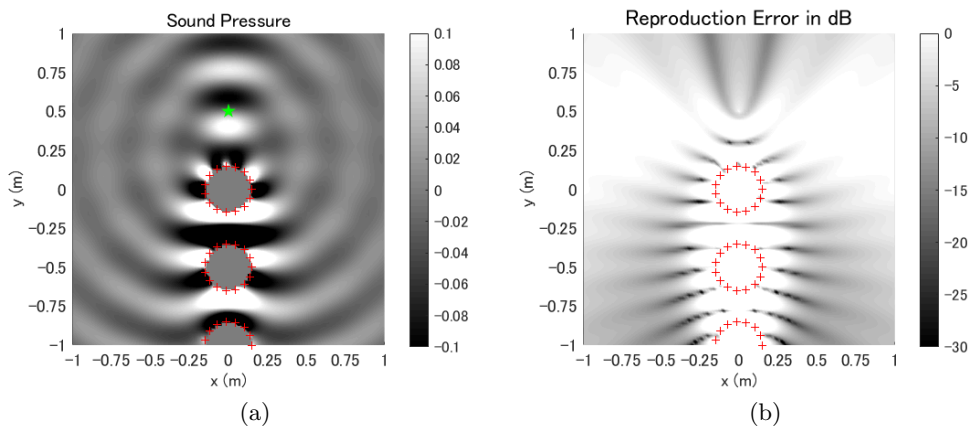
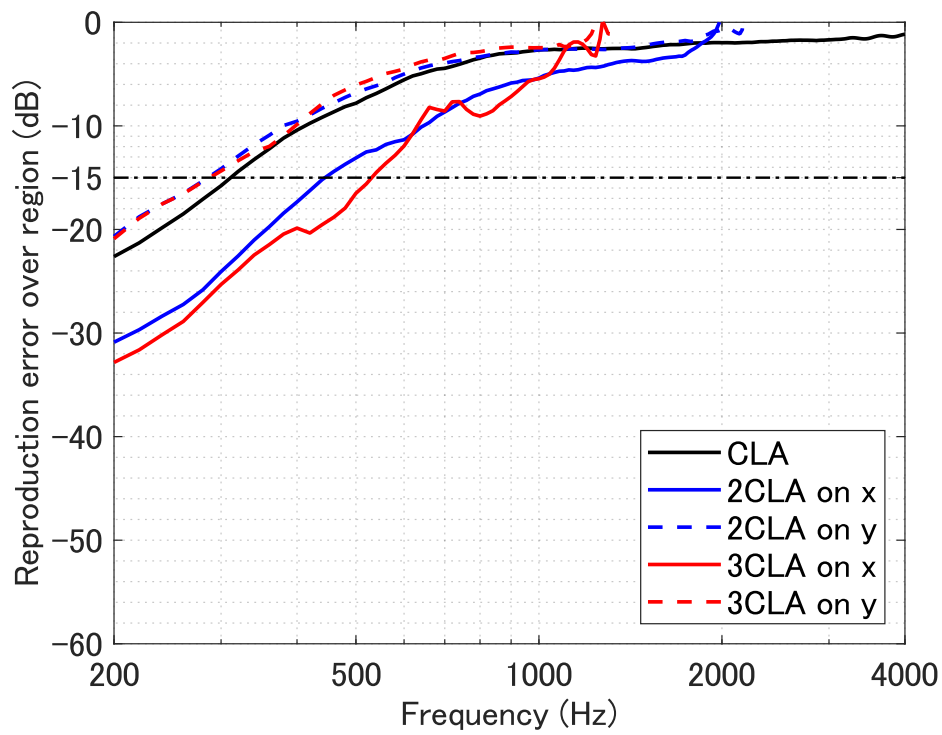


Figure 3.20: Reproducing a focused source using an off-centred 3CLA. (a) Reproduced secondary sound field by 3CLA. (b) Reproduction error.

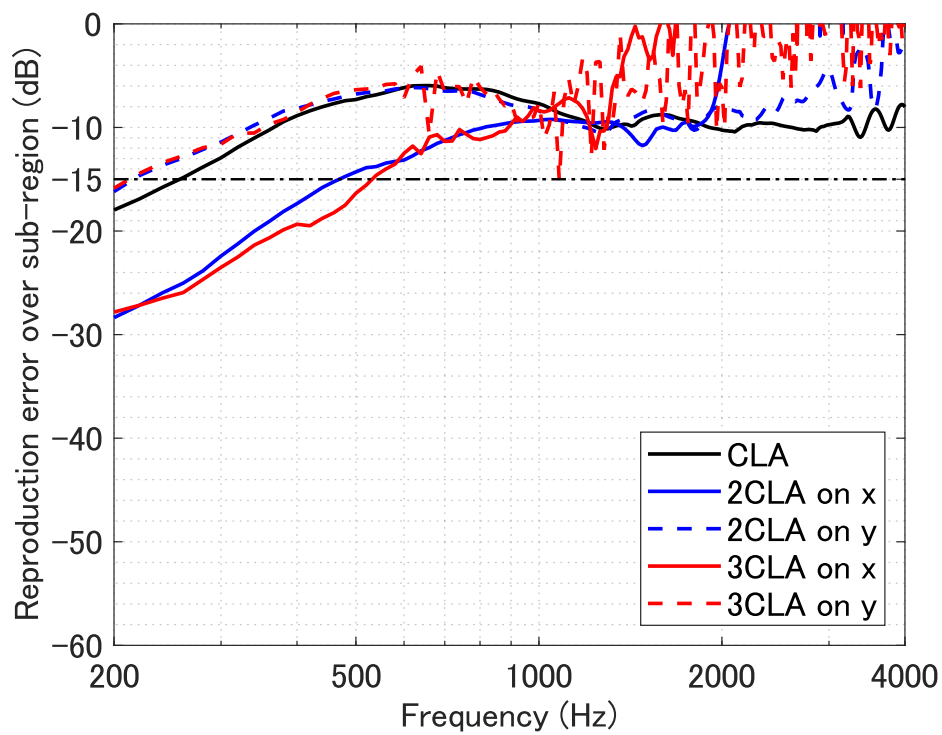
Group B

Since the “on y ” MCLAs in group A had different array-source distances, an additional “on y ” group was compared with a fixed array-source distance. The results of reproducing the same focused source in Fig. 3.10(a) are displayed in Figs. 3.19, 3.20. In the comparisons of Figs. 3.10(b)(c), there is no significant performance difference between the MCLAs and the single CLA for this layout.

As for the comparison in the frequency band of 200-4000 Hz displayed in Fig. 3.21, the performance of CLA was slightly better than those of the MCLAs. The MCLAs also displayed more errors at the higher frequencies. The simulation conditions were identical to those of group A.



(a)



(b)

Figure 3.21: Reproduction error over a region (Group B).

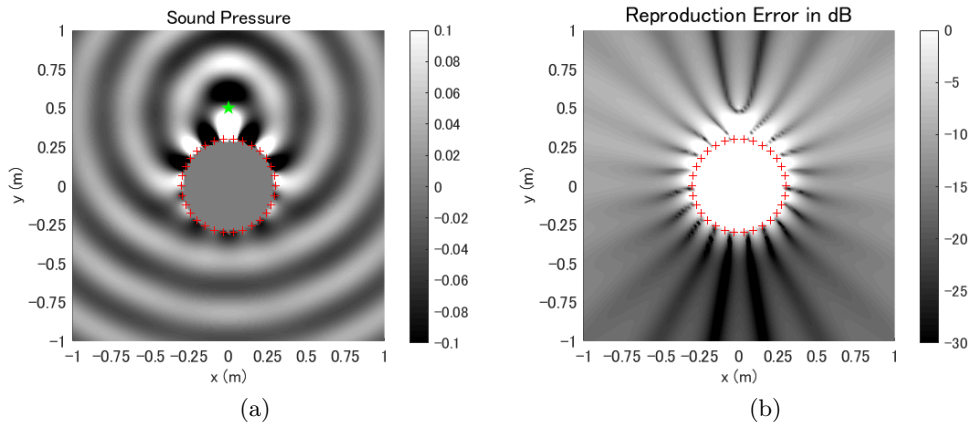


Figure 3.22: Reproducing a focused source using CLA. (a) Reproduced secondary sound field by CLA. (b) Reproduction error.

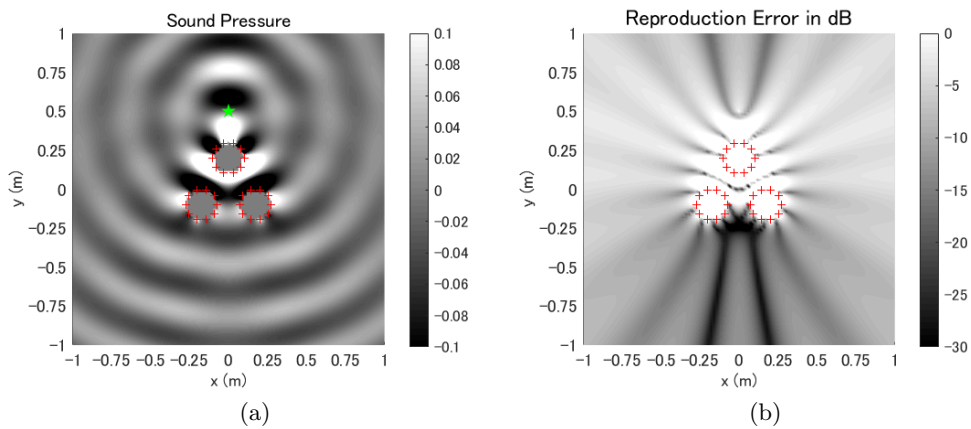


Figure 3.23: Reproducing a focused source using 3CLA. (a) Reproduced secondary sound field by 3CLA. (b) Reproduction error.

Group C

For the last group, the “complete” CLA was compared with distributed MCLAs. The results at 1000 Hz are displayed in Fig. 3.22–3.24. The performance of MCLAs on this condition was even worse than that of the single CLA.

Moreover, in the frequency band of 200-4000 Hz, the CLA outperformed MCLAs, as shown in Fig. 3.25. The simulation conditions were identical to those of group A.

3.6.2 2CLA Properties on Exterior Sound Field Reproduction

As per the results described so far, the performances of 3CLA and 5CLA were unstable at high frequencies. Therefore, 2CLA was adopted as it is easier to build than a larger-number-CLA, and is a more practical model than the other MCLAs. In this part, further discussion on the properties of 2CLA is provided below.

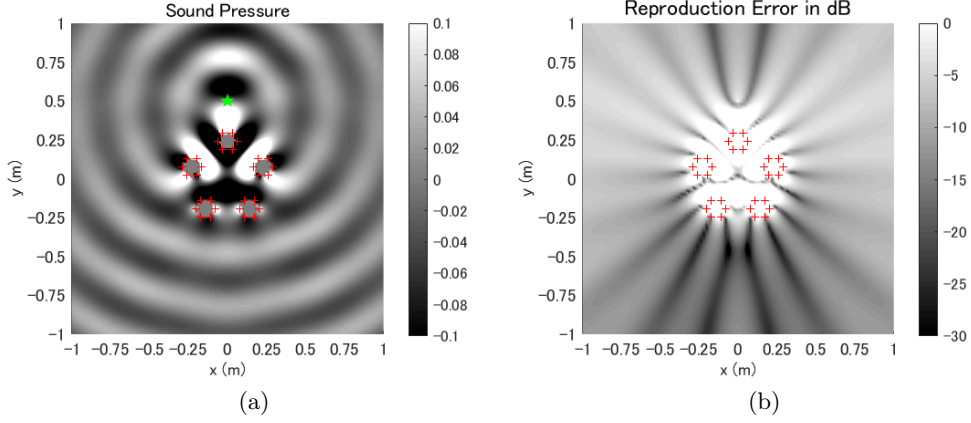
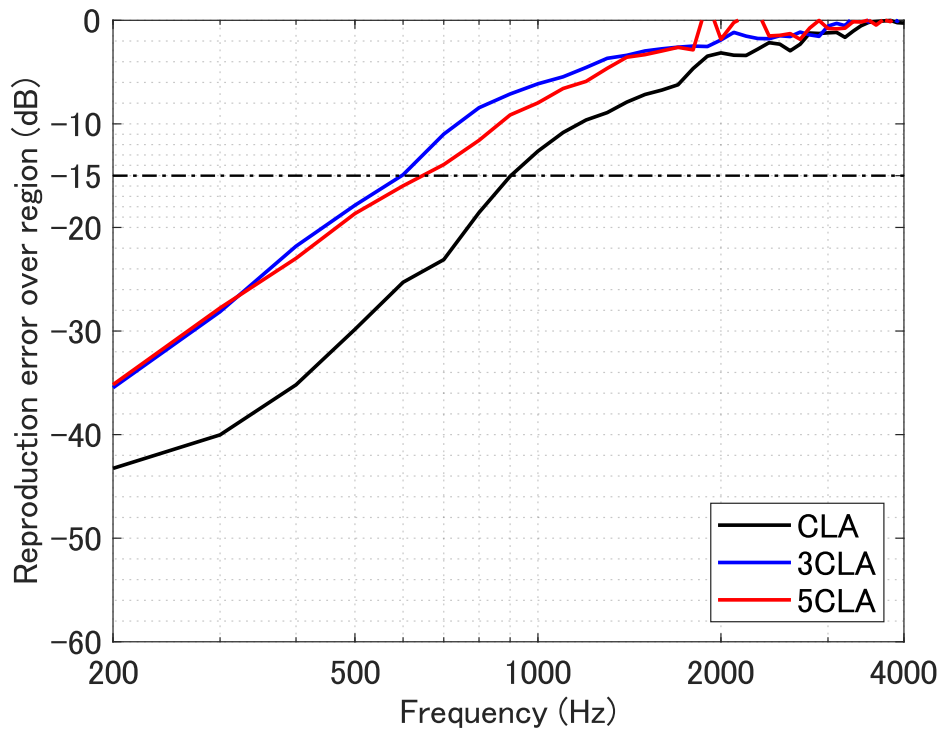


Figure 3.24: Reproducing a focused source using 5CLA. (a) Reproduced secondary sound field by 5CLA. (b) Reproduction error.

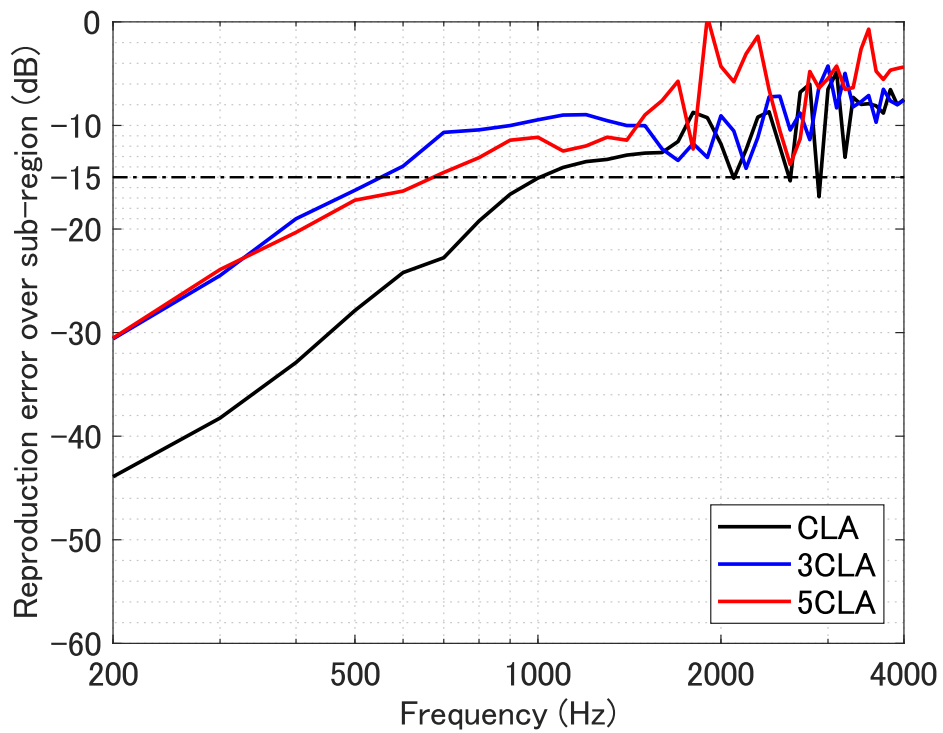
Direction dependence

Considering that 2CLA is an asymmetric model, a simulation was conducted with variable source directions to explore direction dependence. A 2CLA was set as in the previous part, with radii of 0.15 m and centres located at $(-0.25 \text{ m}, 0 \text{ m})$ and $(0.25 \text{ m}, 0 \text{ m})$. The target source had a fixed radius of 0.5 m. Since 2CLA is symmetrical about the x axis and y axis, source directions between 0° and 90° were tested in increments of 2.5° . The sub-region was in the direction of the source: $\Lambda = \{\mathbf{x} \mid \mathbf{O}_\Lambda = (\cos \phi_\odot, \sin \phi_\odot), |\mathbf{x} - \mathbf{O}_\Lambda| \leq 0.2\}$. All other conditions were the same as those of the previous simulations. The reproduction errors in the range of 200-4000 Hz are shown in Fig. 3.26(a). The x and y axes in the figures represent frequency and the source direction, respectively. Colour indicates reproduction error, where the darker colours represent lower errors. The relationship between the maximum controllable frequency and the source direction is shown in (b). The results show a direction dependence such that 2CLA performs better when a lower angle is selected for source direction.

In addition, the direction dependence was tested under conditions similar to that of group B in the previous part; the centres of the 2CLA were located at $(-0.5 \text{ m}, 0 \text{ m})$ and $(0 \text{ m}, 0 \text{ m})$. The array-source distance was fixed for this condition. The results are displayed in Fig. 3.27. Here it is observed that there is no significant direction dependence in the results with the exception of source directions around 90° , which displayed a slightly better performance than those of lower angles.



(a)



(b)

Figure 3.25: Reproduction error over a region (Group C).

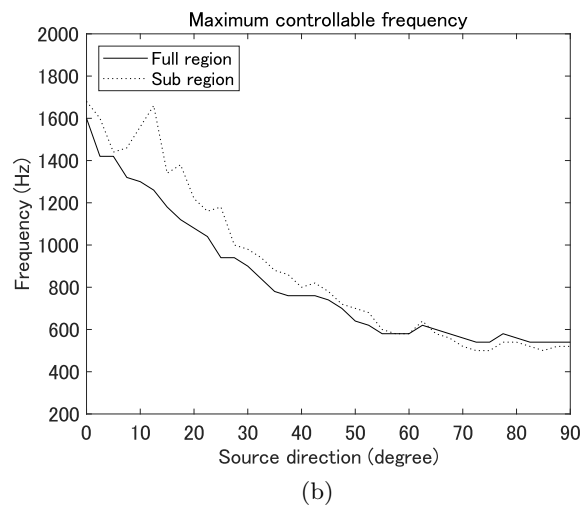
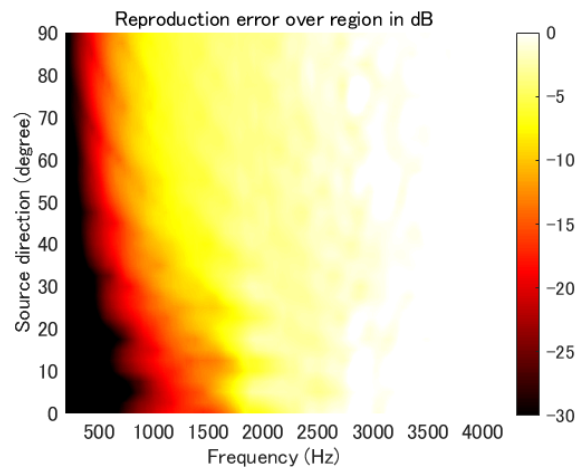
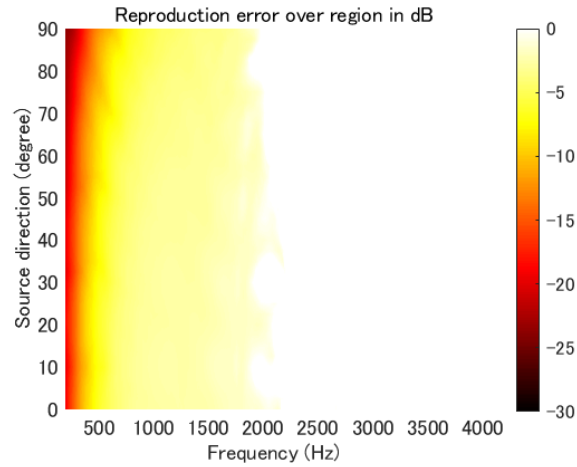
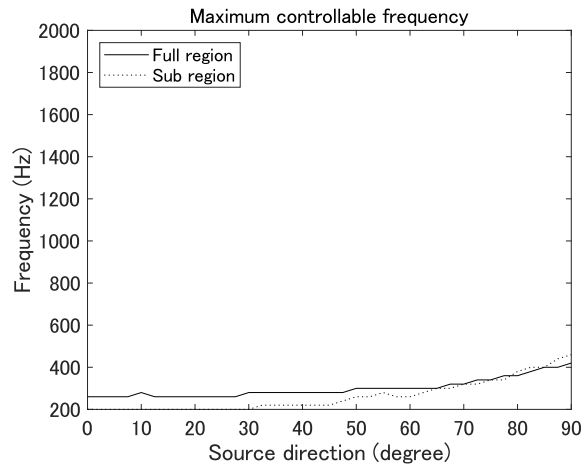


Figure 3.26: Direction dependence of 2CLA on focused source reproduction. (a) Reproduction error over full region; (b) Maximum controllable frequency.



(a)



(b)

Figure 3.27: Direction dependence of an off-centred 2CLA on focused source reproduction. (a) Reproduction error over full region; (b) Maximum controllable frequency.

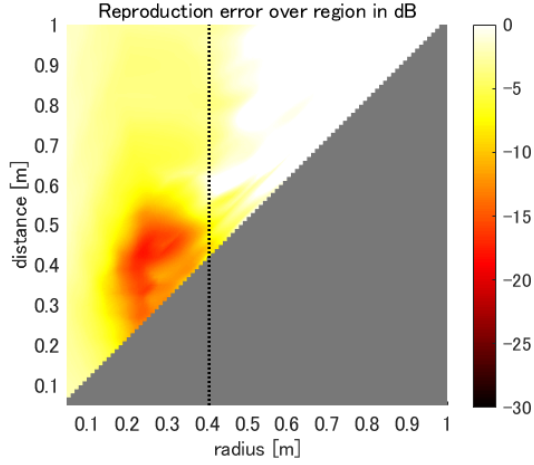


Figure 3.28: The influence of radii and inter-array distance of 2CLA on focused source reproduction. The target source was located at (0 m, 0.5 m). Colour shows the reproduction error over region.

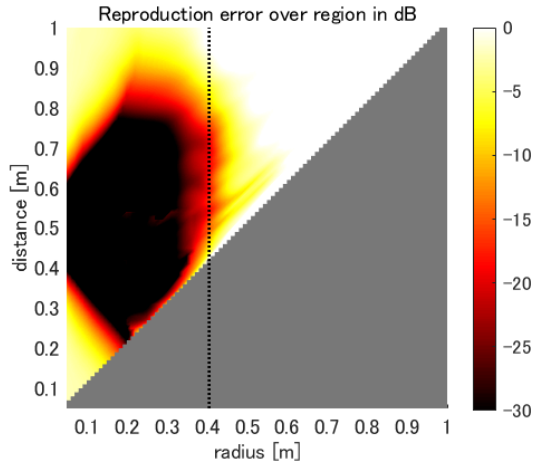


Figure 3.29: The influence of radii and inter-array distance of 2CLA on focused source reproduction. The target source was located at (0.5 m, 0 m). Colour shows the reproduction error over region.

Influence of radii and inter-array distance

Considering the contour of 2CLA, only two characteristics stand out: array radii $r_{0,1}, r_{0,2}$ and inter-array distance $R_{1,2} = R_{2,1}$. The performance of 2CLA is significantly affected by these two characteristics. Therefore, simulations were conducted by changing these two characteristics. The radii and the inter-array distance were varied independently from 0.05-1 m in increments of 0.05 m. The two radii were changed simultaneously (i.e., they were always the same). As the direction and frequency dependence can be inferred from above, the following simulations were conducted with two target sources at 1000 Hz, located at (0 m, 0.5 m) and (0.5 m, 0 m). All other conditions were identical to those of the simulations above.

The results are displayed in Figs. 3.28 and 3.29. The x and y axes in the figures represent the array radii and inter-array distance, respectively. Colour shows the reproduction error. As it is impossible for 2CLA to have $r_{0,s} \geq R_{1,2}$, the only valid results are those in the left-top half of each figure. The dotted line

at $r_{0,s} = \frac{cL_s}{4\pi f} \approx 0.41$ m denotes the radius at which spatial aliasing would occur.

For both target sources, the results show that under the “aliasing radius”, the radius is positively related to performance. Meanwhile, the inter-array distance affects the performance in a more complicated way: neither a too long (i.e., arrays are far away from each other) nor a too short (i.e., arrays are adjacent) distance results in ideal reproduction. A hypothesis to explain the results is: for a short inter-array distance, the results are primarily affected by the array radii, where a small radius is unfavourable for the control; for a long inter-array distance, the 2CLA would be considered as separated arrays that are difficult to be controlled jointly. The right side of the dotted line has high errors, indicating that spatial aliasing significantly affects performance. The results also show that the sources at (0.5 m, 0 m) are better reproduced, which can be attributed to the array-source distance being closer.

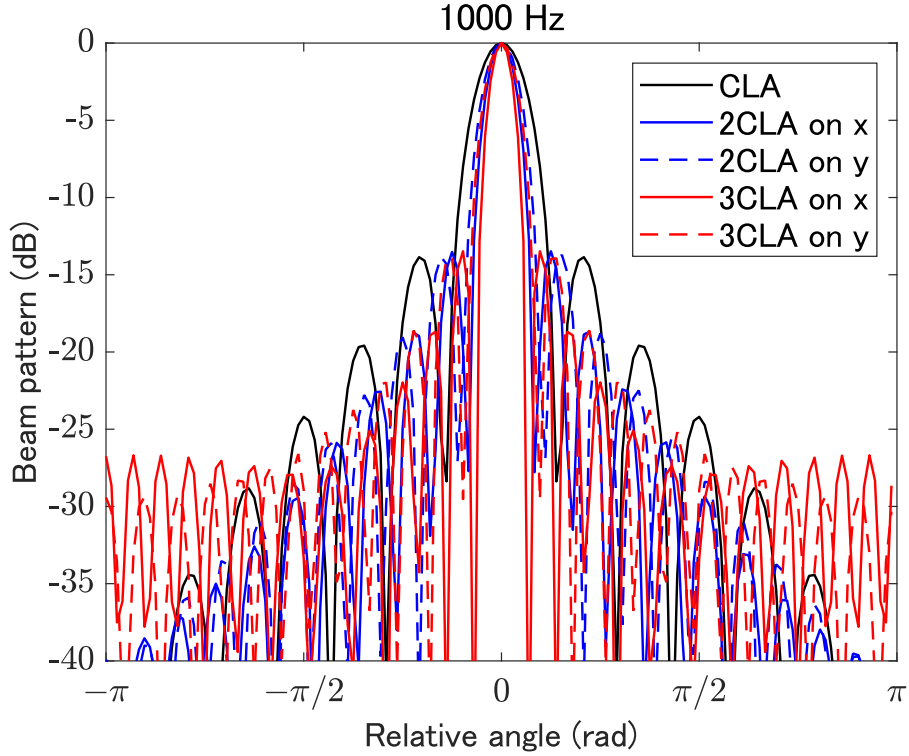


Figure 3.30: Beam patterns of MCLAs in group A. The beam pattern is normalised by the power in the look direction. The angle on the horizontal axis is relative to the look direction.

3.7 Beamforming

Numerical simulations were conducted to assess MCLA for beamforming. MCLA setup was the same as in the previous section, as shown in Fig. 3.9. In the calculation of the transfer functions, reflections up to $R = 12$ were included and the maximum order was truncated at $N = 20$.

In all simulations reported in this section, Tikhonov regularisation, introduced in Sec. 2.6.3, was applied to the MVDR beamformer. The setup consisted of 144 microphones located uniformly on a circle of radius $r = 2$ m centred at $(0 \text{ m}, 0 \text{ m})$. A microphone in the target direction was set as the constrained point, and the other microphones were set as suppression points. The sound pressure \mathbf{f} at the constrained point was set to $1/(4\pi r)$ for all frequencies, thereby maintaining a flat frequency response at the constrained point. The maximum power of the filters was suppressed to under 0 dB by regularisation. For evaluation, 720 observation points were set uniformly on the same circle of the microphones.

3.7.1 Comparison with CLA

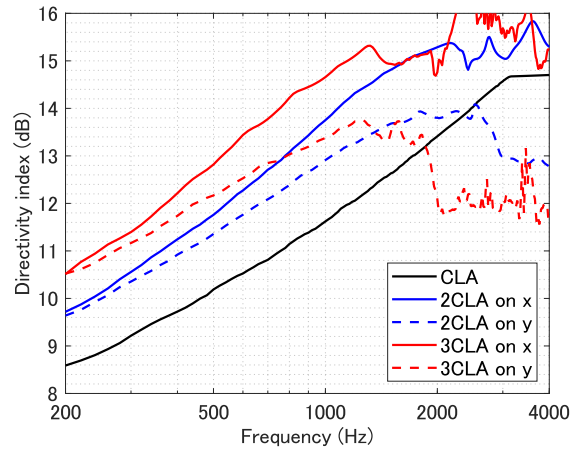
Simulations were conducted to compare groups A and C, introduced in Sec. 3.6.1. Group B is excluded from the discussion because there is no array-source distance in beamforming. In this part, only one look direction at 90° is discussed for simplicity.

Group A

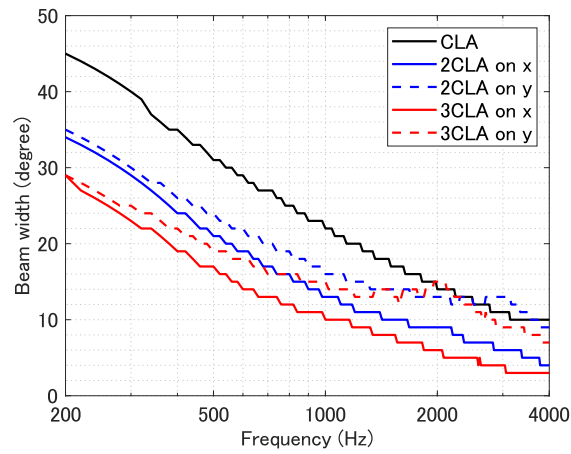
The beam patterns at 1000 Hz are shown in Fig. 3.30. In the results, all MCLAs displayed a sharper main lobe than the single CLA whereas the 3CLAs have larger side lobes in the direction opposite to the look direction.

To further investigate, a simulation was conducted in the frequency band of 200-4000 Hz with the same condition above, the results of which are displayed in Fig. 3.31. The results demonstrate that:

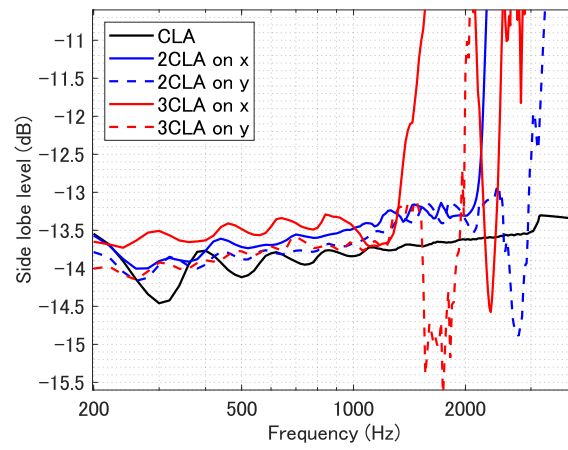
- “on x”, MCLAs outperformed the single CLA in DI and BW.
- “on y”, MCLAs outperformed the single CLA in DI and BW under 2000 Hz but the performance deteriorated at higher frequencies.
- “on x”, MCLAs performed better than “on y” MCLAs.
- 3CLAs outperformed 2CLAs at low frequencies while the performance at high frequencies was problematic.
- SLL of all arrays were similar at low frequencies while with 3CLAs there was an earlier rise compared to 2CLAs for “on x” and “on y”.



(a) DI



(b) BW



(c) SLL

Figure 3.31: DI, BW, and SLL of MCLAs in group A over a frequency band of 200—4000 Hz.

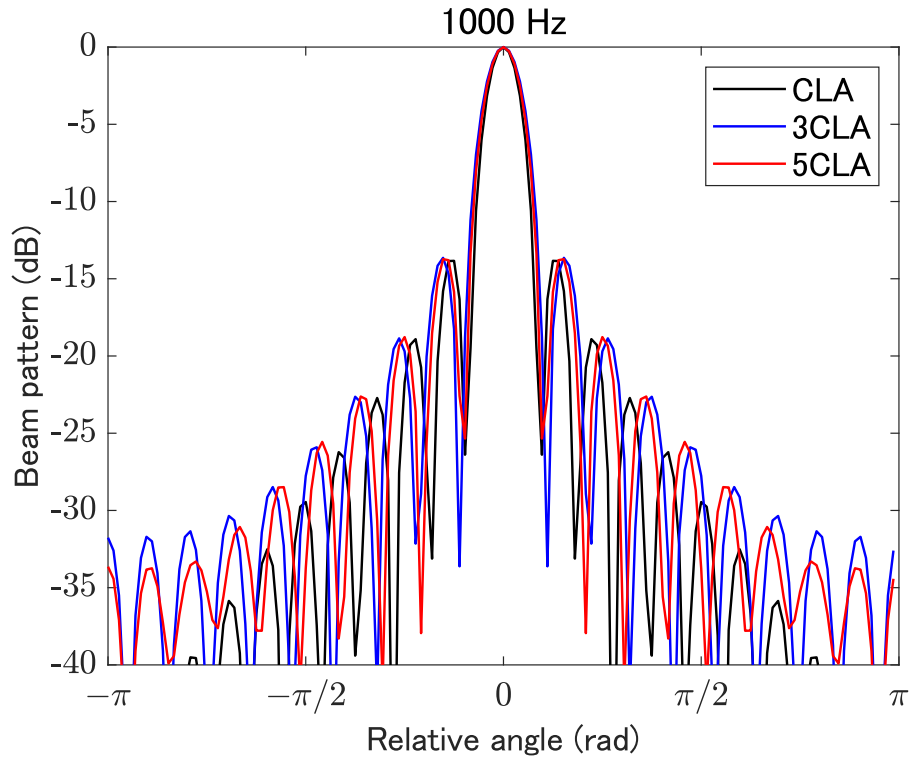
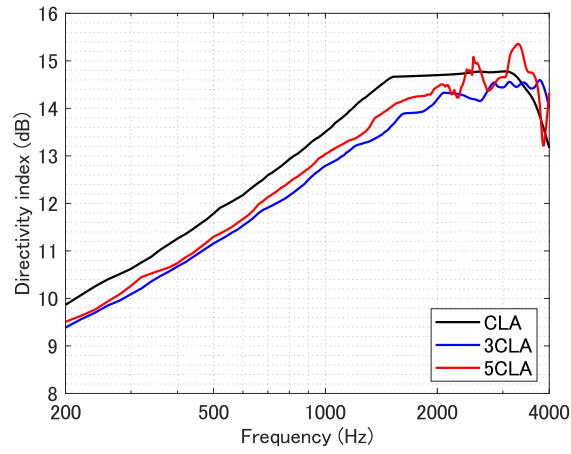


Figure 3.32: Beam patterns of MCLAs in group C. The beam pattern is normalised by the power in the look direction. The angle on the horizontal axis is relative to the look direction.

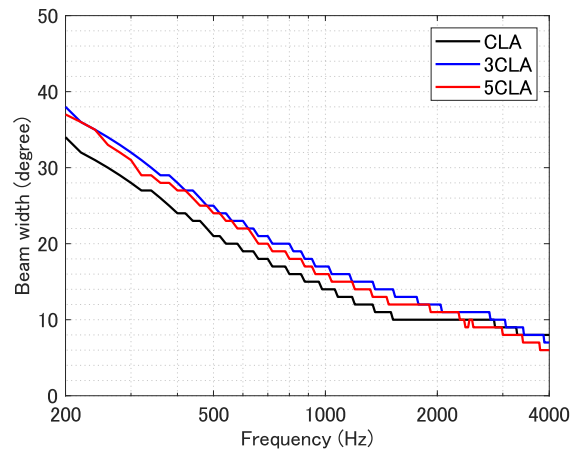
Group C

The beam patterns at 1000 Hz of group C are presented in Fig. 3.32. The results indicate that there is no significant difference between the three arrays.

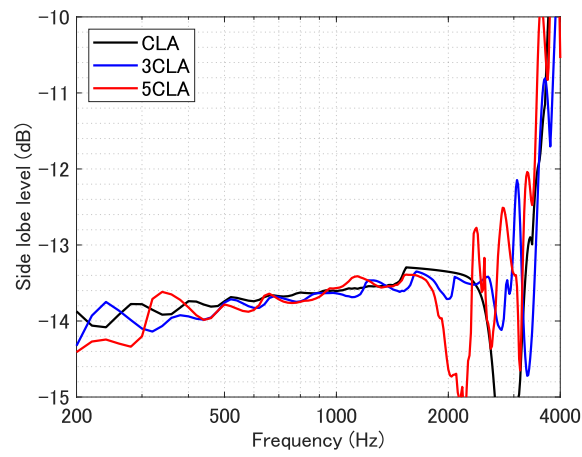
The results for the 200-4000 Hz band are displayed in Fig. 3.33. Similar to the single frequency results, there were no significant differences on beamforming performance between the three arrays in group C whereas single CLA performed slightly better. This is in agreement with the group C comparison in Sec. 3.6.1.



(a) DI



(b) BW



(c) SLL

Figure 3.33: DI, BW, and SLL of MCLAs in group C over a frequency band of 200—4000 Hz.

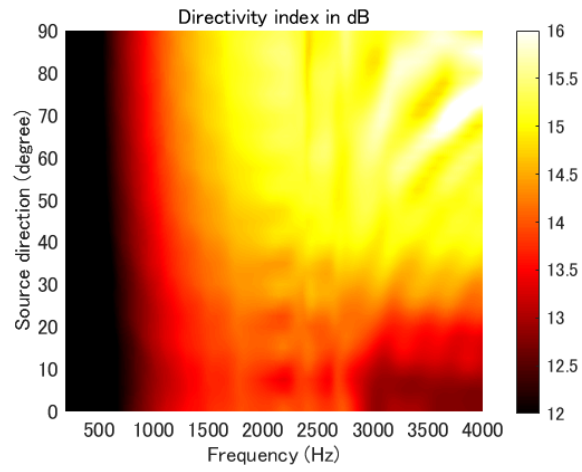
3.7.2 2CLA Properties on Beamforming

According to the results of the previous part, 2CLA has to be considered as a practical model for beamforming. The properties of 2CLA are further discussed.

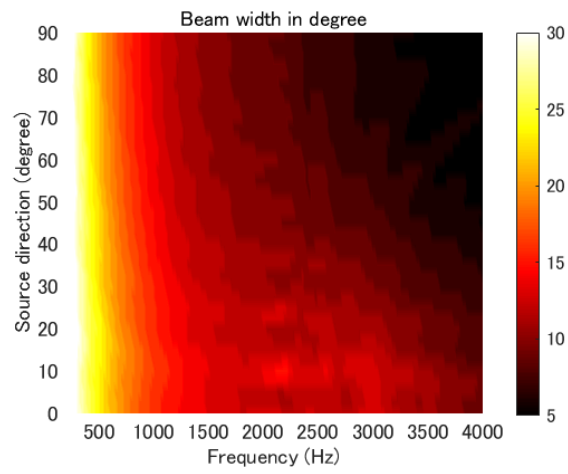
Direction dependence

A simulation was conducted on changing the look direction to explore the asymmetric aspect of 2CLA. Similar to Sec. 3.6.2, angles between 0° and 90° were tested in increments of 2.5° . All other conditions were the same as those of the previous simulation; DI, BW, and SLL were evaluated.

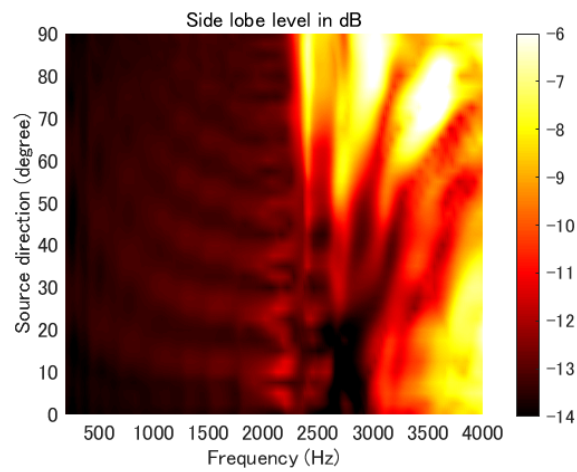
The results are presented in Fig. 3.34. The x and y axes in the figures represent frequency and the look direction, respectively. Colour shows the value of the indices. DI and BW improved with increasing angle at higher frequencies. There was little direction dependence at frequencies below 1000 Hz. At frequencies above 2400 Hz, SLL clearly displayed direction dependence. In contrast, aliasing can arise more easily at larger angles (i.e., “on x ” 2CLA in the previous part) than at smaller angles (i.e., “on y ” 2CLA). Furthermore, for a highly focused beam where the effects of side lobes can be ignored, a small look direction angle can provide high DI and low BW.



(a) DI



(b) BW



(c) SLL

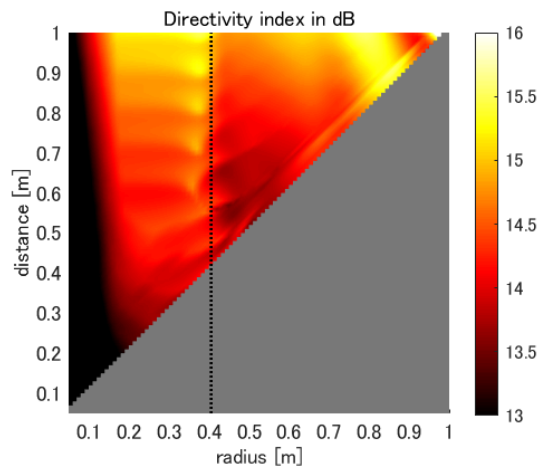
Figure 3.34: DI, BW, and SLL of 2CLA for look directions between 0° and 90° .

Influence of radii and inter-array distance

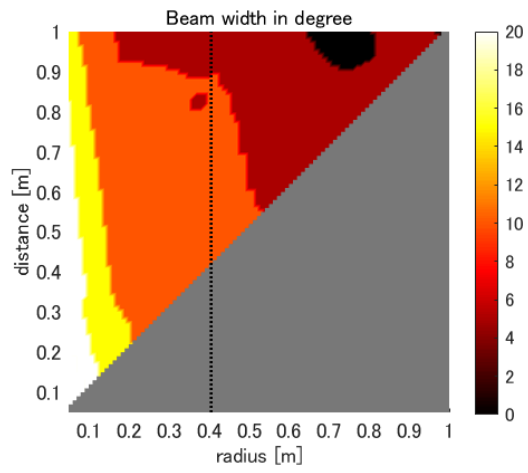
Next, the influence of array radii $r_{0,1}$, $r_{0,2}$ and inter-array distance $R_{1,2} = R_{2,1}$ are discussed. Simulations were conducted with the indicated radii and inter-array distances ranging from 0.05 m to 1 m in increments of 0.05 m. The two radii were changed simultaneously, whereas the radii and inter-array distance were changed independently. The following simulations were conducted with two target sources at 1000 Hz, with look directions at 0° and 90° , excluding direction and frequency dependence as explained above. All the other conditions were the same as those of the simulations above.

The results are displayed in Figs. 3.35 and 3.36. Similar to the results in Sec. 3.6.2, the x and y axes in the figures represent the array radii and inter-array distance, respectively. The only valid results are those in the left-top half of each figure. The dotted line at $r_{0,s} = \frac{cL_s}{4\pi f} \approx 0.41$ m indicates the radius at which spatial aliasing would occur.

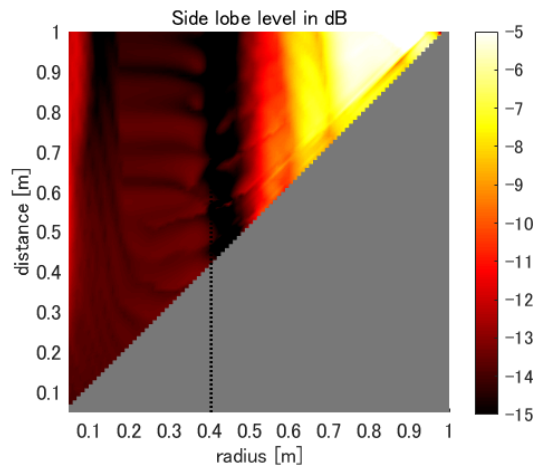
For both look directions, the results show that DI is somehow positively related to the radii and the inter-array distance. However, there are some exceptions. Determining the relationship of DI to radii and the inter-array distance is not that simple. BW was positively related to the two characteristics but was affected primarily by the radii in the 0° look direction and by the inter-array distance in the 90° look direction. For the 0° look direction, SLL was clearly not affected by the radii shorter than the “aliasing radius”. For larger radii, SLL increased rapidly with increasing radii, clearly displaying the negative influence of spatial aliasing. For the 90° look direction, however, SLL was high for large inter-array distances and small radii. The minimum distance between the two circular baffles is relatively large, and this can be another cause of aliasing because of not having uniform sampling.



(a) DI

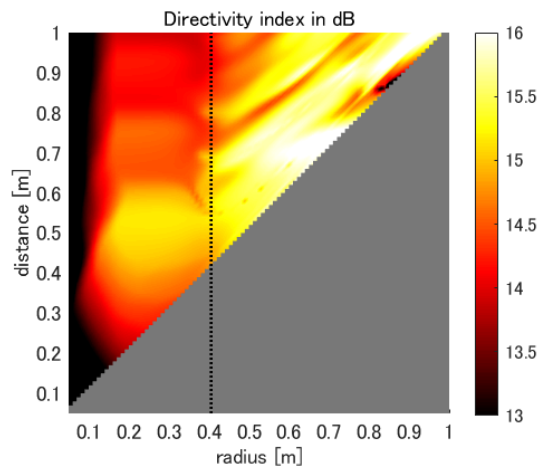


(b) BW

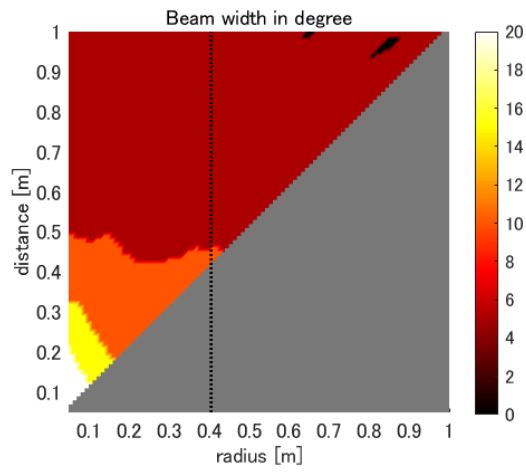


(c) SLL

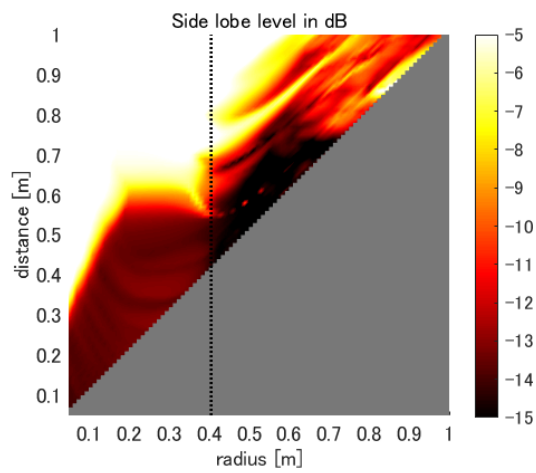
Figure 3.35: Radius and distance dependence of DI, BW, and SLL at 1000 Hz in 0° look direction.



(a) DI



(b) BW



(c) SLL

Figure 3.36: Radius and distance dependence of DI, BW, and SLL at 1000 Hz in the 90° look direction.

3.8 Summary

In this chapter, an MCLA model and its analytical method for spatial control was proposed. The method takes into consideration the multiple scattering effect. It is based on CHE and the addition theorem of cylindrical wave functions. The proposed method allows control of CLAs and their individual harmonic modes. The mode strength of 2CLA is further demonstrated in comparison to conventional CLA. The 2CLA exhibits improved controlling efficiency; it has the potential of reproducing complex sound fields.

Numerical simulations were conducted to discuss interior sound field reproduction, exterior sound field reproduction, and beamforming.

As for interior sound field reproduction, the conventional method has not considered the multiple scattering effect. While real environments have multiple scattering, the mismatch can cause errors in reproduction. The proposed method can avoid this error, thus improving reproduction accuracy.

In exterior sound field reproduction, the performance of MCLAs was compared to that of conventional CLAs. Multiple configurations were discussed in relation to focused source reproduction. The results show that besides the array shape, the array length (length of the direction perpendicular to the source direction) and array-source distance (minimum distance between the source and the loudspeakers) are two key factors affecting reproduction. It is straightforward to demonstrate that reproduction is easier with shorter array-source distances. With a fixed array-source distance, a longer array (perpendicular to the source direction) displays better performance. An increase in multiple scattering (e.g., an increased number of CLAs, a closer inter-array distance together with greater array radii) results in worse performance at high frequencies.

The performance of beamforming was also discussed in comparison with CLAs. In the absence of a “target source”, the array length becomes the most important feature. The results show that longer arrays result in better performances at low frequencies. As for direction dependence, the linear MCLAs performed better with beams perpendicular to their layout. In contrast to exterior sound field reproduction, the multiple scattering effect had little influence on beamforming. The inter-array distance, however, somehow introduced another kind of aliasing issue.

The results show that the multiple scattering effect has no decisive effect on performance. However, the discussions in Sec. 3.2 and Sec. 3.5 explained that it is necessary to take it into consideration. In additional, the comparison between 2CLA and CLA point to the advantages of using an asymmetric array.

Chapter 4

Elliptical loudspeaker array

The results of MCLA demonstrated the advantage of using an asymmetric array. In this chapter, another asymmetric array model is proposed without multiple scatters, namely, the elliptical array. Using elliptical coordinate systems, an analytical sound field reproduction method is proposed for ELA based on Mathieu functions which are the eigenfunctions of the Helmholtz equation. The performance of ELA is also discussed with respect to mode strength, interior sound field reproduction, exterior sound field reproduction, and beamforming.

4.1 Elliptical coordinate system

In this section, the definition of the elliptical coordinate system is introduced and the solutions of the Helmholtz equation with Mathieu functions are explained. An elliptical coordinate system is shown in Fig. 4.1. In this coordinate system, a coordinate is defined as $\boldsymbol{x} = (\xi, \eta)$, where η is the angular coordinate and ξ is the radial coordinate. These coordinates can be transferred to the Cartesian coordinate system using

$$\begin{cases} x = a \cosh \xi \cos \eta \\ y = a \sinh \xi \sin \eta \end{cases}, \quad (4.1)$$

where a represents the distance from the origin to one of the foci located at $F(\pm a, 0)$ in the Cartesian coordinate system. Clearly, an ellipse can be easily expressed as $\xi = \xi_0$ by setting a constant ξ_0 in the elliptical coordinate system.

4.2 Wave representation in elliptical coordinates

Consider a homogeneous Helmholtz equation in the elliptical coordinate system. The Laplace operator in this coordinate system is [89]

$$\nabla^2 = \frac{1}{a^2(\cosh 2\xi - \cos 2\eta)} \left(\frac{\partial^2}{\partial \xi^2} + \frac{\partial^2}{\partial \eta^2} \right). \quad (4.2)$$

The Laplace operator is substituted into the Helmholtz equation and the variables are separated $p(\xi, \eta, \omega) = H(\eta) \cdot \Xi(\xi)$, to obtain

$$\frac{\partial^2 H(\eta)}{\partial \eta^2} + [a - 2q \cos(2\eta)]H(\eta) = 0 \quad (4.3)$$

$$\frac{\partial^2 \Xi(\xi)}{\partial \xi^2} + [a - 2q \cosh(2\xi)]\Xi(\xi) = 0, \quad (4.4)$$

where $q := k^2 a^2 / 4$.

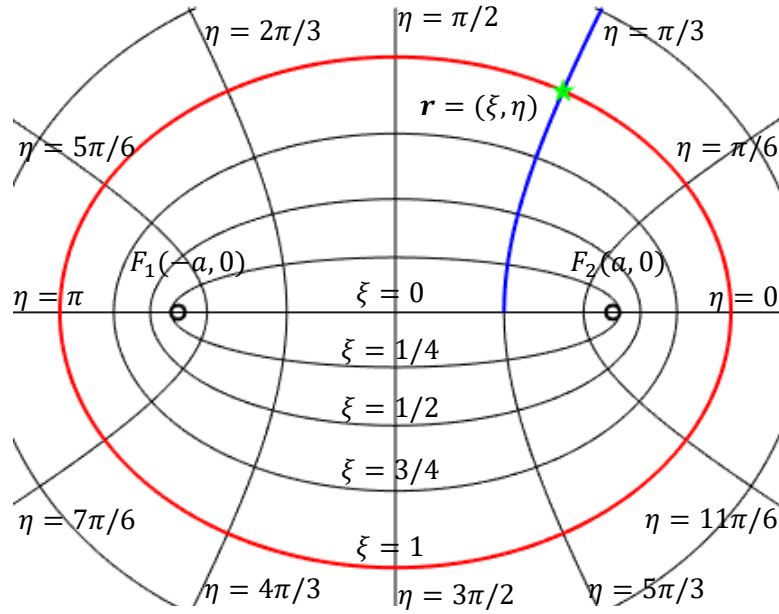


Figure 4.1: Elliptical coordinate system. F_1 , F_2 are the foci of the coordinate system; the red and blue lines represent the curves of $\xi = 1$ and $\eta = \pi/3$, respectively; the green star is their intersection at $\mathbf{x} = (1, \pi/3)$.

4.2.1 Mathieu functions

The Mathieu angular function and Mathieu radial function are the eigenfunctions of (4.3) and (4.4), respectively [90–92]. In this study, the Mathieu angular function and Mathieu radial function of the ζ -th kind are denoted by $me_\nu(q, \eta)$ and $M_\nu^{(\zeta)}(q, \xi)$, respectively. Here, ν is the order of the function. The Mathieu angular function $me_\nu(q, \eta)$ is a solution of Mathieu's differential equation,

$$y''(\eta) + (\lambda - 2q \cos 2\eta)y(\eta) = 0, \quad (4.5)$$

and can be expanded into the following series [92, p. 111],

$$me_\nu(q, \eta) = \sum_{\mu=-\infty}^{\infty} \varsigma_{2\mu}^\nu e^{j(\nu+2\mu)\eta}. \quad (4.6)$$

Here, the coefficient $\varsigma_{2\mu}^\nu$ (q is omitted here) can be obtained with a recurrence relation:

$$-q\varsigma_{2\mu+2}^\nu + [\lambda - (\nu + 2\mu)^2]\varsigma_{2\mu}^\nu - q\varsigma_{2\mu-2}^\nu = 0. \quad (4.7)$$

The Mathieu radial function of the ζ -th kind $M_\nu^{(\zeta)}(q, \xi)$ is a solution of Mathieu's modified differential equation,

$$-Y''(\xi) + (\lambda - 2q \cosh 2\xi)Y(\xi) = 0. \quad (4.8)$$

The Mathieu radial function is calculated by the following equations [92, p.201]:

$$M_\nu^{(\zeta)}(q, \xi) = \begin{cases} Mc_\nu^{(\zeta)}(q, \xi) & \nu \geq 0 \\ (-1)^\nu Ms_{-\nu}^{(\zeta)}(q, \xi) & \nu < 0 \end{cases}, \quad (4.9)$$

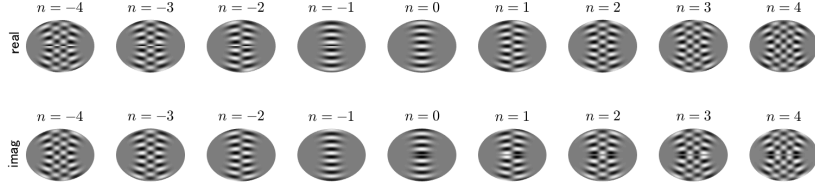


Figure 4.2: Harmonic modes of Mathieu functions with different orders, calculated by $M_\nu^{(4)}(q, \xi)me_\nu(q, \eta)$. The elliptical coordinate system is defined as $a = 1$. All waves are at 1000 Hz.

$$Mc_\nu^{(\zeta)}(q, \xi) = \begin{cases} \frac{1}{\zeta_0^\nu} \sum_{\mu=0}^{\infty} j^{\nu+\mu} \zeta_{2\mu}^\nu J_\mu(\sqrt{q}e^{-\xi}) \mathcal{B}_\mu^{(\zeta)}(\sqrt{q}e^\xi) & \text{even } \nu \\ \frac{1}{\zeta_1^\nu} \sum_{\mu=0}^{\infty} j^{\nu-1+\mu} \zeta_{2\mu+1}^\nu \left[J_{\mu-1}(\sqrt{q}e^{-\xi}) \mathcal{B}_{\mu+1}^{(\zeta)}(\sqrt{q}e^\xi) \right. \\ \left. + J_{\mu+1}(\sqrt{q}e^{-\xi}) \mathcal{B}_{\mu-1}^{(\zeta)}(\sqrt{q}e^\xi) \right] & \text{odd } \nu \end{cases}, \quad (4.10)$$

$$Ms_\nu^{(\zeta)}(q, \xi) = \begin{cases} \frac{1}{\zeta_2^\nu} \sum_{\mu=0}^{\infty} j^{\nu-2+\mu} \zeta_{2\mu+2}^\nu \left[J_\mu(\sqrt{q}e^{-\xi}) \mathcal{B}_{\mu+2}^{(\zeta)}(\sqrt{q}e^\xi) \right. \\ \left. - J_{\mu+2}(\sqrt{q}e^{-\xi}) \mathcal{B}_\mu^{(\zeta)}(\sqrt{q}e^\xi) \right] & \text{even } \nu \\ \frac{1}{\zeta_1^\nu} \sum_{\mu=0}^{\infty} j^{\nu-1+\mu} \zeta_{2\mu+1}^\nu \left[J_{\mu-1}(\sqrt{q}e^{-\xi}) \mathcal{B}_{\mu+1}^{(\zeta)}(\sqrt{q}e^\xi) \right. \\ \left. - J_{\mu+1}(\sqrt{q}e^{-\xi}) \mathcal{B}_{\mu-1}^{(\zeta)}(\sqrt{q}e^\xi) \right] & \text{odd } \nu \end{cases}. \quad (4.11)$$

Here $\mathcal{B}_\nu^{(\zeta)}(\cdot)$ represents the cylindrical functions, in general and specifically the Bessel function, the Neumann function, the Hankel function of the first kind, and the Hankel function of the second kind with $\zeta = 1, 2, 3, 4$, respectively.

In this study, only the Mathieu functions with integer orders are used. Series calculations on Mathieu functions are approximated by a truncation at sufficiently large μ . Further information on definitions and properties of Mathieu functions can be found in [92].

4.2.2 Mathieu function expansion

In this section, a sound field reproduction method is proposed based on Mathieu function expansion (MFE). The method transforms the sound field into the elliptic harmonic domain, and then matches the coefficient of the secondary sound field to that of the primary sound field. Here, an elliptic loudspeaker array is used as the secondary sound source with a driving function that can also be expanded by the Mathieu angular function.

Using the Mathieu angular function and Mathieu radial function, it is possible to expand a sound field at a single frequency [91]:

$$p(\xi, \eta, \omega) = \sum_{\nu=-\infty}^{\infty} \left[\dot{p}_\nu^\triangleleft(q) M_\nu^{(1)}(q, \xi) me_\nu(q, \eta) + \dot{p}_\nu^\triangleright(q) M_\nu^{(4)}(q, \xi) me_\nu(q, \eta) \right], \quad (4.12)$$

where $p(\xi, \eta, \omega)$ is the sound pressure, $\dot{p}_\nu^\triangleleft(q)$ and $\dot{p}_\nu^\triangleright(q)$ are the coefficients of the incident sound field and radiated sound field, respectively. In this study, the

time dependent term is set to $e^{j\omega t}$; therefore, the fourth kind of Mathieu radial function is used for the radiated sound field.

Note that $me_\nu(q, \eta)$ has properties similar to the exponential function $e^{j\mu\phi}$; $M_\nu^{(1)}(q, \xi)$ and $M_\nu^{(4)}(q, \xi)$ have properties similar to the Bessel function and Hankel function of the second kind, respectively [92]. Hence, the expansion has a form similar to CHE [46]:

$$p(r, \phi, \omega) = \sum_{\mu=-\infty}^{\infty} \left[\check{p}_\mu^\triangleleft(k) J_\mu(kr) e^{j\mu\phi} + \check{p}_\mu^\triangleright(k) H_\mu^{(2)}(kr) e^{j\mu\phi} \right]. \quad (4.13)$$

Additionally, different orders of Mathieu functions are orthogonal to each other [92], expressed as

$$\int_0^{2\pi} me_\nu(q, \eta) me_{\nu'}(q, -\eta) d\eta = 2\pi \delta_{\nu\nu'}. \quad (4.14)$$

Thus, MFE refers to (4.12) and the following refers to elliptical harmonic expansion:

$$p(\xi, \eta, \omega) = \sum_{\nu=-\infty}^{\infty} \check{p}_\nu(\xi, q) me_\nu(q, \eta), \quad (4.15)$$

The harmonic modes of MFE are shown in Fig. 4.2. These harmonic modes clearly indicate that an MFE-based method is an asymmetric or direction dependent method. Also, the modes with lower orders have the ability to synthesise sound fields only on the minor axis of the ellipse.

4.2.3 Rigid elliptical scatter

The transfer function of an open array in elliptical coordinates $G(\xi, \eta | \xi', \eta', \omega)$ would be the same as in (2.6). However, for a rigid array with an acoustically rigid surface, the transfer function should be calculated with the Neumann boundary conditions. Consider a loudspeaker located at (ξ', η') outside a rigid elliptic baffle $\xi = \xi_0$, for any $\xi < \xi'$ outside the baffle, the sound pressure at (ξ, η) can be divided into direct sound and scattered sound as displayed in Fig. 4.3. The direct sound $p^\triangleleft(\xi, \eta, \omega)$ is a sound propagating inward and the scattered sound $p^\triangleright(\xi, \eta, \omega)$ is a sound propagating outward:

$$p^\triangleleft(\xi, \eta, \omega) = \sum_{\nu=-\infty}^{\infty} \check{p}_\nu^\triangleleft(q) M_\nu^{(1)}(q, \xi) me_\nu(q, \eta), \quad (4.16)$$

$$p^\triangleright(\xi, \eta, \omega) = \sum_{\nu=-\infty}^{\infty} \check{p}_\nu^\triangleright(q) M_\nu^{(4)}(q, \xi) me_\nu(q, \eta), \quad (4.17)$$

where direct sound can be obtained from the transfer function in (2.6):

$$\check{p}_\nu^\triangleleft(q) = -\frac{j}{4} M_\nu^{(4)}(q, \xi') me_\nu(q, -\eta'). \quad (4.18)$$

The Neumann boundary conditions states that the particle velocities on the surface are 0, which implies that the sum of the derivative of the direct sound pressure and the scattered sound pressure is 0. Applying the Neumann boundary condition to a rigid surface,

$$\sum_{\nu=-\infty}^{\infty} \left\{ \check{p}_\nu^\triangleleft(q) M_\nu^{(1)'}(q, \xi_0) + \check{p}_\nu^\triangleright(q) M_\nu^{(4)'}(q, \xi_0) \right\} me_\nu(q, \eta) = 0, \quad (4.19)$$

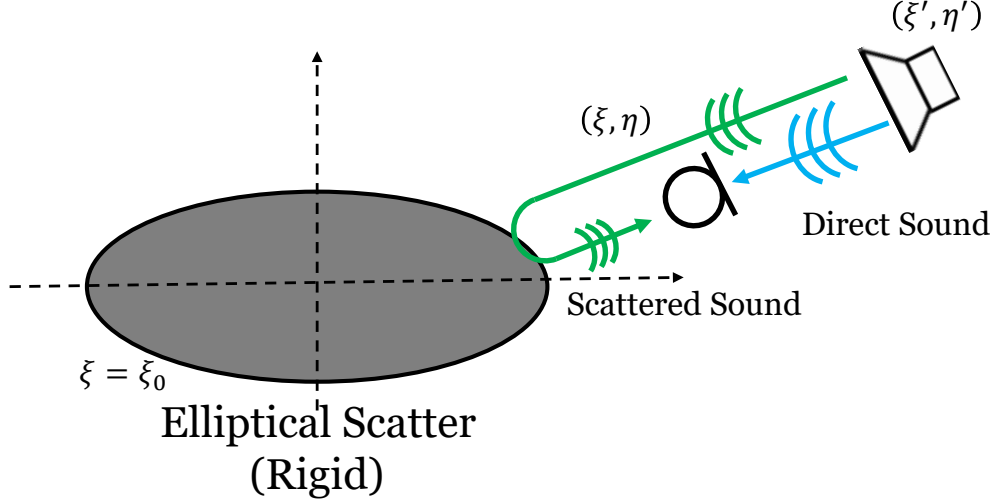


Figure 4.3: A sound field with a rigid elliptical scatter. The sound pressure at the microphone can be described as a sum of direct sound and scattered sound.

Then, the transfer function can be derived as

$$\begin{aligned}
 G^{(\text{ELA})}(\xi, \eta | \xi', \eta', \omega) &= p^{\triangleleft}(\xi, \eta, \omega) + p^{\triangleright}(\xi, \eta, \omega) \\
 &= \sum_{\nu=-\infty}^{\infty} \hat{p}_{\nu}^{\triangleleft}(q) \left[M_{\nu}^{(1)}(q, \xi) - \frac{M_{\nu}^{(1)'}(q, \xi_0)}{M_{\nu}^{(4)'}(q, \xi_0)} M_{\nu}^{(4)}(q, \xi) \right] m e_{\nu}(q, \eta).
 \end{aligned} \tag{4.20}$$

Furthermore, for a rigid elliptic microphone array where microphones are mounted on the rigid surface $\xi = \xi_0$, the Wronskian of the Mathieu function [92] can be used.

$$M_{\nu}^{(1)}(q, \xi) M_{\nu}^{(4)'}(q, \xi) - M_{\nu}^{(1)'}(q, \xi) M_{\nu}^{(4)}(q, \xi) = -\frac{2j}{\pi}. \tag{4.21}$$

Finally, reversing the position of the microphone and the loudspeaker gives the transfer function of a rigid elliptic loudspeaker array:

$$G^{(\text{ELA})}(\xi, \eta | \xi_0, \eta_l, \omega) = -\frac{1}{2\pi} \sum_{\nu=-\infty}^{\infty} \frac{M_{\nu}^{(4)}(q, \xi)}{M_{\nu}^{(4)'}(q, \xi_0)} m e_{\nu}(q, -\eta_l) m e_{\nu}(q, \eta), \tag{4.22}$$

where (ξ_0, η_l) denotes the position of the l -th loudspeaker on the array.

4.3 Mathieu function based sound field reproduction method

Considering an area with a continuous elliptic boundary, a primary sound field can be expressed by the following equation if the source exists either only inside (exterior sound field) or only outside (interior sound field) the area:

$$p(\xi, \eta, \omega) = \begin{cases} \sum_{\nu=-\infty}^{\infty} \hat{p}_{\nu}^{\triangleleft}(q) M_{\nu}^{(1)}(q, \xi) m e_{\nu}(q, \eta) & \text{interior} \\ \sum_{\nu=-\infty}^{\infty} \hat{p}_{\nu}^{\triangleright}(q) M_{\nu}^{(4)}(q, \xi) m e_{\nu}(q, \eta) & \text{exterior} \end{cases}. \tag{4.23}$$

Here, the MFE coefficient of the primary sound field \hat{p}_{ν} can be obtained either analytically by the transfer function in (2.6) or by the expansion of plane wave

in [91, p.1422]. In addition, a method transforming the conventional circular-harmonic-expansion coefficient to the MFE coefficient is introduced in Sec. 4.4.

Now consider the secondary sound field by a continuous elliptic source. The sound field can be expressed as

$$\hat{p}(\xi, \eta, \omega) = \int_0^{2\pi} G(\xi, \eta | \xi_0, \eta, \omega) d_l(\omega) \xi_0 d\eta, \quad (4.24)$$

where (ξ_0, η) is the location of the l -th loudspeaker and $d_l(\omega)$ is the driving signal of the l -th loudspeaker. In [92] and [91], the transfer function in the elliptical coordinate system is described as

$$\begin{aligned} G(\xi, \eta | \xi', \eta', \omega) &= -\frac{j}{4} H_0^{(2)}(k|\mathbf{x} - \mathbf{x}'|) \\ &= -\frac{j}{4} \sum_{\nu=-\infty}^{\infty} M_\nu^{(1)}(q, \xi_{<}) M_\nu^{(4)}(q, \xi_{>}) m_{e\nu}(q, -\eta') m_{e\nu}(q, \eta), \end{aligned} \quad (4.25)$$

where $|\mathbf{x} - \mathbf{x}'|$ denotes the distance between (ξ, η) and (ξ', η') ; $\xi_{<}$ and $\xi_{>}$ denote the smaller and bigger one in ξ and ξ' , respectively. This equation describes the sound pressure at (ξ, η) in a 2-dimensional free field, where a monopole source is placed at (ξ', η') . Additionally, the following conditions should always be satisfied such that $\xi' > \xi$ for interior sound field reproduction and $\xi' < \xi$ for exterior sound field reproduction. Applying MFE to the driving functions,

$$d_l(\omega) = \sum_{\nu=-\infty}^{\infty} \check{d}_\nu(q) m_{e\nu}(q, \eta), \quad (4.26)$$

where $d_\nu(q)$ is the coefficient of the elliptic harmonic expansion.

Thereafter, the secondary sound field is expressed by substituting (4.25) and (4.26) into (4.24):

$$\hat{p}(\xi, \eta, \omega) = \begin{cases} \sum_{\nu=-\infty}^{\infty} \check{\gamma}_\nu^{\Delta}(q) \check{d}_\nu(q) M_\nu^{(1)}(q, \xi) m_{e\nu}(q, \eta) & \text{interior} \\ \sum_{\nu=-\infty}^{\infty} \check{\gamma}_\nu^{\nabla}(q) \check{d}_\nu(q) M_\nu^{(4)}(q, \xi) m_{e\nu}(q, \eta) & \text{exterior} \end{cases}, \quad (4.27)$$

where

$$\begin{cases} \check{\gamma}_\nu^{\Delta}(q) = -\frac{j}{2} \xi_0 M_\nu^{(4)}(q, \xi_0) & \text{interior} \\ \check{\gamma}_\nu^{\nabla}(q) = -\frac{j}{2} \xi_0 M_\nu^{(1)}(q, \xi_0) & \text{exterior} \end{cases}. \quad (4.28)$$

Here, the orthogonality of the Mathieu angular function is applied in the derivation of (4.27). Additionally, the exterior sound field of a rigid elliptic loudspeaker array is given by,

$$\check{\gamma}_\nu^{\nabla}(q) = -\frac{\xi_0}{M_\nu^{(4)'}(q, \xi_0)} \quad \text{for rigid ELA.} \quad (4.29)$$

Furthermore, as a result of the orthogonality of the Mathieu functions, the secondary sound field in (4.27) can be matched to the primary sound field in (4.23) by matching the coefficients in each mode (or order) ν :

$$\check{d}_\nu(q) = \frac{\dot{p}_\nu(q)}{\check{\gamma}_\nu(q)}. \quad (4.30)$$

The driving function in the frequency domain can be obtained as in (4.26). In addition, Tikhonov regularisation can be applied to the method to suppress the level of driving signals.

Regarding discretely placed loudspeakers, the secondary sound field can be expressed as

$$\hat{p}(\xi, \eta, \omega) = \sum_{l=1}^L G(\xi, \eta | \xi_0, \eta_l, \omega) d_l(\omega), \quad (4.31)$$

where L is the number of loudspeakers. The orthogonality of the Mathieu angular function for discrete cases is expressed as

$$\sum_{l=1}^L m e_\nu(q, \eta_l) m e_{\nu'}(q, -\eta_l) = L \delta_{\nu\nu'}. \quad (4.32)$$

NOTE: This has not been proven. (This is used in the thesis because numerical experiments exhibit little error with this equation.) The coefficient $\check{\gamma}_\nu^{(\text{disc})}(q)$ for the discrete condition in (4.27) then becomes

$$\check{\gamma}_\nu^{(\text{disc})}(q) = \frac{L}{2\pi} \check{\gamma}_\nu^{(\text{cont})}(q). \quad (4.33)$$

The coefficient for the continuous condition $\check{\gamma}_\nu^{(\text{cont})}(q)$ was given in (4.28) and (4.29). Finally, the infinite series of order ν is truncated with a maximum order N . In CHE, order truncation always results in a circular low-error area such that $r \leq N/k$ is extrapolated with increasing order [27]. In MFE, due to the difference between the bases, the truncation order results in an elliptic low-error area. The truncation error and a proper truncation order are introduced in Sec. 5.2. Note that another restriction $N < \lfloor (L-1)/2 \rfloor$ should be satisfied to avoid the spatial aliasing problem [93].

4.4 Circle-ellipse transformation

The proposed method in Sec. 4.3 reproduces the sound field analytically by matching the coefficients in MFE. This requires sound field signals recorded by an uncommon elliptic microphone array. In conventional studies of sound field reproduction, a 2D sound field is commonly recorded by a circular microphone array, and then, most often, transformed to the circular harmonic domain. Here, a method is proposed to transform circular harmonic coefficients to MFE coefficients. The flow chart of the proposed method is displayed in Fig. 4.4.

In a 2-dimensional polar coordinate system, denoting the coordinates as $\mathbf{x} = (r, \phi)$, a sound field $p(r, \phi, \omega)$ can be expressed by [46]

$$p(r, \phi, \omega) = \sum_{\mu=-\infty}^{\infty} [\check{p}_\mu^{\leftarrow}(k) J_\mu(kr) e^{j\mu\phi} + \check{p}_\mu^{\rightarrow}(k) H_\mu^{(2)}(kr) e^{j\mu\phi}]. \quad (4.34)$$

Here, $\check{p}_\mu^{\leftarrow}(k)$ and $\check{p}_\mu^{\rightarrow}(k)$ are the μ -th order coefficients of CHE.

Conventional methods for CLAs, such as 2D-HOA [26], synthesise sound fields by matching the coefficients by orders. Those methods often use a circular microphone array to record the sound field and assume that the source exists either inside or outside the array. The sound field observed by the circular microphone array can be expanded as

$$p(r, \phi, \omega) = \begin{cases} \sum_{\mu=-\infty}^{\infty} \check{p}_\mu^{\leftarrow}(k) J_\mu(kr) e^{j\mu\phi} & \text{interior} \\ \sum_{\mu=-\infty}^{\infty} \check{p}_\mu^{\rightarrow}(k) H_\mu^{(2)}(kr) e^{j\mu\phi} & \text{exterior} \end{cases}. \quad (4.35)$$

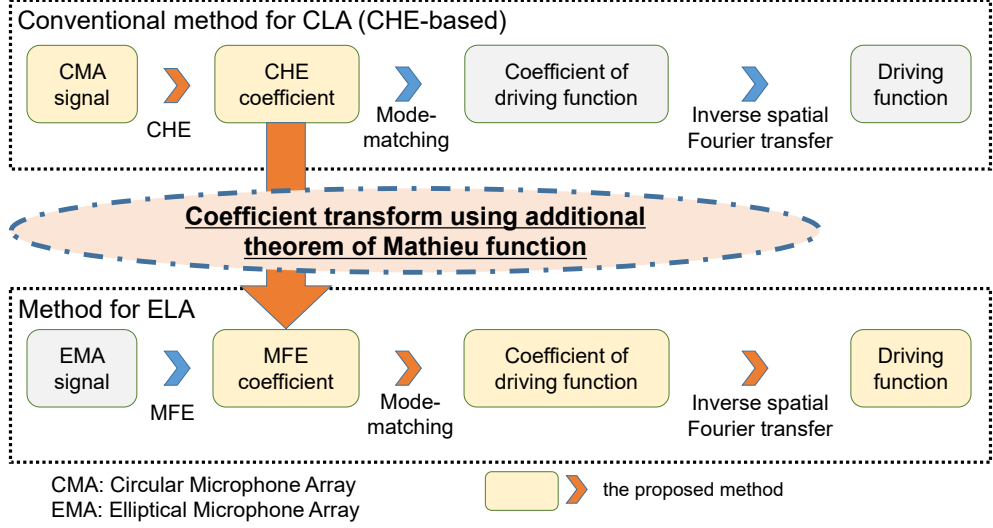


Figure 4.4: A flow chart of the proposed circle-ellipse transformation, with comparison to the conventional CHE-based method and the proposed MFE-based method.

Furthermore, to avoid the forbidden frequency issue of Bessel functions [46], a rigid circular microphone array can be used to record the interior sound field [94].

Letting elliptical coordinates (ξ, η) share the same location in polar coordinates (r, ϕ) , for any $r > a$ (a is the focal distance of the elliptic coordinate system), the following addition theorem of Mathieu function [92, 95] can be used.

$$\mathcal{B}_\mu^{(\zeta)}(kr)e^{j\mu\phi} = \sum_{\nu=-\infty}^{\infty} \tau_{\nu,\mu}^*(q) M_{\mu+\nu}^{(\zeta)}(q, \xi) m e_{\mu+\nu}(q, \eta), \quad (4.36)$$

$$\tau_{\nu,\mu}^*(q) = \begin{cases} j^{-\nu} \zeta_{-\nu}^{\mu+\nu} & , \text{ for even } \nu \\ 0 & , \text{ for odd } \nu \end{cases}. \quad (4.37)$$

Here, $\mathcal{B}_\nu^{(\zeta)}(z)$ represents the cylindrical functions with $\zeta \in \{1, 2, 3, 4\}$. $\zeta_{-\nu}^{\mu+\nu}$ is the coefficient used in calculating the Mathieu functions.

Substituting (4.36) into (4.35) to obtain

$$\begin{aligned} p(r, \phi, \omega) &= \begin{cases} \sum_{\mu=-\infty}^{\infty} \check{p}_\mu^\triangleleft(k) J_\mu(kr) e^{j\mu\phi} & \text{interior} \\ \sum_{\mu=-\infty}^{\infty} \check{p}_\mu^\triangleright(k) H_\mu^{(2)}(kr) e^{j\mu\phi} & \text{exterior} \end{cases} \\ &= \begin{cases} \sum_{\mu=-\infty}^{\infty} \check{p}_\mu^\triangleleft(k) \sum_{\nu=-\infty}^{\infty} \tau_{\nu,\mu}^*(q) M_{\mu+\nu}^{(1)}(q, \xi) m e_{\mu+\nu}(q, \eta) & \text{interior} \\ \sum_{\mu=-\infty}^{\infty} \check{p}_\mu^\triangleright(k) \sum_{\nu=-\infty}^{\infty} \tau_{\nu,\mu}^*(q) M_{\mu+\nu}^{(4)}(q, \xi) m e_{\mu+\nu}(q, \eta) & \text{exterior} \end{cases} \\ &= \begin{cases} \sum_{\nu'=-\infty}^{\infty} \check{p}_{\nu'}^\triangleleft(q) M_{\nu'}^{(1)}(q, \xi) m e_{\nu'}(q, \eta) & \text{interior} \\ \sum_{\nu'=-\infty}^{\infty} \check{p}_{\nu'}^\triangleright(q) M_{\nu'}^{(4)}(q, \xi) m e_{\nu'}(q, \eta) & \text{exterior} \end{cases}. \end{aligned} \quad (4.38)$$

Therefore, the sound field coefficient in MFE is transformed to

$$\begin{cases} \check{p}_{\nu'}^\triangleleft(q) = \sum_{\mu=-\infty}^{\infty} \check{p}_\mu^\triangleleft(k) \tau_{\nu-\mu,\mu}^* & \text{interior} \\ \check{p}_{\nu'}^\triangleright(q) = \sum_{\mu=-\infty}^{\infty} \check{p}_\mu^\triangleright(k) \tau_{\nu-\mu,\mu}^* & \text{exterior} \end{cases}. \quad (4.39)$$

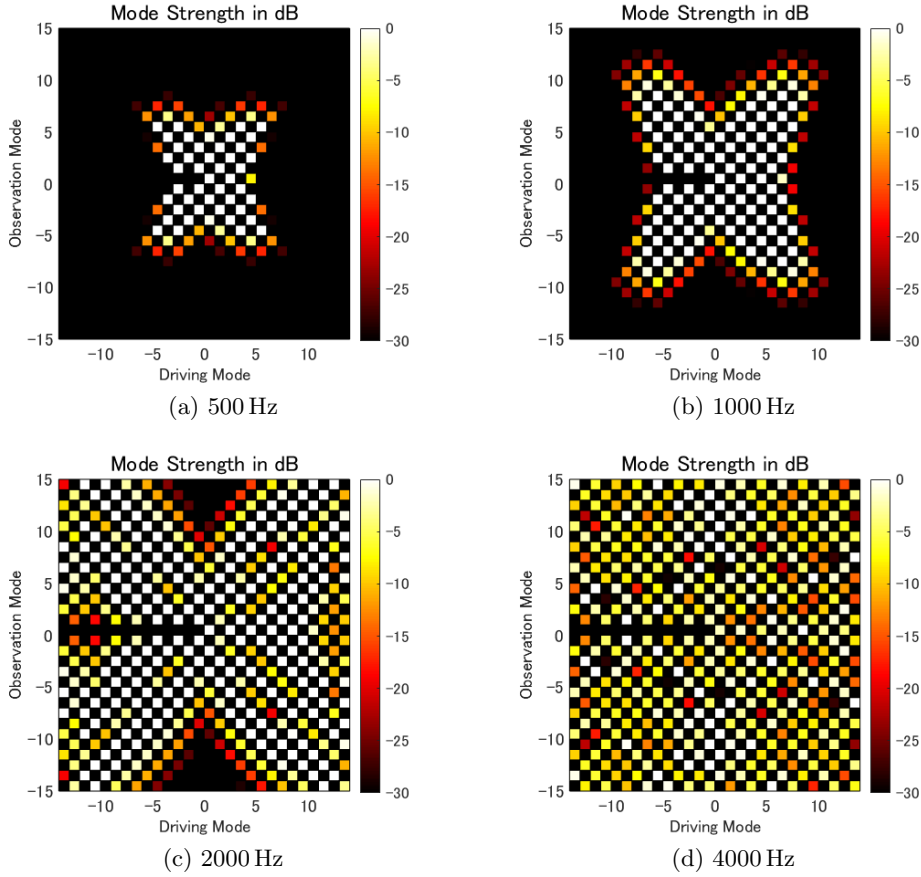


Figure 4.5: Mode strength of a rigid ELA. The ELA has a major-axis of 0.8 m and a minor-axis of 0.3 m

Note that the calculations should be carried out with a sufficiently large truncation order M . Finally, substituting the coefficient $\hat{p}_{\nu'}(q)$ into (4.30), the driving function of the elliptic loudspeaker array is obtained.

$$d_l(\omega) = \sum_{\nu=-N}^N \frac{\sum_{\mu=-M}^M \check{p}_{\mu}(k) \tau_{\nu-\mu, \mu}^* m e_{\nu}(q, \eta)}{\check{\gamma}_{\nu}(q)}, \quad (4.40)$$

N is the truncation order for MFE.

4.5 Mode strength

Here, the mode strength of ELA is discussed. The mode strength discussed in this study is the strength of an ELA mode (MFE mode) with respect to regular sound field modes (CHE mode). Since there is a mismatch in the observation positions, analytically deriving the mode strength of an ELA is rather difficult. Here, each single mode of the ELA is numerically derived for a circular microphone array. Finally, the mode strength is obtained by applying CHE to the microphone array signals.

The mode strength of an ELA is shown in Fig. 4.5. The x -axis represents the driving modes of ELA (in MFE) and the y -axis represents the observation modes for the secondary sound field. The observation mode is the mode observed on the circle centred at the origin O and therefore in CHE. A single driving mode of ELA generates multiple modes in the field, similar to 2CLA in Sec. 3.4. On

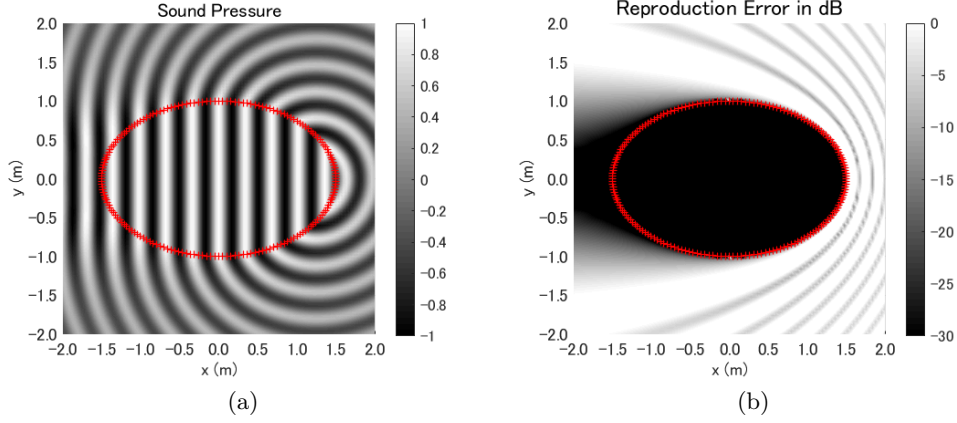


Figure 4.6: A plane wave with direction of arrival $\eta_{//} = 0$ reproduced by an ELA of 180 loudspeakers.

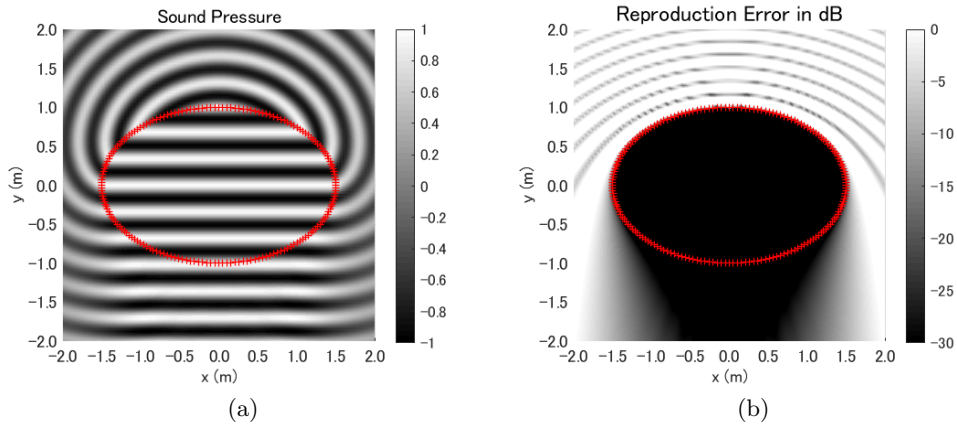


Figure 4.7: A plane wave with direction of arrival $\eta_{//} = \pi/2$ reproduced by an ELA of 180 loudspeakers.

the other hand, the mode strength of 2CLA has the shape of a rhombus while that for ELA has an “X” shape. Furthermore, with ELA, the driving modes and observation modes are strictly correlated by parity.

4.6 Interior sound field reproduction

In this section, numerical simulations are carried out on interior sound field reproduction. The circle-ellipse transformation is also included in the simulations. The difference in the reproducible area of the proposed method and that of the conventional method are discussed for CLA.

4.6.1 MFE-based method

Interior sound field reproduction was performed using the proposed method in Sec. 4.3 without regularisation, with an ELA. The array had 180 loudspeakers located equiangularly in the elliptical coordinate system, which means that $\Delta\eta = \frac{\pi}{90}$ on an ellipse with a major axis of 3 m and a minor axis of 2 m. The elliptical coordinate system was defined with $a = \sqrt{5}/2$, where the ellipse can be described as $\xi_0 \approx 0.80$. The primary sound field was at 1000 Hz ($k \approx 18.48$ and $q \approx 106.72$). Note that the proposed method is direction dependent. Therefore, the

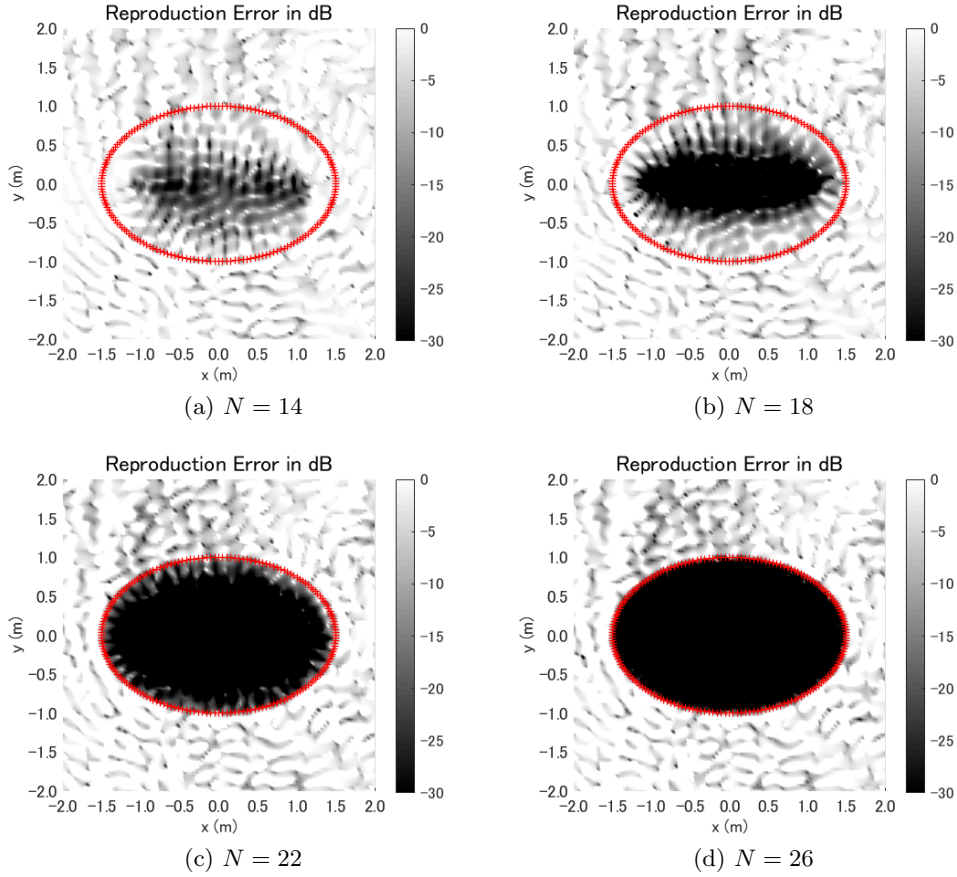


Figure 4.8: Reproduction error in reproducing random plane waves with different truncation orders.

source was tested on both along the major-axis and minor-axis direction of the ellipse. The maximum order N was truncated at 30, which is sufficiently large ($N > \lceil 2\sqrt{q} \cosh \xi_0 \rceil = 28$). For an interior sound field, the coefficients of the primary field were calculated by [91]

$$\hat{p}_\nu^s(q) = \begin{cases} j^\nu m e_\nu(q, -\eta_{//}) & \text{plane wave} \\ -\frac{j}{4} M_\nu^{(4)}(q, \xi_\odot) m e_\nu(q, -\eta_\odot) & \text{cylindrical wave} \end{cases}, \quad (4.41)$$

where $\eta_{//}$ denotes the direction of arrival of a plane wave in elliptical coordinates; (ξ_\odot, η_\odot) denotes the coordinates of a point source.

Figures 4.6 and 4.7 show the results in a $4 \text{ m} \times 4 \text{ m}$ sound field. The target sound fields were a plane wave arriving from the directions of $\phi_{//} = 0$ and $\pi/2$ ($\eta_{//} = \phi_{//}$ for the specific angles), respectively. Red crosses represent loudspeaker locations in all figures. The results display an ideal reproduction, validating that the proposed method can reliably reproduce sound fields with an ELA.

Furthermore, to investigate the influence of truncation order, simulations were conducted by changing the truncation order to 14, 18, 22, 26 under the same conditions. The primary field was set to the sum of 30 random (i.e., random amplitude, random direction, and random phase) plane waves. Figure 4.8 displays the reproduction error. The results show that the reduction of truncation order results in an increase in error. Moreover, the truncation order dictates the shape of the elliptical low-error area. The truncation effect is further discussed in Sec. 5.2.

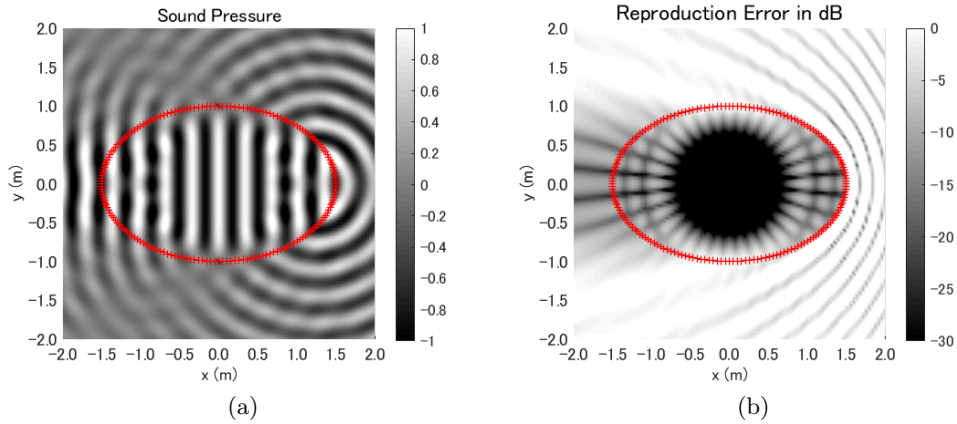


Figure 4.9: A plane wave with direction of arrival $\eta_{\parallel} = 0$ reproduced by an ELA of 180 loudspeakers and a circular microphone array of 24 microphones.

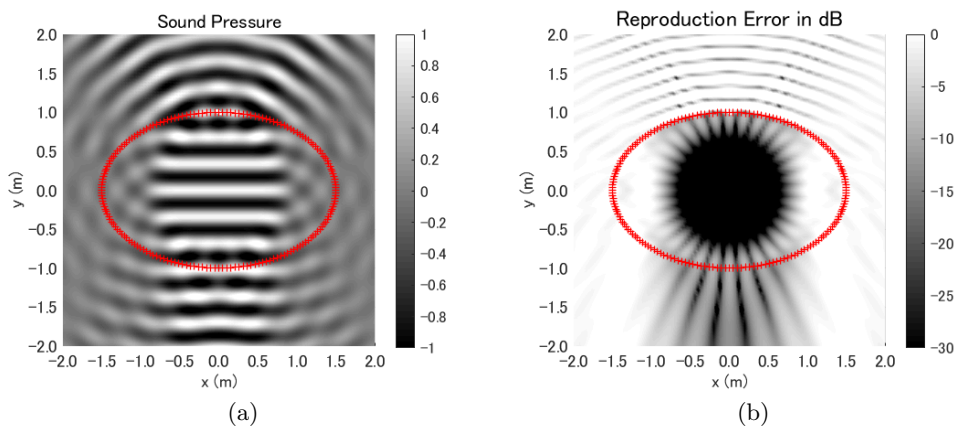


Figure 4.10: A plane wave with direction of arrival $\eta_{\parallel} = \pi/2$ reproduced by an ELA of 180 loudspeakers and a circular microphone array of 24 microphones.

4.6.2 Circle-ellipse transformation

For the circle-ellipse transformation, simulations were only conducted on interior sound field reproduction because interior sound fields are more commonly recorded using circular microphone arrays. The conditions of the previous simulation were used except that the primary sound field was recorded by a circular microphone array. A rigid circular microphone array of radius 0.3 m with 24 microphones was used to record the sound field. The maximum order of CHE was truncated at $\lfloor (M - 1)/2 \rfloor = 11$, which corresponds to the maximum number of orthogonal bases that can be represented with M microphones. The truncation order of MFE was larger than that of CHE because of the requirements of the addition theorem [92, 95].

Simulations were conducted with plane waves arriving from the major-axis direction ($\eta_{\parallel} = 0$) and the minor-axis direction ($\eta_{\parallel} = \pi/2$), at 1000 Hz. Figures 4.9 and 4.10 display the results of a $4 \text{ m} \times 4 \text{ m}$ sound field. The results show a circular low-error area which is different than that of the previous method. The performance of this method has been limited by the truncation order of CHE.

The performances of different truncation orders were compared. To exclude direction dependence, the primary field was set to the sum of 30 random (i.e., random amplitude, random direction, and random phase) plane waves. Figure 4.11

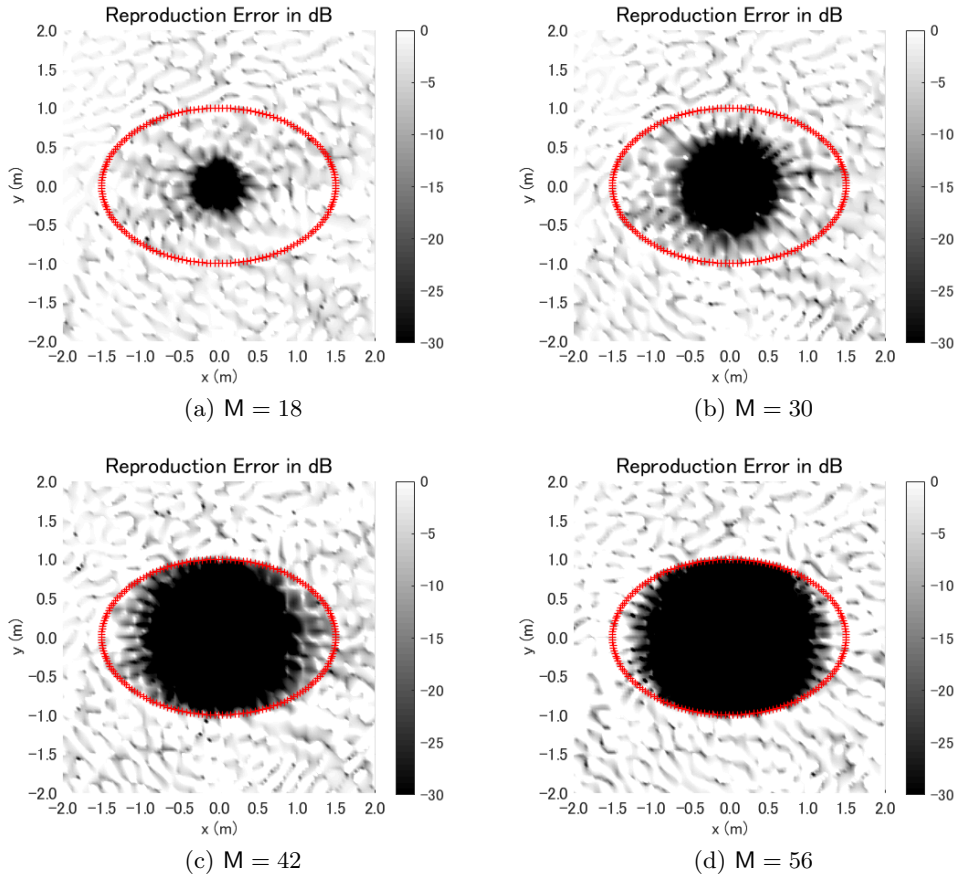


Figure 4.11: Reproduction error in reproducing random plane waves with different number of microphones.

displays reproduction error with number of microphones set to $M = 18, 30, 42,$ and 56 , meaning that the truncation orders were $8, 14, 20,$ and 27 , respectively. The results show that the listening area is limited to a smaller circle area at smaller truncation orders, which corresponds to the results of conventional 2D-HOA studies [26]. This phenomenon is influenced by the truncation order of CHE. Furthermore, the truncation order of MFE may not affect the simulation results because it is restricted to be larger than the truncation order of CHE.

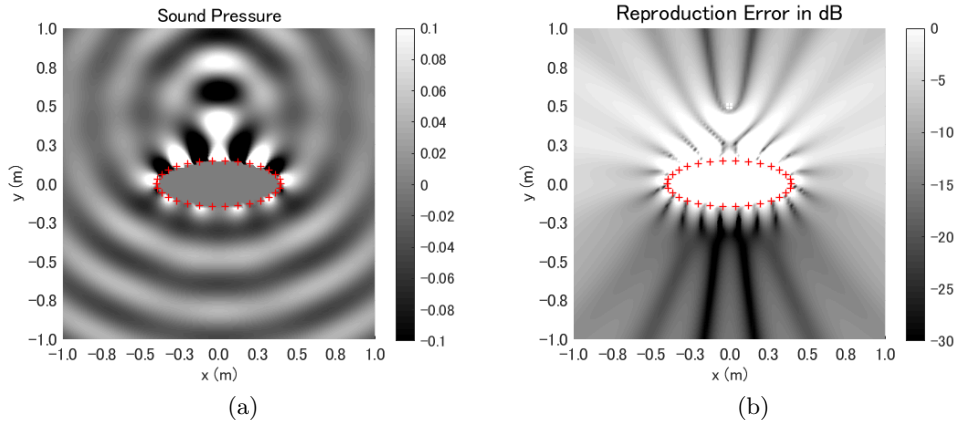


Figure 4.12: Focused source reproduced by an “on x” rigid ELA of 30 loudspeakers.

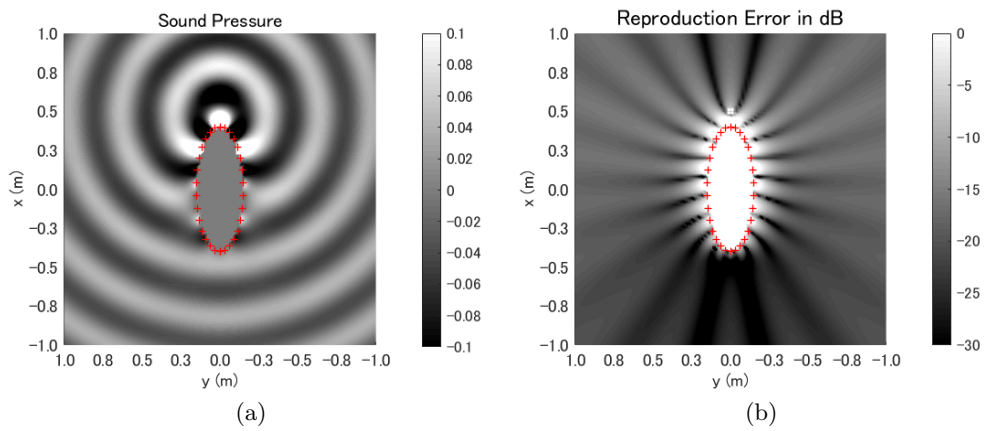


Figure 4.13: Focused source reproduced by an “on y” rigid ELA of 30 loudspeakers.

4.7 Exterior sound field reproduction

In this section, the numerical simulations conducted on exterior sound field reproduction, which is performed by reproducing focused sources, are discussed. The results are compared with those of CLA, 2CLA, and LLA. The influence of changing the shape of the ellipse is also discussed.

4.7.1 Comparison with CLA, 2CLA, and LLA

Comparison with CLA and 2CLA

To test the performance of exterior sound field reproduction, simulations were conducted on focused source reproduction. The target focused source was set at (0.5 m, 0 m), which is the same as in Sec. 3.6.1. Moreover, to avoid the forbidden frequency issue (in (4.10) and (4.11), the same issue of the Bessel function [46] also exists for the Mathieu radial function of the first kind), a rigid ELA was used. There were 30 loudspeakers equiangularly ($\Delta\nu = \frac{\pi}{15}$) mounted on the surface of a rigid elliptical baffle. The lengths of the major axis and the minor axis were 0.8 m and 0.3 m, respectively. Note that this ELA has the same “length” and “width” as those of 2CLA in Sec. 3.6.1 group A. With respect to the comparison in Sec. 3.6.1, both the “on x” (i.e., major axis located on x -axis) and “on y” (i.e., major axis

located on y -axis) ELAs were tested. The simulations were conducted at 1000 Hz; using an elliptical coordinate system with $a = \frac{\sqrt{55}}{20}$, $u_0 \approx 0.39$ and $q \approx 11.74$ were obtained; the truncation order was set to $\lfloor \frac{L-1}{2} \rfloor = 14$; the order for calculating the transfer function was 20. The results of CLA and 2CLA were implemented with the CHE-based method as presented in Sec. 3.3. Tikhonov regularisation was applied to all arrays to suppress the driving functions to under 0 dB.

The results for a $2\text{ m} \times 2\text{ m}$ sound field are shown in Figs. 4.12 and 4.13. Comparing the results to Figs. 3.10, 3.11, and 3.12, it is observed that ELA outperforms single CLA and has a performance close to that of 2CLA.

Next, ELA was compared to CLA and 2CLA in the frequency band of 200-4000 Hz. The primary field included a focused source at (0 m, 0.5 m). The error over the control region was evaluated by (2.69) in the sample ring region (3.35). The results are shown in Fig. 4.14. The performance of ELA was similar to that of 2CLA with the same “length” and “width” of the array, while both ELA and 2CLA outperformed CLA.

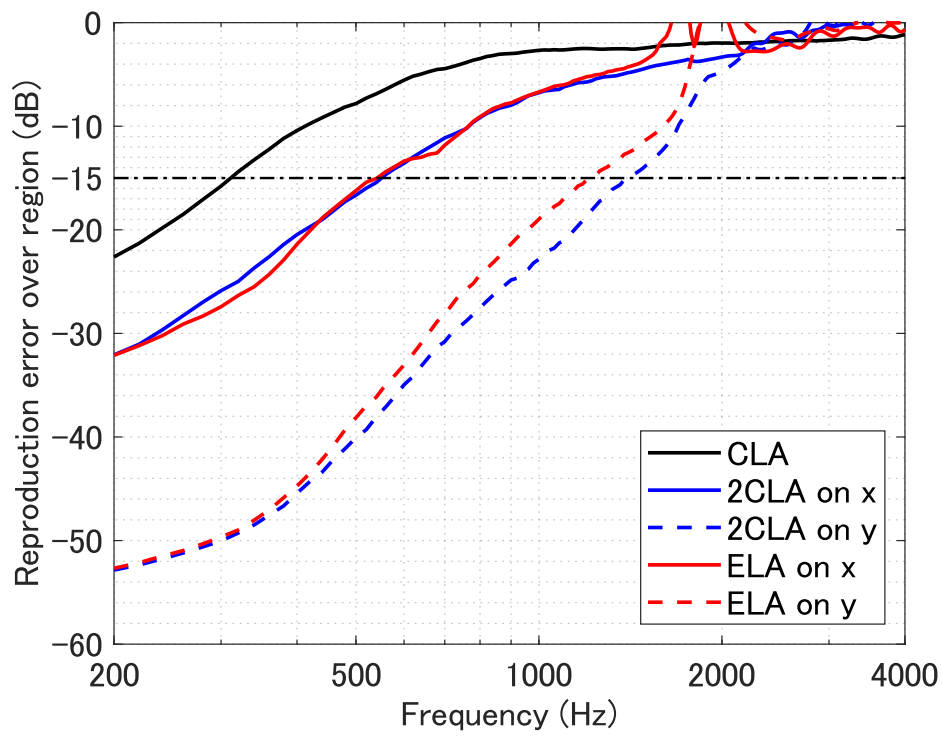
Comparison with CLA, 2CLA, and LLA

Consider that a “flat” ELA has a contour similar to LLA, the performances of ELA, CLA, 2CLA, and LLA were also compared. The results of LLA were implemented with SDM (cf. Appendix A). Since LLA can only reproduce a half field, it is impossible to compare the reproduction error over the full-region. Instead, a sub-region was selected as:

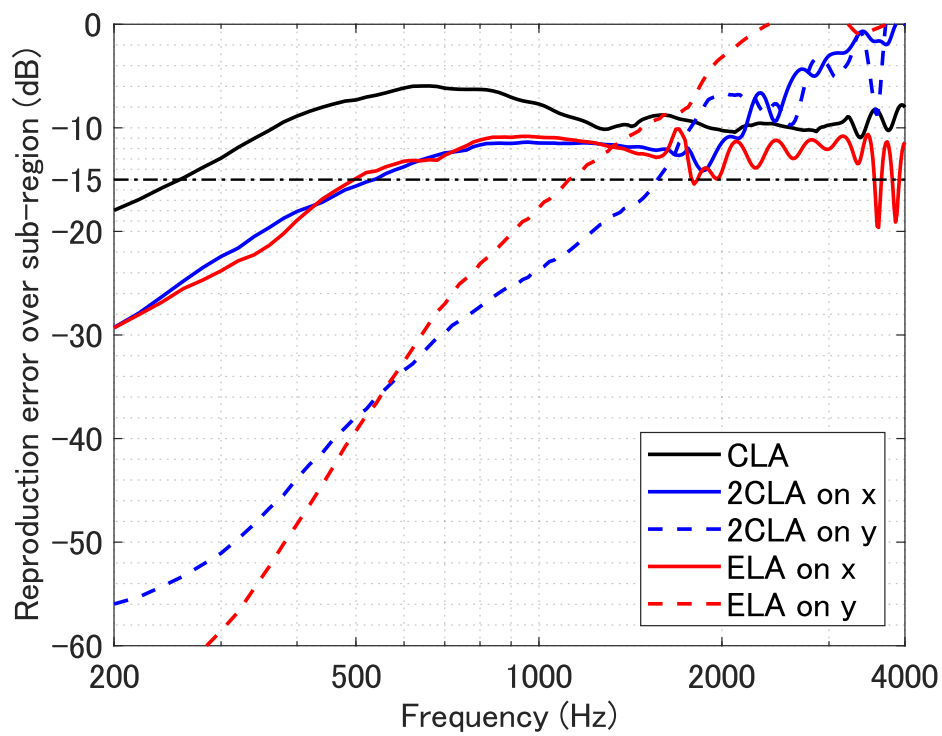
$$\Lambda = \{\mathbf{x} \mid \mathbf{O}_\Lambda = (0, 1), |\mathbf{x} - \mathbf{O}_\Lambda| \leq 0.2\}, \quad (4.42)$$

i.e., a circular region in front of the focused source. The comparisons on reproduction error were carried out on the sub-region in the frequency band of 200-4000 Hz. Two LLAs were tested: one with the same length as that of ELA and 2CLA, namely, 30 loudspeakers uniformly located on a 0.8 m line with loudspeaker interval of approximately 0.03 m; another with the same loudspeaker interval as that of 2CLA, namely, 30 loudspeakers lined up with an interval of $\pi/50$ m with an approximate length of 1.82 m. An additional CLA of radius 0.4 m was added for comparison with length the same as that of ELA and 2CLA. Other arrays, target source, and regions were the same as those of the previous simulation. The “on y ” configurations were excluded from the comparison. The results are displayed in Fig. 4.15. The results are summarised as follows:

- The 0.4-m-CLA performed far better than others at low frequencies; however, the spatial aliasing at approximately 800 Hz was the worst among all arrays. Spatial aliasing is observed at above approximately 2000 Hz, making the performance worse than that of ELA.
- ELA and 2CLA had similar performances as mentioned before; however, ELA performed better above 2000 Hz.
- LLA performed better at high frequencies than low frequencies: an ideal LLA with infinite length would have better performance at low frequencies [49].
- Among all arrays, the 0.8-m-LLA had the worst performance; its performance at high frequencies was similar to that of ELA.
- The 1.82-m-LLA outperformed 2CLA and ELA at frequencies higher than approximately 700 Hz.



(a)



(b)

Figure 4.14: Reproduction error over a region :comparison between ELA, CLA, and 2CLA.

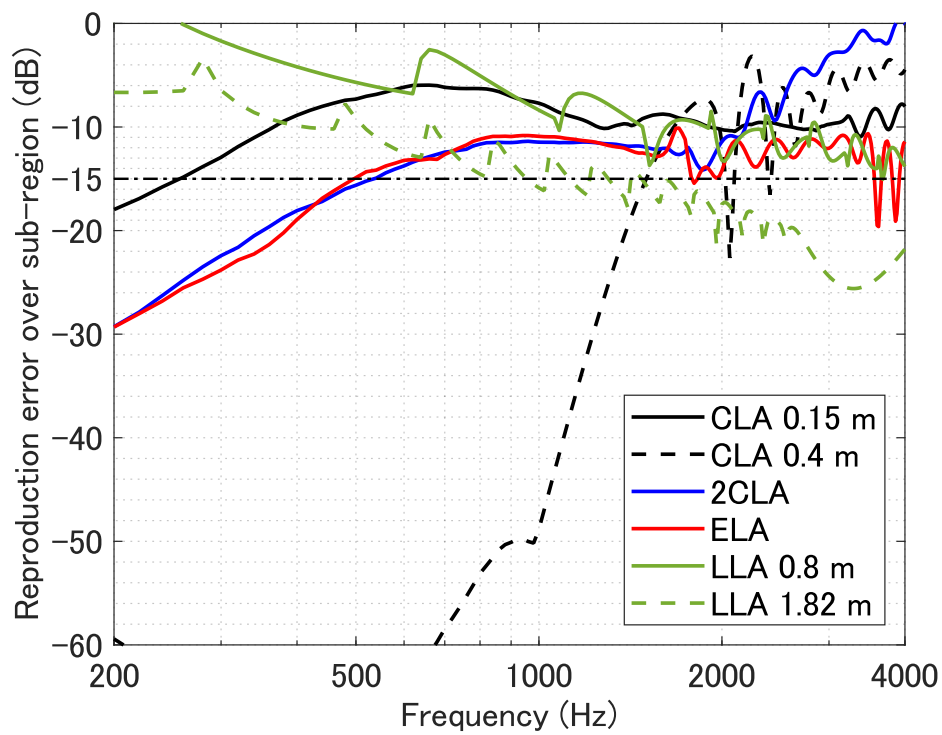
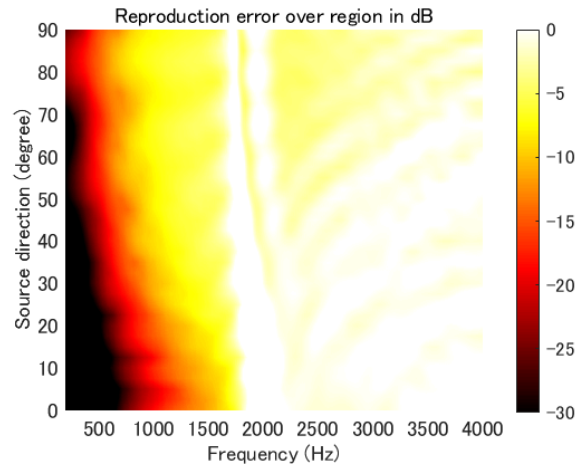
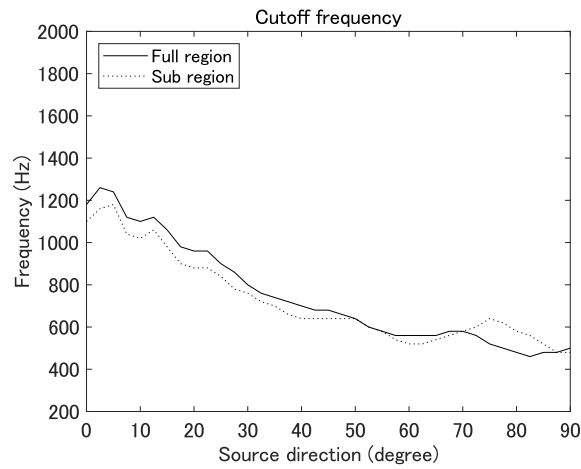


Figure 4.15: Reproduction error over a sub-region: comparisons between ELA, CLA, 2CLA, and LLA.



(a)



(b)

Figure 4.16: Direction dependency of an ELA on focused source reproduction. (a) Reproduction error over full region; (b) Maximum controllable frequency.

4.7.2 ELA Properties on Exterior Sound Field Reproduction

Direction dependency

As ELA is also asymmetrical, the direction dependency is determined by changing the source directions. The same ELA as in the previous part is used. The radius and direction of the target source were the same as in Sec. 3.6.2. All other conditions were identical to those of the previous simulation. The reproduction error for the 200-4000 Hz range are displayed in Fig. 4.16. The x and y axes in the figures represent frequency and the source direction, respectively. Colour shows reproduction error. The relationship between maximum controllable frequency and source direction is displayed in (b). The results show a direction dependence such that ELA performs better at a lower angle of the source direction; note that this is the same for 2CLA.

Influence on array geometry

To investigate how the array shape influences the performance of exterior sound field reproduction, i.e., the efficiency of reproducing a sound field, the results were compared while changing the axis length and/or flattening the array.

The same configurations as in the previous simulations were used, except that the focused source was at a single position (0 m, 0.5 m). The simulations were conducted for a frequency band of 200-4000 Hz.

Four aspects of ELA were investigated:

- (i) how does the axis length perpendicular to the source direction affect performance (with another axis length fixed);
- (ii) how does the axis length in the source direction affect performance (with another axis length fixed);
- (iii) how does flattening affect performance with fixed perimeter of the array;
- (iv) how does flattening affect performance with fixed area of the array.

All ELAs included 30 loudspeakers equiangularly located on the surface.

Flattening \mathcal{F} is a value that describes how flat an ellipse is: $\mathcal{F} = 0$ denotes a circle; $\mathcal{F} \rightarrow 1$ describes an ellipse that is almost a straight line. Flattening is defined as

$$\mathcal{F} = \frac{\mathcal{A} - \mathcal{B}}{\mathcal{A}}, \quad (4.43)$$

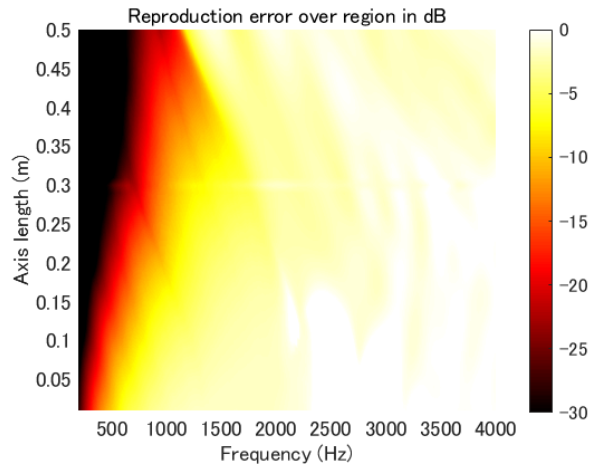
where \mathcal{A} , \mathcal{B} are the major and the minor axis of the ellipse, respectively.

The axis length in the source direction was fixed at 0.3 m in part (i). The axis length perpendicular to the source direction was varied from 0.01 m to 0.5 m. Note that the one with both axes length at 0.3 m was a CLA. Figure 4.17(a) display the reproduction error for a varying axis length. The x and y axes in the figures represent frequency and axis length, respectively. Colour shows reproduction error. The relationship between the maximum controllable frequency and the source direction is displayed in (b). Since the results for CLA were calculated by CHE-based method, the results had a discontinuity at 0.3 m. The results indicate that for a fixed focused source at (0 m, 0.5 m), the axis length perpendicular to the source direction is roughly positively related to the maximum controllable frequency; there was a slight fall at high frequencies.

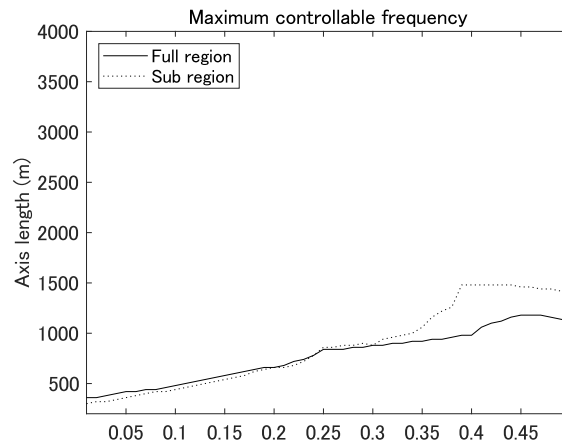
The axis length perpendicular to the source direction was set to 0.3 m in part (ii). The axis length in the source direction was varied from 0.01 m to 0.5 m. Note that the one with both axes length at 0.3 m was a CLA. Figure 4.18 displays the results for (a) Reproduction error over the control region and (b) Maximum controllable frequency.

The results indicate that for a fixed focused source at (0 m, 0.5 m), the increase in the axis length in the source direction is roughly positively related to the maximum controllable frequency; there is little dependency at high frequencies.

In part (iii), the perimeter of the array was set to $3\pi/5$ m, which is the same as that of a CLA with radius 0.3 m. The flattening was varied between 0 and 1. Note that the one with $\mathcal{F} = 0$ denotes a CLA. The reproduction error near $\mathcal{F} = 0$ had a discontinuity, as explained above. The results for varying flattening are displayed in Fig. 4.19. The y axes in the figures represent the flattening. The results indicate that for a fixed focused source at (0 m, 0.5 m), with a fixed perimeter, flattening is negatively related to the maximum controllable frequency, meaning that CLA performs the best.



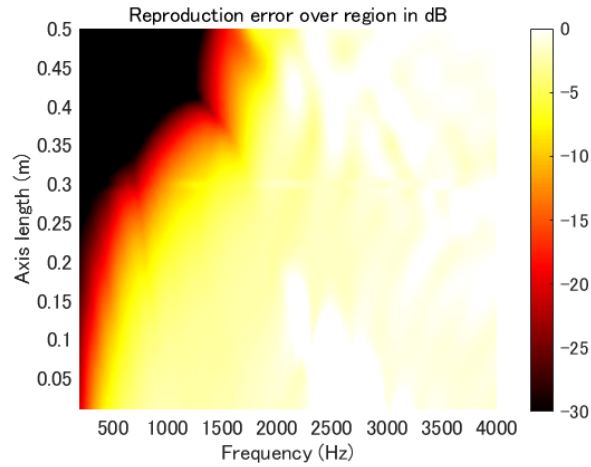
(a)



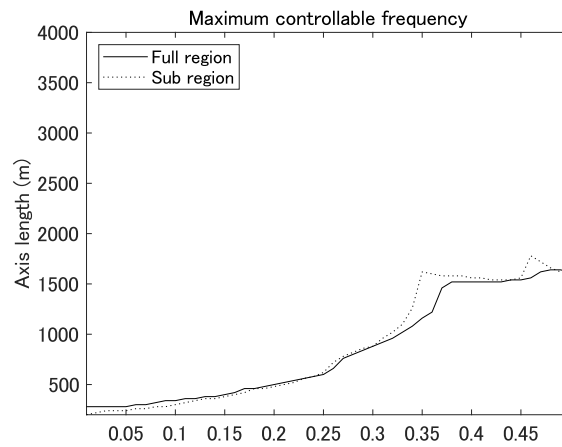
(b)

Figure 4.17: Focused source reproduction results on changing the axis length perpendicular to the source direction. (a) Reproduction error over full region; (b) Maximum controllable frequency.

In part (iv), the area of the array was set to $9\pi/100 \text{ m}^2$, which is the same as that of a CLA with radius of 0.3 m. The flattening was varied between 0 and 1. Note that the one with $\mathcal{F} = 0$ denotes a CLA. The results for (iv) are displayed in Fig. 4.20 indicating that for a fixed focused source at $(0 \text{ m}, 0.5 \text{ m})$, for a fixed area, the flattening is negatively related to the maximum controllable frequency; the dependency is less when the perimeter is fixed.

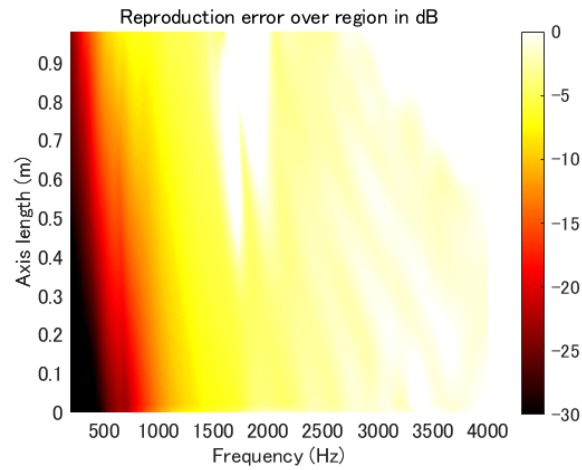


(a)

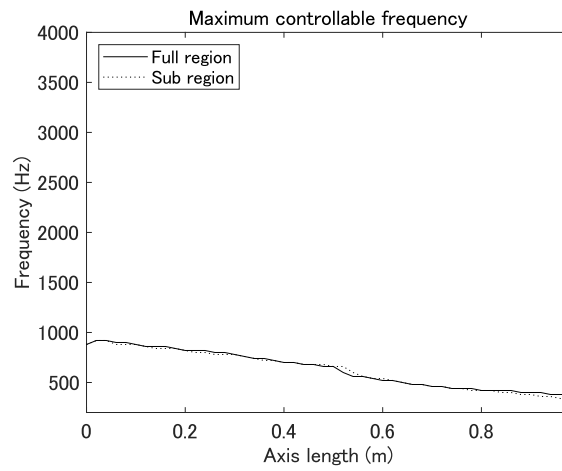


(b)

Figure 4.18: Focused source reproduction results on changing the axis length in the source direction. (a) reproduction error over full region; (b) maximum controllable frequency.

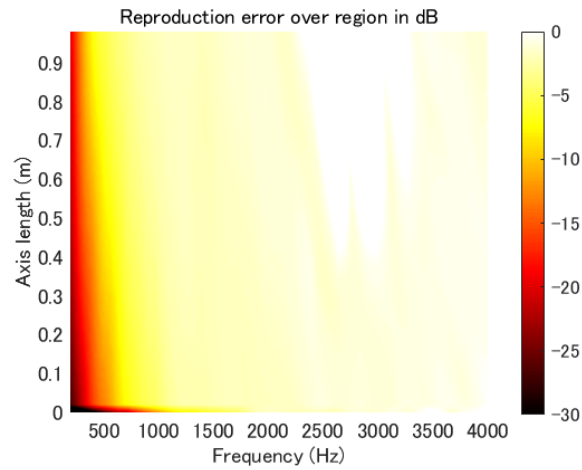


(a)

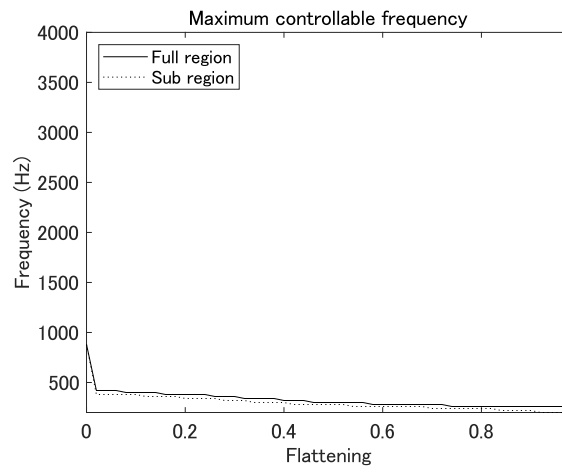


(b)

Figure 4.19: Focused source reproduction results on changing flattening with a fixed perimeter. (a) Reproduction error over full region; (b) Maximum controllable frequency.



(a)



(b)

Figure 4.20: Focused source reproduction results on changing the flattening with a fixed area. (a) Reproduction error over full region; (b) Maximum controllable frequency.

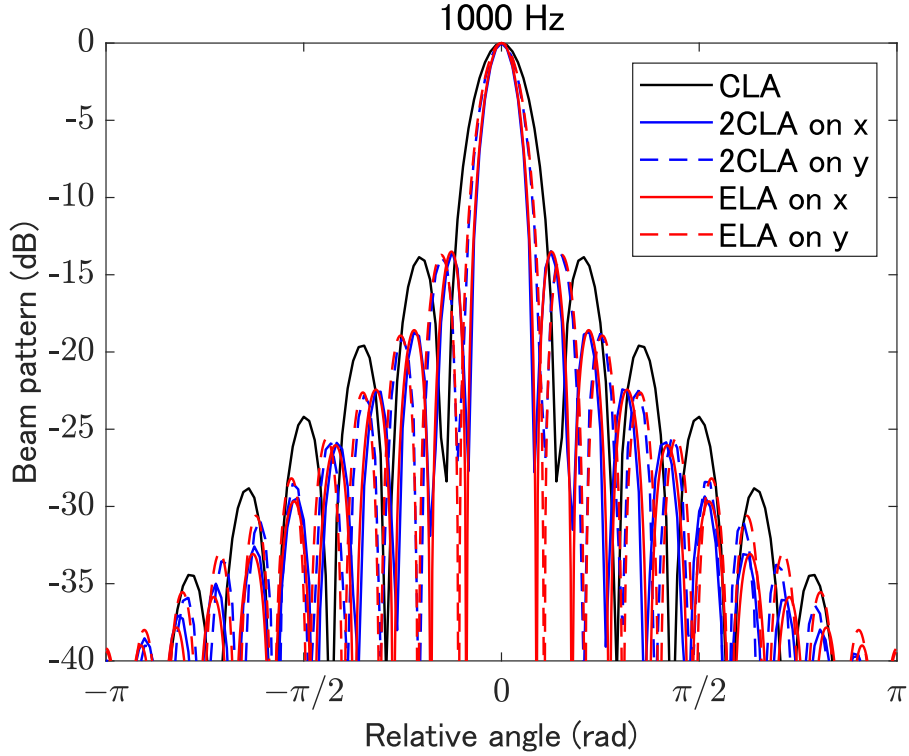


Figure 4.21: Beam patterns of ELAs, CLA and 2CLAs. The beam pattern is normalised by the power in the look direction. The angle on the horizontal axis is relative to the look direction.

4.8 Beamforming

In this section, ELA performance on beamforming is tested. The performance is evaluated using DI, BW, and SLL.

For all simulations reported in this section, the MVDR beamformer with Tikhonov regularisation was employed. Constraint point, suppression points, observation points, and the sound pressure at the constrained point were set as in Sec. 3.7.

4.8.1 Comparison with CLA, 2CLA, and LLA

Comparison with CLA and 2CLA

Simulations were conducted to compare the arrays introduced in Sec. 4.7.1. In this part, only the look direction at 90° is discussed for simplicity. The beam patterns of ELAs, CLA, and 2CLAs at 1000 Hz are displayed in Fig. 4.21. The results of ELAs and 2CLAs of both configurations show negligible difference and outperform CLA. This is also in agreement with the results of focused source reproduction.

The results in the frequency band of 200-4000 Hz are displayed in Fig. 4.22. These results also show negligible difference between ELA and 2CLA (both outperform the CLA) at frequencies below 1700 Hz. For higher frequencies, the “on x” ELA outperforms “on x” 2CLA with higher DI and lower SLL. In contrast, the “on y” ELA has lower DI, higher BW with lower SLL than the “on y” 2CLA; the “on y” configurations display even worse performance than the CLA.

Comparison with CLA, 2CLA, and LLA

Another comparison was conducted with LLA included. The LLAs were the same as in Sec. 4.7.1. In this part, the results are discussed for two look directions: 0° and 90° .

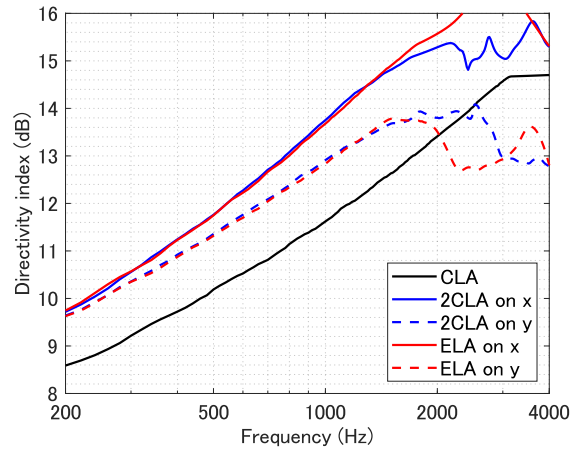
The beam patterns at 1000 Hz are displayed in Fig. 4.23. Look directions were set to (a) 0° ; (b) 90° . The results of ELAs and 2CLAs also show negligible difference. For both (a) and (b), evaluating the sharpness of the beam, the 1.82-m-LLA and 0.4-m-CLA performed better, ELA and 2CLA were next, and the 0.8-m-LLA and 0.15-m-CLA were the worst. The LLAs, however, always exhibited a symmetric beam pattern, meaning that there always is a 0 dB side lobe except for the look direction of 0° (shown in (b)).

To further investigate, a simulation was conducted for the frequency band of 200-4000 Hz. The results are shown in Figs. 4.24 and 4.25. For the look direction of 0° :

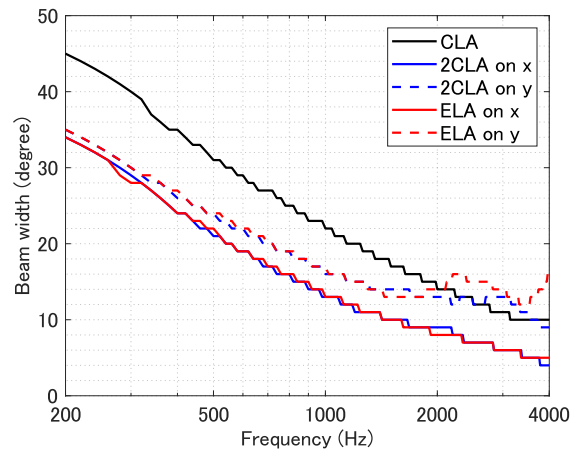
- The 0.4-m-CLA had the best performance, closely followed by the 1.82-m-LLA; however, both of them had a roll-off at above 2400 Hz.
- (As mentioned above) ELA and 2CLA displayed similar performance whereas 2CLA performed better above 1700 Hz.
- The 0.15-m-CLA and the 0.8-m-LLA were the worst pair at low frequencies; however, they outperformed other arrays at above 3000 Hz. The CLA was slightly better than the LLA at high frequencies.

For the look direction of 90° :

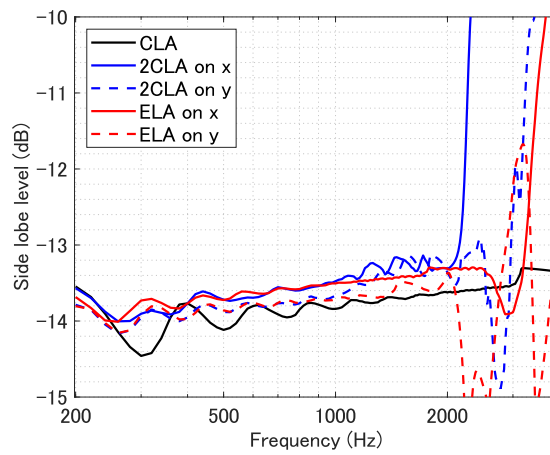
- The 0.4-m-CLA performed best at low frequencies but was overtaken by ELA and 2CLA at approximately 1400 Hz.
- As mentioned above, ELA and 2CLA had similar performance; however, ELA performed better above 1400 Hz.
- The 1.82-m-LLA performance was in between that of 0.15-m-CLA and ELA while the performance potential increased at high frequencies.
- The 0.8-m-LLA was the worst.
- LLAs had a constant SLL at 0 dB thus limiting the applications.



(a) DI



(b) BW



(c) SLL

Figure 4.22: DI, BW, and SLL of ELAs, CLA, and 2CLAs over a frequency band of 200-4000 Hz.

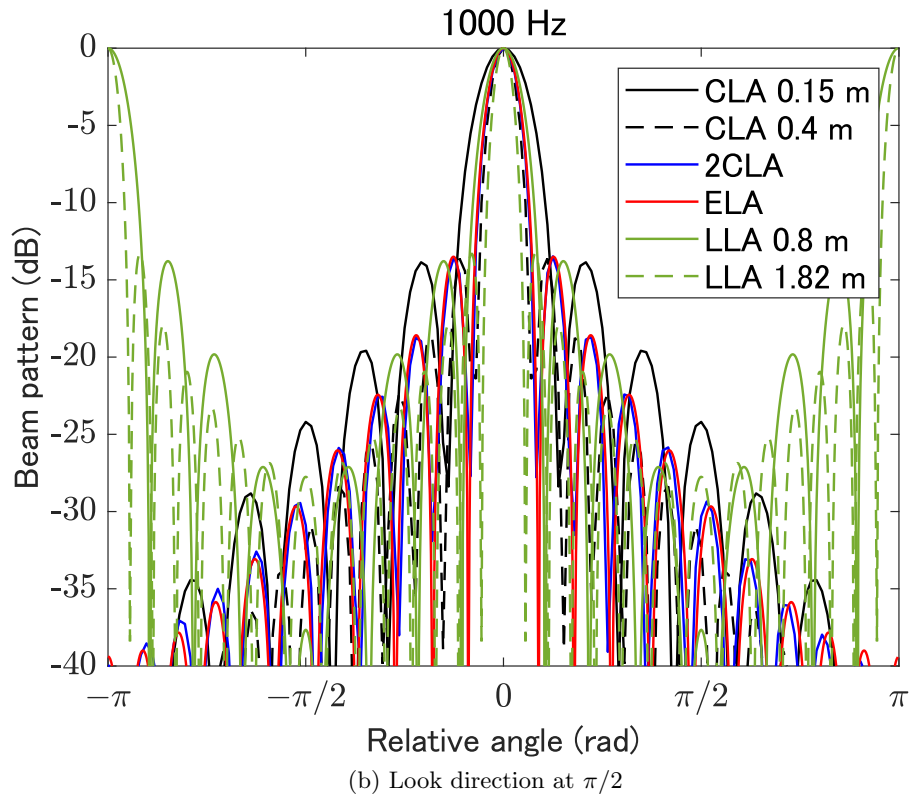
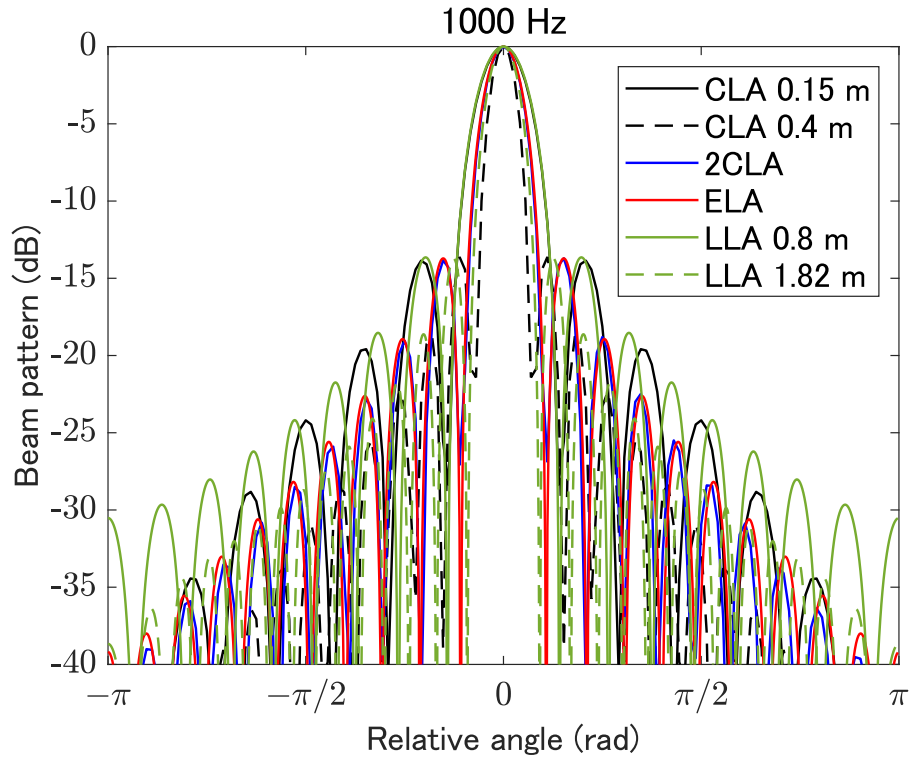
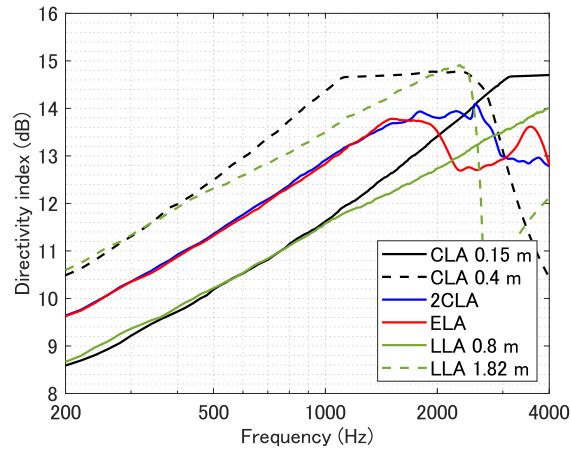
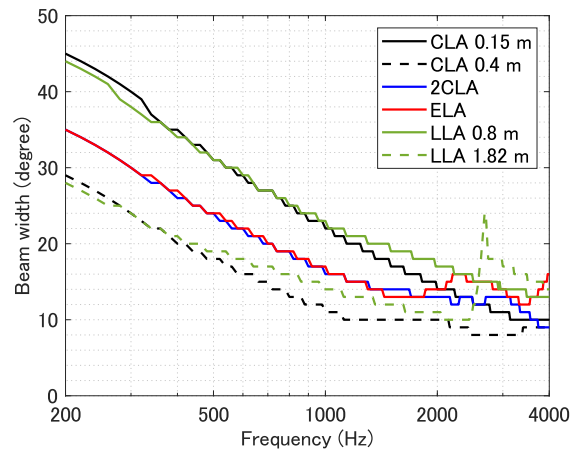


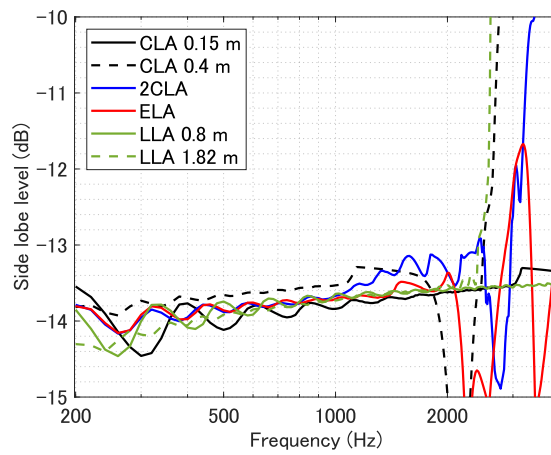
Figure 4.23: Beam patterns of ELA, CLAs, 2CLA, and LLAs. The beam pattern is normalised by the power in the look direction. The angle on the horizontal axis is relative to the look direction.



(a) DI

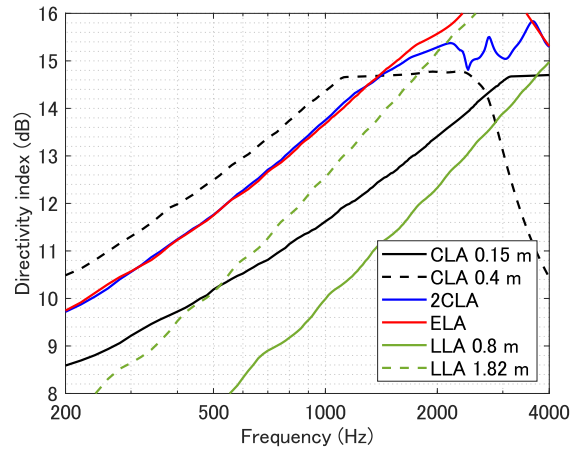


(b) BW

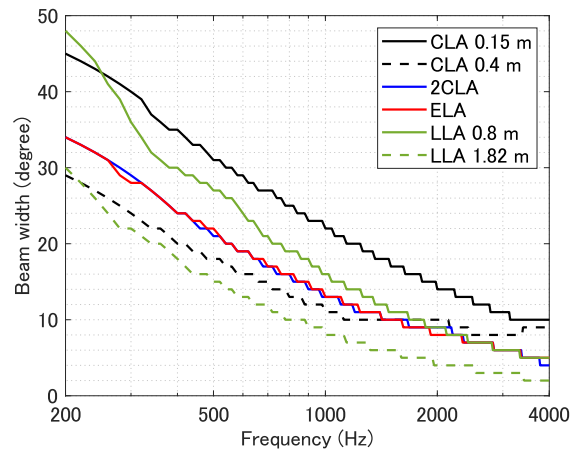


(c) SLL

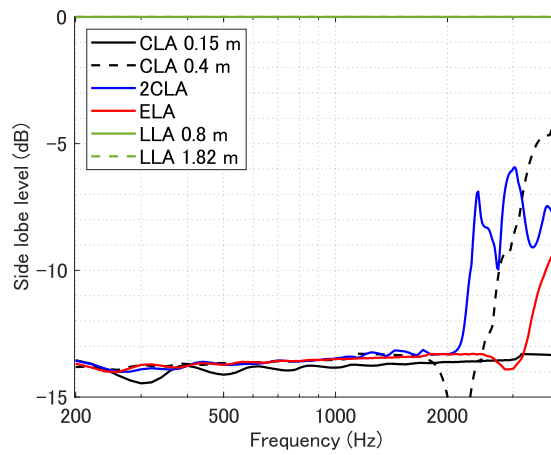
Figure 4.24: DI, BW, and SLL of ELA, CLAs, 2CLA, and LLAs over a frequency band of 200-4000 Hz. The look direction was 0° .



(a) DI



(b) BW



(c) SLL

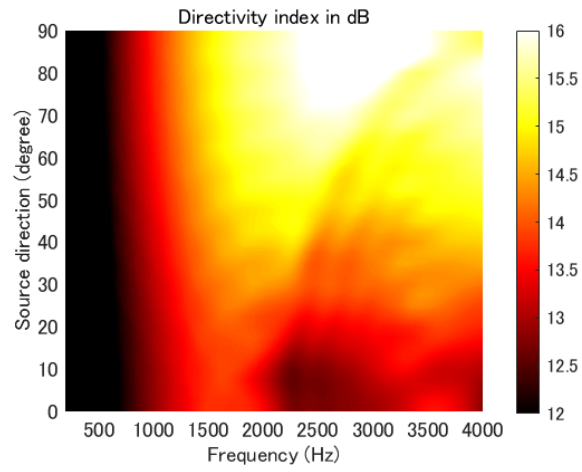
Figure 4.25: DI, BW, and SLL of ELA, CLAs, 2CLA, and LLAs over a frequency band of 200-4000 Hz. The look direction is 90° . LLAs have a constant 0 dB SLL.

4.8.2 ELA Properties on Beamforming

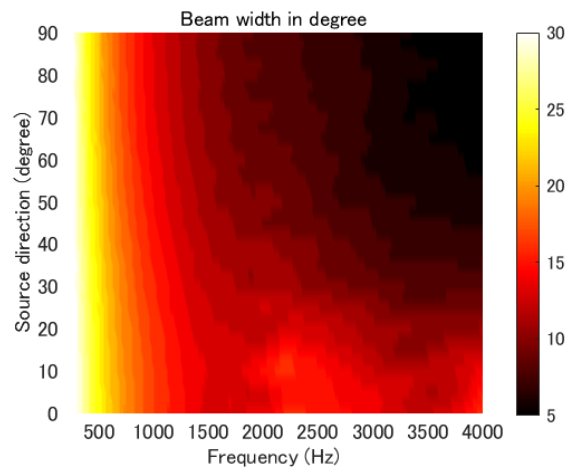
Direction dependency

A simulation was conducted on changing look directions to investigate the asymmetric aspect of an ELA. The angles between 0° and 90° were tested at intervals of 2.5° with the ELA in Sec. 4.7.1. Other conditions were the same as in the previous simulation.

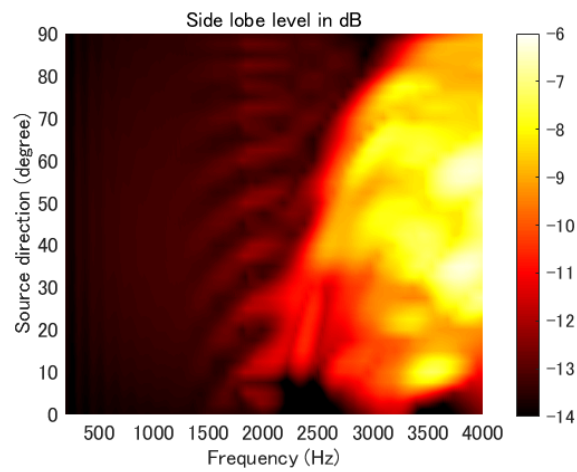
The results presented in Fig. 4.26 show that DI and BW improve with increasing angle at higher frequencies, which is an aspect of 2CLA. There is little direction dependence at frequencies below 1000 Hz. SLL is direction-dependent above 2400 Hz. Comparing with Fig. 3.34, it is observed that the results of ELA are similar to that of 2CLA, except that 2CLA excites SLL at larger angles.



(a) DI



(b) BW



(c) SLL

Figure 4.26: DI, BW, and SLL of ELA in look directions between 0° and 90° .

Influence on array geometry

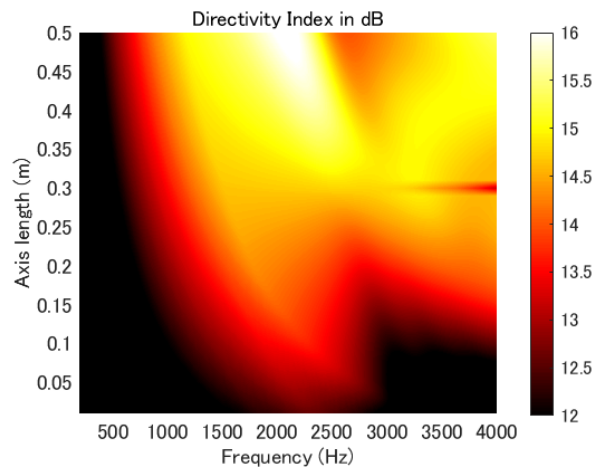
Similar to Sec. 4.7.2, the performance of ELA was investigated by changing the axis length or the flattening of the array. The investigation focused on the influence of four ELA parameters: (i) the axis length perpendicular to the beam direction; (ii) the axis length in the beam direction; (iii) flattening with fixed perimeter; (iv) flattening with fixed area. All tests were carried out for the configurations in Sec. 4.7.2.

Simulations were conducted for an MVDR beamformer, the same as the one in Sec. 3.7. There was a discontinuity in the results near CLA (calculated by CHE-based method).

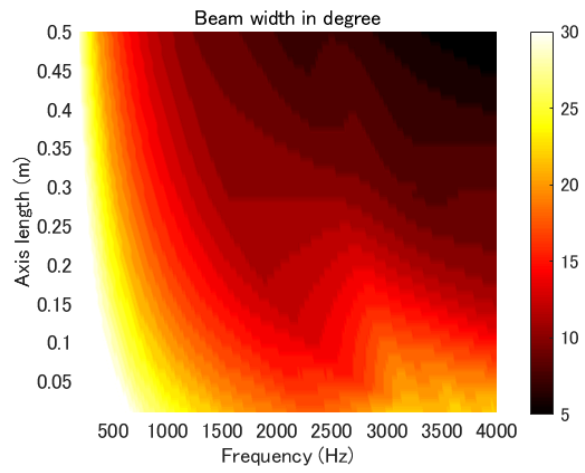
The results on (i) are shown in Fig. 4.27. Note that the 0.3 m axis length ELA was a CLA. The results show that on beamforming, the axis length perpendicular to the beam direction is positively related to DI and BW. The results on SLL indicate that a “flat” ELA tends to have higher SLL than a “round” ELA.

The results on (ii) are shown in Fig. 4.28. Again, the 0.3 m axis length ELA was a CLA. The results show that on beamforming, the axis length in the beam direction is positively related to DI and BW at low frequencies and negatively related at high frequencies (approximately divided at 1500 Hz). The results show negligible dependence between axis length and SLL.

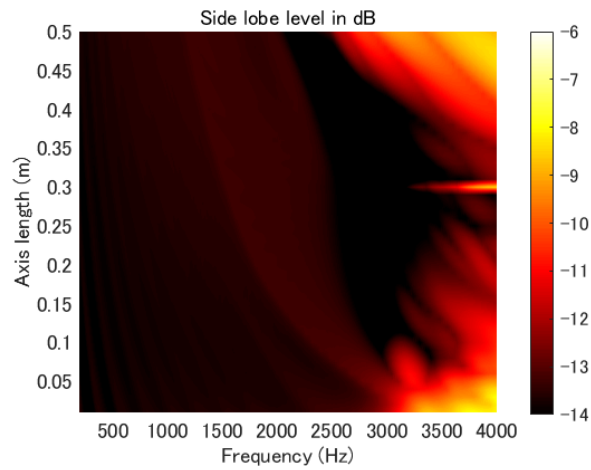
The results on (iii) are displayed in Fig. 4.29. Note that the 0 flattening ELA was a CLA. The results show little dependence between flattening and performance below 3000 Hz. At higher frequencies, a larger flattening has a higher DI along with a higher SLL. The results on (iv) are displayed in Fig. 4.30. The 0 flattening ELA was a CLA. The results show little dependence between flattening and performance in the entire frequency band.



(a) DI

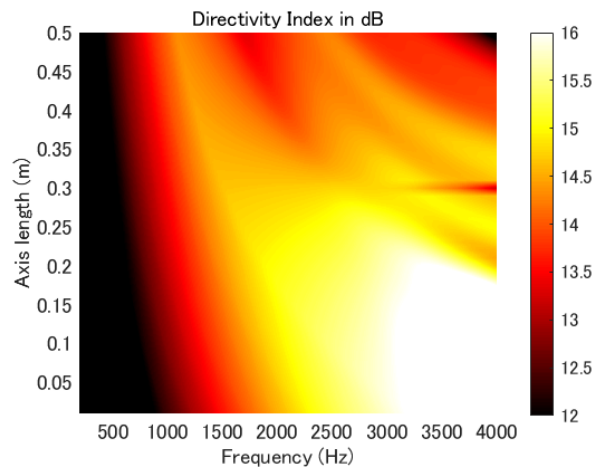


(b) BW

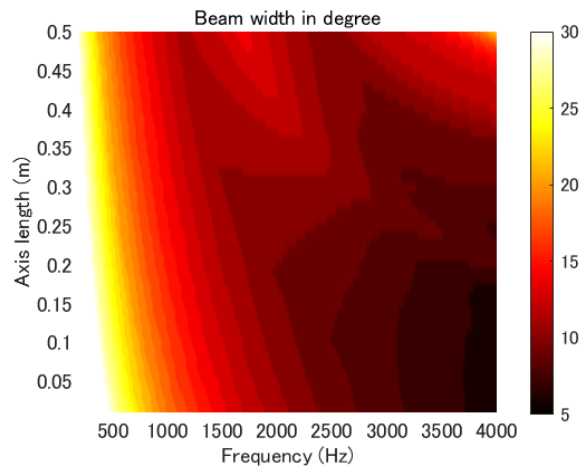


(c) SLL

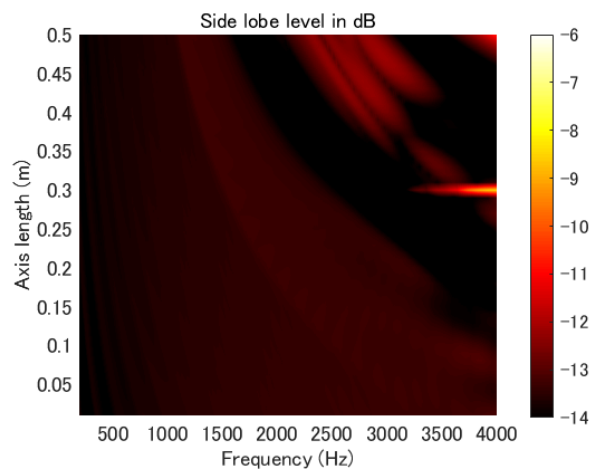
Figure 4.27: Beamforming results on changing the axis length perpendicular to the beam direction.



(a) DI

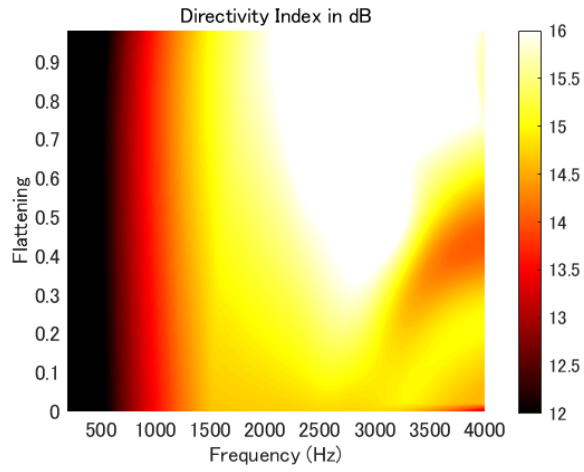


(b) BW

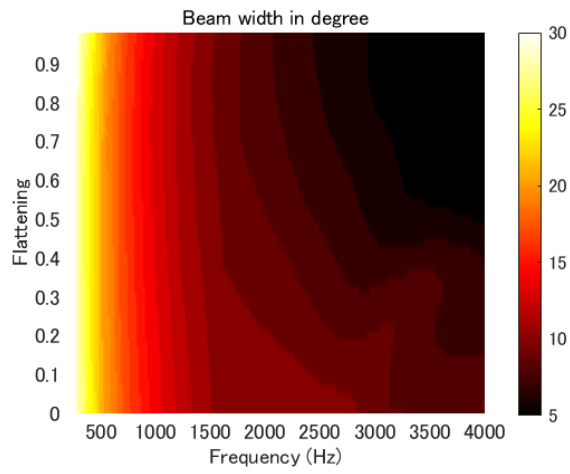


(c) SLL

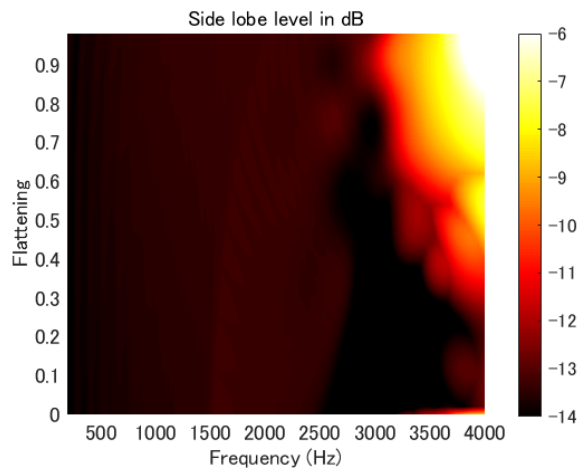
Figure 4.28: Beamforming results on changing the axis length in the beam direction.



(a) DI

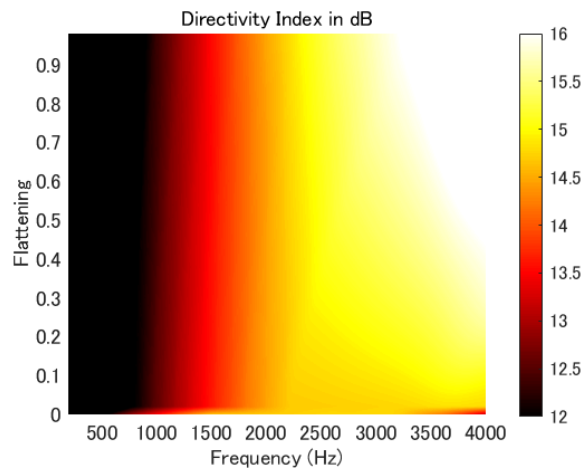


(b) BW

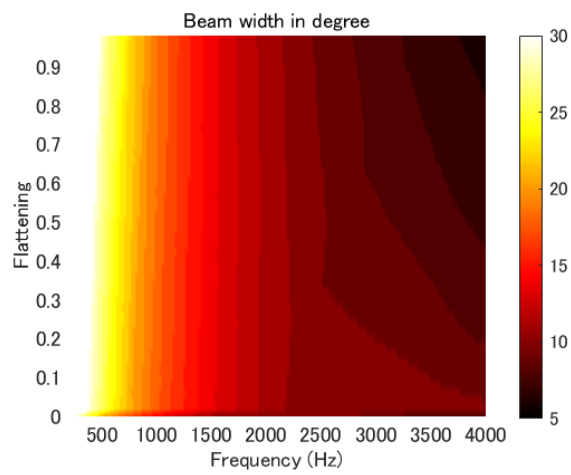


(c) SLL

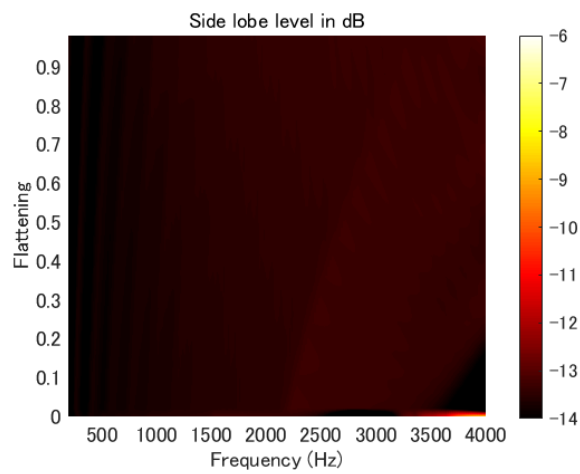
Figure 4.29: Beamforming results on changing flattening with fixed perimeter.



(a) DI



(b) BW



(c) SLL

Figure 4.30: Beamforming results on changing flattening with fixed area.

4.9 Summary

In this chapter, an ELA model was proposed. Compared with the MCLA model proposed in the previous chapter, the ELA model has a complete contour, and therefore, there is no multiple scattering effect. As ELA can be defined in the elliptical coordinate system, a sound field reproduction method based on the eigenfunctions of the coordinate system - the Mathieu functions, was proposed. With the proposed method, the ELA can be controlled through elliptical harmonic modes. A method was further proposed, adopting MFE for circular-array-signals, which allows implementation with the most common circular microphone arrays. The mode strength of an ELA was next investigated. The mode strength of ELA showed potential in reproducing complex sound fields.

As in the previous chapter, numerical simulations were conducted and discussed with respect to interior sound field reproduction, exterior sound field reproduction, and beamforming.

For interior sound field reproduction, both the MFE-based method and the method adopted for circular microphone arrays were validated for sound field reproduction. With order truncation, the MFE-based method displayed an elliptical listening area. However, the order truncation on the circle-ellipse transformation resulted in a circular listening area as with conventional methods for CLA.

Next, the performance of ELA was discussed on exterior sound field reproduction. Conventional CLAs, LLAs were compared with the 2CLA proposed in the previous chapter. The properties of ELA were also investigated in detail. The results show that the ELA and 2CLA of same “length” and “width” had similar performances. The results also show that both ELA and 2CLA outperform conventional arrays. As for the properties of ELA, the direction dependency is similar to that of 2CLA: ELA performed better in the major-axis direction; the axis lengths were roughly positively related to performance; the flattening had a little negative affect on performance. Based on these results, it is hypothesised that instead of the specific array contour, it is the array scale that primarily affects performance.

As for beamforming, comparisons were made with 2CLA, CLA, and LLA. The performances of ELA and 2CLA were similar. The comparison with conventional arrays was similar to the results of exterior sound field reproduction. The performance of the end-fire LLA was competitive. The ELA showed little direction dependence on beamforming. As for the influence of ELA parameters, axis lengths were positively related to performance; flattening was slightly positively related to performance. The ELA parameters had a more direct influence on beamforming than on exterior sound field reproduction. This is in agreement with the hypothesis that beamforming is a simplified model of sound field reproduction.

Chapter 5

General sound field reproduction method based on Mathieu function expansion

The MFE-based method proposed in the previous chapter displays asymmetrical properties. Those properties provide certain advantages in specific situations such as when listeners are sitting in a line (e.g., on a long sofa). In this chapter, the method is generalised to a more versatile method for arbitrary-shaped arrays. The results are discussed with respect to interior and exterior sound field reproduction.

5.1 The general method

For arbitrarily shaped arrays, the MFE-based method can be employed with minor modifications. The properties of MFE, including the elliptical controlling area, are advantages when applied to asymmetric arrays.

The secondary field of an arbitrary array can be described as in (4.31). However, the driving function cannot be simply expanded by the Mathieu angular function. Therefore, another MFE-based method is proposed that can be applied to arbitrary arrays. The method proposed in the previous section expands the driving functions in the wave domain and drives the secondary sources by mode. Using the same approach of matching the MFE coefficient, the proposed method drives the secondary sources individually in the frequency domain, as follows:

By substituting (2.6) into (4.31), we obtain

$$\hat{p}(\xi, \eta, \omega) = \begin{cases} \sum_{l=1}^L \left[\sum_{\nu=-\infty}^{\infty} \gamma_{\nu}^{\triangleleft}(\mathbf{x}_l, q) M_{\nu}^{(1)}(q, \xi) m e_{\nu}(q, \eta) \right] d_l(\omega) & \text{interior} \\ \sum_{l=1}^L \left[\sum_{\nu=-\infty}^{\infty} \gamma_{\nu}^{\triangleright}(\mathbf{x}_l, q) M_{\nu}^{(4)}(q, \xi) m e_{\nu}(q, \eta) \right] d_l(\omega) & \text{exterior} \end{cases}, \quad (5.1)$$

where

$$\begin{cases} \gamma_{\nu}^{\triangleleft}(\mathbf{x}_l, q) = -\frac{j}{4} M_{\nu}^{(4)}(q, \xi_l) m e_{\nu}(q, -\eta) & \text{interior} \\ \gamma_{\nu}^{\triangleright}(\mathbf{x}_l, q) = -\frac{j}{4} M_{\nu}^{(1)}(q, \xi_l) m e_{\nu}(q, -\eta) & \text{exterior} \end{cases} \quad (5.2)$$

are for open arrays.

By utilising the orthogonality of Mathieu functions, the coefficients of the secondary sound field in (5.1) are matched to the primary sound field (4.23) with

$$\begin{cases} \sum_{l=1}^L \gamma_{\nu}^{\triangleleft}(\mathbf{x}_l, q) d_l(\omega) = \dot{p}_{\nu}^{\triangleleft}(q) & \text{interior} \\ \sum_{l=1}^L \gamma_{\nu}^{\triangleright}(\mathbf{x}_l, q) d_l(\omega) = \dot{p}_{\nu}^{\triangleright}(q) & \text{exterior} \end{cases}. \quad (5.3)$$

Rewriting both sides using vector and matrix expressions, the driving function is derived using the least-squares method:

$$\mathbf{d} = (\mathbf{\Gamma}^H \mathbf{\Gamma} + \lambda \mathbf{I}_L)^{-1} \mathbf{\Gamma}^H \dot{\mathbf{p}}, \quad (5.4)$$

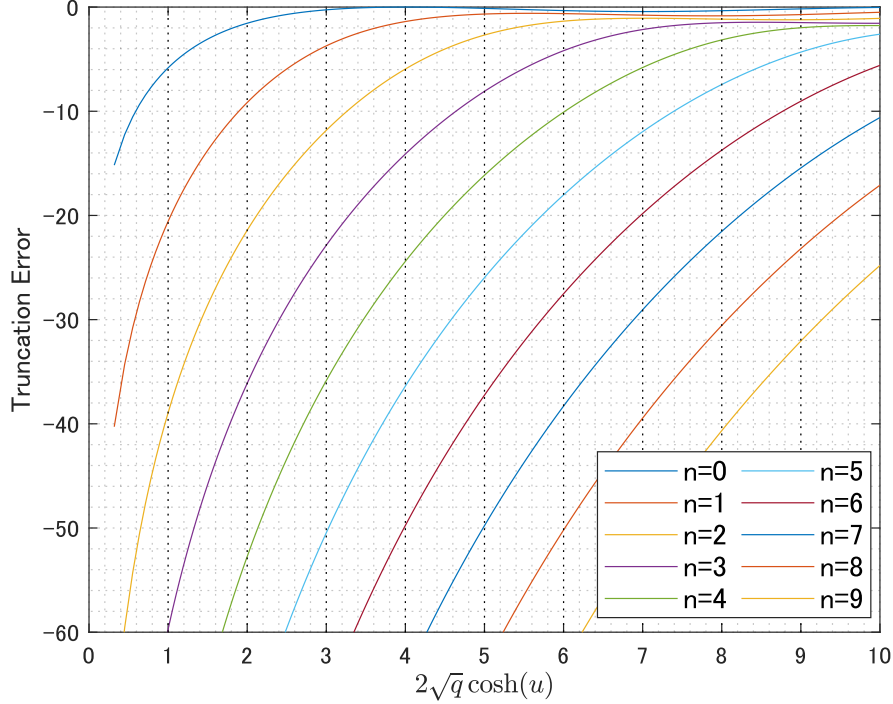


Figure 5.1: Truncation error of plane waves.

where λ is the regularisation parameter,

$$\mathbf{d} = [d_1(\omega), d_2(\omega), \dots, d_L(\omega)]^T, \quad (5.5)$$

$$\mathbf{\Gamma} = [\gamma_1, \gamma_2, \dots, \gamma_L], \quad (5.6)$$

$$\gamma_l = \begin{cases} [\gamma_{-N}^\triangleleft(\mathbf{x}_l, q), \gamma_{-N+1}^\triangleleft(\mathbf{x}_l, q), \dots, \gamma_N^\triangleleft(\mathbf{x}_l, q)]^T & \text{interior} \\ [\gamma_{-N}^\triangleright(\mathbf{x}_l, q), \gamma_{-N+1}^\triangleright(\mathbf{x}_l, q), \dots, \gamma_N^\triangleright(\mathbf{x}_l, q)]^T & \text{exterior} \end{cases}, \quad (5.7)$$

$$\dot{\mathbf{p}} = \begin{cases} [\dot{p}_{-N}^\triangleleft(q), \dot{p}_{-N+1}^\triangleleft(q), \dots, \dot{p}_N^\triangleleft(q)]^T & \text{interior} \\ [\dot{p}_{-N}^\triangleright(q), \dot{p}_{-N+1}^\triangleright(q), \dots, \dot{p}_N^\triangleright(q)]^T & \text{exterior} \end{cases}. \quad (5.8)$$

In the elliptical coordinates, the foci lie on the x -axis of the Cartesian coordinate system. This means that the elliptical controlling area has a fixed direction. To make the method more flexible, a rotation can be applied to the sound field. By rotating the primary field and the secondary field at the same time, it is possible to achieve a rotation of the elliptical area.

5.2 Truncation order

In studies based on circular harmonic expansion or spherical harmonic expansion, suitable truncation order for infinite series has been discussed. Generally, the truncation order is selected by $N \geq [kr]$ [27] or $N \geq [\frac{ekr}{2}]$ [96] based on the property of cylindrical functions, especially the Bessel function. As the proposed method is based on elliptical functions, the truncation order should be reconsidered with respect to the truncation error. Here, the truncation error in the elliptical harmonic expansion is discussed.

As MFE is asymmetric, the truncation error is also direction dependent. Hence, the average truncation error over directions is discussed. The normalised truncation error of plane waves in all directions can be defined as

$$\varepsilon_N = \frac{\int_0^{2\pi} \int_0^{2\pi} |\mathcal{S}(\eta, \eta') - \hat{\mathcal{S}}_N(\eta, \eta')|^2 d\eta d\eta'}{\int_0^{2\pi} \int_0^{2\pi} |\mathcal{S}(\eta, \eta')|^2 d\eta d\eta'}, \quad (5.9)$$

where η' represents the direction of the plane wave,

$$\mathcal{S}(\eta, \eta') = \sum_{\nu=-\infty}^{\infty} j^\nu m e_\nu(q, -\eta') M_\nu^{(1)}(q, \xi) m e_\nu(q, \eta) \quad (5.10)$$

represents the plane wave, and

$$\hat{\mathcal{S}}_N(\eta, \eta') = \sum_{\nu=-N}^N j^\nu m e_\nu(q, -\eta') M_\nu^{(1)}(q, \xi) m e_\nu(q, \eta) \quad (5.11)$$

represents the plane wave truncated at order N . The numerator of (5.9) can be derived as

$$\begin{aligned} \int_0^{2\pi} \int_0^{2\pi} |\mathcal{S}(\eta, \eta') - \hat{\mathcal{S}}_N(\eta, \eta')|^2 d\eta d\eta' &= \sum_{|\nu|>N} \sum_{|\nu'|>N} \left\{ (j^{\nu'})^* j^\nu M_{\nu'}^{(1)}(q, \xi)^* M_\nu^{(1)}(q, \xi) \right. \\ &\quad \times \int_0^{2\pi} m e_{\nu'}(q, -\eta')^* m e_\nu(q, -\eta') d\eta' \\ &\quad \left. \times \int_0^{2\pi} m e_{\nu'}(q, \eta)^* m e_\nu(q, \eta) d\eta \right\} \quad (5.12) \\ &= 4\pi^2 \sum_{|\nu|>N} M_\nu^{(1)}(q, \xi)^2. \quad (5.13) \end{aligned}$$

The orthogonality of the Mathieu function is applied here. Similarly,

$$\int_0^{2\pi} \int_0^{2\pi} |\mathcal{S}(\eta, \eta')|^2 d\eta d\eta' = 4\pi^2 \sum_{\nu=-\infty}^{\infty} M_\nu^{(1)}(q, \xi)^2. \quad (5.14)$$

Therefore, rewriting (5.13) as

$$\begin{aligned} \int_0^{2\pi} \int_0^{2\pi} |\mathcal{S}(\eta, \eta') - \hat{\mathcal{S}}_N(\eta, \eta')|^2 d\eta d\eta' &= \int_0^{2\pi} \int_0^{2\pi} |\mathcal{S}(\eta, \eta')|^2 d\eta d\eta' \\ &\quad - 4\pi^2 \sum_{\nu=-N}^N M_\nu^{(1)}(q, \xi)^2. \quad (5.15) \end{aligned}$$

Using the property of the plane wave: $\int_0^{2\pi} \int_0^{2\pi} |\mathcal{S}(\eta, \eta')|^2 d\eta d\eta' = 4\pi^2$, the following equation is obtained.

$$\varepsilon_N = 1 - \sum_{\nu=-N}^N M_\nu^{(1)}(q, \xi)^2. \quad (5.16)$$

The Mathieu radial functions have the following property:

$$M_\nu^{(\zeta)}(q, \xi) \sim \mathcal{B}_\nu^{(\zeta)}(2\sqrt{q} \cosh \xi), \quad (5.17)$$

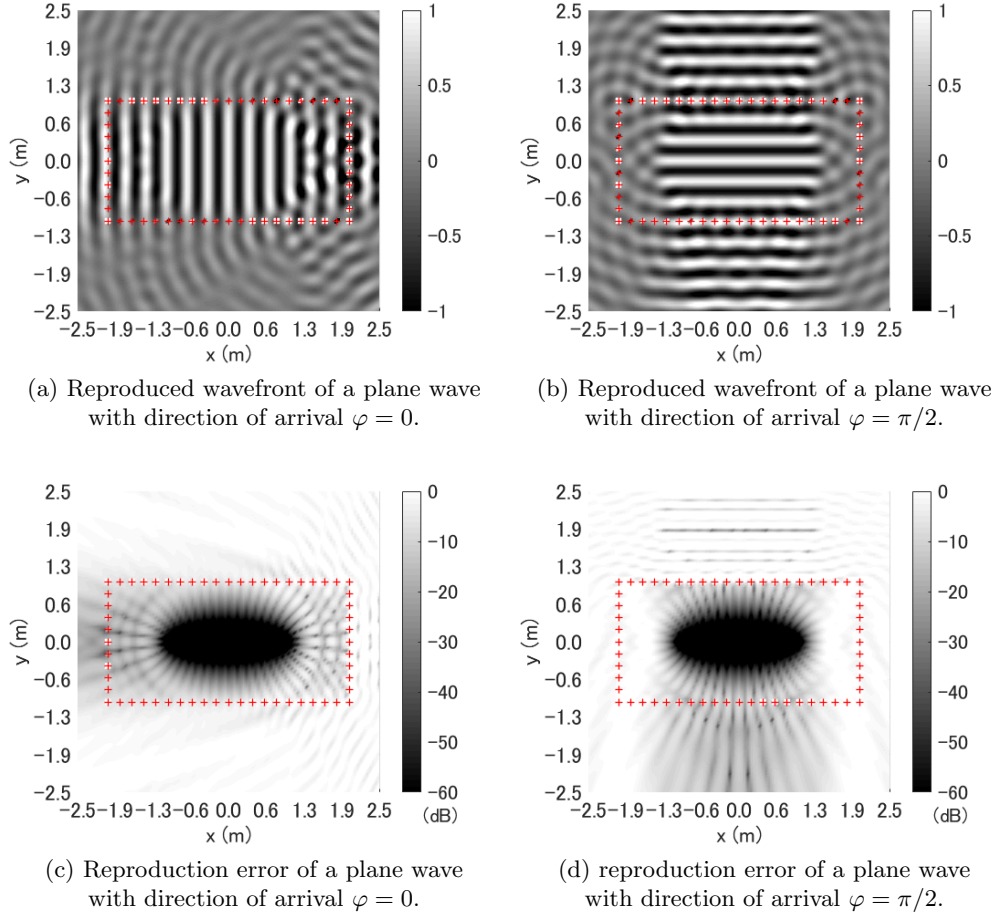


Figure 5.2: Single plane wave reproduced by a rectangular loudspeaker array of 60 loudspeakers.

where $\zeta \in \{1, 2, 3, 4\}$ and $\mathcal{B}_n^{(\zeta)}(\cdot)$ are cylindrical functions. Considering the relationship $N \geq \lceil kr \rceil$, a relationship between $2\sqrt{q} \cosh \xi$ and the truncation error for MFE is established. The results displayed in Fig. 5.1 are similar to the truncation error in circular harmonic expansion. This indicates that the order can be truncated with

$$N \geq \lceil 2\sqrt{q} \cosh \xi \rceil. \quad (5.18)$$

In contrast, the low-error area promised by the maximum order can be obtained by

$$\xi \leq \cosh^{-1} \frac{N}{2\sqrt{q}}. \quad (5.19)$$

5.3 Interior sound field reproduction

For an arbitrarily shaped array, a rectangular loudspeaker array was configured to simulate the sound field reproduction scene in a room. The proposed method was implemented. Sixty loudspeakers were equally spaced at an interval of 0.2 m, on a $4\text{ m} \times 2\text{ m}$ rectangle in a two-dimensional free field. The elliptical coordinate system was defined with $a = 1$. Simulations were conducted at 1000 Hz ($k \approx 18.48$ and $q \approx 192.10$). Here, the truncation order was set to 20. In addition, a

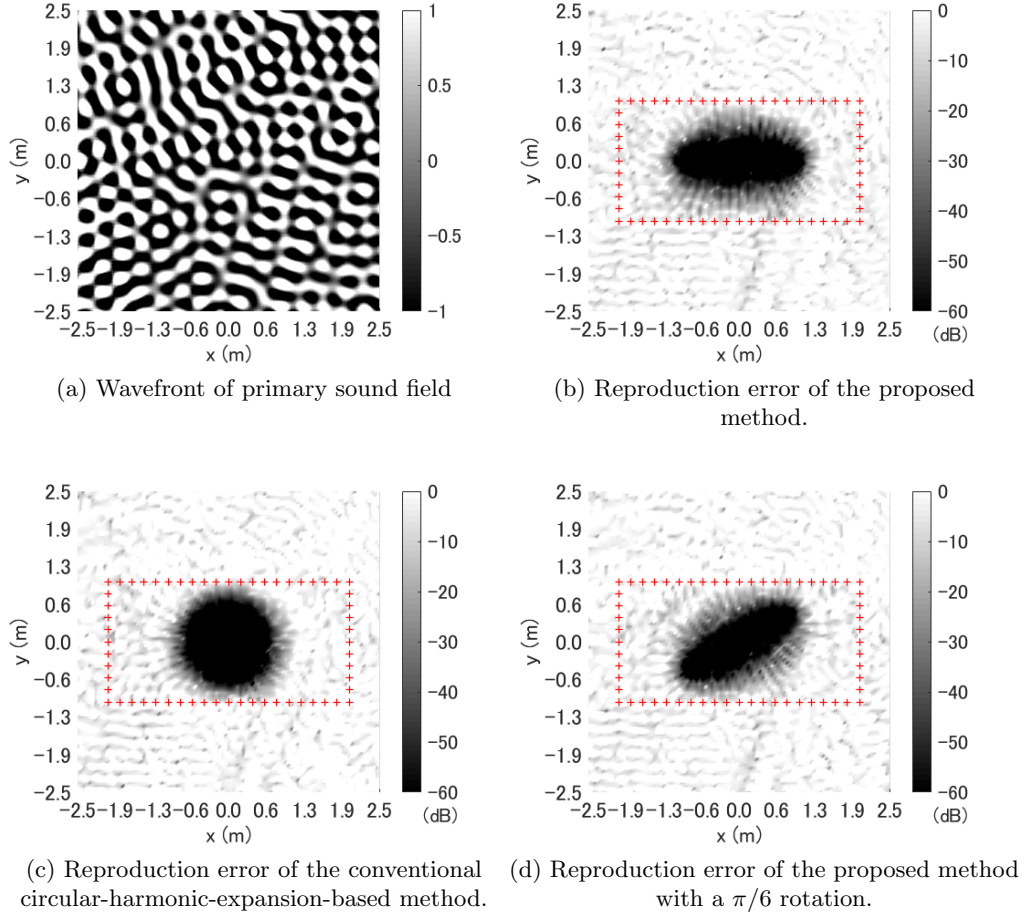


Figure 5.3: Random plane waves reproduced by a rectangular loudspeaker array of 60 loudspeakers.

relatively small L2 regularisation parameter was set as $\lambda = \sigma_{\max}(\mathbf{\Gamma}^H \mathbf{\Gamma}) \times 10^{-6}$, where $\sigma_{\max}(\cdot)$ stands for the maximum eigenvalue.

The results of reproducing a single plane wave are shown in Fig. 5.2. The figure displays the wavefronts and reproduction error in a $5 \text{ m} \times 5 \text{ m}$ sound field. The proposed method reproduced the sound field in elliptical areas.

Next, the proposed method was compared with the conventional circular-harmonic-expansion-based method. To avoid directional dependency, a sound field with 30 random plane waves was tested. The primary sound field is displayed in Fig. 5.3(a). Comparing the reproduction error of the proposed method and the conventional method in (b) and (c), the proposed method reproduced the sound field in a wide elliptical area. This property can benefit some practical scenarios, e.g., listeners sitting on a long sofa. In addition, an example of rotating the elliptical area is provided in (d), which can be applicable to specific listening areas.

5.4 Exterior sound field reproduction

For an example on focused source reproduction, the MFE-based method was applied to a rectangular array. The array size was $0.8 \text{ m} \times 0.4 \text{ m}$ with 24 loudspeakers uniformly arranged on the array contour. Note that the array is an open array. The elliptical coordinate system was defined by $a = \sqrt{55}/20$. An omnidi-

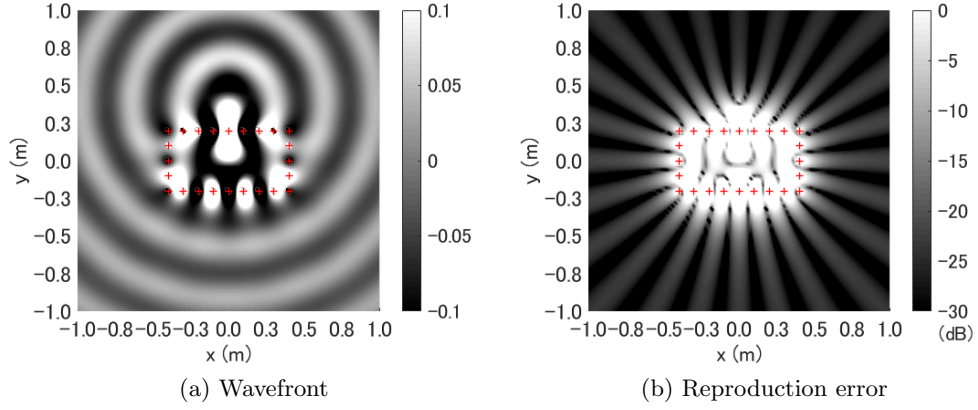


Figure 5.4: Focused source reproduced by a rectangular loudspeaker array of 24 loudspeakers.

rectional focused-source was reproduced at (0 m, 0.4 m) and 1000 Hz ($k \approx 18.48$ and $q \approx 11.74$). The MFE order was truncated at 11. The L2 regularisation parameter was set to $\lambda = \sigma_{\max}(\mathbf{\Gamma}^H \mathbf{\Gamma}) \times 10^{-6}$ as well. Figure 5.4 displays the results. The figure shows the wavefronts and reproduction error in a $2 \text{ m} \times 2 \text{ m}$ sound field. Since exterior sound field reproduction matches the coefficient at infinity, the proposed method has results similar to the circular-harmonic-expansion-based method. Considering that there would be minor applications only, further discussion on exterior sound field reproduction using an arbitrarily shaped array is omitted.

5.5 Summary

In this chapter, a general MFE-based method was proposed for sound field reproduction. The method extended the MFE-based method for ELAs, which was proposed in the previous chapter, to a method that can be implemented for arbitrary-shaped arrays. An appropriate truncation order for MFE was further proposed.

Numerical simulations were conducted on interior sound field reproduction and exterior sound field reproduction. The method was implemented for rectangular arrays. For interior sound field reproduction, the results showed that the method inherited the asymmetric properties of the ELA methods. The method can output an elliptical listening area, which is considered suitable for situations such as multiple listeners sitting on a long sofa. For exterior sound field reproduction, the results showed little difference compared with conventional methods; the application is limited for exterior sound field reproduction.

Chapter 6

Conclusion

The objective of this study was to find a system that comes with a flexible loudspeaker arrangement and available analytical methods so as to diversify the spatial control technique. In spatial control, the control method as well as the configuration of the loudspeaker array are both extremely important. Although it is possible to employ an environment-optimised method, or even an optimised array geometry to achieve high performance, the methods lack robustness in different environments. In contrast, analytical control methods, which are based on physical properties, provide predictable results and are versatile for implementations; however, these methods suffer from limited array geometries. To provide a system that addresses the trade-off between flexibility of loudspeaker arrangement and the method analyticity, the study proposed novel complex array geometries that can be controlled using analytical methods. Aiming at diversifying the sound field, two array models are discussed: multiple circular loudspeaker array (MCLA) and elliptical loudspeaker array (ELA). MCLA contains multiple conventional CLAs with their centre shifted, and it introduces a multiple scattering effect to the sound field. An analytical control method is proposed by shifting coordinate origins with an addition theorem, while taking the multiple scattering effect into consideration. ELA, in contrast, can be defined in an elliptical coordinate system. Its analytical control method is proposed by using the wave function in the elliptical coordinate system, namely, the Mathieu function. Furthermore, this study establishes the MFE (or elliptical harmonic) domain method, which has been hardly explored in the spatial control literature. Not only do the proposed arrays increase the flexibility of loudspeaker arrangement, the overall results show that these arrays outperform the conventional arrays under certain conditions owing to the physics of the design. Examples include the following: MCLA, which can perform as well as a CLA in the same size, is a distributed array model and benefits in the loudspeaker setting in space; ELA can perform an elliptical listening area in interior sound field reproduction, which would be better for a multiple listener condition. Additionally, as a result of the comparison of the proposed array geometry with those of conventional arrays, some key features were established for the design of an ideal array with physical configuration applicable to general spatial control.

The contents of each chapter are summarised as follows.

In Chapter 1, the background, the motivation, and the structure of the study were presented.

In Chapter 2, basic theories of spatial control were introduced. Conventional methods including wave field synthesis, the inverse-filter-based method, and the wave domain method were explained. The three main topics discussed in this study, namely, interior sound field reproduction, exterior sound field reproduc-

tion, and beamforming were introduced along with the evaluation methods used for later chapters.

In Chapter 3, the MCLA model and its analytical method for spatial control that considers the multiple scattering effect were proposed. The proposed method transforms sound field coefficients to different coordinate systems in the wave domain using the additional theorem of Bessel and Hankel functions. The analysis of the harmonic mode of 2CLA demonstrated its potential for reproducing complex sound fields. The results of the numerical simulations demonstrated that:

- The proposed method solves the issue of the multiple scattering effect error introduced by conventional interior sound field reproduction methods.
- MCLA and especially 2CLA of the proposed method outperform conventional CLA at low frequencies both for exterior sound field reproduction and beamforming.
- Instead of the array shape, the array length and array-source distance are likely to be the two main factors affecting the exterior sound field reproduction, whereas the array length is also important in beamforming.

Chapter 3 contributes to spatial control technique an analytical method that considered multiple scattering effect. The multiple scattering effect has been discussed frequently in acoustics studies whereas was incorrectly omitted in spatial control techniques so far. Although the multiple scattering does not exhibit a positive effect on spatial control, it is necessary to be considered during processing as it exists in real environments if the CLAs are acoustically rigid. The proposed method not only provides a tool for the investigations on MCLAs, but also promotes further studies including multiple scattering effect. A recent study on multiple rigid spherical microphone array [97] can be considered as an example.

In Chapter 4, the ELA model was proposed with an elliptical coordinate system. MFE was introduced and a novel wave-domain sound field reproduction method based on MFE was proposed. In addition, another MFE-based method for conventional circular microphone arrays was proposed. Further study of the mode strength revealed that ELA has the potential to reproduce complex sound fields. The results of the numerical simulations were:

- For interior sound field reproduction, the proposed method produces an elliptical listening area whereas the conventional method produces a circular listening area.
- For both exterior sound field reproduction and beamforming, the ELA performance is highly similar to that of 2CLA for the same length and width of the array, implying that the size of the outer contour of an array is more determinative than the array shape. Both proposed array models demonstrate better control efficiencies compared with conventional CLA and LLA.
- The axis lengths of the ELA have a significant influence on the performance of exterior sound field reproduction and beamforming, whereas flattening has little effect if the size of the ELA is fixed.

Overall, the array asymmetry of ELA produces a direction dependent performance; furthermore, extending the length of the array even in one dimension may help improve the performance.

Chapter 4 contributes a new theory for spatial control based on elliptical coordinate system. The use of elliptical coordinate system and eigenfunctions of Helmholtz equation in the coordinate system (i.e. Mathieu functions) has been missing so far in the literature of spatial control. Proposed methods provide analytical solutions on elliptical arrays, which have a great business potential on car audios, smart speakers, etc. Furthermore, the approach in this chapter also encourages the use of other orthogonal coordinate systems including a parabolic coordinate system, bi-polar coordinate system, etc. Recently, a spatial control method based on the three-dimensional spheroid coordinate systems was reported [98].

In Chapter 5, a general MFE-based method was proposed for arbitrary-shaped arrays. In addition, an appropriate truncation order was determined for MFE. The numerical simulations were carried out on rectangular arrays. For interior sound field reproduction, the proposed method produces an elliptical listening area. The method is considered practicable for applications such as home audio systems.

Chapter 5 further contributes to the development of the possibilities of MFE. Showing equivalent properties as using an ELA, the proposed general MFE-based method provides an interface for acquiring the desirable features of MFE on existing audio systems.

In summary, this study shares a novel approach on enhancing the spatial control technique. Conventional studies either focus on an optimal system with specific conditions or retain the use of common basic arrays. The approach in this work, i.e., to propose new complex array geometries that are analytically controllable, meets halfway in that the proposed systems contain advanced but not optimised array geometry. However, it is believed that such a system would provide improved performance in most cases. Throughout this thesis, the possibility of designing such a system is discussed.

The study is expected to make extensions, e.g., detailed discussion on array geometry, implementation with three-dimensional-field compensation, or a three-dimensional theory, to provide an advanced spatial control technique. With the advanced technique, future applications including 3D communication system, 3D television, virtual live concert, etc., become possibilities. In addition, this study can accelerate further development of other irregular arrays that are effective and versatile. As a reference for designing new arrays, it can be inferred from this study that a large-scale array can be designed without obvious multiple scattering effect for spatial control such that the array stretched in one direction features asymmetry, and stretching in the direction perpendicular to the controlling direction (i.e., the direction of the primary source or the target beam) can result in advanced performance. The proposed acoustical methods of this study also share numerous commonalities with studies on other waves, e.g., electromagnetic waves and are expected to have further utilisation in the study of sensor networks or antenna at large.

Appendix A

Spectral Division Method

This appendix explains the theory of the spectral division method (SDM) [43] in two-dimensional fields, which was implemented for LLAs in Chapter 4.

As explained in Sec. 2.2, a plane wave decomposition can describe sound fields in the wavenumber domain. Instead of fixing y to 0 as in (2.23), a sound field can be described as

$$p(x, y, \omega) = \frac{1}{2\pi} \int_{-\infty}^{\infty} \tilde{p}(k_x, y, \omega) e^{-jk_x x} dk_x. \quad (\text{A.1})$$

$\tilde{p}(k_x, y, \omega)$ here can be considered as the wave spectrum of $p(x, y, \omega)$.

Considering the secondary source distribution to be a continuous infinite-length linear array on $x = 0$ and assuming that the sources are monopoles, the secondary sound field can be described as

$$\hat{p}(\mathbf{x}, \omega) = \int_{-\infty}^{\infty} G(\mathbf{x}|\mathbf{x}_0, \omega) d(\mathbf{x}_0, \omega) dx_0, \quad (\text{A.2})$$

where $G(\mathbf{x}|\mathbf{x}_0, \omega)$ is the Green function in the free field and $d(\mathbf{x}_0, \omega)$ is the driving function for the source located at \mathbf{x}_0 . As the Green function between \mathbf{x} and \mathbf{x}_0 in (2.12) is determined by the subtraction $(\mathbf{x} - \mathbf{x}_0)$, the transfer function can be rewritten as:

$$\hat{p}(\mathbf{x}, \omega) = \int_{-\infty}^{\infty} G(\mathbf{x} - \mathbf{x}_0, \omega) d(\mathbf{x}_0, \omega) dx_0. \quad (\text{A.3})$$

The right side of the equation can then be considered a convolution: a multiplication in the wavenumber domain after a spatial Fourier transform. Thus, we have

$$\tilde{\hat{p}}(k_x, y, \omega) = \tilde{G}(k_x, y, \omega) \tilde{d}(k_x, \omega). \quad (\text{A.4})$$

By matching the spectra of the first and secondary sound field along the line $y = y_{\text{REF}}$, the $\tilde{d}(k_x, \omega)$ can be obtained by a division:

$$\tilde{d}(k_x, \omega) = \frac{\tilde{\hat{p}}(k_x, y_{\text{REF}}, \omega)}{\tilde{G}(k_x, y_{\text{REF}}, \omega)}. \quad (\text{A.5})$$

This step determines the name of the method: a spectra division. Note that if no source exists in $y \geq y_{\text{REF}}$ ($y_{\text{REF}} \geq 0$ is assumed for simplicity), the sound field in $y \geq y_{\text{REF}}$ is automatically reproduced once the spectra match at $y = y_{\text{REF}}$ (according to the Kirchhoff-Helmholtz integral equation). Finally, the driving function is obtained by applying a spatial inverse Fourier transform to $\tilde{d}(k_x, \omega)$:

$$d(x, \omega) = \frac{1}{2\pi} \int_{-\infty}^{\infty} \frac{\tilde{\hat{p}}(k_x, y_0, \omega)}{\tilde{G}(k_x, y_0, \omega)} e^{-jk_x x} dk_x. \quad (\text{A.6})$$

In practice, the use of a discrete linear array requires discretisation. Thus, instead of the continuous spatial Fourier transform, a discrete spatial Fourier transform is applied in the method. With N equally spaced samples at intervals of Δx , the discrete spatial Fourier transform can be written as [46]

$$\tilde{f}(2\pi m/L) \approx \Delta x \sum_{q=-N/2}^{N/2-1} f(q\Delta x) e^{-j2\pi m q/N}, \quad (\text{A.7})$$

where $m = -N/2, -N/2 + 1, \dots, N/2 - 1$. The discrete spatial inverse Fourier transform can be written as [46]

$$f(q\Delta x) \approx \frac{1}{N\Delta x} \sum_{m=-N/2}^{N/2-1} \tilde{f}(2\pi m/L) e^{j2\pi m q/N}. \quad (\text{A.8})$$

Substituting the continuous transforms with the discrete transforms for both first and secondary sound field, the discretised SDM can be easily obtained (the details are omitted here).

Appendix B

Exterior Multi-zone Reproduction

In general, exterior sound field reproduction faces accuracy issues when reproducing complete exterior fields, especially when reproducing focused sources. The results in Chapters 2-4 show that the reproduction accuracy is low when reproducing focused sources (compared with the results of interior sound field reproduction). The main reason for this difficulty is that reproducing global exterior fields typically requires higher-order calculations. Boundaries limit interior areas as well as the number of secondary sources because loudspeakers typically require a certain volume of air. This limitation reduces the maximum number of orders that can be reproduced.

The results of focused source reproduction show that the reproduction accuracy is not uniformly distributed over the control region. In addition, focused source reproduction using wave field synthesis yields a triangular listening area [44, 49]. In contrast, focusing the controlling efforts to a specific sub-region, instead of the whole control region, should result in higher reproduction accuracy. In sound field reproduction, the reproduction of selected regions instead of the full region is a major topic referred to as multi-zone reproduction. However, the conventional multi-zone reproduction studies were discussed on interior sound field reproduction only. In this chapter, a CHE-based multi-zone reproduction method for exterior sound field reproduction is proposed.

B.1 Conventional studies

A well-known technique named multi-zone reproduction has been studied over the years [99–104]. The original idea of multi-zone reproduction is to present multiple individual sound fields at the target areas. This can realise private sound zones where listeners can perceive their private sounds without interference from others.

The multi-zone reproduction methods are proposed for interior sound field reproduction (there are also methods for linear arrays). The methods define multiple small control regions inside a global interior field. While general interior sound field methods set a target global interior field, the multi-zone reproduction methods set multiple target fields of small control regions, and then transfer them to a mixed global field. The methods proposed are based mainly on two approaches: the inverse-filter-based approach and the wave domain approach (similar to the conventional sound field reproduction methods introduced in Chapter 2). Note that the wave domain approach uses an addition theorem to convert the offset expansion basis (of the small control regions) to the global expansion basis (of the global interior field).

It has been reported [100, 102] that these methods can achieve a high sound-contrast between the bright-zone, i.e., the listening area and the dark-zone or

quiet-zone. It has also been reported that the methods can improve the reproduction accuracy of the small control regions because the general methods, especially the wave domain methods, have subpar performance at positions far from the centre of the sound field. Multi-zone reproduction methods are expected to provide high performance at each control region.

B.2 Proposed Method

Inspired by conventional multi-zone reproduction studies [99–103], a ‘multi-zone reproduction’ method is proposed in this study for exterior sound field reproduction. As the main purpose of this chapter is to improve the performance in specific local areas, the method is introduced as a local exterior sound field reproduction technique. The main concept of the method is to sacrifice the size of the listening area to achieve higher reproduction accuracy. Rather than reproducing an entire exterior sound field, local interior listening areas are defined. The main method for multi-zone reproduction is to choose multiple areas and reproduce an offset sound field, where both the global field and the local fields are interior, i.e., incident fields. In contrast, in this method, small local areas selected from a global exterior field are considered as interior fields. This results in differences in the transformation of the sound field coefficient such that the basis expressed as a Hankel function is transformed into a basis of Bessel functions.

Figure B.1 presents a basic model of this problem. Multiple local circular areas are defined inside a global exterior field. In the \mathbf{a} -th local area, the primary field is propagating inward and therefore can be expressed as

$$p(\mathbf{x}_a, \omega) = \sum_{\nu=-\infty}^{\infty} \check{p}_{\nu, \mathbf{a}}^{\leftarrow}(k) J_{\nu}(kr_a) e^{j\nu\phi_a}, \quad (\text{B.1})$$

where $\check{p}_{\nu, \mathbf{a}}^{\leftarrow}(k)$ is the local sound field coefficient in the \mathbf{a} -th area. Similarly, the secondary field, which is also an incident field, can be expanded as

$$\hat{p}(\mathbf{x}_a, \omega) = \sum_{\nu=-\infty}^{\infty} \check{p}_{\nu, \mathbf{a}}^{\leftarrow}(k) J_{\nu}(kr_a) e^{j\nu\phi_a}. \quad (\text{B.2})$$

However, if the same sound pressure is being observed in the global field, then the field is propagating outward and thus is described by

$$\hat{p}(\mathbf{x}, \omega) = \sum_{\mu=-\infty}^{\infty} \check{p}_{\mu}^{\rightarrow}(k) H_{\mu}^{(2)}(kr) e^{j\mu\phi}. \quad (\text{B.3})$$

Note that the secondary sound field is a reproduced field by secondary sources:

$$\hat{p}(\mathbf{x}, \omega) = \sum_{l=1}^L G(\mathbf{x}|\mathbf{x}_l, \omega) d_l(\omega), \quad (\text{B.4})$$

which implies that the sound field coefficient of the secondary field is a function of the driving functions. Let θ be a function of the driving functions and

$$\theta_{\mu}(\mathbf{d}, k) = \check{p}_{\mu}^{\rightarrow}(k), \quad (\text{B.5})$$

where

$$\mathbf{d} = [d_1(\omega), \dots, d_L(\omega)]^T. \quad (\text{B.6})$$

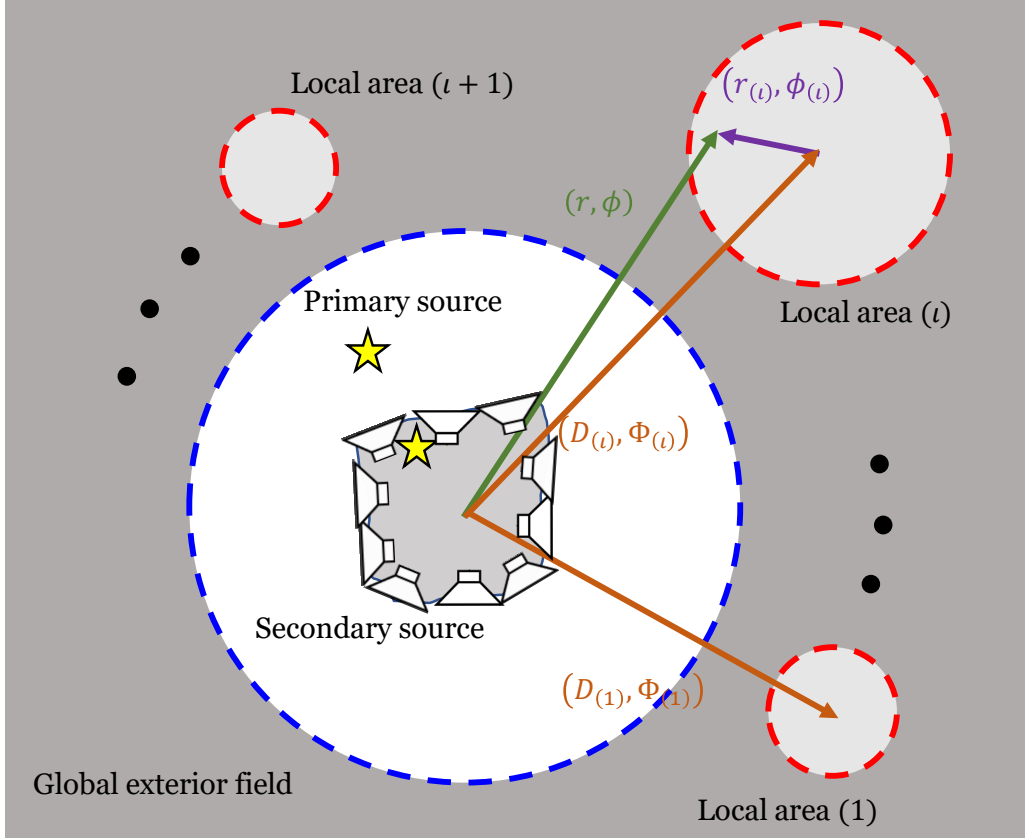


Figure B.1: Model of exterior sound field reproduction. The conventional method reproduces the sound field outside the blue dotted circle and the proposed method reproduces the sound field inside the red dotted circle. Stars represent primary sources and loudspeakers represent secondary sources. The a -th local area is located at (R_a, Φ_a) . $\mathbf{x} = (r, \phi)$ and $\mathbf{x}_a = (r_a, \phi_a)$ are the coordinates of the centre of the global sound field and the a -th local area, respectively.

Next, Graf's addition theorem is applied [78].

$$H_\mu^{(2)}(kr)e^{j\mu\phi} = \sum_{\nu=-\infty}^{\infty} T_{\nu,\mu,a}(k)J_\nu(kr_a)e^{j\nu\phi_a}, \quad (\text{B.7})$$

where

$$T_{\nu,\mu,a}(k) = H_{\mu-\nu}^{(2)}(kR_a)e^{j(\mu-\nu)\Phi_a}, \quad (\text{B.8})$$

to (B.3), which yields

$$\hat{p}(\mathbf{x}_a, \omega) = \sum_{\nu=-\infty}^{\infty} \sum_{\mu=-\infty}^{\infty} T_{\nu,\mu,a}(k)\theta_\mu(\mathbf{d}, k)J_\nu(kr_a)e^{j\nu\phi_a}. \quad (\text{B.9})$$

The condition of Graf's addition theorem $R_a > r_a$ is initially satisfied in the proposed model. When comparing (B.9) to (B.2), based on the orthogonality of the circular harmonics $e^{j\nu\phi}$, we have

$$\check{p}_{\nu,a}^{\leftarrow}(k) = \sum_{\mu=-\infty}^{\infty} T_{\nu,\mu,a}(k)\theta_\mu(\mathbf{d}, k) = \sum_{\mu=-\infty}^{\infty} T_{\nu,\mu,a}(k)\check{p}_\mu^{\rightarrow}(k). \quad (\text{B.10})$$

Multi-zone reproduction studies [100] also use Graf's addition theorem to divide sound fields into small regions (from a large interior field into small interior

fields). By contrast, in the proposed method, the original field is an exterior field, meaning not only should the field be divided, but also transformed into interior fields i.e., a transformation from the Hankel function to the Bessel function.

By matching the coefficients in (B.1) and (B.2), similar to the conventional mode-matching method,

$$\Theta_{\mathbf{d}} = \left[[\mathbf{T}_1^T, \mathbf{T}_2^T, \dots, \mathbf{T}_A^T]^T \right]^\dagger [\check{\mathbf{p}}_1^T, \check{\mathbf{p}}_2^T, \dots, \check{\mathbf{p}}_A^T]^T, \quad (\text{B.11})$$

where † is the pseudo-inverse matrix and

$$\Theta_{\mathbf{d}} = [\theta_{-M}(\mathbf{d}, k), \theta_{-M+1}(\mathbf{d}, k), \dots, \theta_M(\mathbf{d}, k)]^T, \quad (\text{B.12})$$

$$\mathbf{T}_{\mathbf{a}} = \begin{bmatrix} T_{-N_{\mathbf{a}}, -M, \mathbf{a}}(k) & T_{-N_{\mathbf{a}}, -M+1, \mathbf{a}}(k) & \dots & T_{-N_{\mathbf{a}}, M, \mathbf{a}}(k) \\ T_{-N_{\mathbf{a}}+1, -M, \mathbf{a}}(k) & T_{-N_{\mathbf{a}}+1, -M+1, \mathbf{a}}(k) & \dots & T_{-N_{\mathbf{a}}+1, M, \mathbf{a}}(k) \\ \vdots & \vdots & \ddots & \vdots \\ T_{N_{\mathbf{a}}, -M, \mathbf{a}}(k) & T_{N_{\mathbf{a}}, -M+1, \mathbf{a}}(k) & \dots & T_{N_{\mathbf{a}}, M, \mathbf{a}}(k) \end{bmatrix}, \quad (\text{B.13})$$

$$\check{\mathbf{p}}_{\mathbf{a}} = [\check{p}_{-N_{\mathbf{a}}, \mathbf{a}}^{\check{<}}(k), \check{p}_{-N_{\mathbf{a}}+1, \mathbf{a}}^{\check{<}}(k), \dots, \check{p}_{N_{\mathbf{a}}, \mathbf{a}}^{\check{<}}(k)]^T. \quad (\text{B.14})$$

The infinite series are truncated based on the truncation order of the local areas $N_{\mathbf{a}}$ and the truncation order of the global secondary sound field M . Instead of calculating a pseudo-inverse matrix, a least-squares method with regularisation can be applied to avoid the singular matrix problem and indirectly control the gain of the driving function. After all, the driving function \mathbf{d} can be derived from $\Theta_{\mathbf{d}}$. If the secondary source is a circular loudspeaker array, the driving function can be easily derived by

$$d_l(\omega) = \sum_{\mu=-M}^M \frac{\theta_{\mu}(\mathbf{d}, k)}{\mathcal{L}\check{G}_{\mu}(k)} e^{j\mu\phi_l}, \quad (\text{B.15})$$

where $d_l(\omega)$ is the driving function of the l -th loudspeaker, $\check{G}_{\mu}(k)$ is the same one in (2.59).

B.3 Limitations

Area size

Similar to studies on multi-zone reproduction for interior sound fields [100], the controllable area is limited by the truncation order $N_{\mathbf{a}}$. The error in the local areas is sufficiently small if

$$N_{\mathbf{a}} = \left\lceil \frac{ekR_{\mathbf{a}}}{2} \right\rceil \quad (\text{B.16})$$

is satisfied [96]. Therefore, the size of the control areas can be adjusted by selecting the truncation orders for each area. Additionally, the truncation orders should satisfy the following condition determined by the flexibility of the secondary sources:

$$\sum_{\mathbf{a}=1}^A N_{\mathbf{a}} \leq M \leq \left\lfloor \frac{\mathcal{L}-1}{2} \right\rfloor. \quad (\text{B.17})$$

Irreproducible sound fields

In the global exterior sound field reproduction method described in Sec. 2.5.2, there is a boundary surface that covers the primary and secondary sources. The control region is the exterior space of the boundary, where the Fresnel-Kirchhoff integral theorem [49] is satisfied i.e., all sources are on one side of the boundary. This further signifies that the sound field in the control region is theoretically reproducible.

In the proposed method, however, the control region is the interior spaces of the local areas. For each local area, both the primary and secondary sources are initially located outside the boundary of the area. According to the Fresnel-Kirchhoff integral theorem, any primary sound field can be reproduced, but there are still limitations. Secondary sources cannot fully control the sound pressure at the boundaries of local areas because they are in a limited direction range of each local area.

$$\check{p}_{\nu,a}^{\check{\Delta}}(k) = \int_{\Phi_a - \Delta\Phi}^{\Phi_a + \Delta\Phi} \sum_{\nu=-\infty}^{\infty} A_{\nu}(k) e^{j\nu\phi} d\phi, \quad (\text{B.18})$$

where $\Delta\Phi < \pi/2$ and $A_{\nu}(k)$ does not include directional components. This indicates that if the $\check{p}_{\nu,a}^{\check{\Delta}}(k)$ includes components in directions outside the range of the integral in (B.18), then the sound field can be difficult to reproduce using secondary sources e.g., the primary sound field of a source arriving from $(2\pi - \Phi_a)$.

B.4 Results

Simulations were conducted on reproducing different primary sound fields in individual zones (multiple listeners can hear different sounds simultaneously). The results are discussed in terms of bright-zone/dark-zone reproduction.

Here, three individual primary fields were defined for three local areas centred at $(1 \text{ m}, 0)$, $(1 \text{ m}, \pi/2)$, and $(1 \text{ m}, -\pi/2)$. The truncation order of the fields was set to four. The primary fields in the local areas are presented in Fig. B.2(a), where the first field is the field of a focused source located at $(0.5 \text{ m}, \pi/2)$; the second field is a zero field used for generating the dark zone; and the last field is a field of six random sources with random amplitudes and phases located inside a circle of radius $r = 0.5 \text{ m}$ (within the limitations described in Section B.3). All sources have frequencies of 1000 Hz. The local sound field coefficient of the focused source can be derived as

$$\check{p}_{\nu,a}^{\check{\Delta}}(k) = -\frac{j}{4} H_{\nu}^{(2)}(kr_{s,a}) e^{-j\nu\phi_{s,a}}, \quad (\text{B.19})$$

where $(r_{s,a}, \phi_{s,a})$ are the coordinates of the source in the \mathbf{a} -th coordinate system.

A rigid circular loudspeaker array was used at the centre of the global sound field as a secondary source. Thirty loudspeakers were equiangularly mounted on a rigid circular surface with a radius of 0.15 m. A focused source at 1000 Hz was placed at $(0.5 \text{ m}, \pi/2)$ in the global coordinate system. The truncation order for both the conventional and proposed methods was $M = \lfloor (L - 1)/2 \rfloor = 14$. The two local areas selected were centred at $(1 \text{ m}, 0)$ and $(1 \text{ m}, \pi/2)$, where the conventional method displays relatively poor and fair reproduction accuracy, respectively. The truncation orders of the two areas were set to $N_1 = 3$ and $N_2 = 5$. Both methods were implemented using the least-squares method with Tikhonov regularisation, which suppresses the gain of the driving function under 0 dB to avoid distortion on the loudspeakers.

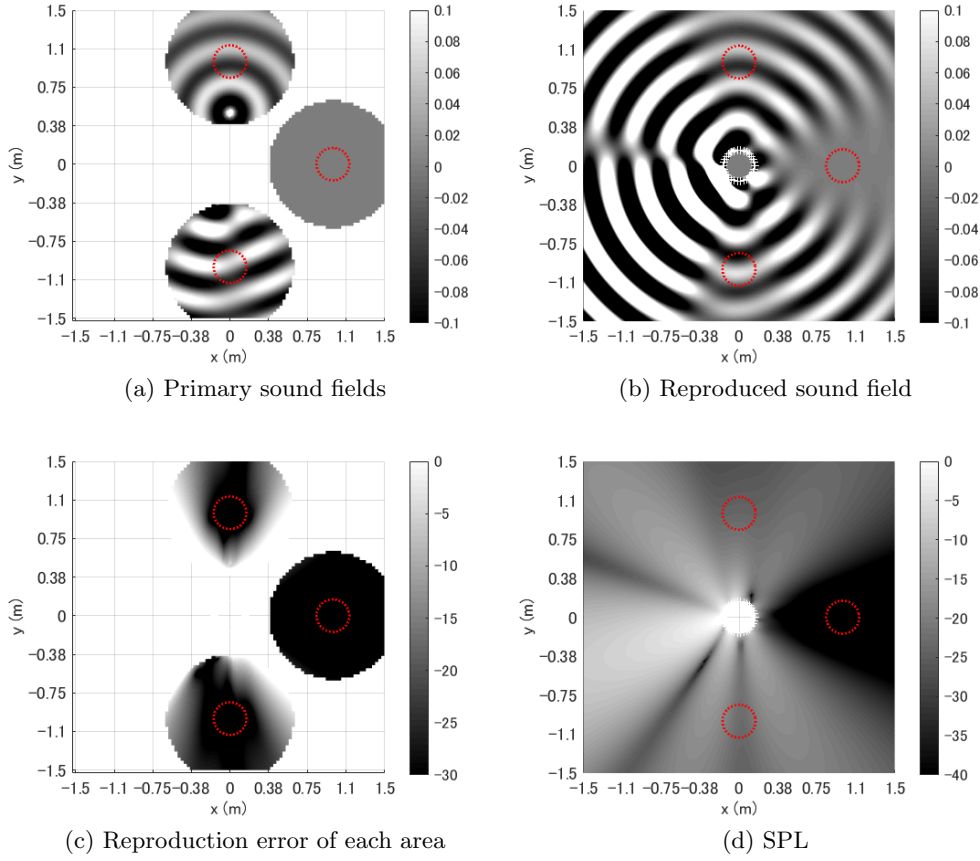


Figure B.2: Results of multi-zone reproduction. The interior areas in the red dotted circles represent the controlling areas. White crosses indicate the locations of secondary sources.

Figure. B.2 presents the results for a 3×3 m² sound field, where (a) is the target primary sound field, (b) is the reproduced sound field, (c) is the reproduction error of (b), and (d) is the sound pressure level (SPL) in the reproduced sound field. The reproduction error is -37.56 dB in the first area and -35.88 dB in the third area. The reproduction error of a zero field cannot be calculated, hence, the SPL of the second area is displayed instead in Fig. B.2(c), showing a great contrast between the bright and dark zones. These results demonstrate the validity of the proposed method for exterior multi-zone reproduction.

Appendix C

Mathieu function based multi-zone reproduction

In addition, a simple (pseudo) multi-zone reproduction can be achieved by using the MFE. Considering the harmonic shapes in Fig. 4.2, a simple mode selection was applied to MFE by using either only the lower orders or all orders except the lower orders.

The bright zone and the dark zone were generated as displayed in Figs. C.1 (a-b). The sound level in the dark zone was at least 30 dB lower than that of the bright zone. Although this system can create only a bright zone along the minor axis and dark zones on both sides, it might still be a practical example as the same system applied to a circular loudspeaker array requires higher orders in the circular harmonic expansion based method. In contrast, it is possible to generate a dark zone along the minor axis by removing the lower orders. Figures C.1 (c-d) display the results associated with this condition. The sound level in the dark (grey) zone was approximately 10 dB lower than that of the bright zone. As the centre components of modes with higher orders are much larger than the side components of modes with lower orders, it is difficult to achieve an ideal dark zone. Note that this method can reproduce plane waves in the minor axis direction only, which means that it is not exactly a multi-zone sound field reproduction method but has the ability to divide the sound field into only two listening zones. Therefore, it can be applied as a low computational cost method for ELA.

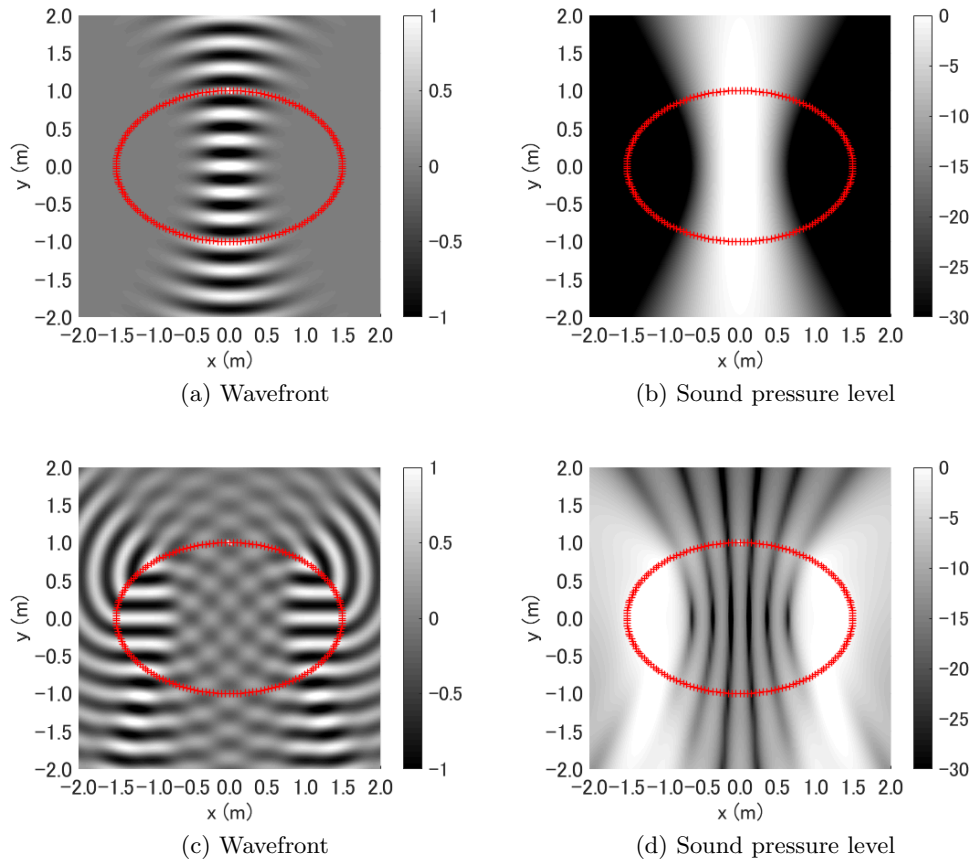


Figure C.1: Reproduced sound field of an ELA of 180 loudspeakers. The primary sound field exhibited a 1000 Hz plane wave arriving from $\phi_{//} = \pi/2$. (a-b): $|\nu| \leq 1$ were used. (c-d): $7 \leq |\nu| \leq 30$ were used.

Appendix D

Experimental results in an anechoic chamber

For the CLA and 2CLA models, loudspeaker array prototypes were built and the measurements were recorded in an anechoic room to assess the performance in real-world environments. This appendix presents the experimental results on exterior sound field reproduction and beamforming.

D.1 Loudspeaker array prototypes

Two CLA prototypes, comprising two finite-length cylindrical loudspeaker arrays, were built using a 3D printer. Both prototypes had a radius of 0.15 m, a height of 0.576 m, and were made out of plastic. Fifteen loudspeaker units (T028S23; Foster Electric Company, Ltd., Japan) were mounted equiangularly on the surface of each cylinder. The photograph of one prototype is shown in Fig. D.1. The prototypes consisted of a flat circular loudspeaker array and two (the top and bottom) transparent cylindrical baffles, which imitated the rigid CLA in two-dimensional space, i.e., an infinite-length rigid cylindrical array. Note that to construct the 2CLA model, the two prototypes are set in parallel.

D.2 Results on exterior sound field reproduction

Sound field measurement

In this study, the experimental data were recorded with a sound field measurement device. The device consisted of a double-axes actuator and a linear microphone array. The actuator can be controlled over a 100-cm-length horizontal axis and a 50-cm-height vertical axis. With a 48-channel linear microphone array (width of 94 cm and microphone spacing of 2 cm) mounted on the actuator, the device could cover a $100 \times 94 \times 50 \text{ cm}^3$ cuboid sound field. Figure D.2 shows the model of the device.

In the following experiments, a two-dimensional horizontal sound field (i.e., a $100 \times 94 \text{ cm}^2$ rectangular sound field) was measured. The impulse response of each loudspeaker was recorded with a 2-sec Log-SS signal [105]. The sampling frequency was 48000 Hz and the length of the impulse responses was 2400 samples. The spatial resolution over the sound field was 51×48 points, which means that the sound field was measured within a $2 \times 2 \text{ cm}^2$ grid. Figure D.3 presents a photograph of a setup of the measurement.

Focused source reproduction using CLA

A CLA (the prototype) was set at the centre of a reference coordinate system. The sound field in $x \in [-0.47 \text{ m}, 0.47 \text{ m}]$, $y \in [0.4 \text{ m}, 1.4 \text{ m}]$ was recorded by the device.

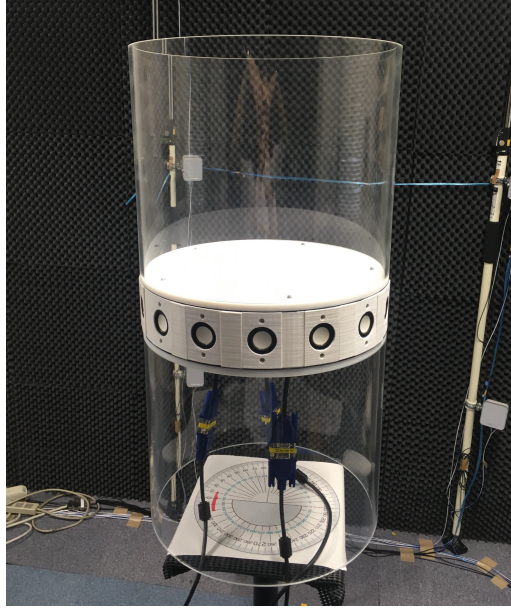


Figure D.1: Photograph of the CLA prototype.

An experiment was conducted for the conventional CHE-based method introduced in Sec. 2.5.2. The primary source was set at $\mathbf{x}_{\odot} = (r_{\odot}, \phi_{\odot}) = (0.5 \text{ m}, \pi/2)$. The target primary sound field is displayed in Fig. D.4, which was theoretically calculated for a two-dimensional free field.

In Fig. D.5, the reproduced sound field of the CLA is displayed: (a) the theoretical results in a two-dimensional free field and (b) the experimental results of the prototype in the anechoic room. The theoretical simulation was implemented on a CLA with 15 loudspeakers mounted on a 0.15 m radius circular baffle. By comparing Fig. D.5 to the target field in Fig. D.4, it is demonstrated that the CLA reproduced the sound field with obvious errors, both under theoretical and experimental conditions.

Focused source reproduction using 2CLA

Then, an experiment was conducted by using the proposed 2CLA model. In the experiment, the 2CLA was constructed by two CLA prototypes. The 2CLA was placed at $(0.25 \text{ m}, 0)$ and $(0.25 \text{ m}, \pi)$. The same part of the sound field was recorded by the device. The proposed method in Sec. 3.3 was implemented for the experiment, reproducing the primary source of the previous experiment.

In Fig. D.6 the reproduced sound field of the 2CLA is displayed: (a) the theoretical results and (b) the experimental results. The theoretical simulation was implemented on a 2CLA model with the same settings of the prototype. Comparisons with the target field and the results of the CLA indicate that 2CLA has improved reproduction (the 2CLA reproduced a focus-like point while the CLA did not). The results of the experiment are similar to the theoretical one, which means that the proposed method can be implemented in real three-dimensional environments. However, it should be noted that mismatches in three-dimensional attenuation can result in errors, in particular amplitude errors.

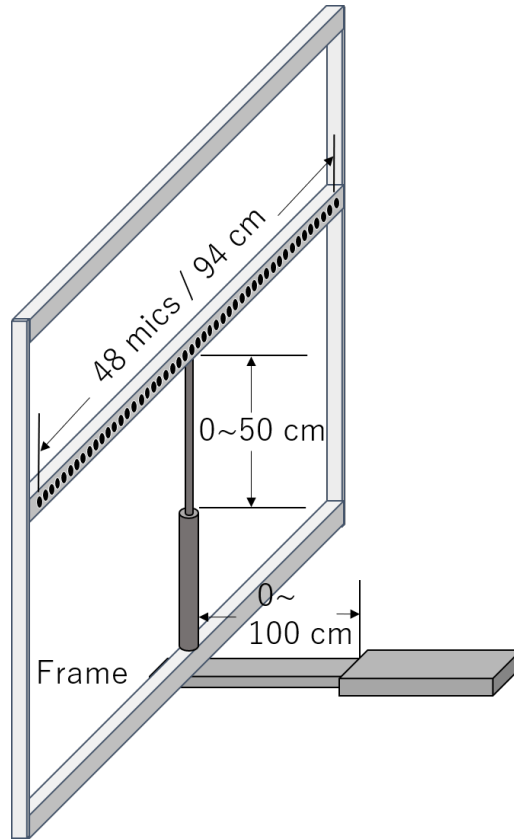


Figure D.2: The model of the sound field measurement device.



Figure D.3: Photograph of sound field measurement setup.

Local sound field reproduction using CLA

Experiments were also conducted on local sound field reproduction method of Sec. B.2. A CLA (the prototype) was set at the centre of the sound field. The sound field in $x \in [-0.47 \text{ m}, 0.47 \text{ m}]$, $y \in [0.4 \text{ m}, 1.4 \text{ m}]$ was recorded by the device.

The primary sound field was the same as that of Fig. D.4. One local area was set at $(1 \text{ m}, \pi/2)$ and the primary source was located at $(0.5 \text{ m}, \pi/2)$. Figure D.7 presents (a) the theoretical simulation results for a two-dimensional field and (b) the results of our experiments. Both theoretical and experimental results indicate that the proposed local sound field reproduction method reproduces sound fields with higher accuracy (as indicated by the curvature of the wavefront)

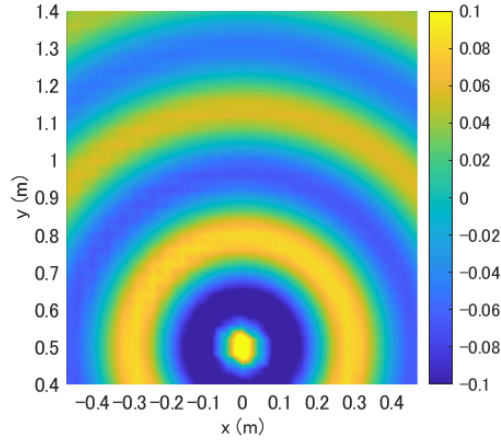


Figure D.4: Theoretical two-dimensional primary sound field of a source located at $(0.5 \text{ m}, \pi/2)$.

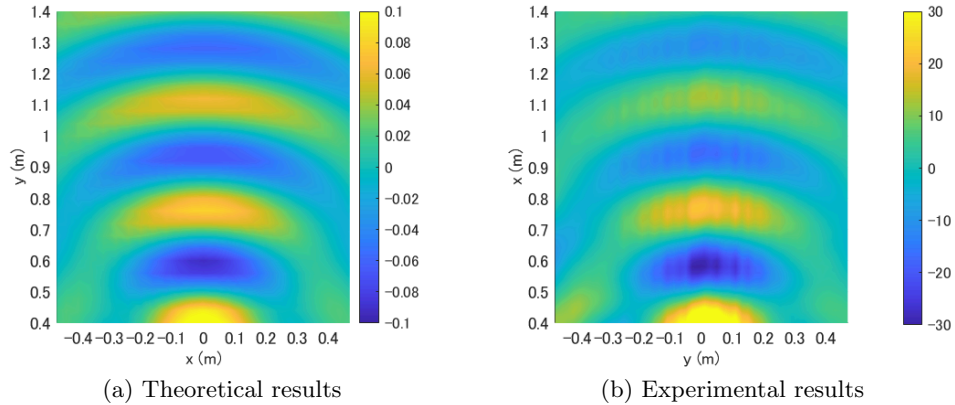


Figure D.5: Focused source reproduced by a CLA using the conventional CHE-based method.

than the global sound field reproduction method of Fig. D.5. The theoretical and experimental results matched with minor errors for the local sound field reproduction method.

D.3 Results on beamforming

In beamforming, the impulse response of the prototype was recorded in an anechoic chamber. Instead of the entire sound field, the directivity pattern on a circular boundary was measured. The setup consisted of 48 microphones over a 120° curve of a 1.5 m radius circle at the centre of the sound field. The microphones were set at every 2.5° , and the measurements were repeated three times to cover a full circle. The centres of the two cylinders were set at $(0.25 \text{ m}, 0)$ and $(0.25 \text{ m}, \pi)$. The loudspeakers and the microphones were set to the same height. Fig. D.8 shows a photograph taken during the measurements. Note that 2CLA was rotated about the centre of the sound field to finish the recording of the measurements, thereby creating the possibility of spatial errors. Furthermore, despite performing a simple calibration of the microphone amplifiers, the results may still contain errors.

After the measurements, the transfer functions of single frequencies were ex-

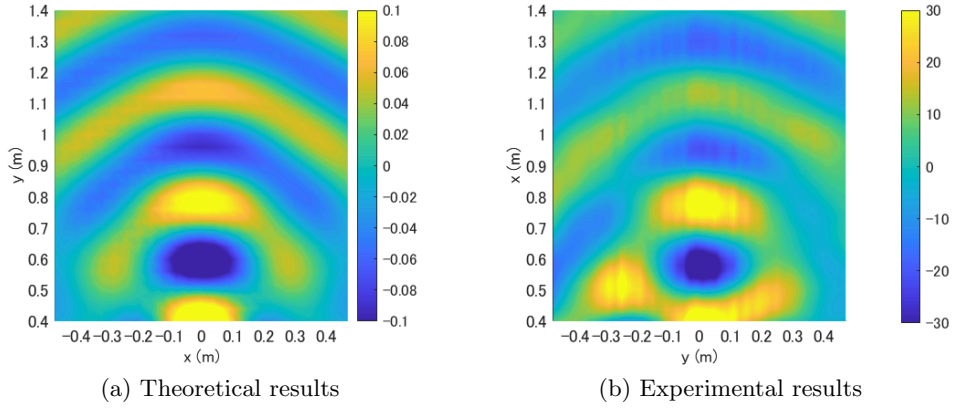


Figure D.6: Focused source reproduced by a 2CLA using the proposed method.

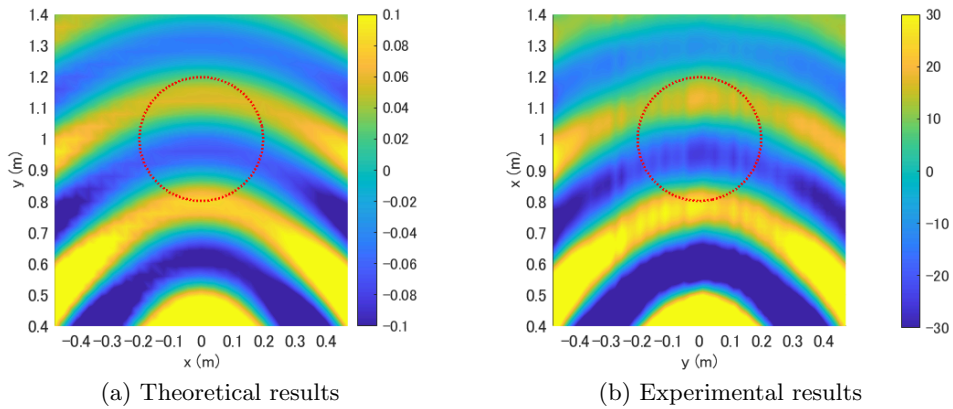


Figure D.7: Focused source reproduced by a CLA using the local sound field reproduction method. The red dotted circles represent the control areas of the proposed method.

tracted from the impulse response and another simulation was conducted on the experimental data. In this simulation, the filters were calculated using the real transfer functions of the prototype. The MVDR beamformer with Tikhonov regularisation was used. The $48 \times 3 = 144$ microphones were set as the constrained point and the suppression points. The sound pressure of the constrained point and the filter suppression were set as in Sec. 3.7, while the radius r was 1.5 m. To compare with the results of the theoretical transfer functions, the transfer functions of the prototype were normalised by the maximum values and divided by $4\pi(r - 0.4 \text{ m})$ for distance attenuation (where $r - 0.4 \text{ m}$ is the distance between the microphone and the closest loudspeaker). The theoretical results were obtained under the same simulation conditions as those of the two-dimensional theoretical transfer functions. Simulations were performed at 500 Hz, 1000 Hz, 2000 Hz, and 4000 Hz in the 0° and 90° look directions.

The directivity patterns for the experimental and theoretical results are displayed in Figs. D.9 and D.10. In Fig. D.9, there are some errors near 0° at 500 Hz and 1000 Hz, attributed to possible spatial errors resulting from multiple measurements. Overall, the performance of the prototype matches the theoretical one approximately, despite finite cylinder length and mismatched attenuation. The results indicate that the proposed method can deliver desirable beams with



Figure D.8: A photograph of the directivity measurement.

a quasi-2CLA system in three-dimensional sound fields.

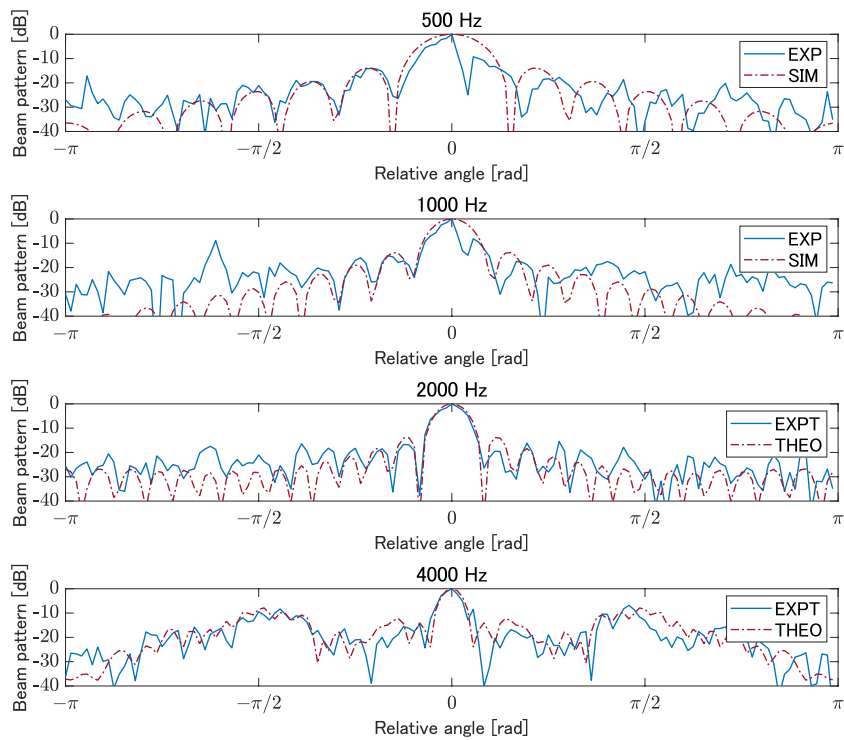


Figure D.9: Beam patterns of experimental data in the 0° look direction. EXPT: experimental results using impulse responses of the prototype; THEO: theoretical results using transfer functions of 2CLA. The angle on the horizontal axis is relative to the look direction.

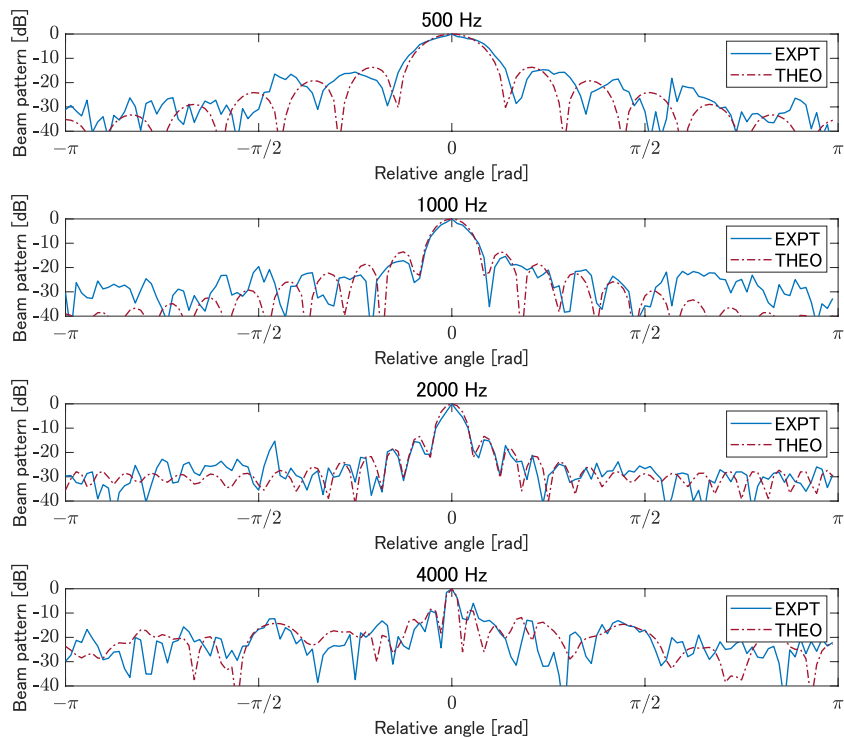


Figure D.10: Beam patterns of experimental data in 90° look direction. EXPT: experimental results using impulse responses of the prototype; THEO: theoretical results using transfer functions of 2CLA. The angle on the horizontal axis is relative to the look direction.

References

- [1] M. Camras, “Approach to recreating a sound field,” *J. Acoust. Soc. Am.*, vol. 43, no. 6, pp. 1425–1431, 1968.
- [2] A. J. Berkhout, “A holographic approach to acoustic control,” *J. Audio Eng. Soc.*, vol. 36, no. 12, pp. 977–995, 1988.
- [3] A. J. Berkhout, D. de Vries, and P. Vogel, “Acoustic control by wave field synthesis,” *J. Acoust. Soc. Am.*, vol. 93, no. 5, pp. 2764–2778, 1993.
- [4] M. A. Gerzon, “Periphony: With-height sound reproduction,” *J. Audio Eng. Soc.*, vol. 21, no. 1, pp. 2–10, 1973.
- [5] J. Daniel, “Spatial sound encoding including near field effect: Introducing distance coding filters and a viable, new ambisonic format,” in *Proc. 23rd Int. Conf. Audio Eng. Soc.: Signal Processing in Audio Recording and Reproduction*, 2003.
- [6] J. Flanagan, J. Johnston, R. Zahn, and G. Elko, “Computer-steered microphone arrays for sound transduction in large rooms,” *J. Acoust. Soc. Am.*, vol. 78, no. 5, pp. 1508–1518, 1985.
- [7] B. D. Van Veen and K. M. Buckley, “Beamforming: A versatile approach to spatial filtering,” *IEEE assp magazine*, vol. 5, no. 2, pp. 4–24, 1988.
- [8] J. Flanagan, D. Berkley, G. Elko, J. West, and M. Sondhi, “Autodirective microphone systems,” *Acta Acustica united with Acustica*, vol. 73, no. 2, pp. 58–71, 1991.
- [9] D. H. Johnson and D. E. Dudgeon, *Array signal processing: concepts and techniques*, Simon & Schuster, Inc., 1992.
- [10] H. L. Van Trees, *Optimum array processing: Part IV of detection, estimation, and modulation theory*, John Wiley & Sons, 2004.
- [11] D. G. Meyer, “Digital control of loudspeaker array directivity,” *J. Audio Eng. Soc.*, vol. 32, no. 10, pp. 747–754, 1984.
- [12] M. M. Boone, W.-H. Cho, and J.-G. Ih, “Design of a highly directional endfire loudspeaker array,” *J. Audio Eng. Soc.*, vol. 57, no. 5, pp. 309–325, 2009.
- [13] B. Rafaely and D. Khaykin, “Optimal model-based beamforming and independent steering for spherical loudspeaker arrays,” *IEEE Trans. Audio Speech Lang. Proc.*, vol. 19, no. 7, pp. 2234–2238, 2011.
- [14] Y. Haneda, K. Furuya, and A. Kataoka, “Evaluating small end-fire loudspeaker array under various reverberations,” *Acoust. Sci. & Tech.*, vol. 32, no. 6, pp. 244–250, 2011.

- [15] F. Olivieri, F. M. Fazi, M. Shin, and P. Nelson, “Pressure-matching beam-forming method for loudspeaker arrays with frequency dependent selection of control points,” in *Proc. 138th Conv. Audio Eng. Soc.*, 2015.
- [16] S. Kondo and K. Okubo, “Mid-air acoustic tweezers for non-contact pick up using multi-channel controlled ultrasonic transducer arrays,” *Japanese Journal of Applied Physics*, vol. 60, no. SD, pp. SDDD16, 2021.
- [17] B. B. Bauer, “Broadening the area of stereophonic perception,” *J. Audio Eng. Soc.*, vol. 8, no. 2, pp. 91–94, 1960.
- [18] V. Pulkki, “Virtual sound source positioning using vector base amplitude panning,” *J. Audio Eng. Soc.*, vol. 45, no. 6, pp. 456–466, 1997.
- [19] K. Hamasaki, K. Hiyama, and R. Okumura, “The 22.2 multichannel sound system and its application,” in *Proc. 118th Conv. Audio Eng. Soc.*, 2005.
- [20] L. S. Davis, R. Duraiswami, E. Grassi, N. A. Gumerov, Z. Li, and D. N. Zotkin, “High order spatial audio capture and its binaural head-tracked playback over headphones with HRTF cues,” in *Proc. 119th Conv. Audio Eng. Soc.*, 2005.
- [21] A. Avni, J. Ahrens, M. Geier, S. Spors, H. Wierstorf, and B. Rafaely, “Spatial perception of sound fields recorded by spherical microphone arrays with varying spatial resolution,” *J. Acoust. Soc. Am.*, vol. 133, no. 5, pp. 2711–2721, 2013.
- [22] A. Ando, “Theory of Three-Dimensional Sound Field Reproduction (高臨場感音響技術とその理論),” *IEICE Fundamentals Review*, vol. 3, no. 4, pp. 33–46, 2010 (in Japanese).
- [23] P. A. Nelson, F. Orduna-Bustamante, and H. Hamada, “Multi-channel signal processing techniques in the reproduction of sound,” in *Audio Engineering Society Conference: UK 7th Conference: Digital Signal Processing (DSP)*. Audio Engineering Society, 1992.
- [24] O. Kirkeby and P. A. Nelson, “Reproduction of plane wave sound fields,” *J. Acoust. Soc. Am.*, vol. 94, no. 5, pp. 2992–3000, 1993.
- [25] S. Ise, “A principle of sound field control based on the Kirchhoff-Helmholtz integral equation and the theory of inverse systems,” *Acta Acustica united with Acustica*, vol. 85, no. 1, pp. 78–87, 1999.
- [26] M. A. Poletti, “A unified theory of horizontal holographic sound systems,” *J. Audio Eng. Soc.*, vol. 48, no. 12, pp. 1155–1182, 2000.
- [27] D. B. Ward and T. D. Abhayapala, “Reproduction of a plane-wave sound field using an array of loudspeakers,” *IEEE Trans. Speech Audio Proc.*, vol. 9, no. 6, pp. 697–707, 2001.
- [28] M. A. Poletti, “Three-dimensional surround sound systems based on spherical harmonics,” *J. Audio Eng. Soc.*, vol. 53, no. 11, pp. 1004–1025, 2005.
- [29] J. Ahrens and S. Spors, “Analytical driving functions for higher order ambisonics,” in *Proc. IEEE Int. Conf. Acoust. Speech and Signal Processing (ICASSP)*, pp. 373–376, 2008.

- [30] S. Koyama, Y. Hiwasaki, K. Furuya, and Y. Haneda, “Inversewave propagation for reproducing virtual sources in front of loudspeaker array,” in *Proc. IEEE 19th European Signal Processing Conference (EUSIPCO)*, pp. 1322–1326, 2011.
- [31] S. Koyama, K. Furuya, Y. Hiwasaki, and Y. Haneda, “Analytical approach to wave field reconstruction filtering in spatio-temporal frequency domain,” *IEEE Trans. Audio Speech Lang. Proc.*, vol. 21, no. 4, pp. 685–696, 2013.
- [32] F. Schultz, G. Firtha, P. Fiala, and S. Spors, “Wave field synthesis driving functions for large-scale sound reinforcement using line source arrays,” in *Proc. 142th Conv. Audio Eng. Soc.*, 2017.
- [33] Y. J. Wu and T. D. Abhayapala, “Spatial multizone soundfield reproduction: Theory and design,” *IEEE Trans. Audio Speech Lang. Proc.*, vol. 19, no. 6, pp. 1711–1720, 2011.
- [34] S. Koyama, K. Furuya, Y. Hiwasaki, Y. Haneda, and Y. Suzuki, “Sound field reproduction using multiple linear arrays based on wave field reconstruction filtering in helicalwave spectrum domain,” in *Proc. IEEE Int. Conf. Acoust. Speech and Signal Processing (ICASSP)*, pp. 271–275, 2013.
- [35] S. Koyama, *Boundary integral approach to sound field transform and reproduction*, Ph.D. thesis, The University of Tokyo, 2014.
- [36] T. Okamoto, “Analytical methods of generating multiple sound zones for open and baffled circular loudspeaker arrays,” in *Proc. IEEE Workshop on Applications of Signal Processing to Audio and Acoustics (WASPAA)*, pp. 1–5, 2015.
- [37] A. Omoto, S. Ise, Y. Ikeda, K. Ueno, S. Enomoto, and M. Kobayashi, “Sound field reproduction and sharing system based on the boundary surface control principle,” *Acoust. Sci. & Tech.*, vol. 36, no. 1, pp. 1–11, 2015.
- [38] S. Koyama, G. Chardon, and L. Daudet, “Joint source and sensor placement for sound field control based on empirical interpolation method,” in *Proc. IEEE Int. Conf. Acoust. Speech and Signal Processing (ICASSP)*, pp. 501–505. IEEE, 2018.
- [39] D. Shinjo, K. Yasueda, and A. Kataoka, “Arrangement of control points by genetic algorithm for multiple sound zone generation using multi-point control method (多点制御法を用いた複数エリア再生における遺伝的アルゴリズムを活用した制御点配置の決定方法),” *IEICE Tech. Rep.*, vol. 118, no. 357, EA2018-83, pp. 15–20, 2018 (in Japanese).
- [40] J. Young and J. Bertrand, “Multiple scattering by two cylinders,” *J. Acoust. Soc. Am.*, vol. 58, no. 6, pp. 1190–1195, 1975.
- [41] J. V. Sánchez-Pérez, D. Caballero, R. Martínez-Sala, C. Rubio, J. Sánchez-Dehesa, F. Meseguer, J. Llinares, and F. Gálvez, “Sound attenuation by a two-dimensional array of rigid cylinders,” *Physical Review Letters*, vol. 80, no. 24, pp. 5325, 1998.
- [42] Y.-Y. Chen and Z. Ye, “Acoustic attenuation by two-dimensional arrays of rigid cylinders,” *Physical Review Letters*, vol. 87, no. 18, pp. 184301, 2001.

- [43] J. Ahrens and S. Spors, “Sound field reproduction using planar and linear arrays of loudspeakers,” *IEEE Trans. Audio Speech Lang. Proc.*, vol. 18, no. 8, pp. 2038–2050, 2010.
- [44] S. Spors, R. Rabenstein, and J. Ahrens, “The theory of wave field synthesis revisited,” in *Proc. 124th Conv. Audio Eng. Soc.*, 2008.
- [45] N. Ueno, S. Koyama, and H. Saruwatari, “Kernel ridge regression with constraint of Helmholtz equation for sound field interpolation,” in *2018 16th International Workshop on Acoustic Signal Enhancement (IWAENC)*, pp. 1–440. IEEE, 2018.
- [46] E. G. Williams, *Fourier acoustics: sound radiation and nearfield acoustical holography*, Elsevier, 1999.
- [47] A. Ando, *Sound field reproduction (音場再現)*, Corona Publishing, 2014 (in Japanese).
- [48] Y. Haneda, “Audio Signal Processing in Wavenumber Domain: Plane Wave, Circular Harmonic, Spherical Harmonic Expansions and Array Signal Processing (音の波数領域信号処理),” *IEICE Fundamentals Review*, vol. 11, no. 4, pp. 243–255, 2018 (in Japanese).
- [49] J. Ahrens, *Analytic methods of sound field synthesis*, Springer Science & Business Media, 2012.
- [50] M. M. Boone, E. N. Verheijen, and P. F. Van Tol, “Spatial sound-field reproduction by wave-field synthesis,” *J. Audio Eng. Soc.*, vol. 43, no. 12, pp. 1003–1012, 1995.
- [51] E. W. Start, *Direct sound enhancement by wave field synthesis*, Ph.D. thesis, Delft University of Technology, 1997.
- [52] E. Verheijen, *Sound reproduction by wave field synthesis*, Ph.D. thesis, Delft University of Technology, 1997.
- [53] W. P. J. De Bruijn, *Application of wave field synthesis in videoconferencing*, Ph.D. thesis, Delft University of Technology, 2004.
- [54] R. G. Oldfield, *The analysis and improvement of focused source reproduction with wave field synthesis*, Ph.D. thesis, University of Salford, 2013.
- [55] S. Spors, H. Wierstorf, M. Geier, and J. Ahrens, “Physical and perceptual properties of focused virtual sources in wave field synthesis,” in *Proc. 127th Conv. Audio Eng. Soc.*, 2009.
- [56] S. Spors and J. Ahrens, “Reproduction of focused sources by the spectral division method,” in *Proc. 4th Int. Symp. Commun. Control, Signal Processing (ISCCSP)*, pp. 1–5, 2010.
- [57] M. Kolundzija, C. Faller, and M. Vetterli, “Reproducing sound fields using MIMO acoustic channel inversion,” *J. Audio Eng. Soc.*, vol. 59, pp. 721–734, 2011.
- [58] J. Hannemann and K. D. Donohue, “Virtual sound source rendering using a multipole-expansion and method-of-moments approach,” *J. Audio Eng. Soc.*, vol. 56, no. 6, pp. 473–481, 2008.

- [59] W. Zhang and T. D. Abhayapala, “2.5 D sound field reproduction in higher order Ambisonics,” in *Proc. 14th International Workshop on Acoustic Signal Enhancement (IWAENC)*, pp. 342–346, 2014.
- [60] F. M. Fazi, M. Shin, F. Olivieri, S. Fontana, and Y. Lang, “Comparison of pressure-matching and mode-matching beamforming for methods for circular loudspeaker arrays,” in *Proc. 137th Conv. Audio Eng. Soc.*, 2014.
- [61] G. Firtha, P. Fiala, F. Schultz, and S. Spors, “On the general relation of wave field synthesis and spectral division method for linear arrays,” *IEEE/ACM Trans. Audio Speech Lang. Proc.*, vol. 26, no. 12, pp. 2393–2403, 2018.
- [62] F. Schultz, G. Firtha, F. Winter, and S. Spors, “On the Connections of High-Frequency Approximated Ambisonics and Wave Field Synthesis,” in *Proc. of German Annual Conference on Acoustics (DAGA)*, pp. 1446–1449, 2019.
- [63] S. Favrot, M. Marschall, J. Käsbaach, J. Buchholz, and T. Weller, “Mixed-order ambisonics recording and playback for improving horizontal directionality,” in *Proc. 131st Conv. Audio Eng. Soc.*, 2011.
- [64] T. Okamoto, “2.5 D higher order ambisonics for a sound field described by angular spectrum coefficients,” in *Proc. IEEE Int. Conf. Acoust. Speech and Signal Processing (ICASSP)*, pp. 326–330, 2016.
- [65] A. Gupta and T. D. Abhayapala, “Three-dimensional sound field reproduction using multiple circular loudspeaker arrays,” *IEEE Trans. Audio Speech Lang. Proc.*, vol. 19, no. 5, pp. 1149–1159, 2011.
- [66] T. Kimura, Y. Yamakata, and M. Katsumoto, “Theoretical study of near 3D sound field reproduction using wave field synthesis (波面合成法を用いた近接三次元音場再生の理論的研究),” *IEICE Tech. Rep.*, vol. 108, no. 20, EA2008-4, pp. 17–22, 2008 (in Japanese).
- [67] T. Kimura, Y. Yamakata, M. Katsumoto, T. Okamoto, S. Yairi, Y. Iwaya, and Y. Suzuki, “Three-dimensional radiated sound field display system using directional loudspeakers and wave field synthesis,” *Acoust. Sci. & Tech.*, vol. 33, no. 1, pp. 11–20, 2012.
- [68] M. Møller, M. Olsen, F. T. Agerkvist, J. Dyreby, and G. K. Munch, “Circular loudspeaker arrays with controllable directivity,” in *Proc. 128th Conv. Audio Eng. Soc.* Audio Engineering Society, 2010.
- [69] M. Kolundžija, C. Faller, and M. Vetterli, “Baffled circular loudspeaker array with broadband high directivity,” in *Proc. IEEE Int. Conf. Acoust. Speech and Signal Processing (ICASSP)*, pp. 73–76. IEEE, 2010.
- [70] M. R. Bai and Y.-H. Hsieh, “Point focusing using loudspeaker arrays from the perspective of optimal beamforming,” *J. Acoust. Soc. Am.*, vol. 137, no. 6, pp. 3393–3410, 2015.
- [71] K. Sato and Y. Haneda, “Sidelobe suppression by desired directivity pattern optimization for a small circular loudspeaker array,” *Acoust. Sci. & Tech.*, vol. 39, no. 3, pp. 243–251, 2018.
- [72] B. Rafaely, *Fundamentals of spherical array processing*, vol. 16, Springer, 2018.

- [73] J. Meyer and G. Elko, “A highly scalable spherical microphone array based on an orthonormal decomposition of the soundfield,” in *Proc. IEEE Int. Conf. Acoust. Speech and Signal Processing (ICASSP)*, vol. 2, pp. II–1781. IEEE, 2002.
- [74] K. Imaizumi and Y. Haneda, “Personal audio reproduction using two wearable end-fire loudspeaker arrays,” *J. Acoust. Soc. Am.*, vol. 140, no. 4, pp. 3057–3058, 2016.
- [75] Y. Ito and Y. Haneda, “Investigation Into Transaural System with Beamforming Using a Circular Loudspeaker Array Set at Off-center Position from the Listener,” in *Proc. 23rd International Congress on Acoustics (ICA)*, 2019.
- [76] Y. Ren and Y. Haneda, “Virtual Source Reproduction Using Two Rigid Circular Loudspeaker Arrays,” in *Proc. Audio Engineering Society 145th International Convention (AES)*, 2018.
- [77] Y. Ren and Y. Haneda, “Two-dimensional exterior sound field reproduction using two rigid circular loudspeaker arrays,” *The Journal of the Acoustical Society of America*, vol. 148, no. 4, pp. 2236–2247, 2020.
- [78] P. A. Martin, *Multiple scattering: interaction of time-harmonic waves with N obstacles*, Number 107. Cambridge University Press, 2006.
- [79] G. N. Watson, *A treatise on the theory of Bessel functions*, Cambridge university press, 1995.
- [80] Y. Ren and Y. Haneda, “How the distance and radius of two circular loudspeaker arrays affect sound field reproductions and directivity controls,” in *Proc. 23rd International Congress on Acoustics (ICA)*, 2019.
- [81] M. A. Poletti, T. D. Abhayapala, and P. Samarasinghe, “Interior and exterior sound field control using two dimensional higher-order variable-directivity sources,” *J. Acoust. Soc. Am.*, vol. 131, no. 5, pp. 3814–3823, 2012.
- [82] M. A. Poletti, T. Betlehem, and T. D. Abhayapala, “Comparison of sound reproduction using higher order loudspeakers and equivalent line arrays in free-field conditions,” *J. Acoust. Soc. Am.*, vol. 136, no. 1, pp. 192–200, 2014.
- [83] M. A. Poletti and T. D. Abhayapala, “Spatial sound reproduction systems using higher order loudspeakers,” in *Proc. IEEE Int. Conf. Acoust. Speech and Signal Processing (ICASSP)*, pp. 57–60, 2011.
- [84] T. D. Abhayapala and A. Gupta, “Spherical harmonic analysis of wavefields using multiple circular sensor arrays,” *IEEE Trans. Audio Speech Lang. Proc.*, vol. 18, no. 6, pp. 1655–1666, 2010.
- [85] P. Samarasinghe, T. Abhayapala, and M. Poletti, “Wavefield analysis over large areas using distributed higher order microphones,” *IEEE/ACM Trans. Audio Speech Lang. Proc.*, vol. 22, no. 3, pp. 647–658, 2014.
- [86] N. Ueno, S. Koyama, and H. Saruwatari, “Sound field recording using distributed microphones based on harmonic analysis of infinite order,” *IEEE Signal Processing Letters*, vol. 25, no. 1, pp. 135–139, 2017.
- [87] M. A. Poletti, T. Betlehem, and T. Abhayapala, “Higher Order Loudspeakers for Improved Surround Sound Reproduction in Rooms,” in *Proc. 133rd Conv. Audio Eng. Soc.*, 2012.

- [88] M. A. Poletti, T. Betlehem, and T. Abhayapala, “Higher-order loudspeakers and active compensation for improved 2D sound field reproduction in rooms,” *J. Audio Eng. Soc.*, vol. 63, no. 1/2, pp. 31–45, 2015.
- [89] G. A. Korn and T. M. Korn, *Mathematical handbook for scientists and engineers: definitions, theorems, and formulas for reference and review*, Courier Corporation, 2000.
- [90] É. Mathieu, “Memoir on vibrations of an elliptic membrane (Mémoire sur le mouvement vibratoire d’une membrane de forme elliptique),” *J. Math. Pures Appl.*, vol. 13, pp. 137–203, 1868 (in French).
- [91] P. M. Morse and H. Feshbach, *Methods of Theoretical Physics Parts I and II*, McGraw-Hill, 1953.
- [92] J. Meixner and F. W. Schäfke, *Mathieu functions and Spheroidal Functions (Mathieusche Funktionen und Sphäroidfunktionen)*, Springer, 1954 (in German).
- [93] H. M. Jones, R. A. Kennedy, and T. D. Abhayapala, “On dimensionality of multipath fields: Spatial extent and richness,” in *Proc. IEEE Int. Conf. Acoust. Speech and Signal Processing (ICASSP)*, vol. 3, pp. III–2837, 2002.
- [94] Y. Ren, K. Imaizumi, K. Tsutsumi, and Y. Haneda, “2D sound field reproduction with elliptical loudspeaker array based on circular microphone array signals,” in *Proc. Audio Engineering Society 148th International Convention (AES)*, 2020.
- [95] K. Saermark, “A note on addition theorems for Mathieu functions,” *Zeitschrift für angewandte Mathematik und Physik ZAMP*, vol. 10, no. 4, pp. 426–428, 1959.
- [96] R. A. Kennedy, P. Sadeghi, T. D. Abhayapala, and H. M. Jones, “Intrinsic limits of dimensionality and richness in random multipath fields,” *IEEE Trans. Sig. Proc.*, vol. 55, no. 6, pp. 2542–2556, 2007.
- [97] S. Kaneko and R. Duraiswami, “Multiple scattering ambisonics: Three-dimensional sound field estimation using interacting spheres,” *JASA Express Letters*, vol. 1, no. 8, pp. 084801, 2021.
- [98] S. Kaneko and R. Duraiswami, “Spheroidal ambisonics: Spatial audio in spheroidal bases,” *JASA Express Letters*, vol. 1, no. 8, pp. 084803, 2021.
- [99] M. Poletti, “An investigation of 2-d multizone surround sound systems,” in *Proc. 125th Conv. Audio Eng. Soc.*, 2008.
- [100] Y. J. Wu and T. D. Abhayapala, “Spatial multizone soundfield reproduction: Theory and design,” *IEEE Trans. Audio Speech Lang. Proc.*, vol. 19, no. 6, pp. 1711–1720, 2010.
- [101] W. Jin, W. B. Kleijn, and D. Virette, “Multizone soundfield reproduction using orthogonal basis expansion,” in *Proc. IEEE Int. Conf. Acoust. Speech and Signal Processing (ICASSP)*, pp. 311–315. IEEE, 2013.
- [102] W. Zhang, T. D. Abhayapala, T. Betlehem, and F. M. Fazi, “Analysis and control of multi-zone sound field reproduction using modal-domain approach,” *J. Acoust. Soc. Am.*, vol. 140, no. 3, pp. 2134–2144, 2016.

- [103] N. Ueno, S. Koyama, and H. Saruwatari, “Listening-area-informed sound field reproduction based on circular harmonic expansion,” in *Proc. IEEE Int. Conf. Acoust. Speech and Signal Processing (ICASSP)*, pp. 111–115. IEEE, 2017.
- [104] K. Yasueda, D. Shinjo, and A. Kataoka, “Multiple-area Sound Reproduction by Multi-point Control Method with Linear Loudspeaker Array (実環境における多点制御法を用いた複数エリア再生),” *IEICE Transactions on Fundamentals of Electronics, Communications and Computer Sciences*, vol. J103-A, no. 1, pp. 9–16, 2020 (in Japanese).
- [105] Y. Kaneda, “Noise reduction performance of various signals for impulse response measurement,” *J. Audio Eng. Soc.*, vol. 63, no. 5, pp. 348–357, 2015.

List of Publications

Journal Papers

- [A1] Y. Ren and Y. Haneda, “Two-dimensional exterior sound field reproduction using two rigid circular loudspeaker arrays,” *The Journal of the Acoustical Society of America*, vol. 148, no. 4, pp. 2236–2247, 2020.
- [A2] Y. Ren and Y. Haneda, “Directivity control using two circular loudspeaker array,” *Journal of Signal Processing*, vol. 23, no. 4, 2019.

International Conferences

- [B1] Y. Ren and Y. Haneda, “2D Local Exterior Sound Field Reproduction Using an Addition Theorem Based on Circular Harmonic Expansion,” in *Proc. IEEE Workshop on Applications of Signal Processing to Audio and Acoustics (WASPAA)*. IEEE, 2021.
- [B2] Y. Ren and Y. Haneda, “Beamforming using two rigid circular loudspeaker arrays: Numerical simulations and experiments,” in *Proc. Audio Engineering Society 150th International Convention (AES)*. Audio Engineering Society, 2021.
- [B3] Y. Ren, K. Imaizumi, K. Tsutsumi, and Y. Haneda, “2D sound field reproduction with elliptical loudspeaker array based on circular microphone array signals,” in *Proc. Audio Engineering Society 148th International Convention (AES)*, 2020.
- [B4] Y. Ren and Y. Haneda, “How the distance and radius of two circular loudspeaker arrays affect sound field reproductions and directivity controls,” in *Proc. 23rd International Congress on Acoustics (ICA)*, 2019.
- [B5] Y. Ren and Y. Haneda, “Directivity control using two circular loudspeaker array,” in *Proc. RISP International Workshop on Nonlinear Circuits, Communications and Signal Processing (NCSP)*, 2019.
- [B6] Y. Ren and Y. Haneda, “Virtual Source Reproduction Using Two Rigid Circular Loudspeaker Arrays,” in *Proc. Audio Engineering Society 145th International Convention (AES)*, 2018.

Domestic Conferences

- [C1] Y. Ren and Y. Haneda, “A 2D Local Exterior Sound Field Reproduction Method Based on an Addition Theorem of Cylindrical Functions (円筒関数の加法定理を用いた2次元外側局所音場再現法),” in *2021 Autumn meeting of the Acoustical Society of Japan*, pp. 171–174, 2021 (in Japanese).
- [C2] Y. Ren and Y. Haneda, “Automatic Measurement and Visualisation over a Three-dimensional Cuboid Sound Field (3次元直方体音場の自動測定および可視化),” in *2021 Spring meeting of the Acoustical Society of Japan*, pp. 363–364, 2021 (in Japanese).
- [C3] Y. Ren and Y. Haneda, “Beamforming using Rigid Elliptical Loudspeaker Array (剛楕円スピーカアレイを用いたビームフォーミングについての検討),” in *2021 Spring meeting of the Acoustical Society of Japan*, pp. 337–338, 2021 (in Japanese).
- [C4] Y. Ren and Y. Haneda, “On Virtual Source Reproduction using Rigid Elliptical Loudspeaker Array (剛楕円スピーカアレイを用いた焦点音源生成についての検討),” in *2020 Autumn meeting of the Acoustical Society of Japan*, pp. 199–202, 2020 (in Japanese).
- [C5] Y. Ren and Y. Haneda, “Applying Circular Microphone Array Signal for Interior Sound Field Reproduction with Elliptical Loudspeaker Array (円形アレイ收音信号を用いた楕円アレイの内部音場再現),” in *2020 Spring meeting of the Acoustical Society of Japan*, pp. 435–438, 2020 (in Japanese).
- [C6] Y. Ren and Y. Haneda, “An Analytical Method of 2-dimensional Sound Field Reproduction for Elliptical Loudspeaker Array (楕円スピーカアレイに対する解析的な2次元音場再現法),” in *2019 Autumn meeting of the Acoustical Society of Japan*, pp. 653–654, 2019 (in Japanese).
- [C7] Y. Ren and Y. Haneda, “A Method for Exterior Sound Field Reproduction in Circular Harmonic Domain Using Two Rigid Circular Loudspeaker Arrays (円調和展開に基づく2つの剛体円形スピーカアレイを用いた外側音場再現),” in *2019 Spring meeting of the Acoustical Society of Japan*, pp. 309–312, 2019 (in Japanese).
- [C8] Y. Ren and Y. Haneda, “Reproduction of Virtual Source Using Two Rigid Circular Loudspeaker Array (2つの剛体円形スピーカアレイを用いた仮想音源生成),” in *2018 Autumn meeting of the Acoustical Society of Japan*, pp. 1511–1514, 2018 (in Japanese).
- [C9] Y. Ren, K. Sato, and Y. Haneda, “Reproduction of Virtual Source Exterior to Circular Loudspeaker Array based on Mode-Matching Approach (円形スピーカアレイの外側へのモードマッチングによる仮想音源生成),” in *2018 Spring meeting of the Acoustical Society of Japan*, pp. 525–526, 2018 (in Japanese).